Short-Pulse Driven Transport Measurements in Dense Plasmas

by

Andrew James McKelvey

A dissertation submitted in partial fulfillment
of the requirements for the degree of
Doctor of Philosophy
(Nuclear Engineering and Radiological Sciences)
in the University of Michigan
2019

Doctoral Committee:

Professor Karl M. Krushelnick, Chair
Professor R. Paul Drake
Dr. Ronnie L. Shepherd, Lawrence Livermore National Laboratory
Associate Professor Alexander G.R. Thomas

Andrew James McKelvey

ajmckelv@umich.edu

ORCID iD: 0000-0001-8921-9313

For Ashley.

ACKNOWLEDGMENTS

My path to the completion of this thesis was a long one. As such, there are many people that deserve a great deal of thanks for making it possible for me to be where I am today. First, I'd like to thank my academic advisor, Karl Krushelnick, for giving me the opportunity and the environment in which to learn about short-pulse laser-plasma physics. The High Field Science group at the University of Michigan was excellent, and I'd like to thank John Nees for teaching me how to set up a laser experiment and the value of super glue. My time at Michigan was made richer by my peers in the solid-target experimental group, Calvin Zulick and Anthony Raymond. Thank you both.

The research presented here would not have been possible without the endless support of my mentor at LLNL, Ronnie Shepherd. I am extremely grateful for the countless hours of discussion, argument, and humor. These were invaluable and provided the fuel to keep going. I would also like to acknowledge Ed Marley and Jaebum Park who went before me as graduate students at LLNL. They walked the same road and were always there to remind me of the light at the end of the tunnel. I would like to thank Elijah Kemp for his immeasurable help with HYDRA. I would like to thank Phil Sterne for his endless patience and enthusiasm when explaining material properties and how they are modeled. Likewise, thanks to Howard Scott for always being willing to take the time to teach a graduate student about radiation transport.

These experiments were all performed at large facilities that required the skills and passion of many people who I can't thank enough. I would like to thank David Hoarty, Matt Hill, and Colin Brown for allowing me to participate in exciting large-scale experiments at Orion and for traveling to help with the LCLS experiment. The staff at all three facilities—Orion, JLF, and MEC at LCLS—all deserve much praise.

Above all others, I'd like to thank Ashley.

PREFACE

This thesis presents work either being prepared by or already reported by the Author in the following publications:

1. **A. McKelvey**, G. E. Kemp, P. A. Sterne, A. Fernandez-Panella, R. Shepherd, M. Marinak, A. Link, G. W. Collins, H. Sio, J. King, R. R. Freeman, R. Hua, C. McGuffey, J. Kim, F. N. Beg, and Y. Ping. Thermal conductivity measurements of proton heated warm dense aluminum. *Scientific Reports* **7**, 7015 (2017).
2. **A. McKelvey**, H. A. Scott, P. Beiersdorfer, G. V. Brown, D. J. Hoarty, C. R. D. Brown, M. P. Hill, L. M. R. Hobbs, S. F. James, K. Krushelnick, and R. Shepherd. Line transfer effects on inferring plasma conditions in buried layer experiments (in preparation).
3. **A. McKelvey**, G. E. Kemp, P. A. Sterne, R. Shepherd, M. Marinak, G. W. Collins, S. Jiang, R. Hua, F. N. Beg, E. Galtier, H. J. Lee, K. Krushelnick, and Y. Ping. Calculation of the optical emission characteristics of differentially heated gold-iron multi-layer targets (in preparation).

During the course of the work presented here, the Author also participated in other research activities that resulted in the following publications:

1. **A. McKelvey**, T. Lockard, G. V. Brown, P. Beiersdorfer, K. Krushelnick, and R. Shepherd. Low-flux calibration of Fuji-BAS image plates using an electron beam ion trap (in preparation)
2. Y. Ping, H. D. Whitley, **A. McKelvey**, G. E. Kemp, P. A. Sterne, R. Shepherd, M. Marinak, R. Hua, F. N. Beg, and J. H. Eggert. Heat-Release Equation-of-State and Thermal Conductivity of Warm Dense Carbon by Proton Differential Heating (in preparation).
3. P. Beiersdorfer, G. V. Brown, **A. McKelvey**, R. Shepherd, D. J. Hoarty, C. R. D. Brown, M. P. Hill, L. M. R. Hobbs, S. F. James, J. Morton, and L. Wilson. High-resolution measurements of Cl15+ line shifts in hot, solid-density plasmas. *Phys. Rev. A.* **100**, 012511 (2019)

4. P. Beiersdorfer, E. W. Magee, G. V. Brown, N. Hell, **A. McKelvey**, R. Shepherd, D. J. Hoarty, C. R. D. Brown, M. P. Hill, L. M. R. Hobbs, S. F. James, and L. Wilson. High resolution, high signal-to-noise crystal spectrometer for measurements of line shifts in high-density plasmas. *Review of Scientific Instruments* **89**, 10F120 (2018).

5. A. E. Raymond, C. F. Dong, **A. McKelvey**, C. Zulick, N. Alexander, A. Bhattacharjee, P. T. Campbell, H. Chen, V. Chvykov, E. Del Rio, P. Fitzsimmons, W. Fox, B. Hou, A. Maksimchuk, C. Mileham, J. Nees, P. M. Nilson, C. Stoeckl, A. G. R. Thomas, M. S. Wei, V. Yanovsky, K. Krushelnick, and L. Willingale. Relativistic-electron-driven magnetic reconnection in the laboratory. *Phys. Rev. E* **98**, 043207 (2018).

6. C. Zulick, A. Raymond, **A. McKelvey**, V. Chvykov, A. Maksimchuk, A. G. R. Thomas, L. Willingale, V. Yanovsky, and K. Krushelnick. Target surface area effects on hot electron dynamics from high intensity laser plasma interactions. *New Journal of Physics* **18**, 063020 (2016).

7. C. A. D. Stefano, C. C. Kuranz, J. F. Seely, A. G. R. Thomas, R. P. Drake, P. A. Keiter, G. J. Williams, J. Park, H. Chen, M. J. MacDonald, A. M. Rasmus, W. C. Wan, N. R. Pereira, A. S. Joglekar, **A. McKelvey**, Z. Zhao, S. R. Klein, G. E. Kemp, L. C. Jarrott, C. M. Krauland, J. Peebles, and B. Westover. Measurements of the energy spectrum of electrons emanating from solid materials irradiated by a picosecond laser. *Physics of Plasmas* **22**, 043113 (2015).

TABLE OF CONTENTS

Chapter

LIST OF FIGURES

Figure

LIST OF TABLES

Table

LIST OF APPENDICES

Appendix

LIST OF ABBREVIATIONS

AA Average Atom

ASE Amplified Spontaneous Emission

AWE Atomic Weapons Establishment

BGK Bhatnagar-Gross-Krook

CPA Chirped Pulse Amplification

CR Collisional Radiative

CXRO Center for X-Ray Optics

DFT Density Functional Theory

EOS Equation of State

FDI Fourier Domain Interferometer

FEL Free Electron Laser

FWHM Full Width at Half Maximum

HED High Energy Density

ICF Intertial Confinement Fusion

IP Image Plate

IMC Implicit Monte Carlo

JLF Jupiter Laser Facility

LCLS Linac Coherent Light Source

LEOS Livermore Equation of State

LLNL Lawrence Livermore National Laboratory

LTE Local Thermodynamic Equilibrium

MD Molecular Dynamics

MEC Matter in Extreme Conditions

NLTE Non-Local Thermodynamic Equilibrium

NRB Net Radiative Bracket

OTR Optical Transition Radiation

PIC Particle-in-cell

PSL Photostimulated Luminescence

QEOS Quotidian Equation of State

QMD Quantum Molecular Dynamics

SASE Self-Amplified Spontaneous Emission

SLAC Stanford Linear Accelerator

SOP Streaked Optical Pyrometer

SPOPA Short Pulse Optical Parametric Amplifier

TE Thermodynamic Equilibrium

TIM Ten Inch Manipulator

TNSA Target Normal Sheath Acceleration

TP Thomson Parabola

WDM Warm Dense Matter

XFEL X-ray Free Electron Laser

ABSTRACT

Accurate transport properties—such as opacity, and electrical & thermal conductivities—provide crucial input for the intricate physics models necessary to describe the dynamics of complex, high energy density (HED) systems. This includes stars, giant planets, and inertial confinement fusion plasmas. However, these theoretical transport models present challenges as the phase space often sits at the intersection of solid, liquid, gas, and plasma where many effects of comparable magnitude must be considered. Additionally, the transient nature of such high energy density materials complicates experimental measurement, and many theories remain sparsely benchmarked by data.

In the laboratory, HED material must be created via some combination of material compression to very high densities or by adding large amounts of energy to the material in a very short time. This thesis focuses on experiments utilizing the second technique. X-ray free-electron lasers (τ_{pulse} <100 fs) or short-pulse lasers (τ_{pulse} <1 ps) are capable of heating materials from room temperature to tens or even many hundreds of eV while keeping densities at appreciable fractions of their ambient value. This allows for the probing of material properties before hydrodynamics phenomena become dominant.

First, an experimental platform designed to constrain thermal conductivity models in warm dense matter is presented. Its basis relies on differentially heating multilayer targets (one high-Z layer and one low- to mid-Z layer) to generate a thermal gradient. This concept was first demonstrated using the Titan laser at the Jupiter Laser Facility, creating an intense proton beam to heat a gold/aluminum multilayer target. The temperature, reflectivity, and expansion of the rear surface were observed with time-resolved diagnostics as the thermal energy from the hot gold layer reached the coldest part of the aluminum layer. The data were compared with hydrodynamics models that self-consistently used the electrical and thermal conductivities to calculate observables. Measured temperatures were too low relative to predictions, possibly indicating the need to decrease tested conductivity models. This experiment was repeated using an X-ray free-electron laser at the Linac Coherent Light Source (LCLS) with gold/iron targets. Data are presented for this work along with calculations and a discussion of how the different drivers impact the experimental design and data quality.

Finally, data from a platform designed to measure opacities using short-pulse lasers at the Orion Laser Facility are presented. Spectroscopic measurements of silicon's K-shell that are both temporally and angularly resolved are benchmarked against the radiation transfer code Cretin. The validity of the commonly-used escape factor approximation is tested against the full solution of the radiation transfer equation and found to be in good agreement for presented experimental conditions. An analysis of the effects of radial gradients on spectroscopically inferred temperatures is found to lead to errors in the peak temperature as large as 50% as well as incorrect cooling rates. This emphasizes the importance of absolute emissivity calibrations and spatially resolved spot size measurements.

This work was performed under the auspices of the U.S. Department of Energy by Lawrence Livermore National Laboratory under Contract DE-AC52-07NA27344.

CHAPTER 1

Introduction

1.1 Applications of dense plasma transport

Dense, ionized material is present in most astrophysical bodies in our universe as well as fusion and laboratory plasmas. Knowledge of individual varieties of stars and planets aids our comprehension of the origin and evolution of our universe as a whole. Similarly, mastering control of experimental plasmas allows us to isolate and understand specific physical mechanisms used in the betterment of our day-to-day lives. Without the ability to observe the center of a giant planet or star or fusion capsule, we must turn to models to link all of the system's energy pathways (conduction, convection, radiation, etc.) to observable quantities. Such models provide a stringent test of human insight as each piece affects the other, often leading to drastically different physical conclusions based on constitutive model assumptions.

For example, uncertainty in the thermal conductivity of iron at conditions found in Earth's core impacts the prediction of when Earth's solid inner core formed, with estimates ranging from as little as 400 million years to 2.5 billion years ago[1]. The presence and size of the inner core strongly impacts the strength and mechanism of the geodynamo that powers our magnetic field. It impacts the heat flow into the mantle and the nucleation rate of light, buoyant elements which determine the convection characteristics in the mantle. Measurements of the paleomagnetic field have been used to constrain the nucleation of the core[2], but if true, recent measurements of the conductivity of iron would force the interpretation of the historic magnetic field records to change, requiring different physical mechanisms[3, 4, 5]. In the next section, I present a system of intense interest to the high energy density physics community that motivated the development of many of the models tested experimentally in the later chapters of this thesis: inertial confinement fusion.

1.1.1 Application: inertial confinement fusion

Thermonuclear fusion of light atoms is the engine that drives heat production in the cores of stars. Learning to create and harness a stable fusion reaction for power production on earth has been a priority in the United States, and elsewhere, since the early 1950's[6]. The appeal lies in the vast abundance of potential fuel, the inherent safety of the self-quenching reaction, and the dramatically-reduced production of long-lived radioactive waste (in comparison to fission energy production). The most easily achieved fusion reaction, due to its high cross-section, is

$$\mathrm{D} + \mathrm{T} \rightarrow \ ^{4}\mathrm{He}(3.5\ \mathrm{MeV}) + \mathrm{n}(14.1\ \mathrm{MeV}) \tag{1.1}$$

where D is a deuterium atom (^{2}H), and T, a tritium atom (^{3}H). The products of this reaction are a helium atom with 3.5 MeV of kinetic energy and a neutron with 14.1 MeV of kinetic energy. In order to fuse and release the combined 17.6 MeV of kinetic energy, hydrogen atoms must overcome the Coulomb potential between them. This potential barrier can be as large as 1 MeV[7]—well above achievable thermal energies. As such, atoms must rely on quantum tunneling, which demands both time and proximity. Creating a fusion reaction that is self-sustaining requires assembling a high material density, heating it up, and keeping it together long enough to generate a large reaction rate. The material is said to ignite when the energy produced by fusion reactions heats the fuel faster than the energy losses causes it to cool. This typically happens when the fusion reaction products efficiently deposit their energy within the fusing region. In a star, this is accomplished quite easily using its gravitational force and tremendous size. In man-made designs, more finesse is required, and different methods of confining the plasma have been developed. These generally split into two categories—(1) inertial confinement fusion (ICF) and (2) magnetic confinement fusion (MCF).

ICF uses the intrinsic inertia of mass to hold the fuel together long enough for sufficient fusion reactions to occur and a burn wave to propagate through the fuel. MCF relies on using strong magnetic fields to hold the plasma together and away from colder material in order to create a steady-state (or long-pulse) burning plasma. ICF is the most heavily-researched confinement method in the United States, partially due to its synergy with the Department of Energy's stockpile stewardship mission, and will be the focus here.

The largest ICF facility in the U.S. is the National Ignition Facility (NIF) and is located at Lawrence Livermore National Laboratory (LLNL). It is an impressive modern facility capable of delivering 1.8 MJ of frequency-tripled (λ=353 nm) laser light with 500 TW in 192 beams on target[8]. Figure 1.1 illustrates the steps in an indirect drive capsule implosion. The fuel capsules are approximately 1.1 mm and consist of an outer ablator layer (CH, Be, or high-density carbon), followed by varied thin layers to mitigate preheating or provide diagnostic features, followed by a deuterium-tritium (DT) ice shell (T$\approx$20 K), and finally a core of DT gas[9]. Optical lasers are focused on the wall of the high-Z hohlraum and converted into thermal energy within the hohlraum. The intense thermal radiation heats the outer ablator layers which rapidly expand, causing the remaining shell to begin imploding. Entropy must be minimized within the converging material in order to reach maximum compression. This is achieved by tailoring the radiation drive to launch consecutively-timed shocks which converge at the capsule center as the implosion stagnates. When this occurs, the central low-density DT fuel—termed the hot spot—reaches maximum temperature and areal density ($T_i \approx$5 keV & $\rho R \approx$0.3 g/cm^2) and initiates the fusion reaction. A burn wave begins and propagates as fusion-product alpha particles stop in the dense plasma fuel surrounding the hot spot. The entire process lasts for approximately 50 ps and releases a large neutron flux that can be harnessed for energy.

The indirect drive ICF approach presents additional challenges, requiring a vast collection of accurate material and transport properties in order to properly design an experiment[9, 11]. Understanding the laser interaction with the hohlraum requires detailed models for laser-plasma in-

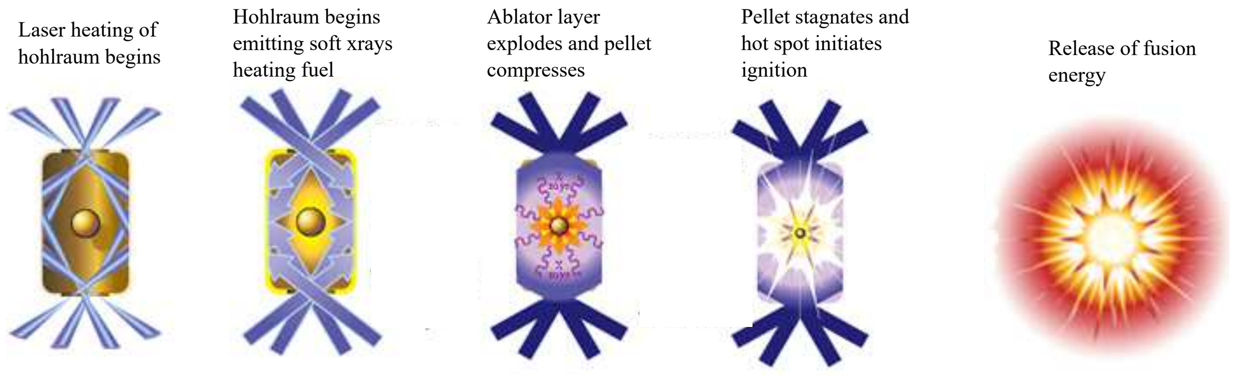

Figure 1.1: Illustration of the capsule implosion sequence for ICF. Figure credit of ref. [10]

teractions, non-thermal electron transport, and atomic physics which determines the opacity under non-local thermodynamic equilibrium (non-LTE) conditions. The imploding fuel pellet transitions through many decades of temperature and density space where the characteristic physics may change. Again, the opacity, ionization state, electron thermal conductivity, and equation of state are all crucial to design a system capable of achieving fusion ignition. Optimizing the overall performance on the road to ignition has focused on understanding and controlling four high-level implosion features—(1) the adiabat (fuel entropy) (2) the implosion velocity (3) the fuel mix and (4) the hotspot shape[9].

As an example, the electron thermal conductivity has a large impact on multiple areas of the indirect drive concept. The electron thermal conductivity at the ablator/fuel (Be/DT) interface plays a role in the growth rate of instabilities and consequent shell mixing[12]. Figure 1.2 shows hydrodynamic simulation results by B. Hammel of LLNL that demonstrate the effect of scaling the Lee & More thermal conductivity model[13] for DT and Be by 0.3 and 3.0 in an imploding ICF shell. The simulation is shown at the time of peak velocity, and the material conditions are approximately 10 g/cc and 10–30 eV—solidly in the warm dense matter regime. A lower conductivity value results in faster instability growth rate and more shell mixing. Also, at the hot spot/fuel interface, heat conducting into the cold shell from the hot spot affects the interior ablation rate and subsequent implosion velocity[14, 15]. Increased ablation of DT mass into the hot spot increases the density, which improves its ability to stop alpha particles and undergo a sustained reaction. However, it

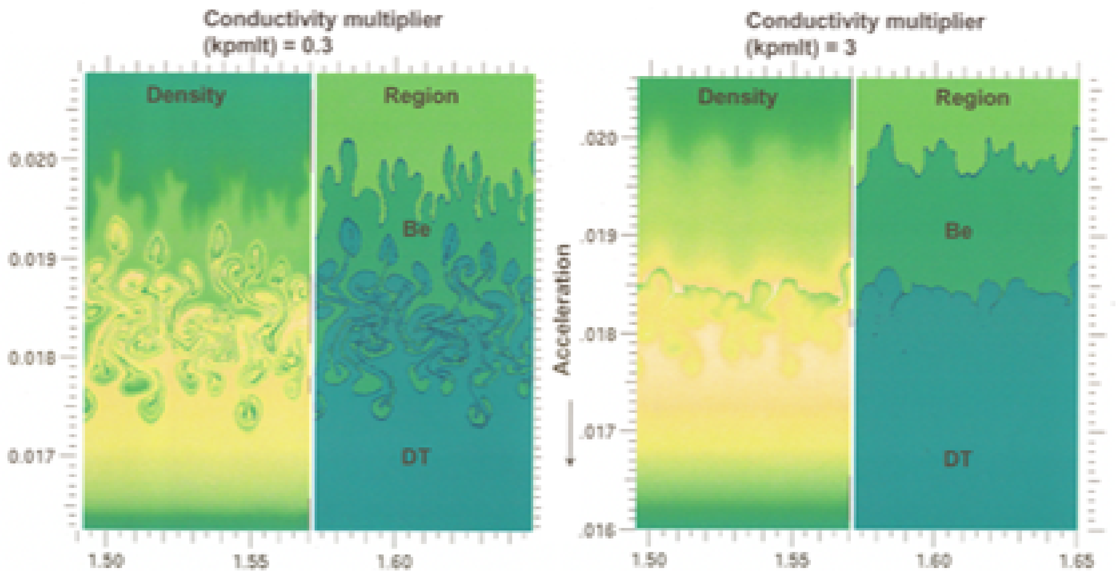

Figure 1.2: Hydrodynamics simulations on a NIF capsule showing the impact on the shell mixing of multiplying the electron thermal conductivity tables by 0.3 and 3.0. Figure credit B. Hammel[12].

also increases the energy required to ignite. These issues motivate simpler experiments used to test the many transport models required by the large-scale 3-D ICF models necessary for capsule design.

1.2 Characteristics of high density plasmas

Dense plasmas generate a unique problem set for modern physicists. To describe the regime, dimensionless parameters are most commonly introduced to quantify the relative importance of effects. One of the most fundamental parameters is the plasma parameter, Γ—the ratio of the potential energy between particles to the thermal energy

$$\Gamma = \frac{E_c}{k_B T} = \frac{(Ze)^2}{r_s k_B T}; \quad r_s = \left(\frac{3}{4\pi n_e}\right)^{1/3} \tag{1.2}$$

where n_e is the electron density, T is the temperature, and r_s is the Wigner-Seitz radius. This measures how strongly many-body interactions impact the system and material. A plasma with

$\Gamma > 1$ is said to be moderately or strongly coupled, with this occurring at high densities or low temperatures. The coupling parameter is closely related to the classical plasma parameter, $N_D = 4/3\pi n_e \lambda_D^3$. We can show that $\Gamma \propto 1/N_D^{2/3}$, and when the plasma is strongly coupled, it can never satisfy the criteria for an ideal plasma of $N_D \gg 1$.

A second parameter, called the electron degeneracy parameter, Θ, specifies when the electrons behave quantum mechanically. It is defined as the ratio of the thermal energy to the Fermi energy.

$$\Theta = \frac{k_B T}{\epsilon_F}; \quad \epsilon_F = \frac{\hbar^2}{2m_e}(3\pi^2 n_e)^{2/3} \tag{1.3}$$

When the system is degenerate ($\Theta \ll 1$), the thermal de'Broglie wavelength, $\lambda_{de} = \hbar/(2mk_BT)^{1/2}$, can become larger than the interparticle spacing, r_s, and the electron wave functions overlap. The degenerate electrons behave in a fundamentally different manner from classical physics, requiring Fermi-Dirac rather than Boltzmann statistics. In degenerate material, only electrons near the chemical potential may participate in transport processes such as conduction.

These effects occur over a wide region of phase space which includes ultracold neutral plasmas[16], but this thesis focuses on materials that are moderately coupled and partially to strongly degenerate at elevated temperatures (above the melting temperature). This phase space is often termed warm dense matter (WDM) or hot dense matter (HDM). In addition to the strongly coupled ions and electrons and degenerate electrons, these systems characteristically have only partial ionization leading to significant collisions with neutrals. The low number of particles per Debye sphere leads to imperfect shielding, and long range order persists.

Theoretical descriptions in this phase space are particularly challenging to develop as there is no small parameter or limiting behavior to exploit. It lies at the intersection of plasma physics and condensed matter physics, where theories from either field are not strictly valid. Traditionally, treatment relied on interpolations between two or more better-developed theories. More accurate models of WDM require detailed quantum mechanical calculations that account for degeneracy and collective effects on the electronic structure of atoms embedded within such a potential. The elevated temperatures stretch the accuracy and computational limits of methods, such as density functional theory (DFT), which was originally developed for much colder material. Even in the subset of HED phase space in which these models are tractable, other properties such as accurate opacities remain a challenge due to inability to treat the large number of atomic transitions self consistently with the many-coupled atoms. Such complex models must always make a determination of which properties can be averaged or excluded entirely, requiring validation over as much of the phase space as possible.

An increase in the number of facilities capable of creating large volumes of HED matter in tandem with a rapid increase in the capability of modern computing has led to intense interest in improving the theoretical models. However, experimental data capable of informing these models remains scarce due to the extreme difficulty in performing quality experiments. A 2009 report commissioned by the U.S. Department of Energy and the National Nuclear Security Administration explicitly highlights the need to develop measurement techniques for transport properties such as electrical and thermal conductivity in the WDM region as well as experimental opacity measurements of hot plasmas[17]. In this thesis, I describe several experimental efforts performed to help remedy this issue.

1.3 Thesis overview

This chapter has outlined the importance of accurate transport models in dense plasmas and the implications they have for our understanding of the world around us. Some of the theoretical and experimental complexities of high energy density (HED) physics, particularly in the warm dense matter (WDM) regime, have been outlined. The remainder of this thesis presents a set of experimental and computational efforts designed to measure electron heat conduction and radiation transfer in dense plasmas.

- Chapter 2 presents the theoretical background information necessary to discuss classical energy transport and some of the concepts behind widely-used quantum methods for dense plasmas with a focus on thermal conductivity and radiative transfer. It then discusses the ways matter interacts with different drivers to create experimental HED conditions.

- Chapter 3 discusses the facilities at which experiments were performed for this work and the basic concepts used for the diagnostics to infer physical parameters.
- Chapter 4 presents an experiment performed at the Jupiter Laser Facility (JLF) to study thermal conductivity in proton-heated warm dense aluminum.
- Chapter 5 presents a follow-up experiment to the work at JLF, performed using the Linac Coherent Light Source (LCLS) at the Stanford Linear Accelerator Laboratory (SLAC), to improve and extend the thermal conductivity measurements to warm dense iron.
- Chapter 6 presents data from experiments at the Orion Laser Facility designed to measure the opacity of dense materials. Temporally and angularly resolved spectroscopic K-shell silicon data are analyzed and compared with collisional radiative modeling to quantify the impact of modeling assumptions, such as escape factors and radial gradients, on the inferred temperature from such an experiment.
- Chapter 7 concludes the thesis with a discussion of the outcomes of each experiment, and directions for the improvement of future work are explored.

1.4 Role of the Author

This section is included to clarify the Author's contribution to the work presented within this thesis. Chapters 1 and 2 were prepared by the Author from archival literature and text books cited as used in order to lay the foundation for the concepts being experimentally investigated. Chapter 3 presents facility and diagnostic information from relevant publications and calibration work performed by the Author. The Author participated in the proton heating experiment on Titan along with collaborators and coworkers from LLNL, UCSD, MIT, and OSU to field diagnostics and collect data. The Author performed the absolute calibration of the optical streak camera using the Europa laser and analyzed the streaked optical pyrometer data. The simulations presented here were performed by the Author with aid from G. E. Kemp and Y. Ping. The Helmholtz solver was implemented into Matlab by G. E. Kemp and expanded by the Author to model the diagnostic data. The XFEL thermal conductivity experiment's optical layout was designed by the Author, Y. Ping, and collaborators from AWE. The Author and Y. Ping designed the targets and the Author participated in data collection with experimental support from collaborators from AWE, LLNL, and MEC staff. The SOP data was analyzed and modeled by the Author. Finally, during his time at LLNL the Author participated in joint AWE and LLNL experiments to measure opacity at the Orion Laser Facility. The data presented in Chapter 6 were collected during one of these experiments. The Author participated in the data collection and target design for the experiment. The data were analyzed by the Author. The collisional-radiative modeling was performed by the Author with help using Cretin from H. A. Scott and guidance from R. Shepherd and H. A. Scott.

CHAPTER 2

Theoretical background

It is the aim of this work to provide experimental measurements of transport properties in dense plasmas. However, direct observation of transport coefficients is often impossible, necessitating the use of integrated models to compare experimental observables with transport theory. In this chapter, I review some of the basic transport theory and models that are in use in the field and available for comparison with the experimental data presented in later chapters. Following the discussion on transport theory, I present a discussion on the absorption mechanisms of the drivers used to heat material in the work presented within this thesis.

2.1 Energy transport in classical plasmas

It goes without saying that the foundation to understanding the systems described in Chapter 1 is accurate knowledge of mass, momentum, or energy exchange mechanisms; this encompasses the field of transport theory. Many formulations of transport theory under various approximations have been extensively developed over the years, but they can all be grouped into one of three descriptions—single-particle, kinetic, or fluid.

The single-particle descriptions comprise the most detailed microscopic models over which averages must be taken to discuss energy flux, while the least detailed—fluid equations—have substantial averaging built in, and macroscopic properties such as electrical conductivity, thermal conductivity, diffusivity, or viscosity appear explicitly. Single-particle descriptions, such as Particle-in-cell (PIC) models, have found tremendous success at modeling highly non-equilibrium phenomena such as hot electron production in intense laser-solid interactions or plasma wakefield accelerators, but these effects belong to systems that are far from equilibrium and conventional transport coefficients will not apply. For this reason, we will not discuss these methods significantly and begin the discussion with kinetic theory.

In this section, I will provide a discussion of common classical transport descriptions including fundamental assumptions, strengths, and challenges of each. Though classical descriptions may not strictly apply in dense systems, they provide the basis for extensions into dense systems.

2.1.1 Kinetic theory

The starting point for most classical transport calculations is kinetic theory. We can describe groups of particles of species, s, by their single-particle distribution function, $f_s(\mathbf{x}, \mathbf{v}, t)$. This description reduces the dimensionality of the model to seven—three spatial, three velocity, and time. A tremendous amount of information about the dynamical nature of plasma species is maintained, but inherent averaging is now a part of the model. The famous Boltzmann equation, which serves as the foundation of the majority of plasma transport theory, can be written as[18]

$$\frac{\partial f_s}{\partial t} + \mathbf{v} \cdot \nabla_x f_s + \frac{\mathbf{F}}{m_s} \cdot \nabla_v f_s = \left(\frac{\partial f_s}{\partial t}\right)_{coll} \tag{2.1}$$

where the last term represents a generalized collision term, known as the collision integral, understood to represent the change to the distribution function from collisions. This equation describes the evolution of a non-equilibrium distribution function under the influence of external forces and collisions. Equation 2.1 with the collision integral set to zero is known as the Vlasov equation, which is simply a statement of the total derivative of the distribution function in phase space. The Boltzmann equation, when applied to plasmas, typically assumes the Lorentz force, $\mathbf{F} = q[\mathbf{E} + (\mathbf{v} \times \mathbf{B})]$.

$$\frac{\partial f_s}{\partial t} + \mathbf{v} \cdot \nabla_x f_s + \frac{q}{m_s} \left[\mathbf{E} + (\mathbf{v} \times \mathbf{B})\right] \cdot \frac{\partial f_s}{\partial \mathbf{v}} = \left(\frac{\partial f_s}{\partial t}\right)_{coll} \tag{2.2}$$

It is in the collision term that all of the particle interaction physics as well as many of the model assumptions occur. Boltzmann's original collision integral is given by[19]

$$C_{ab}(f_a, f_b) = \int \left[f_a(v')f_b(v'_b) - f_a(v)f_b(v_b)\right] |v - v_b|\, d\sigma dv_b \tag{2.3}$$

and uses the argument of ”stosszahlansatz” or molecular chaos where dσ is the differential scattering cross section[20]. It assumes that two particles, uncorrelated prior to their collision, undergo a close-range, hard-sphere collision that can be described by the product of single-particle distribution functions before and after the collision rather than a two-particle distribution function.

$$f(t, \mathbf{x}_1, \mathbf{v}_1, \mathbf{x}_2, \mathbf{v}_2) \approx f(t, \mathbf{x}_1, \mathbf{v}_1) f(t, \mathbf{x}_2, \mathbf{v}_2) \tag{2.4}$$

The other assumptions implicit in the original Boltzmann equation are that the collisions are elastic, occur fast relative to time scales in the problem, and occur in spatial scales small relative to the problem. This description is only valid for binary, hard-sphere collisions found in dilute gases, and much work has gone into various forms of the collision integral that are valid for charged particles.

When discussing plasmas, the collision integral is often simplified by assuming that collisions will restore the distribution to its equilibrium state in some characteristic time, τ. This model is called the Bhatnagar-Gross-Krook (BGK) model[21] and is defined as

$$\left(\frac{\partial f_s}{\partial t}\right)_{coll} = \frac{f_0 - f}{\tau} \tag{2.5}$$

where τ is considered to be velocity-independent. This model greatly simplifies analytic and computational solutions to the Boltzmann equation, but naturally is not acceptable in all cases. It becomes ambiguous when discussing multi-species collisions[22] and introduces large errors in higher moments such as the heat flow[23].

A more complete collision integral is given by the Fokker-Planck equation. The Fokker-Planck equation more generally describes the effects of collisions on the distribution function without relying on a general relaxation time and is given by

$$\frac{\partial f_s}{\partial t} = -\frac{\partial}{\partial \mathbf{v}} \cdot \left(\frac{\langle \Delta \mathbf{v} \rangle}{\Delta t} f_s(\mathbf{v}, t) \right) + \frac{1}{2} \frac{\partial}{\partial \mathbf{v}} \frac{\partial}{\partial \mathbf{v}} : \left(\frac{\langle \Delta \mathbf{v} \Delta \mathbf{v} \rangle}{\Delta t} f_s(\mathbf{v}, t) \right) \tag{2.6}$$

where $\langle \Delta \mathbf{v} \rangle$ represents the coefficient of dynamical friction—describing how particles above the mean velocity slow and particles below it accelerate. This is defined as

$$\langle \Delta \mathbf{v} \rangle = \int F(\mathbf{v}, \Delta \mathbf{v}) \Delta \mathbf{v} d(\Delta \mathbf{v}) \tag{2.7}$$

Additionally, the coefficient of dynamical diffusion, which describes the effect of collisions on the range of velocities, is given by

$$\langle \Delta \mathbf{v} \Delta \mathbf{v} \rangle = \int F(\mathbf{v}, \Delta \mathbf{v}) \Delta \mathbf{v} \Delta \mathbf{v} d(\Delta \mathbf{v}) \tag{2.8}$$

where F is a function given by $\int F(\mathbf{v}, \Delta \mathbf{V}) d\Delta \mathbf{V} = 1$, describing the probability that a particle with velocity **v** at time t will collide and have its velocity changed to $\mathbf{v} + \Delta \mathbf{v}$ at time $t + \Delta t$.

One thing worth remembering is that most collision integrals such as the Lorentz[24] form, the Fokker-Planck form, or the Rosenbluth form for inverse-square forces[25] explicitly use the Coulomb Logarithm—$\ln\Lambda = b_{min}/b_{max}$, where b_{max} is the Debye length $\lambda_D = (k_B T_e / 4\pi e^2 n_e)^{1/2}$ and b_{min} is the classical distance of minimum approach $Z_i e^2 / m_e v_{th}$—in the form of the differential scattering cross-section. This is acceptable for many plasmas but ill-suited to low-temperature, dense plasmas. More realistic plasma screening effects are naturally included through a multi-component dynamical dielectric function in the Lenard-Balescu collision integral[26, 27], but at greatly increased complexity and only mild extension to more strongly coupled systems.

Though the kinetic equations presented here inherently neglect correlation effects due to the basis of the theory in single-particle distribution functions and the closure of the Bogoliubov-Born-Green-Kirkwood-Yvon (BBGKY) hierarchy with the molecular chaos ansantz, implementations of them have nonetheless proved exceptionally useful in dense plasma research. An excellent review by Thomas[28] *et al.* outlines the contributions of Vlasov-Fokker-Planck numerical modeling in the context of Intertial Confinement Fusion (ICF). He points out that VFP codes excel in regions of plasmas where the Debye length is small, which could lead to prohibitively small meshing in PIC models and where the plasma is semi-collisional. Additionally, the collisions tend to smooth out anisotropy in velocity space, making the usual truncations of spherical expansions more justifiable. Finally, due to the fact that it is not stochastically sampling the equations, the noise tends to be much better. The major downside is that the high dimensionality in position and velocity space means these models can still be quite computationally expensive.

2.1.2 Fluid theory

If we seek a simpler, more tractable model with which to work, we can employ the fluid equations. First, we can describe macroscopic properties of the plasma by taking velocity moments of the distribution function itself. The moments, in increasing order, describe the number density (n), average fluid velocity ($\bar{\mathbf{v}}$), the pressure tenser ($\underline{\underline{\mathbf{P}}}$), and the heat flux tensor ($\mathbf{Q}$) or heat flux vector ($\mathbf{q}$):

$$n(\mathbf{x},t) = \int f(\mathbf{x},\mathbf{v}) d^3v \tag{2.9}$$

$$\bar{\mathbf{v}}(\mathbf{x},t) = \frac{1}{n}\int \mathbf{v} f(\mathbf{x},\mathbf{v},t) d^3v \tag{2.10}$$

$$\underline{\underline{\mathbf{P}}}(\mathbf{x},t) = m\int (\mathbf{v}-\bar{\mathbf{v}})(\mathbf{v}-\bar{\mathbf{v}}) f(\mathbf{x},\mathbf{v},t) d^3v \tag{2.11}$$

$$\mathbf{Q}(\mathbf{x},t) = m\int (\mathbf{v}-\bar{\mathbf{v}})(\mathbf{v}-\bar{\mathbf{v}})(\mathbf{v}-\bar{\mathbf{v}}) f(\mathbf{x},\mathbf{v},t)^3 dv \tag{2.12}$$

$$\mathbf{q}(\mathbf{x},t) = \frac{m}{2}\int (\mathbf{v}-\bar{\mathbf{v}})^2(\mathbf{v}-\bar{\mathbf{v}}) f(\mathbf{x},\mathbf{v},t) d^3v \tag{2.13}$$

These are easily related to other physical quantities; for example, we may multiply eq. (2.9) by m to get mass density or q to get charge density, or multiply eq. (2.10) by the charge density to get the current density $\mathbf{j} = qn\bar{\mathbf{v}}$.

Taking this method and applying it to the entire Boltzmann equation, 2.1, we can arrive at the well-known fluid equations. To derive these, we multiply through by quantities we expect to be conserved such as mass ($\mathbf{v}^0$), momentum ($\mathbf{v}^1$), or kinetic energy ($\mathbf{v}^2$). Derivations of these equations may be found in numerous texts[29, 18, 30]. The zeroth-moment equation is achieved by integrating the Boltzmann equation over velocity-space.

$$\frac{\partial n}{\partial t} + \nabla \cdot (n\bar{\mathbf{v}}) = 0 \tag{2.14}$$

Here, the integral of the collision term going to zero is a statement that, even in a simple two fluid model, elastic collisions can't change the total number of particles of a species. Note here that this zeroth-moment equation contains $\bar{\mathbf{v}}$, a first-moment quantity.

Repeating the process for the next moment, momentum, unsurprisingly yields the following momentum transfer equation:

$$m\frac{\partial (n\bar{\mathbf{v}})}{\partial t} + m\frac{\partial}{\partial t} \cdot (n\bar{\mathbf{v}}\bar{\mathbf{v}}) = nq(\mathbf{E} + \bar{\mathbf{v}} \times \mathbf{B}) - \frac{\partial}{\partial t} \cdot \underline{\underline{P}} - R_{ei} \tag{2.15}$$

where we again see an addition from a higher-order moment, the pressure tensor $\underline{\underline{P}}$, and the term R_{ei} results from integrating the collision operator in this moment. Intraspecies collisions can't change the total species momentum, but interspecies collisions can. This effect is often approximated with $\mathbf{R}_{ei} = \nu_{ei} m_e n_e (\bar{\mathbf{v}}_e - \bar{\mathbf{v}}_i)$, where ν_{ei} represents an average momentum exchange collision rate.

The next moment gives the energy flow equation

$$\frac{3}{2}\frac{\partial P}{\partial t} + \frac{5}{2}P\nabla \cdot \bar{\mathbf{v}} = -\nabla \cdot \mathbf{q} + \mathbf{R}_{ei} \cdot \bar{\mathbf{v}} - \left(\frac{\partial W}{\partial t}\right)_{Eei} \tag{2.16}$$

where the off-diagonal terms in the pressure tensor have been neglected and $(\partial W/\partial t)_{Eei}$ represents the rate at which electrons transfer energy to ions via collisions. At this point, we have equations for the balance of mass, momentum, and energy. However, we need more information on the heat flux, the collision rate, and the energy exchange rate. This problem will persist and some extra physical insight must be supplied to provide closure to the system, such as a Fourier's law and a separately derived EOS to relate pressure, temperature, and density.

Recasting equations (2.14)–(2.16) in more directly relevant forms given by Drake[31], with radiation pressure and generic forces included, gives us

$$\frac{\partial \rho}{\partial t} + \nabla \cdot \rho \bar{\mathbf{v}} = 0 \tag{2.17}$$

$$\rho \left(\frac{\partial \bar{\mathbf{v}}}{\partial t} + \bar{\mathbf{v}} \cdot \nabla \bar{\mathbf{v}} \right) = -\nabla (p + p_R) + \nabla \cdot \underline{\sigma}_\nu + \mathbf{F}_{EM} + \mathbf{F}_{other} \tag{2.18}$$

$$\frac{\partial}{\partial t} \left(\rho \epsilon + \frac{\rho \bar{\mathbf{v}}}{2} + E_R \right) + \nabla \cdot \left[\rho \bar{\mathbf{v}} \left(\epsilon + \frac{\bar{\mathbf{v}}^2}{2} \right) + p \bar{\mathbf{v}} \right] = -\nabla \cdot \mathbf{H} - \mathbf{J} \cdot \mathbf{E} + \mathbf{F}_{other} \cdot \bar{\mathbf{v}} \tag{2.19}$$

where p_R is the radiation pressure, $\underline{\sigma}_\nu$ is the viscous stress tensor, $F_{EM} = \rho_c \mathbf{E} + (\mathbf{J} \times \mathbf{B})/c + \nabla p_R$, E_R is the radiation field energy density, and the energy flux, $\mathbf{H}$, is given by $\mathbf{H} = F_R + (p_R + E_R)\mathbf{u} + \mathbf{Q} - \underline{\sigma}_\nu \cdot \mathbf{u}$.

At this point, we have a system of equations that relate macroscopic quantities, but we have lost nearly all of the detailed physical insight provided by the distribution functions or individual particle trajectories. This comes with the great benefit of having a system of equations that can be solved rapidly and over much larger time and space steps, but the drawback is that we now need to provide all of the physics ourselves through transport coefficients and equation of state.

Classically, the transport coefficients can be calculated through techniques such as the Chapman-Enskog expansion[32]. In this expansion, the equilibrium distribution function, $f^{(0)}$, is expanded in terms of the Knudsen number $\epsilon = \lambda_{mfp}/L$ where L is a hydrodynamic length relevant to the problem, and the Knudsen number is assumed to be small.

$$f = f^{(0)} + \epsilon f^{(1)} + \epsilon^2 f^{(2)} + \cdots \tag{2.20}$$

The higher terms in the expansion represent the perturbed components of the isotropic distribution and are assumed to be small, so terms quadratic in $f^{(1)}$ are neglected. Substituting this expansion into the Boltzmann equation and isolating orders of the expansion yields an equation for $f^{(1)}$ in terms of $f^{(0)}$, which can be assumed Maxwellian and therefore relate $f^{(1)}$ to local macroscopic quantities. A similar process using a Cartesian tensor expansion was performed by Braginskii[19] and later improved by Epperlein and Haines[33] to get classical transport coefficients for fully ionized plasma that are still commonly used.

Fluid codes remain the most accessible method of modeling an integrated experiment, so tremendous effort has gone into creating detailed transport models that can be integrated into the existing fluid codes to provide accurate predictive capabilities.

2.2 Energy transport in dense plasmas

In dense plasmas, the basic assumptions of a classical plasma break down. In this case, the system is better described as a dense quantum fluid where the ions are correlated, the electrons are Fermi-degenerate, and large-angle collisions become important. There has been substantial effort put into developing theoretical models that describe these systems more accurately. One of the most successful techniques of the last several decades uses Density Functional Theory (DFT) to calculate the electronic structure and couples it to a classical molecular dynamics calculation to determine the ionic structure. However, these techniques become computationally demanding above $\mathrm{T}_e \approx 10$ eV. Alternatively, Path Integral Monte Carlo (PIMC) can capture many-body quantum effects via the system density matrix through Feynman's path-integral formulation, but this method struggles at low temperatures. This leaves intermediate temperature regimes without satisfactory theoretical calculations. PIMC results were not available for the experimental regimes found in this thesis and won't be discussed further; see review by Kang and Dai for more details[34]. Due to the complexities of the above approaches, simplified models such as Average Atom (AA) models are commonly employed where the electronic properties of a single spherical "average" ion are calculated in the DFT framework. These models are part of a larger set of models loosely described as neutral pseudo-atom models. The following sections will discuss the basics of each of these approaches in preparation for discussion of their predictions of thermal conductivity in Section 2.3.

2.2.1 Density functional theory

DFT is one of the most widely used techniques to calculate the detailed electronic structure of dense systems. It is a theoretical framework that provides an alternative solution to the many-electron Schrödinger equation in terms of a system's density. The basis of the theory lies in the Hohenburg-Kohn theorem[35] which describes a system of electrons under the influence of an external potential $V_{ext}(\mathbf{r})$. First, it states that for a non-degenerate ground state, the external potential and therefore the total energy, $E[n(\mathbf{r})]$, is a unique functional of the electron density, $n(\mathbf{r})$, given by

$$E[n(\mathbf{r})] = \int d\mathbf{r}\ n(\mathbf{r}) V_{ext}(\mathbf{r}) + F[n(\mathbf{r})] \tag{2.21}$$

where $F[n(\mathbf{r})]$ is an unknown functional of the electron density only. Furthermore, the energy functional, $E[n(\mathbf{r})]$, is minimized when $n(\mathbf{r})$ is the unique ground state configuration. These statements provide the link between the system density and the Hamiltonian, which determines the ground-state many-electron wave function and, by extension, the system properties. The second statement provides a variational method through which to arrive at the correct density function—minimization of the total energy. At this point, if we had the exact form of F, it would provide an exact description of the ground state system, hence this method is often termed an *ab initio* method.

In reality, the exact form of $F[n(\mathbf{r})]$ is unknown, but it can be written in terms of components that contribute to the total energy

$$F[n(\mathbf{r})] = T[n(\mathbf{r})] + E_{ee}[n] \tag{2.22}$$

where T is the kinetic energy of the system, E_{ee} represents the electron-electron interactions. Both of these terms are not exactly known. From this point, approximations can be made for these terms to arrive at the commonly-known Thomas-Fermi model, which is often applied when effects from detailed shell structures can be neglected.

In 1965, Kohn and Sham[36] outlined a far more precise framework which now serves as the modern basis of DFT. Their idea was to solve for a virtual system of non-interacting electrons. This allows for the exact calculation of the kinetic and Coulombic energies, lumping all of the uncertain, complex effects such as exchange and correlation into an exchange potential, $V_{xc}[n]$. They stated that for a system of non-interacting electrons to have the same density as the interacting system under an external potential, the non-interacting electrons must experience an additional effective potential, $V_s(\mathbf{r})$, given by

$$V_s(\mathbf{r}) = V_{ext}(\mathbf{r}) + e^2 \int d^3r' \, \frac{n(\mathbf{r}')}{|\mathbf{r} - \mathbf{r}'|} + V_{xc} \tag{2.23}$$

where the terms are the external potential in the interacting system, the Coulomb potential, and the exchange potential. The wave function for this system is constructed from a set of orbitals that satisfy

$$\left(-\frac{\hbar^2}{2m}\nabla^2 + V_s(\mathbf{r})\right) \psi_i(\mathbf{r}) = \epsilon_i \psi_i(\mathbf{r}) \tag{2.24}$$

where ϵ_i is the orbital energy of the ith Kohn-Sham (KS) orbital and the N total orbitals must obey

$$n(\mathbf{r}) = \sum_i^N |\psi_i(\mathbf{r})|^2 \tag{2.25}$$

Thus, the system is simplified greatly, assuming an accurate model for the exchange functional exists. If one provides a trial density function or potential, the system can be iterated to consistency, and the energy minimized.

The exchange and correlation functional is instrumental in capturing the effects necessary to describe warm dense matter. It is also the only term not exactly known: it is where all the error creeps into the formally exact framework, and is therefore an area of intense, active research. For WDM in particular, as the temperature rises, the effects of temperature on the ground state must be considered. As such, methods including Finite-Temperature DFT (FT-DFT)[37, 38] are typically used, though this introduces the challenges of finding energy functionals of both density and temperature, and greatly increases the computational cost due to the expanded orbital basis set required to resolve higher energy states[39]. Methods such as Orbital-Free DFT (OF-DFT)[40] seek to increase computation speed at finite temperatures by creating functionals that do not explicitly rely on the KS orbitals, but typically sacrifice accuracy.

2.2.2 Molecular dynamics models

Molecular Dynamics (MD) is another particle-particle approach that differs from PIC models. In this framework, one describes an ensemble of N ions and calculates the total forces each particle feels. This is done by finite-differencing Newton's law of motion, with interparticle potentials as the force, and using sub-femtosecond time steps.

$$\frac{d^2 r_i}{dt^2} = \frac{f_i}{m}; \quad f_i = -\nabla_i V(r_i, ..., r_N) \tag{2.26}$$

The real art behind this method goes into creating accurate potentials that describe the near- and long-range forces on the particles. Two primary methods exist: an all-particle-MD method uses classical point particle representations for both electrons and ions, while an ion-only-MD uses a classical treatment for the ion dynamics only[41]. All-particle MD methods typically attempt to capture the quantum nature of the electrons with two-body quantum statistical potentials (QSP) defined in the equilibrium state[41]. This concession introduces uncertainty in the models, but makes the methods more robust and computationally tractable. These methods have been employed in hot dense plasmas, where the degeneracy is less important to study electron-ion temperature equilibration[42] and electrical and thermal conductivities[43].

Alternatively, in ion-only-MD, the electrons are handled in the quantum mechanical framework. The most common implementation in warm dense matter is called Quantum Molecular Dynamics (QMD), which uses DFT with the external potential given by the ion positions at each time step to calculate the total wave functions within the simulation volume[44]. These calculations typically rely on the Born-Oppenheimer approximation, which allows the total wave function to be described by individual electronic and nuclear terms, to separate calculation of the ion and electron motions. Figure 2.1 demonstrates the exchange between the DFT and MD processes as implemented in modern QMD codes.

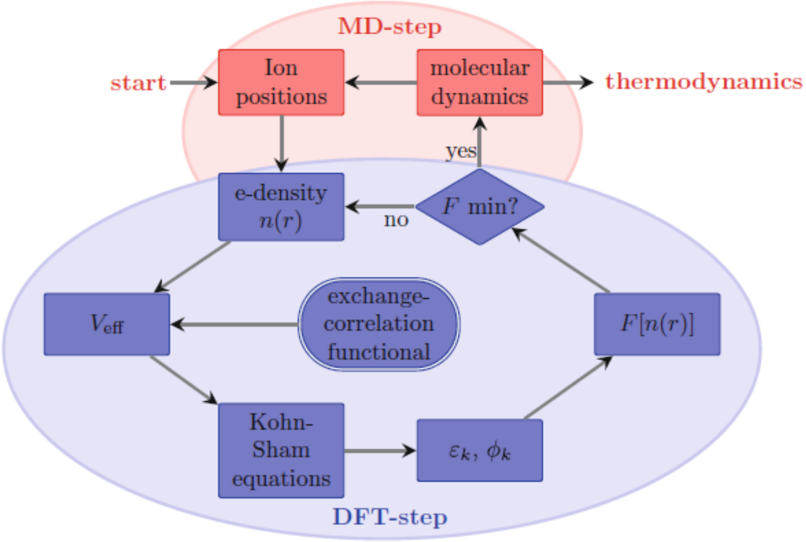

Figure 2.1: Calculation flowchart in a typical QMD simulation. Given an ion distribution, KS equations are iterated to consistency (the ground state reached) and the electron system potential passed back to the MD routines. Figure by W. Lorenzen *et al.*[45] reprinted with permission.

The major advantage of QMD is requires very little external input or approximation—just the exchange-correlation functional—and is therefore believed to be very accurate. The downside is that the DFT solutions at each time step must be calculated for all electrons of each atom in the simulation volume. This is far too costly to calculate for more than ∼32–256 particles evolving over times longer than several picoseconds. Tightly bound electrons are often replaced with effective potentials to reduce the computational burden, but this adds uncertainty to the intended *ab initio* method. As temperatures rise or densities fall, the number of plane waves required to provide a full basis set grows dramatically, and the computations become untenable. Even utilizing the large-scale computing resources available at U.S. national laboratories, these calculations can only reasonably be carried above solid densities (1–10 g/cc) up to temperatures of ≈10 eV, or at reduced densities around 0.1 g/cc up to ≈1–2 eV[46]. QMD methods are a growing staple in calculating transport coefficients for WDM, but for the moment are largely used to benchmark more accessible theories in the absence of accurate experimental data.

2.2.3 Average atom calculations

As an alternative to calculating the detailed evolution of a many-atom system, we can apply some of the same concepts from DFT to a single spherically symmetric atom. Variations of this concept exist, such as the neutral pseudo atom (NPA)[47, 48, 49], but here we focus on the average atom model outlined by Liberman[50] and implemented in codes such as Inferno[51] and Purgatorio[52]. These models are intended to be valid for arbitrarily high densities where relativistic effects may become important, so they employ solutions to the Dirac equation rather than the Schrödinger equation.

A complex polyhedral atomic cell is represented as a sphere, imposing radial symmetry. In the center of the sphere is all of the positive charge of the nucleus, Z. The radius of the cavity is chosen to be the Wigner-Seitz radius, $R_{ws} = 3/(4\pi n_i)^{1/3}$, and the charge neutrality boundary condition is imposed as

$$\int_0^{R_{ws}} 4\pi r^2 \rho_{tot}(r) dr = Z \tag{2.27}$$

where the total density ρ_{tot} is explicitly composed of contributions from the bound and free electrons.

$$\rho_{tot}(r) = \rho_{bound}(r) + \rho_{continuum}(r) \tag{2.28}$$

$$4\pi r^2 \rho_{bound}(r) = \sum_i f(\epsilon, \mu) 2|\kappa_i| \left[P_i^2(r) + Q_i^2(r)\right] \tag{2.29}$$

$$4\pi r^2 \rho_{cont}(r) = \int_i^\infty d\epsilon f(\epsilon, \mu) \sum_\kappa 2|\kappa| \left[P_{\kappa,\epsilon}^2(r) + Q_{\kappa,\epsilon}^2(r)\right] \tag{2.30}$$

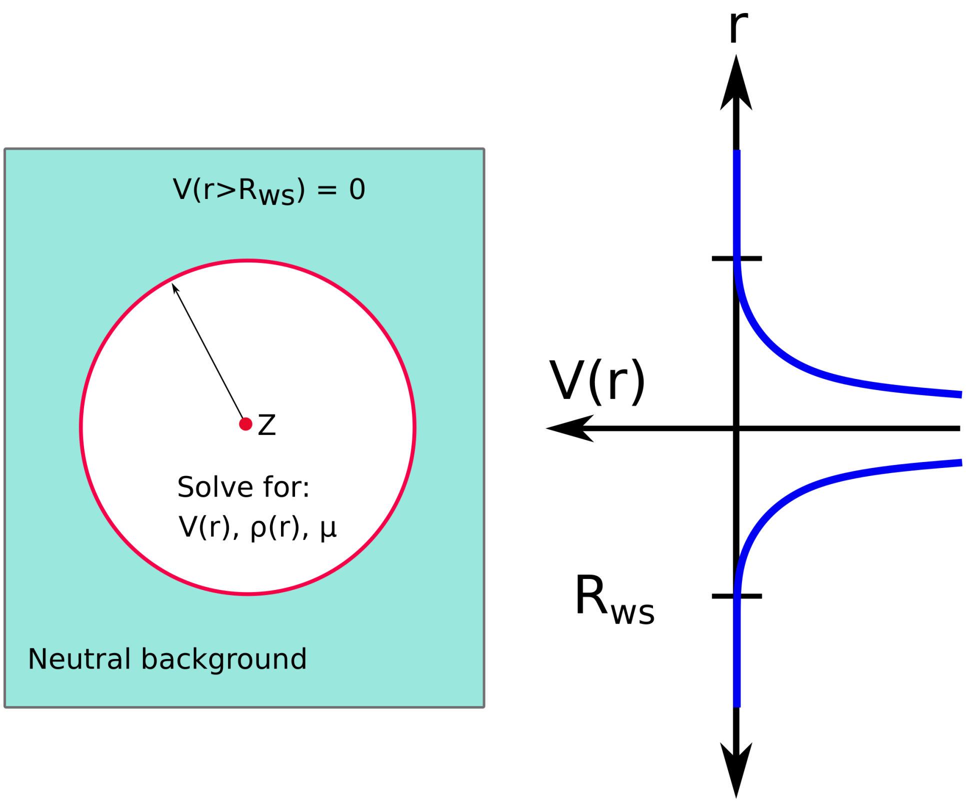

Figure 2.2: Simple representation of the average atom model.

In the above equations, $f(\epsilon, \mu) = (1 + e^{(\epsilon-\mu)/T})^{-1}$ is the Fermi distribution; μ, the chemical potential; P and Q, the major and minor components of the radial Dirac equation; κ, a spin-angular momentum channel; and i, the index of discrete bound states. The wave functions are populated according to their statistical weights given by the Fermi function, and the chemical potential—which roughly determines the boundary between negative energy-bound states and positive energy-free states—is varied to enforce (2.27). The functional of the total internal energy is minimized through iteration of the density and corresponding potential functions until the ground state is reached. The exchange-correlation term in the potential is calculated under the Local Density Approximation (LDA)[53] which assumes the exchange and correlation terms can be expressed with forms relevant to a homogeneous electron gas at the local density.

The forms of the self-consistent wave functions within the sphere are matched to analytic forms of the continuum wave functions[54] for a free-electron gas outside of the sphere, where the potential is zero, yielding phase shifts at the boundary. These phase shifts contain information necessary to calculate the differential cross-section of a plane wave scattering off of a single ion center which is used to calculate relaxation times and electrical conductivity[55] in Purgatorio. Generally, the primary goal of average ion calculations is to use knowledge of the internal energy at a given density and temperature to calculate the electron contribution to the Helmholtz free energy, and construct the equation of state[56].

This model represents an obvious simplification, and as such has some drawbacks. The nature of taking an ”average” ion radius means that the model will give fractional shell occupations and ionization energies. In fact, the definition of average ionization is ambiguous in this model and can be defined as the total continuum electrons, or just the electrons in the ideal density of states (ignoring quasi-bound resonant states), or just the value of the total density evaluated at the ion sphere surface[56]. Additionally, the model is a single-site scattering center which is known to not be accurate in the WDM regime, altering the density of states[57] and therefore the inferred transport properties and effects. Also, it has been discussed that some effects such as chemical bonding that occurs in the interstitial region between atoms, such as transient covalent bonding in carbon, will not be captured in traditional AA models[58].

In spite of these potential limitations, the simplifications of AA models reduce computational requirements and speed calculation times by 2-5 orders of magnitude when compared with QMD simulations[46]. This allows the model to be applied over many logarithmic decades of temperature and density phase space—a crucial requirement if one wants to make accurate tables for use in hydrodynamics codes—while maintaining the vast majority of the effects of shell structure on the free energy of the electron configuration.

2.3 Thermal Conductivity

Measuring thermal conductivity is the aim of a large portion of the experimental efforts presented in this thesis, so a discussion of it and the theoretical models developed to calculate it are in order. Thermal conductivity refers to the rate at which heat is transferred through a system; this is measured (in watts per square meter) by the heat flux, **q**. The local heat flux is proportional to the local temperature gradient through Fourier's law

$$\mathbf{q} = -\kappa_{th}\nabla T \tag{2.31}$$

where the thermal conductivity, κ_{th}, is the constant of proportionality given in units of W/m/K. If we wish to know how a spatially-dependent temperature profile evolves in time, we use the heat transport equation, given in one dimension by[59]

$$\rho c_p \frac{\partial T}{\partial t} - \nabla \cdot (\kappa_{th}\nabla T) = Q_V \tag{2.32}$$

where ρ is the mass density, c_p is the specific heat at constant pressure, and Q_V any volumetric sources of heat. This is defined for a stationary, homogeneous, isotropic solid.

Analytic solutions to this equation under many initial and boundary condition assumptions can be found in most thermal transport texts, but here we follow Hahn and Özisik[59]. The simplest problem of interest is the propagation of heat through a semi-infinite slab at $T = 0$ with the boundary at $x = 0$ held at constant temperature T_b, shown in figure 2.3.

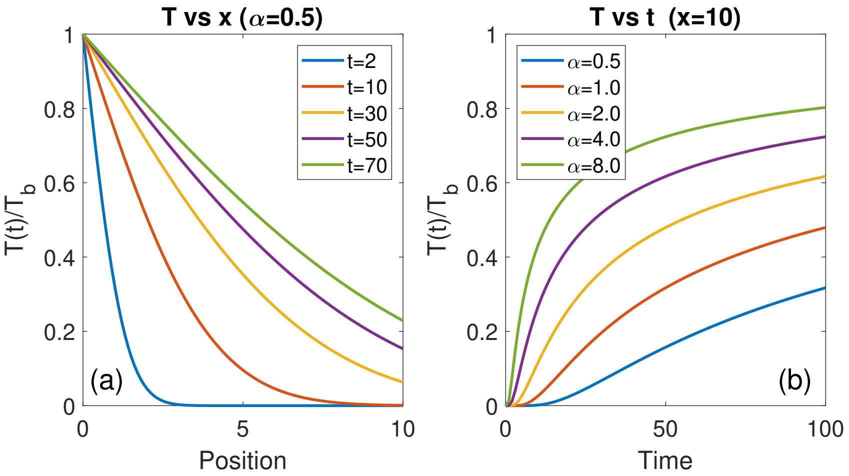

Figure 2.3: Basic solution to the heat equation for semi-infinite medium at zero temperature with fixed boundary temperature, T_b.

The heat equation, (2.32), has a solution for these conditions given by

$$T(x,t) = T_b \left[1 - erf\left(\frac{x}{\sqrt{4\alpha t}}\right)\right] \tag{2.33}$$

where $\alpha = \kappa_{th}/(\rho c_p)$ is the thermal diffusivity and erf is the standard error function given by $erf(x) = \frac{2}{\sqrt{\pi}}\int_0^x e^{-t^2}dt$. Following the discussion of Ping *et al.*[60], we look at the solution to (2.32) in Fig.2.3(a), which demonstrates the evolution of the thermal gradient in time. If we were to measure the temperature at a specific position in time, we would see something like the curves in Fig. 2.3(b). These show a strong dependence on the thermal diffusivity; a measurement of temperature in time would contain the effects of the thermal conductivity, the density, and the specific heat. This provides the foundation of the thermal conductivity measurements that is presented in later chapters.

At the microscopic level, heat is transported through collisional processes between particles. In a solid material, this can be due to collisions with electrons or vibrational excitations of ions (phonons). As the material heats up, the disorder makes phonon contributions less important. In the liquid/plasma state, electron-ion collisions dominate the energy transport. This is due to the large mass difference, m_e/m_i; the collision frequency between ions is much smaller and the resulting heat flux due to ion collisions is much less than that due to electron-ion collisions. This is not the case in strong magnetic fields, where the electrons are trapped in cyclotron orbits, and the ion contribution can be much larger[20, 61], though those situations are not considered in this thesis.

For the work found within this thesis, we limit discussion of thermal conductivity to its unmagnetized classical regime where it is subject to the constraints of (1) small temperature gradients relative to the particle mean free path, (2) no electric fields, and (3) no electric current. In the following sections, we will discuss basic definitions of thermal conductivity and the heat transport equation, how thermal conductivity is derived in plasmas starting with the classical Spitzer-Harm derivation, how the electric coefficients are related through the Onsager coefficients, and then move into explanations of the theoretical models against which data were compared in this thesis before finishing with a brief discussion of the Wiedemann-Franz law which related electrical and thermal conductivity.

2.3.1 Landau-Spitzer-Härm theory

The classical theory for thermal conductivity of a Lorentz gas—which assumes full ionization, non-interacting electrons, and fixed ions—can be solved from kinetic theory. A standard approach, here following the treatment of Atzeni[7], uses a VFP equation of the form

$$\frac{\partial f}{\partial t} + \mathbf{v} \cdot \nabla_x f - \frac{e\mathbf{E}}{m} \cdot \nabla_V f = \frac{2\pi n Z e^4}{m^2} \ln\Lambda_e \nabla_V \cdot \left(\frac{\nabla_V f}{v} - \frac{\mathbf{v}(\mathbf{v} \cdot \nabla_V f)}{v^3} \right) + C_{ee}(f) \tag{2.34}$$

where the first term on the right is the electron-ion collision integral based on a relaxation rate formulation shown by Shkarofsky *et al.*[62] to be appropriate, and $C_{ee}(f)$ is the electron-electron collision integral historically ignored. The thermal conductivity is given by the third moment of the distribution function, eq. (2.13), but we require the non-equilibrium part of the distribution function. This is done by expanding the distribution function in Legendre polynomials and keeping only the first two terms.

$$f(v) = f_0(v) + f_1(v) cos\theta \tag{2.35}$$

The angle, θ, represents the angle of anisotropy of the distribution in velocity space, and f_0 is taken to be a Maxwellian distribution. Substituting this into the full VFP equation, and keeping only terms involving cosθ gives

$$\frac{\partial f_1}{\partial t} + v\frac{\partial f_0}{\partial z} - \frac{eE}{m}\frac{\partial f_0}{\partial v} = -\frac{4\pi n Z e^4}{m^2 v^3} \ln\Lambda_e f_1 \tag{2.36}$$

In steady state ($\partial/\partial t = 0$), the first order perturbation is given as

$$f_1(v) = -\frac{v^4 m^2}{4\pi n Z e^4 \ln\Lambda_e} \left(\frac{\partial f_0}{\partial z} - \frac{eE}{mv}\frac{\partial f_0}{\partial v} \right) \tag{2.37}$$

The electric field is solved for with the help of the first velocity moment and the condition that the electric current caused by f_1 must vanish in order to satisfy charge neutrality, yielding

$$eE = -\frac{5}{2}k_B\frac{dT}{dz} \tag{2.38}$$

Equations (2.38) and (2.37) together give an explicit formula for $f_1(v)$, which can be used with the appropriate moment equation to give the heat flux; the proportionality constant to the temperature gradient being κ_{th}, the thermal conductivity.

$$\kappa_{th} = \left(\frac{8}{\pi}\right)^{3/2} G(Z)\frac{(k_BT)^{5/2}k_B}{Ze^4m^{1/2}\mathrm{ln}\Lambda_e} \tag{2.39}$$

Here, $G(Z) \approx (1 + 3.3/Z)^{-1}$ is a fit to take into account the fact that electron-electron collisions, neglected in eq. (2.34), act to re-normalize the electron distribution function and reduce the conductivity. It was for detailed numerical solutions demonstrating this effect as a simple coefficient to the Lorentz values that Spitzer and Härm[63] bear the name of this classical theory.

2.3.2 General statement of electron transport coefficients

Often, the coefficients for electron transport are written in a form that dates back to the work of Onsager[64, 65] on the mutual interaction of irreversible processes. The basic statement is that any force, **F**, imposed on a system will result in a current, **j**, given by

$$\mathbf{j} = L \cdot \mathbf{F} + O(\mathbf{F}^2) \tag{2.40}$$

where L represents the matrix of transport coefficients, taken to be scalar in isotropic media. Real systems have multiple currents that are not independent; the set of equations describing i currents under the influence of j forces can be written as

$$\mathbf{j}_i = \sum_j L_{ij}\mathbf{F}_j \tag{2.41}$$

For electrons in a plasma, we can write the relationships for electron and heat currents in terms of electric field (potential gradients) and temperature gradients *a posteriori*.

$$\mathbf{j}_e = L_{ee}\mathbf{E} + L_{eq}(-\nabla T) \tag{2.42}$$

$$\mathbf{j}_q = L_{qe}\mathbf{E} + L_{qq}(-\nabla T) \tag{2.43}$$

A key feature of the present framework is the reciprocal relation $L_{12} = L_{21}$. It can be taken as a statement that the system will produce the minimum entropy possible; each potential will feel a restoring force from symmetric potentials in the system.

If $L_{12} = L_{21}$ holds true, then the Onsager transport coefficients must have the same units, and (2.42) and (2.43) are incorrect. The correct forms are given in many texts (e.g., Ziman[66]) as

$$\mathbf{j}_e = eS_{11} \cdot [e\mathbf{E} + T\nabla(\mu/T)] + eS_{12} \cdot (\nabla T)/T \tag{2.44}$$

$$\mathbf{j}_q = -S_{21} \cdot [e\mathbf{E} + T\nabla(\mu/T)] - S_{22} \cdot (\nabla T)/T \tag{2.45}$$

where the electric field force has been broken up into the sum of the force resulting from an external electric field and the force caused by a temperature-dependent gradient in the chemical potential, μ. This is often absorbed into **E**, interpreted to be an observed electric field[66]. The traditional electrical conductivity is defined under isothermal ($\nabla T = 0$) conditions, so one recognizes the standard coefficient from Ohm's law, $\mathbf{j}_e = \sigma\mathbf{E}$.

$$\sigma(\omega) = e^2 S_{11} \tag{2.46}$$

The thermal conductivity is obtained under conditions of no current flow, $\mathbf{j}_e = 0$, so substituting (2.44) into (2.45) for **E** and recognizing the thermal conductivity κ_{th} as the term in front of the temperature gradient yields

$$\kappa_{th} = \frac{S_{11}S_{22} - S_{12}S_{21}}{TS_{11}} \tag{2.47}$$

These equations are general within the framework of small-amplitude perturbations, assuming these are the only relevant thermodynamic forces within the plasma, so are often the starting point when calculating transport coefficients. These can be derived from kinetic theory by relating the first and third moments of the distribution function (obtained through a linearized solution to the Boltzmann equation) to the electric and heat currents. Solutions of this form using a relaxation approximation for the collision integral are given by Ziman[66] and Ashcroft & Mermin[67]. More complicated solutions considering more realistic collision integrals are demonstrated by Lampe[68, 69]. The coefficients can alternatively be calculated from linear response theory using Kubo-Greenwood current-current correlation functions[70].

2.3.3 The degenerate calculations of Hubbard and Lampe

At the other extreme of the density spectrum is the case of completely degenerate systems, such as those found in stars with electron densities exceeding 10^{24} cm^{-3}. Early work by Hubbard[71] performed transport calculations for fully-degenerate and weakly-coupled electrons with intermediately-coupled ions($\Gamma < 40$). He utilized the Lorentz gas model, assuming that e-e collisions have negligible impact on the distribution function at sufficiently high degeneracy, and a Kubo-type generating equation for transport coefficients from linear response theory[72].

Shortly thereafter, Lampe improved the calculation of the thermal conductivity[68] using a kinetic equation based on the quantum Lenard-Balescu transport equation. The solution used a Chapman-Enskog linearization of the transport equation[32] that assumed a Maxwellian for the ions and a Fermi distribution for the electrons. The resulting Fermi-Dirac integrals were approximated using a Sommerfeld expansion, which is an expansion around a small electron degeneracy parameter[67] ($K_B T_e/E_F \ll 1$). Lampe showed that inclusion of the previously neglected electron-electron interactions led to an insignificant change in the electrical conductivity but found substantial reduction (25-50%) in the thermal conductivity for the phase space where electrons are strongly degenerate and the ions and electrons weakly coupled ($T > 10^7$ K and $10^{27} < n_e < 10^{30}$ cm^{-3}). The inclusion of the dynamic screening through the random-phase-approximation (RPA) dielectric function was also shown to reduce the thermal conductivity by a smaller amount.

Following his first paper, Lampe extended his calculation to partially-degenerate plasmas[69] by again using the quantum Lenard-Balescu equation linearized in the Chapman-Enskog approach. The Fermi-Dirac integrals are directly represented, and the transport coefficients are expressed using the first two polynomial approximations, which Lampe states is necessary in the non-degenerate regime. The primary approximations in this approach were the assumption that all collisions result in small momentum transfer (weakly coupled), and that the electrons and ions are all statically screened. The statically screened assumption was a necessary concession required to make the theory tractable in the partially degenerate regime. Finally, Hubbard and Lampe tabulated the combined theories of their papers for thermal conductivities in stellar matter[73] where temperatures are typically high enough to satisfy the weak-coupling requirements. This work, like Spitzer's for classical plasmas, again reiterated the importance of including electron-electron collisions in calculating the thermal conductivity, even in degenerate matter.

2.3.4 The Rinker model

One of the early implementations of an average atom (AA) model to calculate dense plasma conductivities was performed by Rinker[74] with the intent of creating wide-reaching tabulated values for use in hydrodynamic codes. These tables are part of the Sesame library and contain tabulated electrical and thermal conductivities as well as the average ionization values used in those calculations. These tables are in common use and will be compared with experimental data in later chapters.

The early Rinker tables[75], tables ending in the number 1 or 3 (for example Sesame 2371**1** for aluminum or Sesame 2214**1** and 2214**3** for iron), were centered around the calculation of the electrical resistivity using the modified Ziman formula, described by Evans *et al.*[76] as

$$\eta = -\frac{1}{3\pi\alpha}\left[\frac{\Omega_0}{Z_i}\right]^2 \frac{1}{\Omega_0}\int_0^\infty d\epsilon \frac{d}{d\epsilon} f_{\beta\mu}(\epsilon) \int_0^{2p} dq\; q^3 S(q)\sigma_\epsilon(q) \tag{2.48}$$

where η is the resistivity; Z_i is the number of free electrons per atom; Ω_0, the atomic volume; $f_{\beta\mu}$, the Fermi-Dirac distribution with $\beta = 1/k_B T$; $q = p' - p$, the momentum transfer; $S(q)$, the ionic structure factor; σ_ϵ, the electron-ion cross-section for momentum transfer; α, the fine structure constant; and ϵ, the incident energy. Rinker points out that to make use of this relation, four quantities must be specified—(1) the free electron density, (2) the chemical potential, (3) electron-ion scattering cross-section, and (4) ion-ion structure factor.

In principle, quantities (1)–(3) can be given self-consistently by an AA code, but simplifications were made in order to facilitate ease of calculation. The free electron density, Z_i, was given as the integral over the free-electron density of states weighted with the Fermi function:

$$Z_i = \int_0^\infty d\epsilon f_{\beta\mu}(\epsilon) \frac{dN_f}{d\epsilon} \; ; \frac{dN_f}{d\epsilon} = \frac{\Omega_0}{\pi^2} p(M + \epsilon) \tag{2.49}$$

In the above equation, p is the momentum, M represents the electron rest mass energy, and ϵ the kinetic energy. The chemical potential and scattering cross-section are dependent on the ionic potential used. Rinker states that standard solutions such as Liberman's[50] can produce a discontinuity in the self-consistent potential which can non-physically impact the low-energy scattering amplitudes. For this reason, he neglects the variational principle and provides his own potential, given by an interpolation function (in temperature and density space) that asymptotically approaches a Hartree-Fock-Slater mean-field approximation in the low-T, low-ρ region and a Thomas-Fermi-Dirac potential in the high-T, high-ρ phase space. The mean-field approximation potential accounts for the average force an electron feels in the field of the others, but neglects electron correlations[77]. The chemical potential is determined using this potential and the AA condition of charge neutrality, with the form of the potential being tweaked on an element-by-element basis to provide agreement with known melting-point resistivities and feasible conduction-band electron states. Finally, the structure factor is chosen as a function that essentially interpolates between the smooth Debye-Hückel form and the strongly peaked Percus-Yevick form.

With the electrical resistivity (and inversely, conductivity) thus calculated, Rinker computes the thermal conductivity[78] by taking Lampe's[69] electrical conductivity and replacing the electron-ion Coulomb logarithm with one that replicates his values over the entire phase space. The thermal conductivity exactly follows Lampe's work, but with this alternate Coulomb Logarithm. The belief is that this alleviates the reliance on the Born approximation implicit in Lampe's collision cross-sections and extends the model validity to strong ion-ion coupling ($\Gamma_{ii} < 200$) while preserving the validity at arbitrary degeneracy.

An improved version of the calculations—Sesame transport tables ending in 4 (for example Sesame 2214**4** for iron)—was later published by Rinker following the first set of tables[79]. The primary difference in this calculation is that the ionic potentials (and chemical potential) are determined self consistently by partial wave analysis rather than manually, as in the previous calculations. As before, these potentials blend with a Thomas-Fermi-Dirac potential as the calculation moves to high temperatures and densities. These potentials directly impact the density of states and elastic scattering cross-sections. Additionally, the assumed structure factor is taken to be that of a one-component plasma from the work of Rogers *et al.*[80].

2.3.5 The Lee & More model

Perhaps the most widely used thermal conductivity model in applied calculations is the model of Lee and More[13]. Its success can largely be attributed to the ease with which it can be implemented into codes for in-line calculations using different ionization models while maintaining respectable accuracy over most of the phase space.

The need for a model such as this arose from the increasing demand on computational models to design and understand laser-driven High Energy Density (HED) experiments in the 1980's when the primary models available were those of Spitzer[63] and Braginskii[19]—which are only valid for fully-ionized, non-degenerate plasmas—or that of Hubbard and Lampe[73]—valid for degenerate, but still fully-ionized and non-magnetized plasmas.

The model is based on a simple solution to the Boltzman equation with a relaxation time approximation for the collision operator, where the relaxation time has contributions from electron-ion and electron-neutral combined scattering using Matthiessen's rule, defined as

$$\frac{1}{\tau_c} = \frac{1}{\tau_{ei}} + \frac{1}{\tau_{en}} \tag{2.50}$$

with $\tau_{ei} = 1/n_i v \sigma_{ei}$, and $\tau_{en} = 1/n_0 v \sigma_{en}$. Electron-electron collisions are *not* included in the model, and this is expected to have inaccuracies below Z = 5–10 according to the authors[13]. The Coulomb log is formulated as

$$\ln\Lambda = \frac{1}{2}\ln\left(1 + \frac{b_{max}^2}{b_{min}^2}\right) \tag{2.51}$$

where b_{max} is the combination of the ion and electron Debye-Hückel screening lengths, λ_{DH}. This length is degeneracy-corrected, written as

$$\frac{1}{\lambda_{DH}^2} = \frac{4\pi n_e e^2}{k(T_e^2 + T_F^2)^{1/2}} + \frac{4\pi n_i \bar{Z}^2 e^2}{kT_i} \tag{2.52}$$

and is used for b_{max} unless it is smaller than an undefined interatomic distance, R_0, commonly taken to be the Wigner-Seitz radius[81], in which case R_0 is used for b_{max}. The minimum impact parameter, b_{min}, is taken as the largest value between the classical distance of closest approach and the de-Broglie wavelength,

$$b_{min} = \max\left[\frac{\bar{Z}e^2}{3kT_e}\,,\ \frac{h}{2m_e v_{th}}\right] \tag{2.53}$$

though the total Coulomb log value is clamped at a minimum value of 2.

The electron transport coefficients for non-magnetized plasmas using Fermi statistics for the electrons are given as

$$\sigma = \frac{n_e e^2 \tau_c}{m_e} A^{\alpha}\left(\frac{\mu}{kT_e}\right) \tag{2.54}$$

$$\kappa_{th} = \frac{n_e k k T_e \tau_c}{m_e} A^{\beta}\left(\frac{\mu}{kT_e}\right) \tag{2.55}$$

$$S = \frac{k}{e} A^{\gamma}\left(\frac{\mu}{kT_e}\right) \tag{2.56}$$

where σ is the DC electrical conductivity, κ_{th} is the thermal conductivity, and S is the thermoelectric power. The relaxation time for the plasma phase is given by

$$\tau_c = \frac{3\sqrt{m_e}(kT_e)^{3/2}}{2\sqrt{2}\pi\bar{Z}^2 n_i e^4 \ln\Lambda}\left[1 + exp\left(\frac{-\mu}{kT_e}\right)\right] F_{1/2} \tag{2.57}$$

and the A^α, A^β, A^γ coefficients are given as functions of μ/kT and Fermi-Dirac integrals

$$A^\alpha\left(\frac{\mu}{kT_e}\right) = \frac{4}{3}\frac{F_3}{[1 + exp(-\mu/kT_e)](F_{1/2})^2} \tag{2.58}$$

$$A^\beta\left(\frac{\mu}{kT_e}\right) = \frac{20}{9}\frac{F_4[1 - 16F_3^2/(15F_4F_2)]}{[1 + exp(-\mu/kT_e)](F_{1/2}^2)} \tag{2.59}$$

$$A^\gamma\left(\frac{\mu}{kT_e}\right) = \frac{5}{3}\frac{F_{3/2}}{F_{1/2}} - \frac{4}{3}\frac{F_3}{F_2} \tag{2.60}$$

$$F_j\left(\frac{\mu}{kT_e}\right) = \int_0^\infty \frac{t^j\ dt}{1 + exp(t - \mu/kT_e)} \tag{2.61}$$

The validity of these equations was tested by numerically calculating the partial-wave scattering cross-section off of Thomas-Fermi potentials and substituting this into the relaxation-time solutions to the Boltzmann equation, and reasonable agreement was demonstrated over wide conditions.

The model spans a wider phase space than the traditional plasma; Lee and More point out that (2.57) is only valid in the plasma state and propose different relaxation times in terms of mean free paths for solid and liquid materials. The melting temperature is defined by

$$T_m = 0.32[\xi/(1+\xi)]^4 \xi^{2b-2/3}\ \ (eV) \tag{2.62}$$

where $b = 0.6Z^{1/9}$ and $\xi = 9.0Z^{0.3}\rho/A$. The mean free path, l_{mfp}, below melting is defined as

$$l_{mfp} = \begin{cases} 50R_0(T_m/T) & T < T_m \\ 50R_0(T_m/T)(1/\gamma) & T \geq T_m \end{cases} \tag{2.63}$$

where γ is, in principle, defined for each metal to match the increase in resistivity upon melting. However, in practice, it is sometimes set to a constant. The HYDRA simulations described in later chapters use a value of 1.35 for γ.

Figure 2.4 shows the different regions in which the physical model for the collision time, τ_c, changes. Regions 1 and 2 represent the ideal plasma state, with region 2 taking R_0 for b_{max} rather than the Debye length. Region 3 uses the clamped Coulomb log value of 2 in equation 2.57. Region 4 represents a minimum conductivity valley where $l_{mfp} < R_0$, and so τ is manually set to $\tau = R_0/\bar{v}$. Finally, region 5 represents the solid and liquid regions where Bloch-Grüneisen theory is applied. In application, all types of collision time are calculated and the maximum one is used to generate transport coefficients. The shaded region in figure 2.4 shows the temperature-density space where WDM typically sits; it is clear that an experiment can traverse between regions 2–5 very quickly or exist in all simultaneously. The theory in these regions is quite simple and known to be questionable. In fact, many experiments, such as those described later in this thesis, largely fail to access regions in this model where plasma physics-based theory is used.

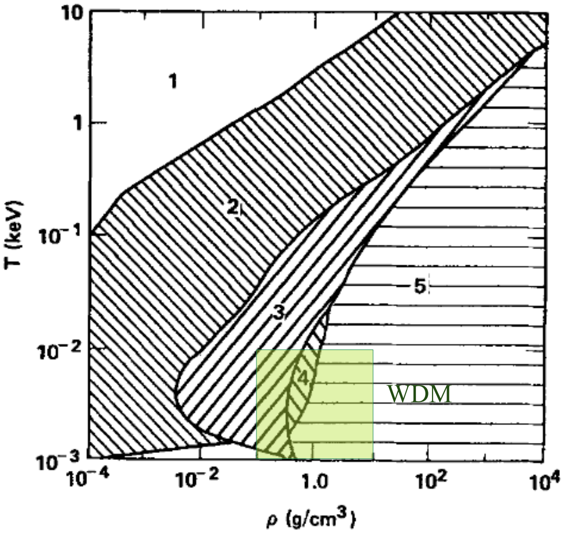

Figure 2.4: Regions where different models are applied in the model of Lee & More. Warm dense matter occupies regions 3–5, where model assumptions are the most simplified. Figure adapted with permission from [13].

The traditional Lee & More model was improved by Desjarlais[82] in this low-temperature region, with a particular focus on the metal-insulator transition. Correction is made to the ionization fraction, typically calculated with a Thomas-Fermi model, by using a Saha model with ad hoc pressure ionization correction that is smoothly blended to give Thomas-Fermi results at high temperature and density. The electron-neutral cross-section, which was constant in the original version, was calculated in the Born approximation using a screened polarization potential and parameterized to be temperature and density dependent. Finally, a new coefficient, $p_2 \in \mathrm{O}(1)$, was added to allow tuning of the minimum electron relaxation time (region 4) to available data. Together, these results allowed the electrical conductivity calculation to reproduce measurements done by DeSilva and Katsouros[83] of exploding aluminum and copper wires in glass capillaries.

2.3.6 The Purgatorio model

Purgatorio[52] is an AA model based on Liberman's Inferno[51], as discussed in section 2.2.3. Here, we discuss Purgatorio specifically and how it is used to calculate the conductivities compared with data in Chapters 4 & 5.

Much of the development work put into Purgatorio centered on how to accurately handle bound-state resonances. In the model, bound states—those below the chemical potential—are represented as discrete Eigenvalues. As the density increases and the Wigner-Seitz radius decreases, bound states are raised to higher energies. Roughly speaking, when the average radius for a particular shell is greater than or equal to the ion-sphere radius, it enters the continuum and becomes a quasi-bound resonance before becoming free[84]. Each shell (s, p, d, f, etc.) has a characteristic shape, and these impact the scattering cross-section quite strongly. These resonances can be very sharp as they cross the continuum line, and on a finite simulation grid, can be missed in numerical integrations. This has implications for thermodynamic consistency of EOS tables calculated from numerical derivatives of neighboring density-temperature points[56]. Purgatorio uses an adaptive-energy gridding method based on Gaussian quadrature[52] and a phase-shift tracking method[56, 85] to provide very robust numerics and thermodynamically-consistent quantities.

The phase shifts used for tracking numerical stability also have physical significance and are the necessary input to calculate the electrical and thermal conductivity. The electrical conductivity is calculated using the extended Ziman formula[76] as used by Rinker[75]. The primary difference in calculation of the electrical conductivity results from improvements in the self-consistent field model (more stringent numerical methods and convergence requirements, and inclusion of a LDA exchange and correlation potential), slight differences in how the average ionization is applied, and a different structure factor. The approach taken for the thermal conductivity is entirely different.

The Ziman formula is based on relaxation time approach where resistivity is calculated on the assumption that electrons in a metal are accelerated until they collide with scattering centers in some mean time, τ. This is represented in Drude-like form as

$$\eta = \frac{1}{nZ_i}\left(\frac{1}{\tau}\right) \tag{2.64}$$

where nZ_i is the charge carrier density. The relaxation time is dependent on the scattering cross-section and the free-electron velocity distribution, given as

$$\left(\frac{1}{\tau}\right) = -\frac{1}{3\pi Z_0}\int_0^\infty \sigma(\epsilon)\frac{\partial f(\epsilon,\mu)}{\partial \epsilon}d\epsilon \tag{2.65}$$

where Hansen[55] points out that Z_0 must be the number of free electrons in the ideal density of states (ignoring quasi-bound resonance contributions), but the number of charge carriers, Z_i, does not have to be. The scattering cross-section in the traditional Ziman formula is based on the free-electron scattering from a pseudo-potential representation of the ion. These approximate pseudo-potentials do not accurately capture effects from resonances of quasi-bound states. The t-matrix formulation of Evans[76] represents the scattering cross-section as the integral of the angle-dependent differential cross-section over all scattering angles, θ, modulated by the ion structure factor, $S(q)$, as a function of q where q is the momentum transfer vector, $q^2 = 2p^2$[1-cosθ].

$$\sigma(\epsilon) = \int_0^{2p} q^3\left(\frac{d\sigma(p,\theta)}{d\theta}\right)S(q)dq \tag{2.66}$$

The ion structure factors are not calculated self-consistently, and must be specified. The model of Baiko *et al.*[86] was chosen. The angle-dependent differential cross-section is given in terms of Legendre polynomials as

$$\frac{d\sigma(p,\theta)}{d\theta} = \frac{1}{p^2}\left[\left|\sum_{\kappa} |\kappa| e^{i\delta_\kappa(p)} sin(\delta_\kappa(p)) P_l(cos\theta)\right|^2 + \left|\sum_{\kappa} \frac{|\kappa|}{i\kappa} e^{i\delta_\kappa(p)} sin[\delta_\kappa(p)] P_l^1(cos\theta)\right|^2\right] \tag{2.67}$$

where P_l and P_l^1 are the Legendre and associated Legendre polynomials; p, the relativistic dispersion relation such that $p^2 = \varepsilon(2 + \varepsilon\alpha^2)$; and the scattering phase shifts, δ_k, are determined by matching the numeric solution to the Dirac equation within the Wigner-Seitz radius to analytic solutions outside of it (see Yuan *et al.* for analytic forms[54]).

The Ziman theory has no direct link to thermal conductivity. In order to incorporate the electron-scattering physics calculated by Purgatorio, the electron thermal conductivity is obtained using the Wiedemann-Franz law (see Section 2.3.7) in conjunction with the calculated electrical conductivity[87]. A proportionality constant, the Lorenz number, is chosen from the transport model of Lee & More[13]—specifically, the ratio of equations (2.58) and (2.59)—which is a function of Fermi-Dirac integrals, the electron temperature, and the chemical potential, which are self-consistently determined with Purgatorio. In the case of thermal conductivity, the effects of electron-electron collisions must explicitly be added to the Ziman approach. This is accomplished by modifying the effective relaxation time (total relaxation frequency) to be the sum of e-e and e-i scattering contributions, invoking Matthiessen's rule to give $\nu_\kappa = \nu_{ei} + \nu_{ee}$. The e-i relaxation time is given by eq. (2.65), and the e-e relaxation time is taken from the semi-empirical fits given by Potekhin *et al.*[88] and later improved to arbitrary degeneracy by Cassisi *et al.*[89]. The thermal conductivity is then given in terms of the combined e-e & e-i relaxation time, τ_κ and the Lee & More derived Lorenz number, L_{LM}, as

$$\kappa_{th} = L_{LM} k_B^2 T \, n Z_i \left(\frac{1}{\tau_\kappa}\right) \tag{2.68}$$

2.3.7 The Wiedemann-Franz law

Initially proposed in 1853, the Wiedemann-Franz law[90] provides a link between the electrical and thermal conductivities through the Lorenz number, L, which is a constant for most metals.

$$\frac{\kappa_{th}}{\sigma_{DC}} = LT \tag{2.69}$$

The Wiedemann-Franz law (WFL) was proven valid in the degenerate strong and weak coupling regimes by Chester and Thellung[72] using the linear response framework of Kubo[91]. They concluded that it was valid in both regimes, and the Lorenz number took the exact value of $\pi^2/3(k_B/e)^2$ (note: commonly values of L are quoted by the value of the pre-factor, $\pi^2/3 = 3.29$, with physical constants excluded) provided (i) electrons are scattered elastically (by impurities or lattice vibrations), (ii) the electrons move independently of one another and follow Fermi-Dirac statistics, and (iii) the Boltzmann equation is valid.

In the non-degenerate case, the Lorenz factor can be calculated using electrical and thermal conductivities as defined by Spitzer[63]. For a Lorentz plasma, $L = 4.0$, and with the electron-electron collisions included, it decreases to 1.5966[92].

The primary requirement ensuring validity of the Wiedemann-Franz law is elasticity of the electron collisions[93, 67]. In order to break the relationship, we require an effect that can impact one current (thermal or electric) while leaving the other untouched. The electric charge of an electron will not change in a collision, so electric current can only change via velocity changes. However, for thermal currents, an inelastic collision can change the energy an electron carries in addition to its velocity. Thus, inelastic collisions are expected to break the symmetry.

In warm dense matter, the relationship is not well understood. No experimental validations of the WFL exist. Several authors have presented Lorenz factors calculated from QMD simulations of warm dense hydrogen[70, 94] and aluminum [95]. For densities above several g/cc, the results appear to remain between the degenerate limit of 3.29 and the classical limit of 1.5966. However, the calculations by Holst *et al.* demonstrate substantial deviations (up to an order of magnitude) for densities of 0.01–1 g/cc and for temperatures of 10–50 kK.

2.4 Equation of State models

The equation of state (EOS) refers to a system of equations that describe the thermodynamical properties of matter. An EOS describes the relationships between variables that are dependent on each other such as pressure, temperature, density, entropy, etc. that together fully characterize the material. The most widely known, basic EOS would be the ideal gas model given (for a plasma) by

$$p = \frac{\rho(1+Z)k_BT}{Am_p} \tag{2.70}$$

and

$$\rho\epsilon = \frac{p}{\gamma - 1} \tag{2.71}$$

where p is the pressure; ρ is the density; Z, the degree of ionization; A, the atomic mass; ϵ, the internal energy; and γ, the ratio of specific heats C_p/C_V given by $\gamma = 1 + 2/n$ for a gas with n degrees of freedom.

The primary assumption of these relations is that the particles will be weakly interacting. For a plasma with average kinetic energies greatly exceeding energies from Coulombic potentials—at high temperatures, low densities, and full ionization—this is a fair approximation. However, for most HED plasmas of interest, these conditions do not hold, and more sophisticated EOS models are required to obtain accurate predictions. In the following sections, I discuss the construction of three commonly used equation of state models—QEOS, LEOS, and Sesame.

2.4.1 QEOS

In 1988, R. M. More *et al.* introduced a now widely-utilized model called the Quotidian Equation of State (QEOS)[96]. As the name quotidian—meaning everyday or commonplace—suggests, this model was designed for simplicity while still maintaining accuracy (better than 15–20%) over the wide temperature and density ranges found in ICF and laser-produced plasma experiments. The work points out the growing use of hydrodynamic modeling to interpret experimental results and, with that in mind, prioritized features that would allow Z scalability, smooth and numerically stable functions, and inexpensive computation.

The model's basic construction relies on the assumption that electron and ion contributions to the free energy can be treated individually and summed. This approach requires an additional corrective term to account for chemical bonding effects present at solid density as quantum effects are not accurately treated. The Helmholtz free energy (from which internal energy, pressure, and entropy can be derived) of such a model takes the following form:

$$F(\rho, T_e, T_i) = F_i(\rho, T_i) + F_e(\rho, T_e) + F_b(\rho, T_e) \tag{2.72}$$

where each of the ion, electron, and binding terms are expressed using often unrelated semiempirical models relevant to that species. This decomposition provides the foundation for most EOS models and is a big assumption—especially in dense systems. Recent work by Burnett *et al.*[97] uses QMD to explore the validity of this. The pressure (p), entropy (S), and energy (E) are related to the free energy as follows[96]

$$p = \rho^2 \frac{\partial F}{\partial \rho} \tag{2.73}$$

$$S = -\frac{\partial F}{\partial T} \tag{2.74}$$

$$E = F + TS \tag{2.75}$$

and thermodynamic consistency is defined as

$$\rho^2 \left(\frac{\partial E}{\partial \rho} \right) = p - T \left(\frac{\partial p}{\partial T} \right) \tag{2.76}$$

The electron-thermal contribution is modeled with Thomas-Fermi theory, which is just the simple case of the AA model discussed earlier where the radial density function is related to the self-consistent potential through the Poisson equation. This theory can be scaled based on atomic mass and charge and is preferred, for this reason, over more accurate electronic structure models that include exchange, correlation, or improved kinetic energy terms. A single table can be calculated and quickly scaled for any element or mixture.

The use of Thomas-Fermi theory for the electrons means that at solid density for metals, the electron pressure is a few megabars. Chemical bonds provide the necessary energy to hold material at equilibrium conditions at zero pressure. To account for this, the bulk modulus, $B = \rho(\partial p_{tot}/\partial\rho)_{\rho_0}$, is used to calculate fitting parameters to the semiempirical bonding correction.

Finally, the ion contribution is based on a generalization of the Cowan model[7] which smoothly transitions from an ideal gas behavior at high temperatures and low densities, to a liquid metal, to a cold crystal dominated by lattice vibrations at high low temperature and high density. This is another semiempirical model that scales between solid, liquid, and gas regimes based on the Debye temperature (Θ_D), the melting temperature (T_m), and the Grüneisen coefficient (γ_s). The Helmholtz free energy from the ions is given by

$$F_i = \left(\frac{k_B T_i}{A M_p}\right) f(u, w) \tag{2.77}$$

where $u = \Theta_D(\rho)/T_i$ and $w = T_m(\rho)/T_i$ are scaling variables that determine whether the system is in the fluid, high-temperature solid, or low-temperature solid phases, and f provides the functional behavior of each regime in terms of u and w. In practice, the Debye temperature, melting temperature, and Grüneisen coefficient are all represented as empirical formulas that are tweaked to provide agreement with available data.

2.4.2 LEOS

An alternative model available at LLNL is the Livermore Equation of State (LEOS). This model is the successor of QEOS and reaffirms many of the same computational goals, but makes efforts to improve specific aspects of the tables. These aspects include the modeling of shock-Hugoniot curves, diamond-anvil isotherms, liquid-vapor critical points, and the addition of molecular degrees of freedom[98]. Away from these portions of phase space, LEOS tables very closely match the QEOS model.

These improvements are implemented into the overall table structure by including more flexible fitting functions for the zero-Kelvin energy isotherm, the Grüneisen gamma function, and cold cohesive energy equation. Specific experimental data such as shock velocity measurements often display discontinuities at solid-solid phase transitions, which the original QEOS model could not fit. Break points were added to the fitting process, providing the necessary flexibility to match these data.

EOS models such as LEOS are pre-calculated onto a logarithmically-spaced temperature-density grid[99]. A major factor in the accuracy of EOS models as-used is in the numerical interpolation methods that hydrodynamics codes use to access the table. Poor interpolation subroutines can lead to thermodynamic inconsistency and negative-valued properties such as bulk-modulus and sound speed. For this reason, the LEOS data library contains and is designed to use its own subroutines to perform bilinear or bicubic interpolation between table values.

Ultimately, each table for a given element, compound, or mixture will be loosely based on this framework but have normalizations and semiemperical fits to whatever data or trusted detailed simulations were available at the time of construction.

2.4.3 Sesame

The Sesame collection of tables[100] were one of the first wide-spread, publicly available, tabulated EOS models. The first tables were created by J. Barnes and J. Rood starting in 1971[101], though many authors have contributed to the large library maintained by Los Alamos National Laboratory.

The models of the EOS are constructed with the same idea of separable contributions to the free energy, and various models are employed for the electron, ion, and cold correction curves.

As an example, Figure 2.5 shows the regions where various models are implemented in the

Sesame 3712 table for aluminum, the descriptions from which can be found in [101]. The exact construction will differ for each table, with less-important elements receiving less detail, and documentation for each table should be consulted prior to use.

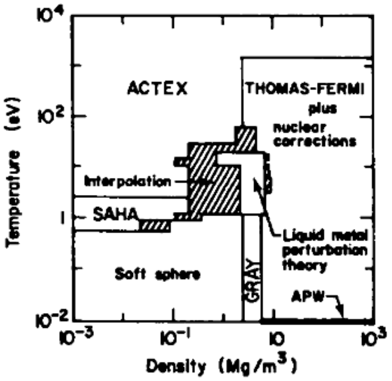

Figure 2.5: Phase space diagram indicating where different models are applied in the Sesame 3712 aluminum table. The shaded region between models, corresponding to WDM, is interpolated over. Figure reprinted with permission from ref. [101].

2.5 Radiative transfer

When matter exists at elevated temperature such that it is significantly ionized, radiation plays a strong role in the transport of energy and is a powerful tool in determining the state of the plasma. The photon distribution function, the specific intensity, $\mathbf{I}(\mathbf{r}, \mathbf{n}, \nu, t)$, is described using the 1-D radiative transfer equation as[102]

$$\left[\frac{1}{c}\frac{\partial}{\partial t} + \mu\frac{\partial}{\partial z}\right] \mathbf{I}(\mathbf{r}, \mathbf{n}, \nu, t) = \eta(\mathbf{r}, \mathbf{n}, \nu, t) - \chi(\mathbf{r}, \mathbf{n}, \nu, t)\mathbf{I}(\mathbf{r}, \mathbf{n}, \nu, t) \tag{2.78}$$

where $\mathbf{r}$ is the radiation position; $\mathbf{n}$, the propagation unit vector; $\mu = \cos(\theta)$ where θ is the angle between the +z and propagation direction; ν is the frequency; t, the time; η, the emissivity; and χ, the absorptivity. Equation (2.78) takes the form of a conservation equation. The two terms on the left describe the change in the specific intensity along a unit vector in time and space. The terms on the right represent source and sink terms with the emissivity term, η, describing how matter adds to the specific intensity as radiation propagates through it and the absorptivity term, χ, describing how photons are lost (or scattered) by matter as they propagate.

Both of these terms critically depend on ionization distribution and excited state populations. In Thermodynamic Equilibrium (TE), this is determined by the local state variables such as pressure and temperature. For this condition to hold, elastic collisions must distribute the electrons and ions into a Maxwellian distribution, and the medium must be optically thick such that all radiation processes experience detailed balance, forming a Planckian distribution. In TE, the ionization distribution of the matter is given by the Saha ionization equation (following the notation of Hubeny and Mihalas[103])

$$\frac{N_I}{N_{I+1}} = n_e \frac{U_I}{U_{I+1}} \left(\frac{h^2}{2\pi m_e k_B T} \right)^{3/2} e^{\chi_I / k_B T} \tag{2.79}$$

where the subscript I represents an ionization stage such that N_I, U_I, and χ_I represent the number density, partition function, and ionization potential of ionization stage I. The excited state populations denoted by subscript i are determined within an ionization stage by the Boltzmann excitation equation

$$\frac{n_i}{N_I} = \frac{g_i}{U_I} e^{E_i / k_B T} \tag{2.80}$$

where g_i is the statistical weight, and E_i is the excited level energy.

In reality, plasmas can never be in TE due to finite sizes, gradients, and boundary layers all driving the radiation out of detailed balance. In the case where the particle distributions are still Maxwellian at the local temperature, the plasma may be classified as being in LTE, and the Saha and Boltzmann equations remain valid. In this situation, parts of the radiation spectrum may be in equilibrium, but strong lines often are not. For a specific transition to be in LTE, the collisional de-excitation rate from the upper level must greatly exceed the spontaneous decay rate. Chung *et al.*[104] provide a simple estimate of densities for which this occurs, defined as

$$n_e[\mathrm{cm}^{-3}] \geq 1.6 \times 10^{12} T_e[\mathrm{eV}]^{1/2} E_{mn}[\mathrm{eV}]^3 \tag{2.81}$$

where E_{mn} is the transition energy.

With the populations determined, the total emissivity (η_{tot}) and absorptivity (χ_{tot}) may be determined. There are contributions from photons created by bound electrons transitioning between energy levels (bb), photons created by free electrons interacting with bound electrons (bf), and free electrons colliding with ions (ff). The total emissivity and absorptivity values are assumed to be the superposition of all of these added linearly and independent of each other. The sums span the occupation numbers of all levels i, all ions j, and all elements k with u and l representing upper and lower bounds, written as[103]

$$\begin{aligned}\chi_{tot}(\mathbf{n},\nu) = &\sum_k \sum_j \Bigg[\\ &\sum_{u>l} \sum_l \left[n_{ljk}\phi_{lu,jk}(\mathbf{n},\nu) - (g_l/g_u) n_{ujk}\psi_{ul,jk}(\mathbf{n},\nu)\right] (B_{lu,jk}h\nu/4\pi) + \\ &\sum_i \left(n_{ijk} - n^*_{ijk}e^{-h\nu/kT}\right) \alpha^{bf}_{ijk}(\nu) \ + \ n_e n_{jk} \left(1 - e^{-h\nu/kT}\right) \alpha^{ff}_{jk}(\nu,T)\Bigg] \quad \left[cm^{-1}\right]\end{aligned} \tag{2.82}$$

$$\begin{aligned}\eta_{tot}(\mathbf{n},\nu) = &\sum_k \sum_j \Bigg[\sum_{u>l} \sum_l n_{ujk}\psi_{ul,jk}(\mathbf{n},\nu)(A_{ul,jk}h\nu/4\pi) + \\ &(2h\nu^3/c^2)e^{-h\nu/kT}\left[\sum_i n_{ijk}\alpha^{bf}_{ijk}(\nu) + n_e n_{jk}\alpha^{ff}_{jk}(\nu,T)\right]\Bigg] \quad \left[ergs/cm^3/sec/Hz/str\right]\end{aligned} \tag{2.83}$$

where ϕ_{lu} is the line absorption profile; ψ_{ul}, the line emission profile; B_{lu}, the Einstein absorption probability; A_{ul}, the Einstein coefficient for spontaneous emission; α, the process-relevant cross-section; and superscript * denotes the LTE quantity. Thus, with accurate frequency dependent data for the absorption cross-sections and line profiles for each transition, the radiation transfer equation (2.78) may be solved.

2.5.1 Collisional radiative (NLTE) models

When the assumptions of LTE do not apply, such as in boundary layers of stars or optically-thin laboratory plasmas, more general methods of determining the ionization and population balance must be used. These models are generally called NLTE or collisional radiative models and are employed in widely-used simulation codes such as FLYCHK[105], CRETIN[106], or SCRAM[107].

When the Saha and Boltzmann equations are no longer valid, the excited states must be determined explicitly via a set of coupled rate equations of the form

$$\frac{dn_i}{dt} = n_i \sum_{j\neq i}^{NL} (R_{ij} + C_{ij}) - \sum_{j\neq i}^{NL} n_j (R_{ji} + C_{ji}) \tag{2.84}$$

where NL represents the total number energy levels, and R_{ij} and C_{ij} the rates of radiative and collisional transitions from state i to j, respectively.

Radiative processes include spontaneous and stimulated decay, photoabsorption, and photoionization. The general form of a radiative rate for a bound-bound absorption transition is given by[103]

$$R_{ij} = B_{ij} \int_0^\infty \oint \mathbf{I}(\nu, \mathbf{n}) \phi_{ij}(\nu, \mathbf{n}) \left(\frac{d\Omega}{4\pi}\right) d\nu = B_{ij} \int_0^\infty \phi_{ij}(\nu) J_\nu d\nu \equiv B_{ij} \bar{J}_{ij} \tag{2.85}$$

where B_{ij} is the Einstein coefficient for stimulated absorption, I_ν is the local intensity given by the transfer equation (2.78), and $\phi(\nu)$ is the absorption line shape profile. The reverse downward process is given by

$$R_{ji} = A_{ji} + B_{ji} \int_0^\infty \oint \mathbf{I}(\nu, \mathbf{n}) \psi_{ji}(\nu, \mathbf{n}) \left(\frac{d\Omega}{4\pi}\right) d\nu \tag{2.86}$$

where A_{ji} and B_{ji} are the Einstein coefficients for spontaneous and induced emission probabilities, respectively, and ψ_ν is the emission line shape profile ($\psi_\nu = \phi_\nu$) under the assumption of complete redistribution (valid when collisional rates greatly exceed radiative rates). It should be noted that a complete model would require radiative rates for bound-free and free-free interactions in addition to the given bound-bound rates.

Collisional processes refer to excitation/ionization by collisions between species within the plasma, most commonly electrons. These take the general form of

$$n_i C_{ij} = n_i n_e \int_{v_0}^{\infty} \sigma_{ij}(v) f(v) v dv \tag{2.87}$$

where σ_{ij} is the cross-section of an impact causing transition $i \rightarrow j$ to occur as a function of the electron velocity, and $f(v)$ is the electron distribution function. These cross-sections are often measured or derived from more involved calculations but always depend on local thermodynamic quantities such as the average ionization, electron density, electron temperature, and electron distribution function.

Constructing a complete atomic model is a daunting task that requires detailed data or calculations for the Gaunt factors, the oscillator strengths, the excited state energies, and all relevant cross-sections. In practice, detailed models are most commonly built using HULLAC[108] or FAC[109]. The number of available transitions grows rapidly with the atomic number. Figure 2.6 shows the statistical weight (approximately equal to number of transitions) that a detailed model containing single- and some doubly-excited states may have as the number of electrons increases. Simply storing a rate matrix that contains 10^6 transitions may occupy as much as a terabyte of computing memory[110], causing the problem to quickly become intractable.

A review by Hansen in ref. [110] discusses the balance that must be struck between state-space completeness and computational tractability. The complexity of NLTE models has led to an ongoing workshop series in the NLTE modeling community to compare, benchmark, and improve codes[111, 112, 113, 114, 115, 116, 117, 118].

The high degree of complexity required for NLTE model construction often means any additional physics is implemented in simplified ways. At high density, ionization potential depression is frequently incorporated using ad hoc models such as the one by Ecker and Kroll[119] or Stewart and Pyatt[120]. The line shape function, ϕ_ν, is sensitive to the uncertainty principle (natural line

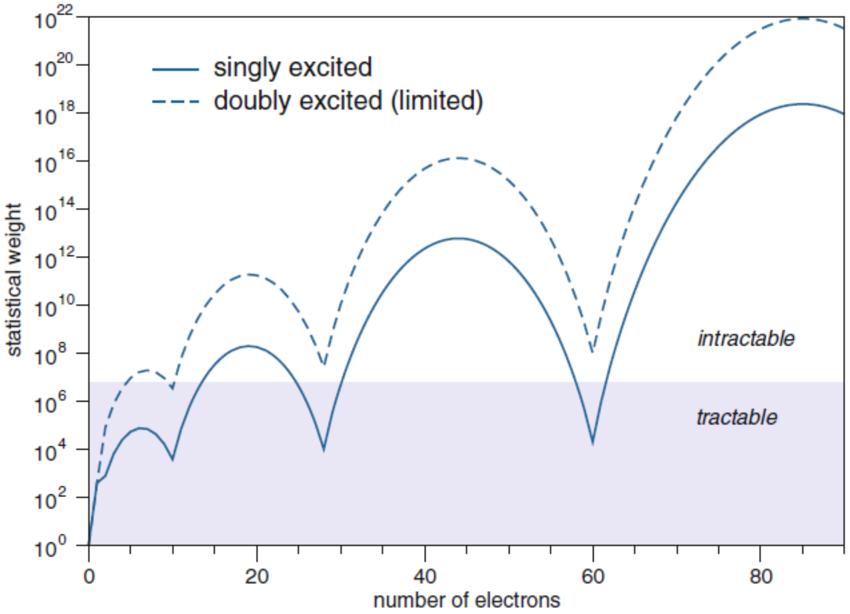

Figure 2.6: Statistical weight per ion in a detailed model as a function of the number of bound electrons. The solid line includes all single excitation states to principle quantum number ($n_{max} = 8$) from valence and first inner shell electron. The dashed line includes double-excited states from the valence and first inner shells to the same maximum n. The shaded region indicates approximately where detailed calculations become intractable due to computing limitations. Figure credit to S. Hansen[110] reprinted with permission.

widths), local electric fields (Stark effects), magnetic fields (Zeeman effects), and velocity distributions (Doppler effects) and can differ for absorption or emission lines, just to name a few. These effects are often simplified or calculated with external codes at even greater computational expense. Opacity effects are often neglected entirely, assuming an optically-thin plasma, or integrated via simplified models such as the escape factor formalism. Great success has been achieved matching experimental plasma spectra to theory, but many assumptions within the calculations remain untested due to the complexity associated with obtaining sufficiently accurate measurements.

2.5.2 Escape factor approximation

If we take another look at the net radiative transition rate from level j to i,

$$n_j R_{ji}^{net} \equiv n_j A_{ji} + n_j B_{ji} \bar{J}_{ij} - n_i B_{ij} \bar{J}_{ij} \tag{2.88}$$

we see that the solution of the rate itself is dependent on the frequency-averaged mean intensity $\bar{J}_{ij} = \int_0^\infty J_\nu \phi_{ij}(\nu) d\nu$. This is a form of the very quantity we are trying to solve for in the transfer equation (2.78), and these rates make the rate matrix non-linear and much more costly to solve. The escape factor approximation simplifies this by calculating an *effective* spontaneous emission rate—including the effects of stimulated emission and absorption—that is independent of the radiation field. This can be expressed as[103]

$$n_j A_{ji} + n_j B_{ji} \bar{J}_{ij} - n_i B_{ij} \bar{J}_{ij} \equiv n_j A_{ji} Z_{ji} \tag{2.89}$$

where Z_{ji} is known as the Net Radiative Bracket (NRB). Using the definition of the line source function as the ratio of the emissivity to the absorption, $S_{ij} = \eta_{ij}/\chi_{ij} = n_j A_{ji}/(n_i B_{ij} - n_j B_{ji},)$, the NRB can be expressed exactly as

$$Z_{ji} = 1 - \frac{\bar{J}_{ij}}{S_{ij}} \tag{2.90}$$

This is not immediately helpful as it still depends on the intensity. However, Irons proved that the emission-weighted average escape coefficient is equal to the emission-weighted escape probability over the entire volume (known as Irons Theorem[121])

$$\langle Z \rangle = \langle P_e \rangle \tag{2.91}$$

where the angle brackets of a function f are given by

$$\langle f \rangle = \frac{\int f(\tau) S(\tau) d\tau}{\int S(\tau) d\tau} \tag{2.92}$$

and the escape probability is defined as a global probability that a photon created anywhere within the volume escapes. Thus, if a satisfactory escape probability can be calculated, Irons Theorem indicates that using the escape factor formalism should be a reasonable approach.

Since the escape probability is a globally-averaged quantity, its formulation is sensitive to the geometry and absolute size of the problem. Details of the spectral line shape across the volume must also be considered. Irons published a series of papers that described, reviewed, and elaborated on escape factors in the late 1970's[122, 123, 124, 125].

The approximation is a method of expediting the exact transfer problem, so historically the escape factors have been solved and tabulated for specific line shapes and symmetric geometries. Mancini *et al.*[126] have calculated escape factors for Stark-broadened lines and tabulated them for spherical geometry. Bhatia and Kastner have similarly done so for Doppler profiles in cylindrical[127] and planar[128] geometries. More recently, Phillips *et al.*[129] reviewed commonly used escape factor formulations (Holstein, Apruzese, Rose, and Capriotti) for 0-D radiation transfer codes, all of which are presented as approximate analytic formulae as functions of τ_0, the geometric average optical depth at line center. It is stressed that care must be exercised when choosing the chord along which τ_0 is calculated, and it may not be the same for the calculation of population balance as it is for calculating the observed emission spectrum.

2.6 HED Drivers

All of the experimental studies found in this thesis involve the creation of samples of matter at extreme conditions. High energy density (HED) material is generally defined as having pressures exceeding 1 Mbar, or an energy density greater than 10^{11} J/m^3[17]. To create these same conditions in the laboratory, we require drivers capable of converting solids, liquids, and gases—generally at ambient temperature—to plasmas in large enough volumes for systematic study.

Technologies in use today capable of accomplishing this feat, include pulsed-power drivers, long-pulse optical lasers, short-pulse optical lasers, and x-ray free electron lasers. These primary drivers are frequently used to create intense secondary sources of x-rays, electrons, or ions which may themselves be used as drivers. Each of these technologies rely on different mechanisms to couple energy from the driver to the sample, which has important implications for how the system equilibrates and evolves. Understanding the physics in these coupling processes remains an area of focused study essential for complete understanding of these generated plasmas. In the following sections, I will discuss the mechanisms by which the HED drivers used in this thesis couple energy to matter at solid density.

2.6.1 Heating with lasers

Since the application of Chirped Pulse Amplification (CPA)[130] to optical lasers, laser systems have grown increasingly capable of delivering tremendous energy to very small volumes of materials in extremely short time periods, making them a common choice of driver in the creation of HED matter. Short-pulse lasers are particularly suited to delivering energy before material has time for hydrodynamic motion ($\ll$100 ps), making them a sensible choice for experimental studies of transport quantities such as those described in this thesis.

An incoming laser pulse with photon energy less than the material's ionization energy, U_{ion}, may directly ionize ambient material by multi-photon ionization, tunnel ionization, or barrier suppression ionization. Multi-photon ionization occurs when the minimum number of necessary photons (n) interact simultaneously with an atom to overcome the binding energy, imparting a kinetic energy, K_E, of

$$K_E = n\hbar\omega - U_{ion} \tag{2.93}$$

to the now-free electron. Tunneling ionization occurs when the oscillating potential of the laser's electric field sums with the atomic Coulombic potential binding an electron

$$U(x) = -\frac{e^2}{x} - exE_0cos(\omega t) \tag{2.94}$$

and the effective barrier height is reduced. The electrons may then quantum-mechanically tunnel through the reduced potential well and become free. Barrier suppression ionization occurs when the laser potential is sufficiently intense that the atomic potential is reduced beyond the ionization energy, and ionization is achieved directly.

The Keldysh parameter[131, 132] determines which of these mechanisms is dominant based on the laser intensity:

$$\gamma_K = \sqrt{\frac{U_{ion}}{2U_p}} = \sqrt{\frac{2U_{ion}m_e\omega_0^2}{(eE_0)^2}} = \sqrt{\frac{U_{ion}(eV)}{1.87 \cdot 10^{-13} I(W/cm^2)\lambda_\mu^2(\mu m)}} \tag{2.95}$$

where U_p is the ponderomotive potential of the laser. When γ_K is much less than 1, tunneling ionization is dominant, and when γ_K is much greater than 1, multi-photon ionization is preferred. The intensity of many short-pulse lasers exceeds 10^{18} W/cm^2, so ambient material is rapidly ionized by the rising edge of the laser pulse. As such, the majority of the laser pulse interacts with an ionized plasma. However, even at intensities as low as 10^{12} W/cm^2, ionization by the nanosecond pedestal that accompanies CPA lasers is possible and must be considered if a long scale-length pre-plasma is undesirable. Once a small degree of ionization is present, collisional ionization will rapidly increase the number of free electrons.

Optical lasers interact primarily with electrons in matter due to the relative mass difference between ions and electrons and the inability of the ions to move at the laser frequency. The sinusoidal electric field of the laser causes electrons to oscillate, or quiver, in response. The velocity of the electron oscillating in the electric field, $E_L = E_0 cos(\omega t - kz)$, is given as[133]

$$\frac{p_{osc}}{m_e c} = \frac{\gamma v_{osc}}{c} = \frac{cE_0}{m_e c\omega_0} = \sqrt{\frac{I\lambda_\mu^2}{1.3 \times 10^{18}}} \tag{2.96}$$

where p_{osc} is the momentum of the oscillating electrons; γ, the relativistic factor; E_0, the laser electric field amplitude; I, the laser intensity in W/cm^2; and λ_μ, the laser wavelength in μm. Writing laser absorption fractions in terms of the factor $I\lambda_\mu^2$ allows for easy comparison between laser systems and focal geometries.

In the following sections, I will describe some of the more energetically important absorption mechanisms that exist in the experiments described within this thesis. In any laser-plasma experiment, many mechanisms will be active simultaneously or at various points during the laser pulse depending on the exact laser parameters—focal spot, wavelength, intensity, polarization, contrast ratio, angle of incidence—and the specific material properties impacting ionization and the created scale length. Understanding the dominant mechanism(s) allows for a deeper understanding of the spatial/temporal deposition of energy as well as the energy spectrum and angular distribution of the excited electrons. This is important in order to understand the deviations from LTE assumptions under which most models are held. The discussion in this section closely follows Gibbon's[134] and Kruer's[135] texts, unless otherwise mentioned.

2.6.1.1 Inverse Bremsstrahlung

Inverse bremsstrahlung, also referred to as collisional absorption, occurs when electrons are accelerated in the incident laser's electric field and then collide with the stationary ions thereby removing energy from the electric field. The classical theory for the inverse bremsstrahlung absorption coefficient is given according to Pfalzner and Gibbon[136] as

$$\kappa_{IB} = 1.89 \times 10^6 \frac{Z n_e^2 \ln\Lambda}{T_e^{1/2} \nu_0^3} \left(1 - \frac{\omega_p}{\omega_0}\right) \left(1 - e^{-h\nu_0/k_B T_e}\right) \;[cm^{-1}] \tag{2.97}$$

Looking at equation (2.97), we can see that inverse bremsstrahlung is most efficient for high densities, high Z materials, and low temperatures. The absorption coefficient is maximized when the plasma frequency matches the laser frequency at the critical surface. The decreasing efficiency with increasing temperature is caused by the strong decrease ($\propto v_{th}^{-3}$) of the classical collision frequency with increasing thermal velocity. It is for this reason that inverse bremsstrahlung is the dominant absorption mechanism for laser intensities $<10^{15}$ W/cm^2, especially in plasmas with long scale lengths, but becomes ineffective when high laser intensities create local high-temperature collisionless plasmas.

2.6.1.2 Resonance Absorption

Resonance absorption occurs when the laser is incident at oblique angles and a component of the laser's electric field is parallel to the electron density gradient (P polarization). The pulse will reach a turning point and reflect at a density below the critical density given by $n_c\cos^2\theta$, where θ is the angle relative to the target normal. An evanescent wave may propagate a characteristic distance given by the collisionless skin depth, $l_s = c/\omega_p$, and resonantly excite an electron plasma wave. The energy in the plasma wave is subsequently dispersed to the plasma in secondary mechanisms such as particle trapping at low intensities or wave breaking at high intensities.

Naturally, the amplitude of the electric field that may tunnel to the critical surface will depend on the scale length, L_n, and the laser frequency, ω_0. Following conventional derivations, the efficiency of the resonance absorption mechanism is given as a function of the dimensionless parameter $\tau = (\omega_0 L_n/c)^{1/3}\sin\theta$ by

$$\phi(\tau) \approx 2.3\tau e^{-2\tau^3/3} \tag{2.98}$$

The total absorption fraction, f_{ra}, given by

$$f_{ra} \approx \frac{\phi^2(\tau)}{2} \tag{2.99}$$

The efficiency, $\phi(\tau)$, has a global maximum at $\tau \approx 0.8$. If the scale length is too long, no electric field can tunnel to the critical surface and excite a resonance. If the scale length is too short, the electron density modulations that give rise to the electron plasma wave cannot be supported, and again no resonance will occur[137]. For this reason, resonance absorption is an important absorption mechanism to consider but is only dominant for specific conditions.

2.6.1.3 Vacuum Heating

Vacuum heating, or ”not-so-resonant” resonance absorption as named by Brunel[138], becomes important for high intensity interactions on sharp density gradient targets with P polarization. Electrons near the target surface and within a skin depth will experience oscillations in the laser field approximated by $x_p \approx eE_0/m_e\omega^2 = v_{osc}/\omega$. These electrons are pulled out of the target, beyond the Debye sheath, and into the vacuum, then accelerated by the half-cycle of the laser field into the target. However, the velocities picked up by the electrons put them beyond the collisionless skin depth (l_s) that the laser can access, and the electrons are lost to the laser's influence, accelerated deeper into or through the target as suprathermal electrons. Vacuum heating is one of the important mechanisms in short-pulse experiments where high contrast and intensity are present.

2.6.1.4 Relativistic j x B heating

When the laser intensity grows sufficiently high, the electron oscillation velocity (v_{osc}) approaches the speed of light, and the magnetic component of the Lorentz force ($e\mathbf{v}_{osc} \times \mathbf{B}_0$) becomes appreciable. The resulting force is recognizable as the ponderomotive force [139]

$$f_p = -\frac{m_e}{4}\frac{\partial v_{osc}^2(x)}{\partial x}(1 - cos(2\omega_0 t)) \tag{2.100}$$

where the second high-frequency term acts in much the same way as the electric field in vacuum heating, though the driving frequency is now twice the laser frequency. Just as in vacuum heating, electrons near a sharp density gradient are pulled into the vacuum, accelerated back into the target, and shielded from the laser beyond a skin depth resulting in hot electron generation and collisional heating.

2.6.1.5 Hot electron generation

All of the previously mentioned laser-absorption mechanisms as well as parametric decay instabilities such as stimulated Raman scattering (SRS) or two plasmon decay (TPD) generate suprathermal electron populations. These populations are colloquially referred to as ”hot electrons,” and much effort has gone into characterizing how the laser intensity, $I\lambda^2$, impacts the temperature scaling.

A review of hot electron temperature scalings from $I\lambda^2 = 10^{15}$–10^{20} W/cm^2 is given along with a comparison of experimental data from 1992–2000 by Gibbon in ref. [134]. At the lower end of this intensity range, long-pulse mechanisms such as inverse bremsstrahlung and parametric decay instabilities (arising due to excitation of plasma waves) are responsible for hot electron creation and $T_h \propto (I\lambda^2)^{1/3}$. At the opposite extreme, with intensities greater than 10^{19} W/cm^2, relativistic effects dominate, and the temperature is expected to be proportional to the ponderomotive potential felt by an electron, $T_h \propto (I\lambda)^{1/2}$, commonly referred to as the Wilks scaling after predictions from early 2-D PIC simulations[140].

These scalings were investigated experimentally by Beg *et al.*[141] for intensities up to 10^{19} W/cm^2, yielding the commonly-used Beg scaling with $T_h \propto (I\lambda)^{1/3}$. This was experimentally verified by Chen *et al.*[142] up to 10^{21} W/cm^2 who found a very similar scaling, $T_h \propto (I\lambda)^{0.34}$. The discrepancy between the ponderomotive scaling predicted by simulations and experimentally-validated Beg scaling was explained by Haines[143] as the simple fact that relativistic electrons will travel a distance greater than the skin depth before seeing even a quarter of the laser wavelength, and thus will not pick up the full ponderomotive potential.

The effect of these hot electrons is to create high-energy bremsstrahlung, ionization of the target by generating inner-shell holes (which are most commonly observed as K-alpha radiation), and to create extremely strong electric fields from the large charge separation of hot electrons and initially immobile ions. The following several sections will describe how these effects lead to bulk heating utilized in the experiments in Chapters 4 and 6.

2.6.1.6 Heating by electron refluxing

The full Beg scaling discussed in the previous section[141] predicts hot electron temperatures of 0.2–1.0 MeV for laser intensities of 10^{18}–10^{20} W/cm^2 with a laser wavelength of 1064 nm. For copper, the range of electrons with these energies is 76–710 μm[144]—much larger than typical short-pulse laser target dimensions of tens of microns. This means that electrons initially accelerated by the laser can stream through the target. The highest-energy electrons will escape, rapidly setting up a sheath field, which acts to trap and reflect lower-energy electrons at both target surfaces. This effect is known as electron refluxing and has been the subject of numerous experimental studies for thin targets where electrostatic field formation is expected to be important[145, 146, 147, 148].

An early semi-analytic model was presented by J. Myatt *et al.*[149] based on the capacitance created by the escaping electrons in an ideal, electrically-isolated, thin disk. The model relates the electron temperature (assuming a Boltzmann distribution) (T_e), laser conversion efficiency into hot electrons ($\eta_{L\to e}$), heated radius (r), and laser energy (E_L), providing an estimate of the refluxing efficiency, η_r,

$$\kappa = \frac{7.08 \times 10^{-2} r T_e^2}{\eta_{L\to e} E_L} = \frac{1}{\Phi} e^{-\Phi} \tag{2.101}$$

$$\eta_r = 1 - e^{-\Phi} \tag{2.102}$$

This efficiency is found to be greater than 90% in experiments with favorable conditions for generating sheath fields[150, 149, 148]. The refluxing efficiency provides a measure of how many hot electrons remain within the target and deposit their full energy through collisional processes. This was experimentally diagnosed by measuring the absolute K-α emission from thin targets irradiated with short-pulse lasers. Measurements were compared with a single-pass model and the refluxing model— which simply assumed that the trapped electrons were allowed to collisionally slow down—and excellent agreement was found with the refluxing model. This observation was later replicated by Neumayer *et al.*[151] who verified refluxing as the dominant mechanism by comparing K-α emission from thin targets with targets backed with sufficiently thick (5 mm) aluminum substrates. This process can lead to efficient heating in excess of 200 eV[148, 152] in the experiments outlined by Nilson *et al.*, and 800 eV in the case of Nakatsutsumi *et al.*[147].

2.6.1.7 Heating by cold return current

Another effect caused by hot electrons accelerated via interaction of an intense laser pulse with solid density target is ohmic heating. This effect was described by Glinsky[153] and further elaborated on by Bell *et al.*[154]. Bell's calculation estimates the target conditions for a 1 ps, 1 μm wavelength, 30 μm focal spot laser incident with an intensity of 10^{18} W/cm^2. He finds that the hot electron population generated by such an interaction generates a 24 MA current; assuming it remains in a cylindrical volume, this corresponds to a tremendous 3200 MG magnetic field with 5 kJ of stored energy. This greatly exceeds even the laser energy that gave rise to this electron current, and is thus energetically impossible. Therefore, the hot current must be negated by a return current: $j_{total} = j_{fast} + j_{thermal} \approx 0$.

We determine the energy deposited in the target material by assuming that the cold current, given by $j_{thermal} = \sigma_e E$, is supported by a great many thermal electrons that ohmically deposit energy according to $j^2_{thermal}/\sigma_e$. We expect this to be a very rapid heating method, occurring during the laser pulse itself and vanishing once the presence of a hot current vanishes. Particle-in-cell (PIC) simulations performed by Kemp *et al.*[155] suggest that in thin targets, the resistive heating vanishes once the hot electrons reach the back surface and refluxing begins. Experimental work by Brown *et al.*[156] on the Orion buried-layer platform—some of which will be described in Chapter 6 of this thesis—indicate that resistive heating is the dominant heating mechanism. The effects of refluxing were ruled out by using a long-pulse laser to ablate the target's rear surface, thus destroying the formation of a strong sheath field, and then heating with the short-pulse laser. Similar temperatures were observed with and without the rear surface disruption. Recent theoretical work by Compant La Fontaine[157] indicates that for the conditions outlined by Brown[156]—a 50 μm focal spot with a short scale length and laser-normalized vector potential, $a_0 = 1$—the return current heating is actually at a global maximum with almost 40% of the hot electron energy lost to thermal currents, supporting Brown's conclusions.

2.6.2 Heating with proton beams

For the experiment outlined in Chapter 4, we used the Titan short-pulse laser and solid Cu foils to generate a proton beam for isochoric heating. As such, I briefly review the acceleration and absorption of proton beams using high-intensity lasers here.

Protons and ions are most commonly accelerated via laser using the Target Normal Sheath Acceleration (TNSA) method[158]. This occurs when energetic, hot electrons are accelerated through a target resulting in rapid formation of a strong sheath field of magnitude GV/m[134]. Impurity atoms on the rear surface, predominantly made of hydrogen and carbon, are ionized (collisionally or by barrier suppression[159]) and accelerated in the strong field up to tens of MeV. Initial experimental observations of these beams were described by Clark *et al.*[160], Snavely *et al.*[146], Hatchett *et al.*[161], Maksimchuck *et al.*[162], and Krushelnick *et al.*[163]. Researchers showed that large numbers of protons ($>10^{13}$) could be accelerated into a beam with a cone of 20–45 degrees with total conversion efficiencies from laser energy to total proton energy reportedly as high as 10%.

These proton beams have been used extensively for isochoric heating of matter, both as a heating source[164, 165, 166] and for direct studies of proton stopping power[167, 168]. Ions deposit energy due to collisions with bound electrons of the target material according to the Bethe formula

$$S = \frac{dE}{dx} = -\frac{4\pi n_e Z_p^2 e^4}{m_e v_p^2}\left[\ln\left(\frac{2m_e v_p^2}{\bar{I}(1 - v_p^2/c^2)}\right) - \frac{v_p^2}{c^2}\right] \tag{2.103}$$

where Z_p is the particle charge, v_p is the projectile's velocity, and $\bar{I}$ is average ionization potential. The review by Ahlen[169] outlines many correction terms which may be applied within the brackets of eq. (2.103) such as relativistic or density corrections, multiple Coulombic scattering, or nuclear interactions. For the experiment outlined in Chapter 4, only the relativistic correction will be sizable, and the dominant absorption process will be proton Coulomb collisions with the target material's atomic electrons; energy loss due to material ion recoil or nuclear reactions is expected to be small.

2.6.3 Heating with XFELS

X-ray free-electron lasers XFEL such as the LCLS at the Stanford Linear Accelerator (SLAC) belong to the fourth generation of advanced light sources. They represent a significant advance and provide peak brightnesses of $>10^{34}$ photons/s/mm^2/mrad^2 0.1% BW—more than 10 orders of magnitude greater than third-generation light sources[170]. With the use of refractive beryllium optics to focus the x-ray pulse, the LCLS x-ray pulse can exceed 1x10^{18} W/cm^2, and for the experiments presented in this thesis, it becomes an excellent, tunable heating source.

The interaction process differs from the laser heating mechanisms listed above because the photon energy is now high enough to directly photoionize atoms. In fact, for XFEL energies (1–20 keV), photoionization is the most probable process between photoionization, coherent scattering, or incoherent scattering. In order to determine which electrons are most preferentially ionized, we can look at a simple Kramers cross-section[171, 172]

$$\sigma_{pi} = \kappa \sum_n \frac{64\pi\alpha a_0^2}{3\sqrt{3}} \frac{\omega_n n}{(Z_i+1)^2} \left(\frac{I_n}{h\nu}\right)^3 \tag{2.104}$$

where n, ω_n, Z_i, I_n, $h\nu$, and κ are the principle quantum number, number of bound electrons in the nth shell, ionization state, ionization energy, photon energy, and a fitting parameter, respectively. Each electron shell contributes to the cross-section, but the dominant contribution will always come from the transition with the highest ionization energy, i.e., the inner shells. For this reason, the primary interaction of an XFEL pulse with a target will always take the form of photoionization of the highest energy shell the pump wavelength can access.

The extremely high brightness of the XFEL pulse creates a large population of atoms with singly or doubly ionized K-shells and photoelectrons with kinetic energy equal to the difference between the drive photon energy and the ionization potential—often several keV. The ionized atoms will recombine rapidly on the time scale of 10–100 fs, either by autoionization (Auger decay) or by a radiative process. The fluorescence yield is the factor that describes the probability with which the excited state will decay by a radiative process rather than an Auger decay. Figure 2.7 shows the fluorescence yield for a K-shell hole as calculated by Krause[173]. The probability that an excited state decays by ejecting an Auger electron decreases as atomic number increases. The kinetic energy of an ejected Auger electron is equal to the difference between the binding energy of the K-shell hole, the binding energy of the shell the relaxing electron starts in, and the binding energy the ejected electron starts in. In the case of the most common Auger process, $KL_1L_2, 3$—denoted as such because of the K-shell hole filled by an electron from the L_1 shell, and the ejected electron originating in the L_2 or L_3 shells—this takes the form $E_{kin} = E_K - E_{L1} - E_{L2,3}$. These values have been tabulated by Larkins[174], and typical Auger energies are on the scale of 1–10 keV.

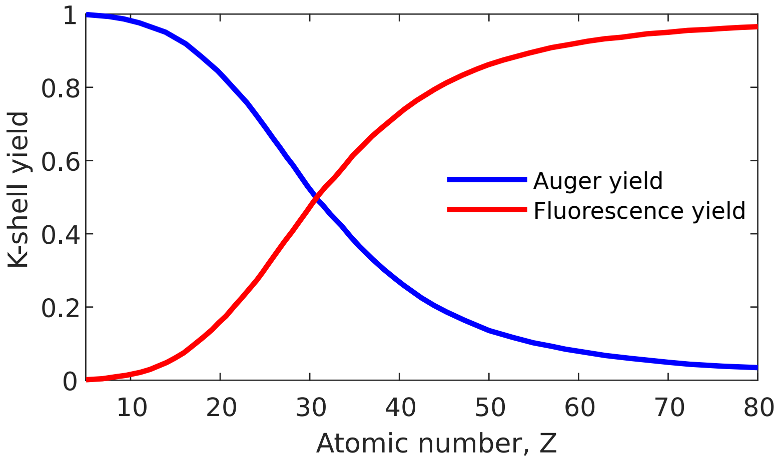

Figure 2.7: Fluorescence (red) and Auger (blue) yield for K-shell vacancies as a function of atomic number, Z, based on theoretical calculations by Krause[173].

Thus, following the matter's interaction with the XFEL pulse, the matter is left in a highly nonequilibrium state with the ejection of keV photoelectrons, keV Auger electrons, and characteristic radiation. For experiments that seek to probe material properties on femtosecond time scales, the equilibration process is of fundamental interest. This is an active area of study, requiring collisional radiative models with large quantities of accurate atomic data that track both electron and radiative populations, such as those outlined by Sentoku *et al.* in ref. [172]. For the experiment presented in this thesis, the equilibration of the energetic particles is expected to occur in less than a picosecond, with subsequent equilibration between electrons and ions in several more picoseconds—much shorter than even the temporal resolution of the instruments—and it is sufficient to know just the spatial energy deposition.

CHAPTER 3

Methods

In this chapter, I review the operating parameters of facilities from which the experimental data presented in this thesis were collected. After discussing the facilities, the main plasma diagnostics used herein are explained, and performance characteristics such as energy responses and sensitivities are documented.

3.1 Experimental HED facilities

3.1.1 Titan at the Jupiter Laser Facility

Titan is a kW-class Nd:glass laser housed and operated at Lawrence Livermore National Laboratory's Jupiter Laser Facility (JLF). It is a dual-beam platform, with one long-pulse beam from the Janus laser capable of delivering 1 kJ of energy in a 1 ns pulse of 1053 nm light, and one short-pulse (SP) beam capable of delivering 250 J in 1–10 ps pulses of 1053 light. The SP contrast ratio between the main pulse peak and the nanosecond pedestal is typically 10^5, with the pre-pulse beginning approximately 3 ns prior to the main pulse arrival[175]. The pre-pulse is measured on-shot using a calibrated, fast (20 ps resolution) optical diode paired with a fast (12 or 16 GHz) oscilloscope. An additional low-energy short-pulse probe beam can be delivered to the chamber which can be compressed to 0.5 ps or chirped to 100 ps in the fundamental frequency, or doubled with a beta barium borate (BBO) crystal to a wavelength of 527 nm. The experiment in Chapter 4 used the short-pulse beam and the probe beam in its uncompressed, chirped, and frequency-doubled configuration. The final focusing was performed with an f/3 off-axis-parabola and the spot size monitored with a far-field monitor on shot.

3.1.2 Callisto & Europa at the Jupiter Laser Facility

At the time of the work done in this thesis, Callisto—previously one JLF's user facility platforms—had been converted to a smaller-scale laser to be used for diagnostic calibration. It is a Ti:Sapphire laser capable of delivering 800 nm, 100 mJ pulses at 10 Hz to the target chamber. This setup is ideal for the calibration of x-ray crystal spectrometers and x-ray streak cameras, as discussed in the following sections. Additionally, Callisto's beam could be converted to 30 mJ of 400 nm light using a second harmonic KDP crystal. Making use of this along with a Fabry-Perot interferometer allowed measurement of the temporal resolution of optical and x-ray streak cameras. Utilizing the same setup, but separating the pulses by a known amount with a micrometer, the sweep linearity could also be measured.

The Europa laser—another Ti:Sapphire device—was also available as a minimally-supported platform. In the configuration that existed during the time of this work, it was capable of producing 10 mJ, 100 fs pulses of 800 nm light at a 10 Hz repitition rate to an optics table. The beam was often frequency-doubled with a KDP crystal and used for calibration of optical streak cameras. The doubled light was measured using a commercially available Ocean Optics spectrometer to have a bandwidth of 10 nm and a central wavelength of 405 nm. This provided an ideal calibration source that was bright enough (photons per picosecond) to calibrate streak cameras on the fastest sweep speeds. Conventional calibration sources, such as comb generators, do not possess sufficient brightness and can only calibrate significantly slower sweep speeds.

3.1.3 LCLS at the Stanford Linear Accelerator Center

LCLS, built at SLAC, was the first hard x-ray Free Electron Laser (FEL). In a FEL, an electron beam is accelerated to relativistic speeds and then passed through a periodic array of alternating-pole magnetic fields, called an undulator. The magnetic fields force the electrons to begin moving in a sinusoidal path, emitting synchrotron radiation whose wavelength is dependent on the undulator period, magnetic field strength, and electron kinetic energy. The electrons are normally out of phase, and the emitted radiation is therefore incoherent. However, if the electron beam is bright enough, the intensity of the emitted radiation field will influence the electron beam itself through the ponderomotive force[176]. This interaction leads to micro-bunching of the electron beam, and all of the electrons will ultimately bunch into spaces based on the wavelength of the synchrotron radiation. The evenly-spaced electrons will all be in phase and emit coherently, leading to extremely bright x-ray pulses. This process is known as Self-Amplified Spontaneous Emission (SASE) and is the primary mode of operation for LCLS. A second mode, known as self-seeding, uses SASE-produced radiation—spectrally filtered using diffraction off a diamond crystal—to seed a specific frequency in the primary undulator. This reduces the spectral bandwidth of output pulses by 40–50 times at the cost of total pulse energy[177].

At LCLS, the electron beam is injected part way into the linear accelerator and accelerated to relativistic energies ranging from 4.3–14 GeV. The undulator is 132 meters long, after which the electrons are dumped, and the x-ray pulses are transported to one of seven experimental hutches. Each hutch has a designated purpose and a suite of diagnostics tailored to specific types of study, which are outlined in a review by Bostedt et al.[178].

For the work in this thesis, experiments were performed at the MEC end station described by Nagler *et al.* in [179]. This facility was designed for the purpose of studying WDM and is the only hutch to pair high-power optical lasers with the FEL. The facility has both a Nd:glass long-pulse laser and Ti:Sapphire short-pulse laser. The long system can deliver 1 J/ns, up to 25 joules of doubled light in two separate pulses, with a repetition rate of approximately 7 minutes. The short-pulse laser can produce 1.5 joules in 50 fs pulses, with a repetition rate of 5 Hz, or amplified in the final amplifier of the long-pulse system to 7 joules at the long-pulse repetition rate. The FEL can be tuned from 2.5–11 keV, with pulse energies ranging from 2–4 mJ in SASE mode. The beam can be focused to sizes ranging from 2–100 μm using beryllium compound refractive lenses. The pulse duration is 5–200 fs. The beam contains a third harmonic component, but it contains less than one percent of the pulse energy and is not focused as tightly by the Be lenses.

3.1.4 Orion at the Atomic Weapons Establishment

Orion is a large-scale laser facility at the AWE in Aldermaston, United Kingdom[180, 181]. Fundamentally, it is a Nd:glass laser with ten long-pulse beams that can deliver 500 J of 351 nm light in 0.1–5 ns, temporally shaped pulses and two short-pulse beams which can deliver 500 J of 1054 nm light in 0.5 ps pulses. For the experiments in this thesis, one of these short-pulse beams is frequency-doubled to 527 nm and can deliver 100 joules. The maximum energy was limited by damage thresholds in the sub-aperture doubling crystal. Later, the facility added a second sub-aperture doubling crystal that could increase the maximum energy to 200 J, but two focal spots had to be aligned onto the target[182]. As with most Nd:glass systems, the shot rate is limited by cooling in the gain media, and short pulse experiments achieve 3–6 shots per shot day depending on the complexity of target alignment.

The target chamber is 4.2 meters in diameter and is equipped with six Ten Inch Manipulator (TIM). These vacuum chambers contain diagnostic payloads insertable into the target chamber under vacuum and allow image plates to be cycled without venting the larger vacuum chamber. TIM-based diagnostics are typically aligned with mechanical pointers placed at the target chamber's center without a target present. Positions are saved, and motion control can return diagnostics to their correct positions to better than 25 μm. Individual targets are inserted and aligned via the target inserter and the chamber's imaging system with an accuracy often greater than 10 μm.

One of the most important features for short pulse experiments is the contrast ratio. Substantial effort has gone into minimizing the ratio between the nanosecond pedestal and main pulse. The Orion short-pulse beams demonstrated 10^{-7}–10^{-8} after initial construction. Later, a Short Pulse Optical Parametric Amplifier (SPOPA) system was installed after the oscillator, which increases the pulse energy into the nanosecond-OPA, lowering the gain required and thereby reducing the amplitude of the ns pedestal. This SPOPA system improved the contrast by three orders of magnitude to 10^{-10}, which was reconstructed over a series of shots using two diodes with varied filtering.

Additionally, frequency doubling was measured to improve the contrast of the infrared pulse (pre-SPOPA) by six orders of magnitude. The combination of the two could not be measured, but the total contrast is estimated to be 10^{-18}[181, 183].

3.2 Plasma diagnostics

3.2.1 Ultra-fast Streak cameras

A common tool for making time-resolved measurements—one used in all the experimental work in this thesis—is the ultra-fast streak camera. Streak cameras operate on the basic principle of converting incident radiation into electrons and then temporally dispersing, or sweeping, them on the read out screen. This is schematically illustrated in fig. 3.1.

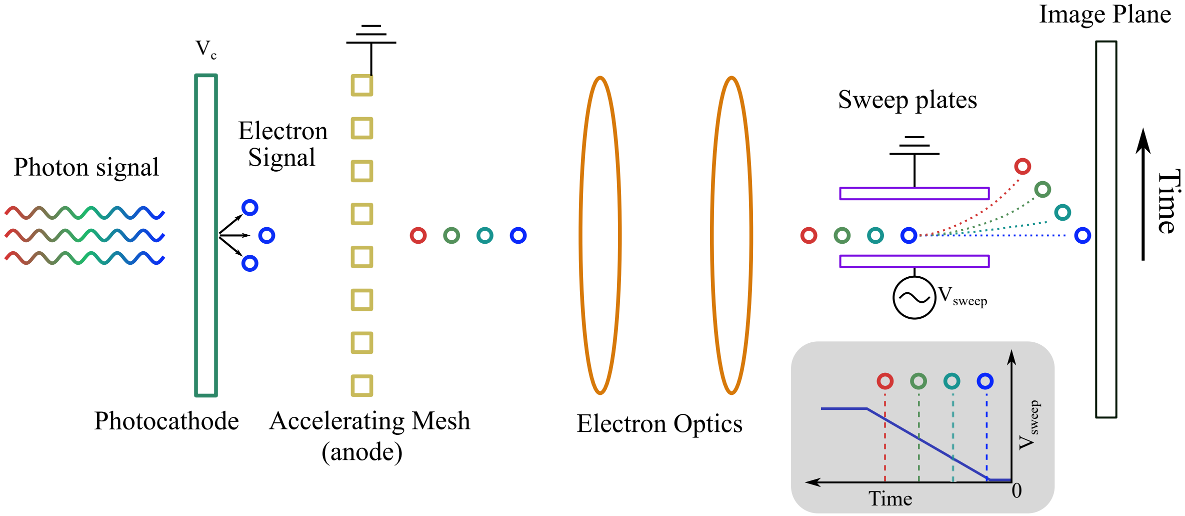

Figure 3.1: Conceptual layout of a streak camera. Photons are incident from the left, converted to electrons via the photoelectric effect, and then accelerated through an anode mesh. The photocathode surface is imaged to the output surface, usually with electrostatic electron optics. The electron pulse experiences a time-varying electric field as it passes the sweep plates, resulting in a different physical trajectory for each moment in time, thereby providing temporal resolution in one dimension and spatial information along the second.

The best time resolution achievable by a streak camera is conventionally determined by assessing each of the resolution limiting effects and adding them in quadrature, though because the mechanisms are not fully independent this merely provides an estimate. The most important of these effects were described by Murnane *et al.*[184]:

$$\Delta t_{min} = \sqrt{\Delta t_{dc}^2 + \Delta t_{pc}^2 + \Delta t_{sc}^2} \tag{3.1}$$

where Δt_{dc} is due to the finite entrance slit size in the temporal direction, Δt_{pc} is due to the energy spread in the electron distribution, and Δt_{sc} represents the temporal spreading due to space charge effects.

The finite entrance slit impacts the resolution based on its image size on the output screen, Δx, and sweep speed, v_s, as $\Delta t_{dc} = \Delta x / v_s$. The fact that emitted electrons aren't mono-energetic means that the fastest electrons outrun the slowest, causing broadening of an electron bunch in time. The presence of an axial electric field, $V(z)$, will impact the propagation time of an electron emitted with energy eV_0 according to[185]:

$$t_{pc} = \sqrt{\frac{m}{2e}} \int [V_0 + V(z)]^{-1/2} dz \tag{3.2}$$

In most cases the dominant contribution to Δt_{pc} occurs where the electrons are moving the slowest—in the anode cathode gap. Under the assumption that the emitted energy eV_0 is approximately equal to the distribution FWHM, $e\Delta V_0$, and both are much smaller than the accelerating voltage, eq. (3.2) may be used to approximate the temporal spread $\Delta t_{pc} \approx \sqrt{m/2e}(\Delta V_0^{1/2}/E)$. However, when the time of flight through the streak tube, t_{dr}, is long, the dispersion in the drift region must also be included as $\Delta t_{dr} = 0.5\ t_{dr}\ e\Delta V_0/E$[186]. Multiple authors have presented models for space charge broadening in streak tubes, including Kalibjian[187] and Qian *et al.*[188], and details will not be presented here. However, this effect quickly becomes the dominant broadening mechanism in streak tubes if the signal is allowed to become too strong. Space charge acts to spatially spread propagating electron bunches, increasing Δt_{dc}, but it can also strongly impact the electron energy distribution further increasing $\Delta t_{pc,dr}$. Finally, additional effects such as off-axis aberrations, fringe and leakage fields, electrons born with high divergence angles, finite beam size within the sweep plates experiencing different sweep field strengths, and chromatic aberration all contribute to the final resolution, greatly increasing the complexity of considerations required for a successful design.

The creation of a streak camera with temporal resolution on the scale of <1 ps requires compromise. Typically, the biggest term results from dispersion caused by the width of the electron energy distribution. This occurs due to fundamental material limitations; currently available x-ray cathodes (Au, CsI, KBr, etc.) have FWHM widths in secondary electron energy distribution of approximately 1–5 eV. Thus, to minimize the dispersion, an extremely high extraction field is required, but again we hit a fundamental limit: DC electric fields break down above 5–10 kV/mm. With the maximum kinetic energy electrons can obtain set by the breakdown thresholds of vacuum, the only remaining lever is reducing the distance electrons must propagate. However, as with geometric optics, making the optical system shorter is the equivalent of going to a smaller f/#, and off-axis aberrations become severe, dramatically limiting the length of usable slit a streak camera may use. For any design, choices must be made about prioritizing performance characteristics such as usable cathode length, temporal resolution, spatial resolution, and dynamic range. Commercial devices have already made the choice of what to prioritize, and this should be considered by the user when selecting a device for a measurement.

3.2.1.1 Optical streak cameras

For the experiments presented within this thesis, optical streak cameras were utilized to make pyrometry measurements as discussed below in Section 3.2.2.2. The primary difference between an optical streak camera and x-ray streak camera is the photocathode material used. For optical streak cameras, the most commonly used photocathode is S20 ($SbNa_2KCs$), with spectral sensitivity in the range of 350–850 nm. Some applications require sensitivity out into infrared wavelengths, in which case a S1 (AgOCs) cathode can be used out to 1100 nm, though with less quantum efficiency through the whole range, as shown in fig. 3.2. The time resolution of optical streak cameras is often similar to or slightly worse than x-ray streak cameras. The incident photon energies are 1–3 eV in the visible range, and so the primary photoelectrons determine the electron distribution

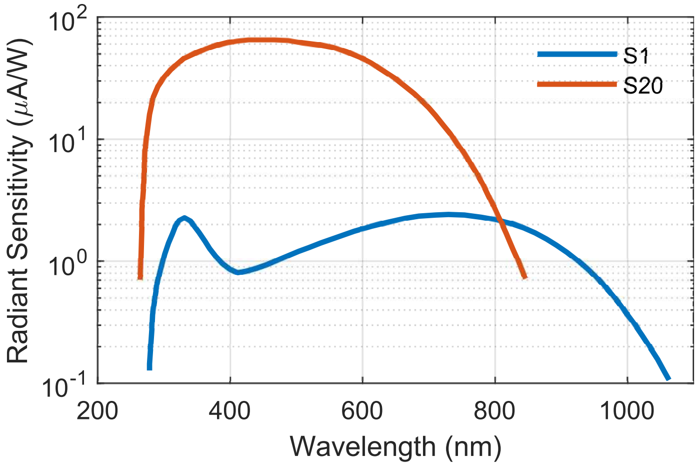

Figure 3.2: Response functions for optical streak camera photocathodes S1 and S20. Data from ref. [189].

function—that is, those resulting from direct photoionization rather than collisional ionization–and have distribution widths on the order of 0.1–1 eV[189] depending on the material and the incoming photon energy. This narrow spread results in less temporal dispersion than x-ray streak cameras. However, these cathodes degrade rapidly in atmospheric conditions, requiring the streak tubes be sealed within their own vacuum environment. For that reason, optical streak cameras are typically operated with lower acceleration voltages far from breakdown thresholds, to ensure stability and increase longevity.

3.2.1.2 X-ray streak cameras

X-ray streak cameras were used for the experiments presented in Chapter 6 to obtain time-resolved spectral measurements. Typical photocathodes for x-ray streak cameras include Au, Al, CuI, KBr, KI, and CsI. Devices in the x-ray regime are defined by highly-energetic primary photoelectrons (and Auger decay electrons), and the electron population used within the streak tube stems from secondary electrons created by collisional ionization and plasmon deexcitations within the cathode material. The absorption process as well as the transport and escape of secondary electrons was investigated theoretically and experimentally in a series of papers by Henke *et al.*[190, 191, 192]. The width of the secondary electron distribution was found to be significantly broader than primary photoionizations due to the stochastic nature of the process but very nearly independent of the energy of the incoming x-rays in the range of 0.1–10 keV. The simplest photocathode, a thin Al layer, was found to have a 4.9 eV FWHM with a peak at 1.3 eV, Au a 3.8 eV FWHM and 1.3 eV peak, and CsI a 1.5 eV width and 0.5 eV peak. Some materials such as KI or KBr have narrower distributions but 2–5x lower sensitivity than CsI.

Due to its high sensitivity, low peak energy, and narrow secondary-electron distribution, CsI is one of the most commonly used x-ray photocathodes in streak cameras and the only one used within this work. Figure 3.3 shows the Henke data for (a) the secondary-electron yield and (b) the secondary-electron distribution for a CsI transmission photocathode.

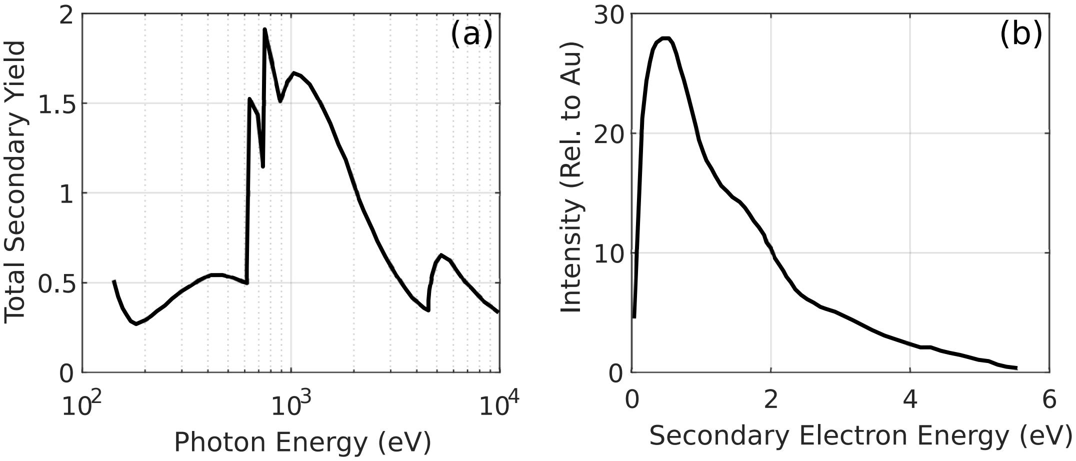

Figure 3.3: Measured response characteristics for a 1020 Åthick Cesium Iodide transmission photocathodes[192]. Figure (a) shows the secondary-electron yield and (b) the secondary-electron distribution function with E_{pk} = 0.5 eV and ΔE = 1.5 eV.

At the Orion laser facility, two types of x-ray streak cameras are used. The first, manufactured by Axis Photonique Inc[193], uses a Photonis bilamellar streak tube, providing independent focusing of the spatial and temporal axes using a quadrupole lens and pre/post temporal focusing electrodes. It uses a DC extraction field and a slit acceleration anode, which contributes to its excellent spatial resolution. It has a manufacturer-stated time resolution of $<$1 ps, a spatial resolution 40 μm, a dynamic range of 6[194], and 18 mm of usable cathode length.

The second camera—developed by R. Shepherd and colleagues at LLNL to support short-pulse laser plasma experiments[195, 196]—is called the TREX. Its pulse-charged photocathode reaches 300 kV/cm, accelerating electrons to 15 kV in the 500 μm (mesh) anode cathode gap, making it capable of 500 fs temporal resolution. This high acceleration voltage can be applied during the experiment and then dissipated before the formation of an electronic avalanche, allowing for orders-of-magnitude improvement in the extraction field when compared with conventional DC extraction biases. The TREX also uses a bilamellar electron optics design, sketched in figure 3.4, that allows independent focusing of the spatial and temporal axes. Splitting the focal axes acts to suppress some of the effects of space charge, relative to cylindrical lens designs, by reducing electron density at the geometric ray crossover point. There is minimal angular filtering of the accelerated electrons, resulting in a spatial resolution of $\sim$140 μm in the center 12 mm of the 28 mm cathode. The high-divergence electrons slightly reduce the spatial resolution but result in an increased dynamic range of 20–40. A substantial amount of the author's effort while at LLNL was directed toward improving the off-axis spatial resolution of the TREX in preparation for a streaked, high-resolution crystal spectrometer designed to measure time-resolved line shapes at Orion.

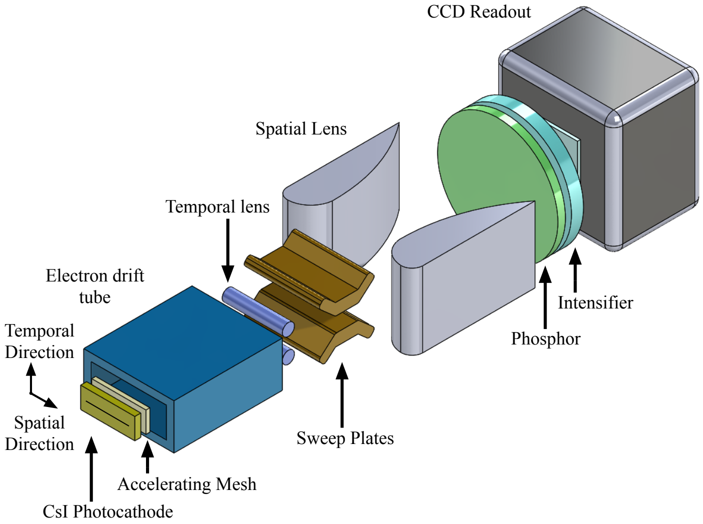

Figure 3.4: Schematic drawing of the LLNL TREX.

3.2.2 Streaked Optical Pyrometer

In some plasmas of interest—particularly those termed WDM, where the temperature is several to tens of eV,and the density is near solid—the atoms are not ionized far enough to provide bright spectral lines. In these instances, another temperature diagnostic is helpful. A Streaked Optical Pyrometer (SOP) uses the thermal self-emission from a heated material to diagnose the time-dependent temperature.

Any ideal body in thermal equilibrium with its environment will emit radiation isotropically into 2π steradians (assuming planar geometry) according to Planck's law, shown here following the notation found in Mahan[197] where $i_b(\lambda, T)$ is the spectral radiance:

$$i_b(\lambda, T) = \frac{2hc^2}{\lambda^5} \frac{1}{e^{\frac{hc}{\lambda k_B T}} - 1} \tag{3.3}$$

A feature of Planck's law is that, for all wavelengths, the value of the spectral radiance will always increase with temperature. So a 2 eV black body will have less spectral radiance at all wavelengths than a 3 eV black body. This enables a theoretically simple temperature diagnostic for looking at any heated material. If one assumes that a plasma is in LTE—that is, $T_e = T_i$—and that the surface is emitting as a black body, then one can use eq. (3.3) to calculate a temperature from the total photon count. Figure 3.5(a) shows the generalized Planck function obtained by dividing Planck's law by T^5, which represents all variations of the function. The peak is at x = 2.9, in agreement with Wien's Law

$$\lambda_{max} = \frac{b}{T} \tag{3.4}$$

where b = 2.898 x 10^{-3} m·K. The second pane in fig. 3.5 shows the function calculated for four temperatures between 2 and 3.5 eV. The peak emission shifts to lower wavelengths as temperature increases, but the total emission increases according to the Stefan-Boltzmann law, $e_b = \sigma \mathrm{T}^4$. From a diagnostic standpoint, measurement of the temperature will have the greatest sensitivity if the measurement is made at a wavelength near the peak. This is shown in fig. 3.5(c), where the shortest wavelength plotted (250 nm) yields the greatest change in emitted power per eV of temperature.

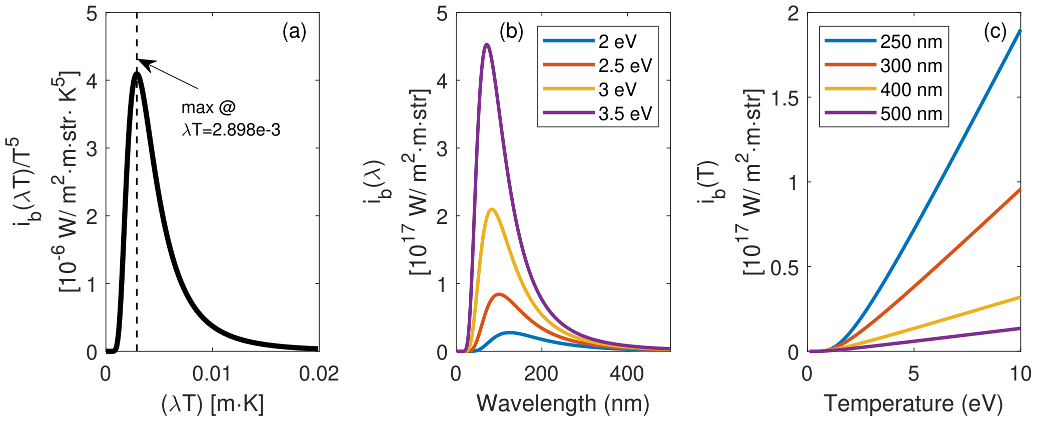

Figure 3.5: Representations of the behavior of Planck's Law. Panel (a) shows the generalized Planck function which has been normalized by T^5 and is only a function of (λT), (b) shows eq. (3.3) for several WDM temperatures as a function of wavelength, and (c) shows i_b as a function of temperature at several wavelengths.

Thus, for WDM sources, the ideal measurement would be made in the ultraviolet (UV) or extreme ultraviolet (EUV) wavelength ranges 100–300 nm. However, sensitivities for the optical streak camera photocathode, throughput of optical elements, and availability of bright UV calibration sources all provide challenges to a SOP designed for such short wavelengths. For this reason, many implementations, including those found within this thesis, opt for visible wavelengths.

An optical streak camera provides a measurement's time dependence. For the work in Chapter 4, a Hamamatsu C7700 high dynamic range optical streak camera was used with the SOP. For the experiment discussed in Chapter 5, an ultra-fast Axis Photonique optical streak camera was used. The energy calibrations of the Axis optical streak camera were performed by collaborators[198], hence, I will focus on the calibration work I performed on the Hamamatsu camera at JLF. The general layout of a SOP is shown in figure 3.6.

3.2.2.1 Emission from real surfaces

Planck's law represents the maximum emission any optically-thick surface can produce; real surfaces usually do not emit at this level, especially not at all frequencies. The ratio of a surface's actual emitted intensity to that of a true black body surface is known as the emissivity[197]. Such

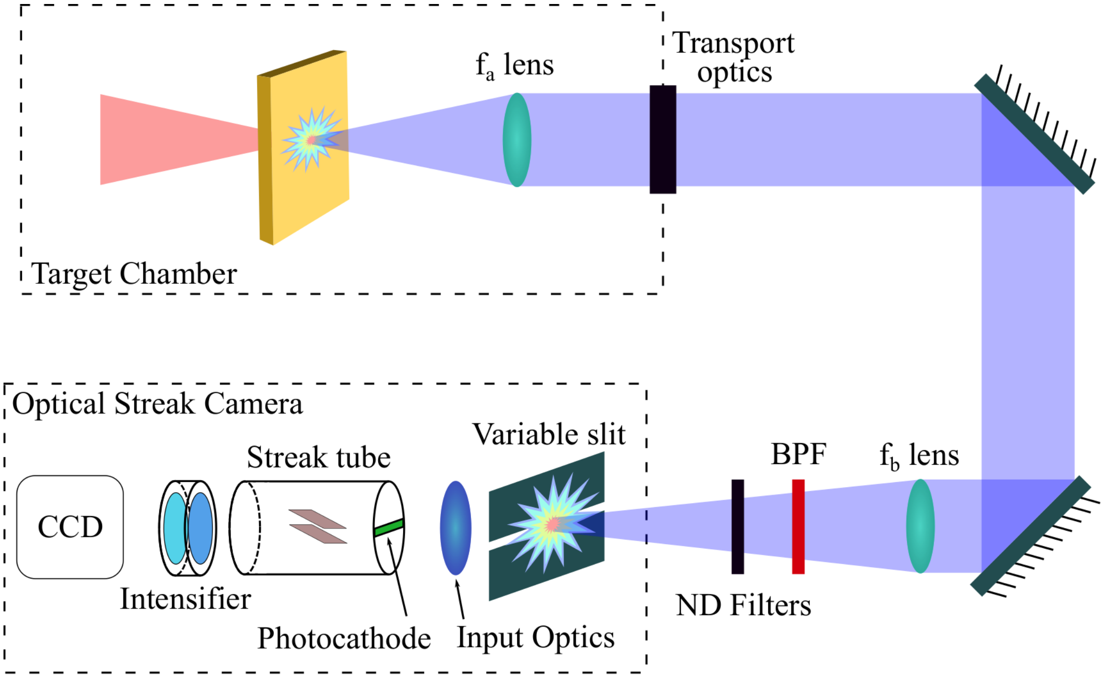

Figure 3.6: Schematic layout of the SOP used in this work. The heated region of the target is imaged with lens f_a, transported to the optical streak camera, and re-imaged onto the streak camera cathode with final lens f_b with magnification $M=f_b/f_a$. The wavelength range is selected with a narrow band pass filter (BPF), and the intensity is attenuated with neutral density (ND) filters to prevent degradation of the temporal resolution due to space-charge effects.

non-ideal surfaces are sometimes referred to as gray surfaces. Note, this is not to be confused with the grey atmosphere approximation used in radiation transport texts such as Mihalas's[199], where the opacity is assumed independent of frequency. Grey surfaces can result in solids due to surface structure, but in a plasma, they generally result when the plasma is optically thin to the radiation, or the current material conditions do not possess enough available states to redistribute the radiation in the wavelength band being observed. The emissivity correction modifies Planck's law as

$$i_{\lambda,e}(\lambda,T) = \varepsilon(\lambda)\, i_b(\lambda,T) \tag{3.5}$$

where $0 < \varepsilon < 1$ is the emissivity.

In a macroscopic description, the total balance of energy at a surface can be described by

$$1 = R(\lambda) + T(\lambda) + \alpha(\lambda) \tag{3.6}$$

where the reflectivity, R, transmissivity, T, and absorptivity, α, are all normalized to the total energy in the system. This balance should also include scattered light. If the surface is optically thick, the transmission is zero, and the absorptivity is simply the difference between the total energy and reflected portion.

A perfect black body will, by definition, absorb all incident radiation: it is both a perfect emitter and absorber. However, Kirchoff's law of thermal radiation extends this to non-ideal surfaces, relating the emissivity to the absorptivity.

$$\alpha(\lambda) = \varepsilon(\lambda) \tag{3.7}$$

Thus, we arrive at a description of the expected, observed emission for a real surface in terms of experimental observables:

$$i_{\lambda,e}(\lambda, T) = \alpha(\lambda)\, i_b(\lambda, T) = (1 - R(\lambda)) i_b(\lambda, T) \tag{3.8}$$

All SOP measurements from the experiments presented in this thesis are accompanied by reflectivity measurements in order to make this necessary correction. The material conditions vary rapidly in time, requiring a time-resolved reflectivity measurement to accompany the time-resolved absolute emissivity measurement of the SOP.

3.2.2.2 Absolute calibration of Hamamatsu optical streak camera

In order to apply the above concepts and develop a functioning SOP diagnostic, an accurate, absolute calibration of the optical streak camera and accompanying optics is required. In this section, I discuss the calibration work I performed at the Europa laser on the Hamamatsu optical streak camera.

Obtaining sensitivity of the optical streak camera and CCD readout in counts per incident joule were the primary goals. For reasons stated in the previous section in addition to the readily-available Ti:Sapphire, the calibration was performed at 405 nm.

The compressed Ti:Sapphire beam was doubled using a a Potassium Dihydrogen Phosphate (KDP) crystal, and the 800 nm fundamental light was dumped using three dielectric mirrors with $>99\%$ reflectivity each. The 800 nm component was minimized at each reflection by varying incidence angle and viewing the spectrum in real time with an Ocean Optics visible spectrometer. For energy calibrations, the beam was collimated to a 1 mm spot size. The total energy per pulse of the 10 Hz beam was measured after all of the transport optics but before the optical streak camera input using an Ophir pyroelectric energy meter (PE9-F) with an Ophir Vega reader and Starlab computer software. This setup had a manufacturer-given calibration accuracy of $\pm 7\%$ at 400 nm. A set of Thorlabs neutral density filters were calibrated by measuring 2000 pulses before and after each individual filter, and the error—given as the standard error of the mean, $\sigma = \sigma_{std}/\sqrt{N}$—was less than one percent due to good statistics. The standard deviation of the pulse energy was 17.5% $\pm 2.5\%$.

The optical streak camera was timed in and triggered 50 ns before the light's arrival at the streak camera. The fine tuning of the timing delay was performed using a delay box and continuously-variable delay unit. The Hamamatsu requires focusing of the front and rear optics for the wavelength being used. The rear is adjusted in a focus mode by maximizing the sharpness of the cosmic ray readout noise in the intensifier set at high gain. The front optics are set by focusing a resolution target at the entrance slit back lit by 400 nm light. The front entrance slit was opened fully so that the entire pulse measured by the calorimeter could enter the streak camera. Care was taken to ensure that any surface reflections generated in the optics chain were not measured in the calorimeter or incident onto the streak camera cathode. Energy calibration was performed at the fastest sweep window, 0.5 ns, and was used for the experiments discussed in later chapters. Additionally, it was performed at two gain settings of the unit's intensifier—30 and 50 (where gain settings can range from 1 to 60). The 30 femtosecond pulse is much shorter than the optical streak camera's time resolution, so with the slit fully open, swept images appear similar to static images of the laser spot. This is shown for five pulse energies in fig. 3.7. Care was taken to ensure beam smoothness, with no parts of the laser spot causing non-linear space-charge effects.

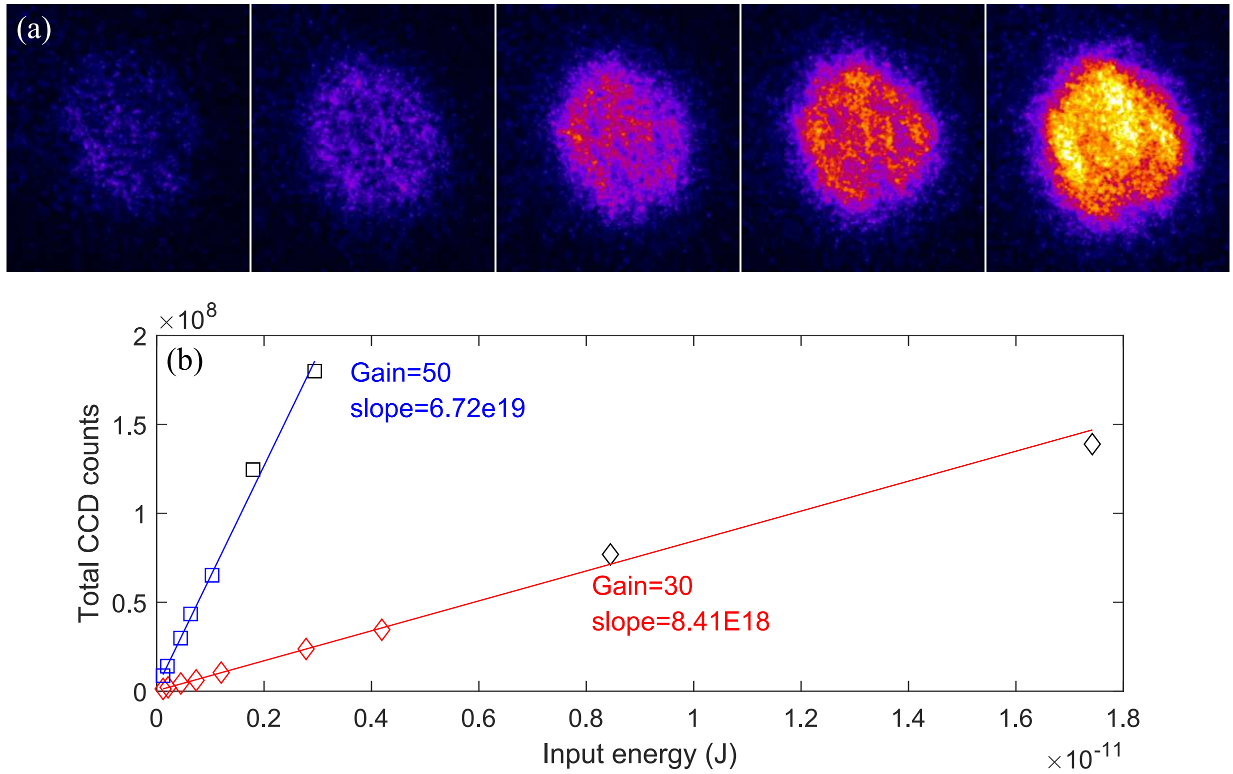

Figure 3.7: (a) Streaked images of the frequency-doubled Europa laser spot at five different pulse energies recorded with the JLF OSC6 Hamamatsu C7700 with the entrance slit fully open. (b) Energy calibration measurements for the JLF OSC6 Hamamatsu streak camera. The slopes of each set of measurements give the sensitivity at 400 nm in CCD counts per incident joule.

The pulse energy was selected using an available combination of neutral density filters, then taking a 2000 pulse energy measurement of the resulting beam. Thirty single-shot exposures were taken at each energy on the 0.5 ns sweep speed. The background counts are subtracted from each image and the total counts within the spot summed within a constant area for all images. This was performed for a series of 7–9 energy values for gain settings of 30 and 50. Analysis results are shown in fig. 3.7(b) with the final sensitivities at 400 nm for a gain setting of 30 being **8.41x10^{18} counts/J**, and the gain 50 sensitivity being **6.72x10^{19} counts/J**. This calibration includes the effects of the input optics, S-20 photocathode, streak tube, intensifier, output optics, and CCD. Thus, changes to any portion of the instrument render the result prone to error. The most likely cause for deviation from this calibration would be damage of the photocathode due to incident light.

Following the energy calibration, several other aspects of the streak camera performance were characterized such as the temporal resolution, the actual slit width, the intensifier gain response, and measurement of the onset of space-charge effects.

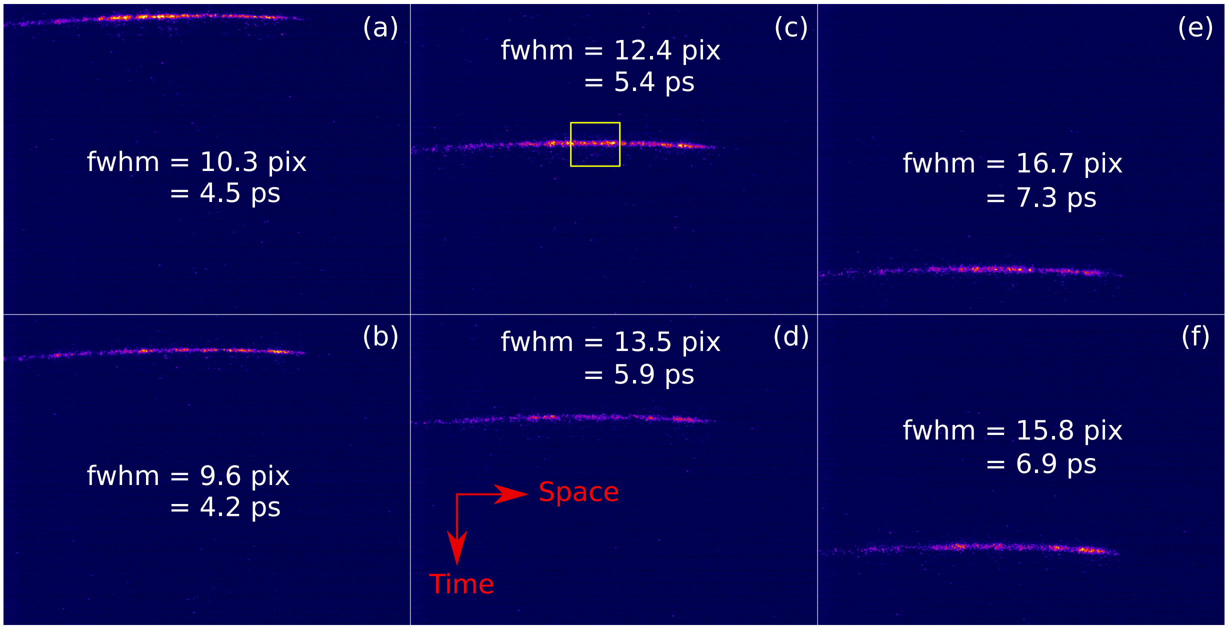

Figure 3.8: Streaked images of the Europa short pulse to measure the temporal resolution of the OSC6 streak camera. Streaks were taken with a 20 μm slit at positions near the top, middle, and bottom of the sweep window. The yellow box shows a sample region over which the annotated FWHM values were taken. Pixels were converted to time using the sweep length of 446 ps (provided by Hamamatsu) over 1024 pixels.

With a short-pulse laser, the temporal resolution can be measured in one of two ways. The simplest method is to ensure that the entrance slit is closed far enough that the spatial size (in the temporal direction) does not limit the time resolution and streak the pulse. The temporal FWHM of the resulting streak, along with knowledge of the total sweep window, gives the limiting resolution. These measurements should always be taken with the lowest possible signal to obtain the optimum response, so the intensifier gain and signal should be maximized. This is shown in fig. 3.8 for the JLF OSC6 Hamamatsu, **where the average time resolution is approximately 6 ps**. The resolution is better near the top of the sweep window than the bottom, possibly due to stray electric or magnetic fields, imperfect focusing in the electron optics near the edges, or changes in the sweep pulse near the edge of the sweep window.

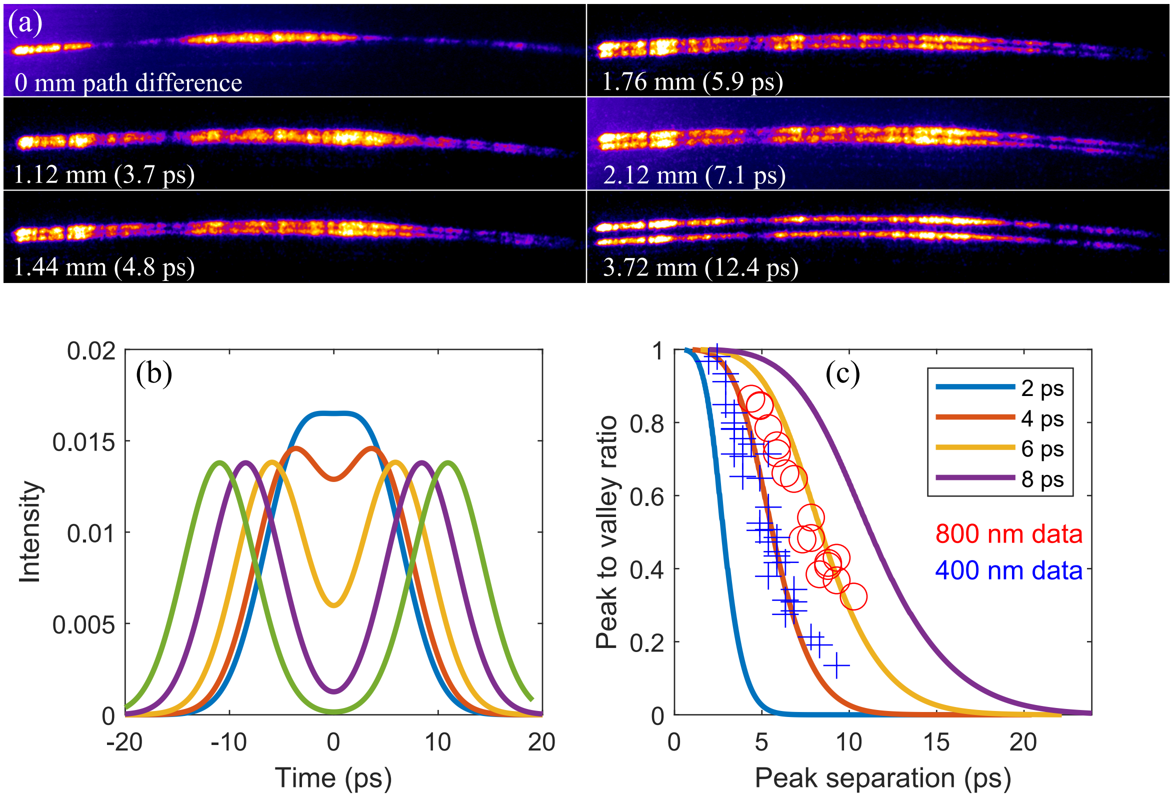

Figure 3.9: Temporal resolution calibration of the OSC4 Hamamatsu streak camera. Fig. (a) shows the raw streaked data for six path length differences of the Michelson interferometer arm, (b) shows calculated Gaussian distributions of equal intensity separated by increasing times, and (c) shows theoretical peak-to-valley ratios for four time resolutions and experimental results for 800 nm and 400 nm illumination. Results indicate that shorter wavelength illumination produces increased temporal resolution. The measured resolution is slightly more than 4 ps at 400 nm and slightly less than 6 ps at 800 nm.

A second and more precise method involves splitting the incident pulse using a Michelson interferometer. The zero-time position occurs where the interference fringes are strongest, using the streak camera to view this in focus mode with the slit open. The fringes were only visible at all over a 200 micron distance, providing experimental verification that the pulse duration was much less than 1 picosecond. Once the pulses overlap in time, the length of one arm can be increased with high accuracy using a micrometer and the temporal offset between the two pulses determined based on the speed of light (300 μm/ps). In this manner, the resolution can be defined at any chosen contrast ratio between the two pulses. This method was performed for a second unit of the same type, the OSC4 at JLF, and shown in fig. 3.9. Additionally, if measurements are taken across the sweep window, the sweep linearity and length of the sweep window can be measured and verified for acceptability. A perfect sweep linearity would have zero deviation from a constant mm/ps value displacement of the electrons within the sweep tube across the entire sweep window.

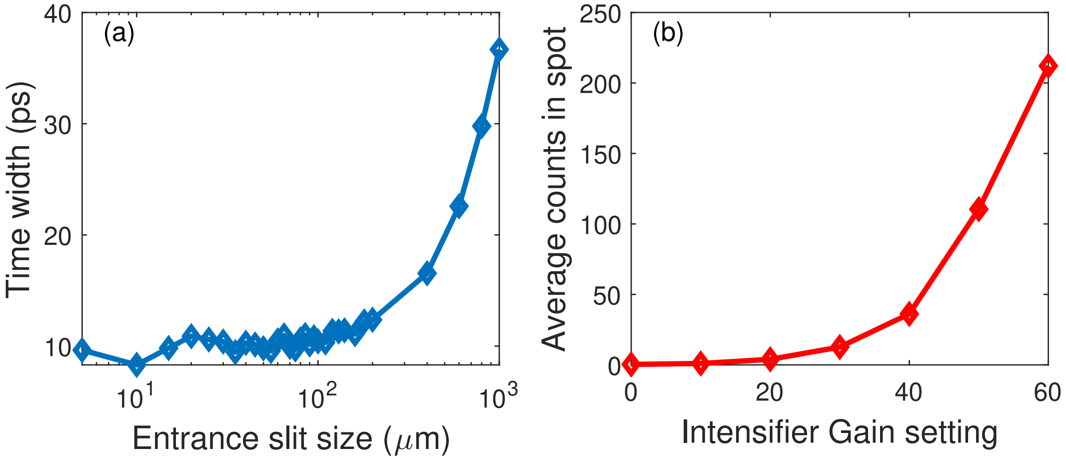

Figure 3.10: Supplemental calibrations for OSC6. Figure (a) shows the behavior of the time resolution as a function of increasing slit width, and (b) shows the increase in signal level as a function of the intensifier gain settings.

Related to the temporal resolution is the minimum slit size. The minimum time resolution is a combination of space charge effects, spatial image size, and electron energy spread. Therefore, beyond a point, reducing the entrance slit will not continue to improve time resolution as other effects dominate. To determine at what size this occurred, swept images were recorded at the full range of slit sizes from 5 μm to 1 mm. This can be seen in Fig 3.10 (a). Note that below 100 μm, the time resolution is approximately constant at 10 ps, indicating that any slit size less than this will maximize signal and have minimal impact on minimum resolution. The value of 10 ps is higher than the average value of 6 ps measured in Fig. 3.8, likely because of space charge resolution degradation. In general, using larger slit sizes permits more signal in experimental configurations which may be flux starved and minimizes impact of dust/debris and physical imperfections on the slit.

At times, experimental data may be collected at gain settings other than those at which the energy calibration was performed. A calibration of the intensifier gain would be sufficient to scale the above energy calibration, but it was not available. To provide this data, I collected shots at seven gain settings at fixed input energy. Due to time limitations, these were single-shot measurements rather than an average, and the intensity carries the uncertainty of Europa's pulse energy fluctuation. These results are shown in fig. 3.10(b). The ratio of the mean counts at gain 50 to gain 30 is 8.7, as compared with the ratio of the calibration values at gain 50 and 30 in fig. 3.7, which is 8.0.

3.2.2.3 Calculation of temperature from SOP data

We now discuss the calculation of temperature from the data. Simply put, Planck's law can be solved in terms of observed counts, with the emissivity correction and other geometrically-measured constants:

$$Counts(t) = t_{dwell} A_{source} \Omega \varepsilon_{FDI}(t) \int_{\lambda_{min}}^{\lambda_{max}} T_{system}(\lambda) BPF(\lambda)\, \eta_{OSC}(\lambda) \frac{2hc^2}{\lambda^5} \frac{1}{e^{hc/\lambda k T(t)} - 1} d\lambda \tag{3.9}$$

Here, t_{dwell} is the time per pixel determined by the streak camera sweep speed; A_{source} is the area of the emitting region determined from the spatially-resolved axis of the streak camera; Ω, the solid angle of the first collection optic; ε_{FDI}, the emissivity 'gray body' correction determined from the FDI reflectivity measurement converted to emissivity through Kirchoff's law; T_{system}, the transmission through the transport optics chain; BPF, the band pass filter transmission; and finally η_{OSC}, the optical streak camera's response function. This equation is solved iteratively by guessing temperatures at each time step until the calculated counts match the measurement. It is also by taking partial derivatives from this equation that the total error contributions from uncertainties due to various geometrical system measurements are assessed.

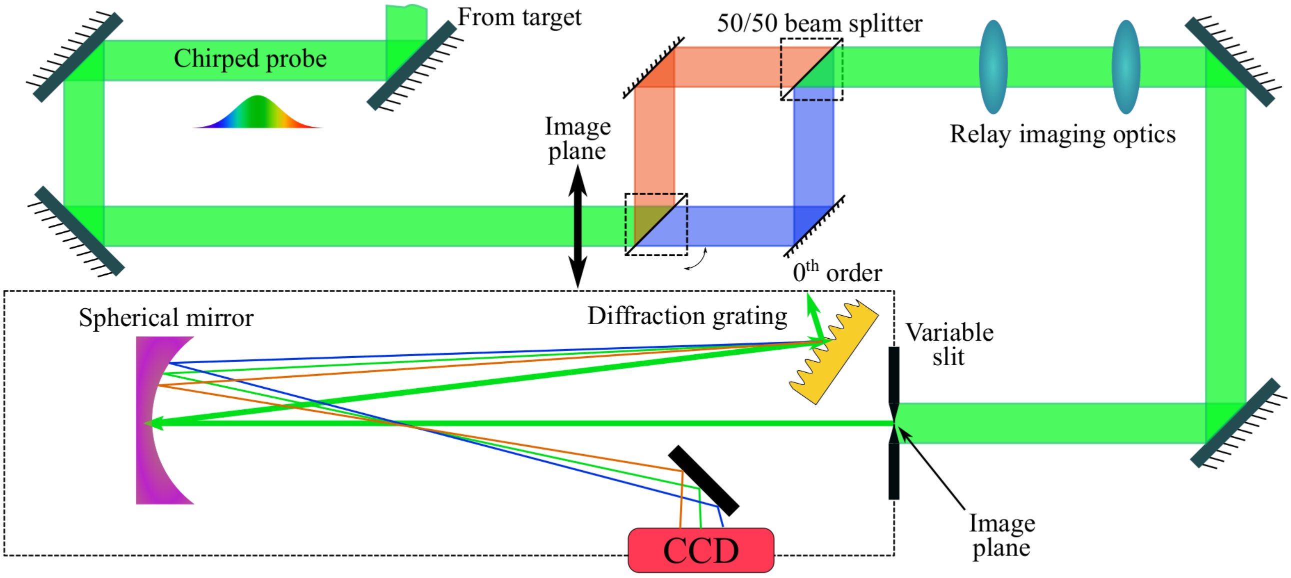

Figure 3.11: Layout of LLNL FDI used at Titan and LCLS experiments.

3.2.3 Fourier Domain Interferometer

The chirped-pulse Fourier Domain Interferometer (FDI) is a diagnostic designed to measure time-resolved phase and normalized reflectivity from an expanding surface in short-pulse laser experiments[200]. The basic phase and reflectivity measurement relies on optically probing a surface with a spot large enough to capture unheated and heated regions. The target surface is imaged onto the input of a Mach-Zehnder interferometer. Path lengths are kept equal, but the wavefronts are tilted such that the heated region is interfered with the reference unheated region. The fringe shifts then contain the phase difference between the heated critical surface and cold critical surface. Time resolution is achieved by spectrally chirping the probe so that the perturbation to the probe wavefront at any given time is encoded in a specific wavelength. After the interferometer, the probe is imaged onto a slit and then dispersed with a spectrometer. The final image is spatially resolved in one dimension and spectrally (i.e., temporally) resolved in the other. The schematic drawing of the FDI used in this thesis is shown in fig. 3.11.

3.2.4 Thomson Parabola

The Thomson Parabola (TP) ion spectrometer provides information on which ion species are accelerated and the energy spectrum of each species. To achieve this, parallel electric and magnetic fields disperse ion species onto differing parabolic tracks[201]. Fig. 3.12 shows the basic design of a TP.

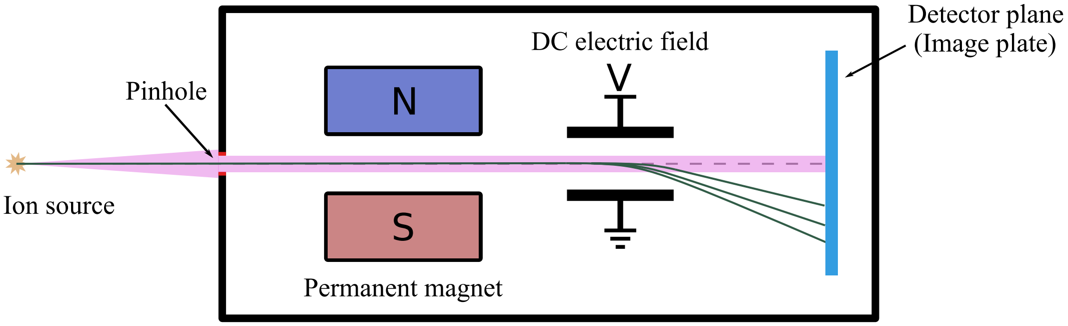

Figure 3.12: Schematic representation of a Thomson parabola ion spectrometer. Parallel electric and magnetic fields are applied to a mixed-species ion beam to disperse it in two dimensions based on charge-to-mass ratio and velocity.

The entrance aperture limits source divergence and therefore plays a role in determining the total flux and energy resolution. The magnetic and electric fields act on the incoming ion beam in perpendicular directions. The acceleration on ions from the electric field is only dependent on the charge-to-mass ratio, q/m_i, causing a separation by ion species in the vertical direction in fig. 3.12. The amount of electric deflection, x_e, is given in a small-angle approximation by[202]

$$x_e = \frac{q \cdot \int E d\ell}{2 \cdot KE} \left(D_1 + \frac{d_1}{2} \right) \tag{3.10}$$

where q is the ion charge; $\int E d\ell$, the potential between electrodes; KE, the kinetic energy of the ions; D_1, the electric drift length; and d_1, the electrode length. The magnetic field separates ion species by both charge-to-mass ratio and velocity with a deflection, x_m, as given by

$$x_m = \frac{q \cdot \int B d\ell}{\sqrt{2 \cdot m_i \cdot KE}} \left(D_2 + \frac{d_2}{2} \right) \tag{3.11}$$

where q is the ion charge; $\int Bd\ell$, integral of the magnetic field across the gap; d_2, the axial length over which magnetic field is applied; and D_2, the magnetic drift length.

The resulting data is a two-dimensional image with a zeroth-order dot (where all uncharged particles and x-rays impinge) and a series of parabolic arcs. Each represents an ion species, with the distance along the arc containing energy dispersion. Absolute particle counts can be determined from geometric distances, the entrance aperture, and response data of the film (Fuji BS image plate).

3.2.5 X-ray crystal spectrometers

One of the most practical ways of diagnosing the extremely small and short-lived laboratory plasmas is by looking at characteristic radiation given off by atomic transitions. Atomic transitions provide information about the electronic and ionic configurations within the atoms of the heated material. The observed transitions are proportional to the density of specific states which are impacted by the radiation field, collision kinetics, electric and magnetic fields, bulk motion, energetic particles, and thermodynamic state.

We can measure the intensity of specific transitions using crystal spectrometers. Many crystalline materials have lattice spacings of several to tens of angstroms, more suitable to x-rays than the micron-scale size of most diffraction gratings. For most of the spectroscopy-based work presented in this thesis, I used crystal spectrometers to view transitions in the 1–10 keV range.

X-ray crystal spectrometers come in varied layouts with a multitude of crystal geometries. However, all are based on elastic scattering from the electrons of atoms found in periodic crystal lattice planes. When the path lengths of scattered photons between planes are the same, constructive interference occurs, and x-rays appear to be reflected according to Bragg's law[203]:

$$m\lambda = 2d\sin\left(\theta_b\right) \tag{3.12}$$

where m is the diffraction order; λ, the photon wavelength; $2d$, the lattice spacing of the crystal;

and θ_b, the angle between the crystal plane and the incoming ray. A polychromatic x-ray source, typically on the scale of 100 μm or less for short-pulse laser-plasmas, acts as a point source that illuminates the entire crystal. At each Bragg angle, a specific wavelength is 'reflected', resulting in a spectrum on the output screen. The natural divergence of the source provides the necessary variation in Bragg angle along the crystal, but if more or less dispersion is required, different spectrometer geometries may be used.

The intrinsic resolution of a crystal is determined by a parameter known as the rocking curve. This is the range of angles over which constructive interference will occur for a given energy, centered at the nominal Bragg angle. The width of the rocking curve is determined by imperfections in the crystal lattice and thus may significantly differ for each crystal type, but may also be strongly impacted by crystal thickness, bending geometry, and aging. The rocking curve width, $\Delta\theta_B$ as measured in μrad, can be related to an energy uncertainty through Bragg's law as

$$\frac{\lambda}{\Delta\lambda} = \frac{\tan\theta_B}{\Delta\theta_B} \tag{3.13}$$

This provides the crystal intrinsic resolution which is naturally energy-dependent. The integral of the rocking curve at each energy is known as the integrated reflectivity, which is used for energy corrections to measured spectra. Thus, mosaic-type crystals like Highly Oriented Pyrolitic Graphite (HOPG) have excellent reflectivity (broad rocking curves) but poor intrinsic resolution, where perfect crystals such as quartz have excellent resolution and poor reflectivity.

Finally, to compare the measured data with theoretical models, a spectral sensitivity curve must be constructed that matches the calculated intensity units [J/cm^2/s/Hz/str] to the measured units, typically [PSL/pixel]. The finite size of detector elements means that the measurement integrates a Δt, ΔE, and $\Delta\Omega$, and the total energy carried by photons within the pixel is converted to Photostimulated Luminescence (PSL) (image plate) or secondary electrons (streak camera). The nonlinear dispersion off of crystals requires the calculation of response functions to account for the difference in the solid angle and energy width of a pixel along the spectrum. Additionally, detector responses and filter transmissions must be included. The total response function relating the measured intensity (I_m) to the theoretical intensity (I_{th}) is $I_{th} = I_m \cdot S$, where S is

$$S = E\frac{4\pi}{\Omega_{pix}}\frac{d\theta}{dE}\frac{1}{R_\theta}\frac{1}{\eta_{det}T_{filt}} \tag{3.14}$$

such that E is the energy per photon; Ω_{pix}, the solid angle of a pixel; $d\theta/dE$, the dispersion at film plane; R_θ the crystal-integrated reflectivity; η_{det}, the detector response (cathode, film, or CCD); and T_{filt}, the total filter transmission.

3.2.5.1 Flat crystal spectrometer

The simplest spectrometer geometry, and the one used on the TREX streak camera at Orion, is the flat crystal spectrometer. The geometry for this layout is shown in figure 3.13. This configuration benefits from simple implementation and ease of obtaining high-quality crystals of sufficient thickness to get high diffraction efficiencies. Also, the flat crystals are free of strains caused by bending processes, and data available in the literature—such as rocking curves and integrated reflectivities—are likely more accurate.

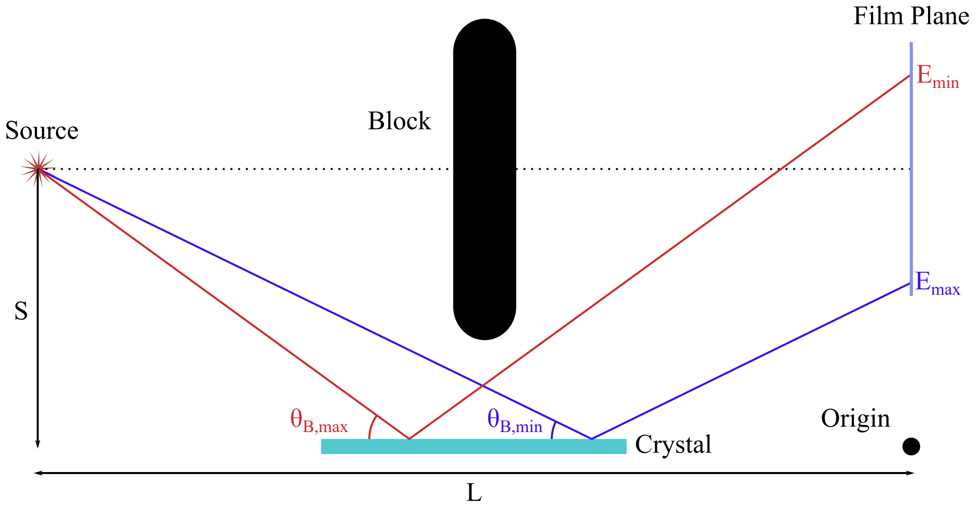

Figure 3.13: Geometric layout of the flat crystal spectrometer used with TREX streak camera at Orion laser facility. The streak camera entrance slit is placed in the film plane with a tantalum block used to exclude view of the source.

The dispersion of such a spectrometer on the image plane can be expressed as

$$E(y)\ [eV] = \frac{1.2398}{2b\ [\mu m]} \frac{\sqrt{\alpha^2+1}}{\alpha} \quad ; \quad \alpha = \frac{y+S}{L}\ [cm] \tag{3.15}$$

where $2b$ is the crystal lattice spacing, and α is a variable containing geometric lengths defined in fig. 3.13 with y being the vertical position on the image plane. Rarely is the image plate precisely located when scanned, making an additive factor necessary to translate the data until the dispersion relation matches all identifiable spectral features.

In the above geometry, rays in both the dispersive and perpendicular axes follow the inverse square law. The solid angle of a detector element is calculated as a rectangle at the total path length of its corresponding spectral ray, $\Omega \approx (a \cdot b)/L_{tot}$. The rectangle is the pixel size in the transverse axis, and the projected pixel size at the Bragg angle in the dispersive axis.

3.2.5.2 Convex crystal spectrometer

In many instances, more spectral coverage is desired than what a flat crystal spectrometer can provide, making a convex crystal useful. Relative to a flat crystal, this geometry yields more dispersion (eV/pix) on the front curvature of the crystal and less on the decreasing surface. It mitigates resolution loss due to source broadening. A typical geometry for this type of instrument is sketched in figure 3.14, similar to one described by L. N. Koppel and J. D. Eckels[204]. The layout as shown corresponds to the MKII spectrometer designed and built by the staff at AWE for the Orion experiments.

The theoretical dispersion is a bit more complex, best solved numerically using the relationships below, with θ as the independent variable:

$$\theta_B = \tan^{-1}\left(\frac{S - r\cdot\cos\theta}{h - r\cdot\sin\theta}\right) + \theta = \delta + \theta \tag{3.16}$$

$$\alpha = 2\theta + \delta = \theta_B + \theta \tag{3.17}$$

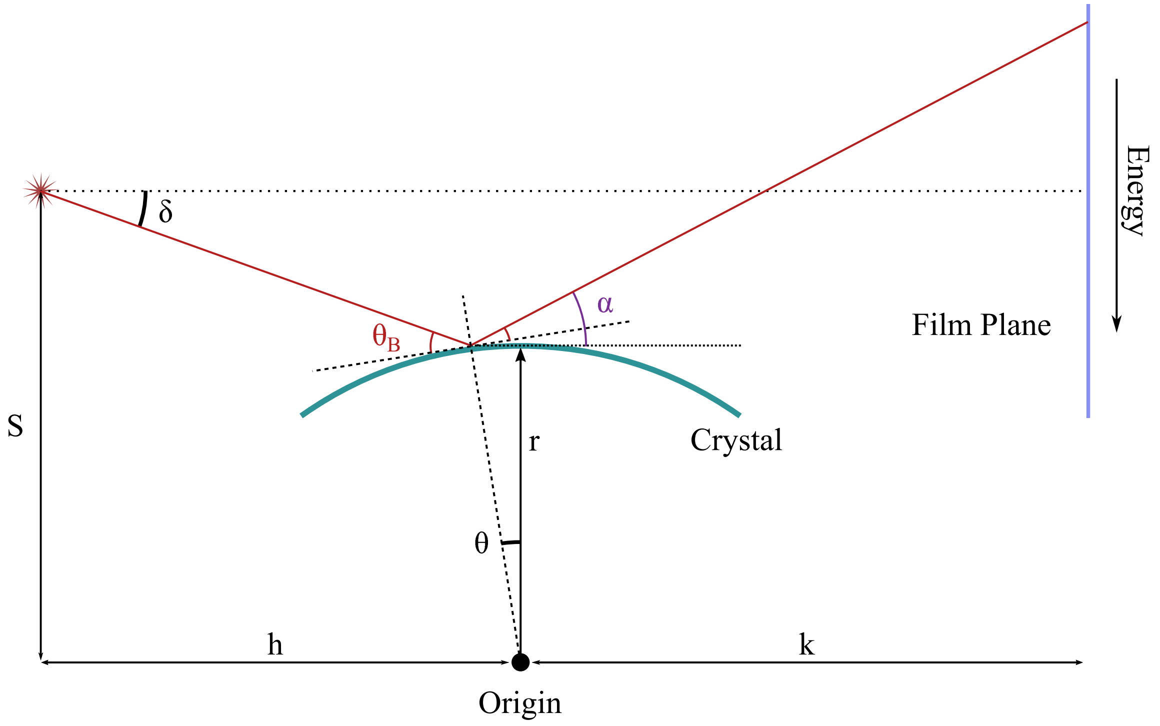

Figure 3.14: Schematic drawing of convex crystal spectrometer geometry used in Orion time-resolved and time-integrated spectrometers.

$$y(\theta) = (k + r\text{sin}\theta)\text{tan}\alpha + r\text{cos}\theta \tag{3.18}$$

Here, y is the height on the image plane, and θ is positive counter-clockwise, zero at the crystal apex, and negative in the clockwise direction. Figure 3.15 shows a comparison between the curved and flat crystal dispersions with the flat crystal placed at the apex of the circle for a CsAP crystal and typical MKII configuration (Table 3.1). Assuming a detector resolution element is 100 μm, as is the case for image plate detectors, the spectral resolution due to geometry is shown in panel (b). Beck *et al.*[205] measured rocking curve widths for CsAP of 1.05 mrad at 1000 eV and 0.22 mrad at 2500 eV. This corresponds to intrinsic crystal resolutions of 525 and 893. Thus, the limiting resolution will be due to the crystal material at low energy and due to the geometry at high energy, with an approximate average of 600.

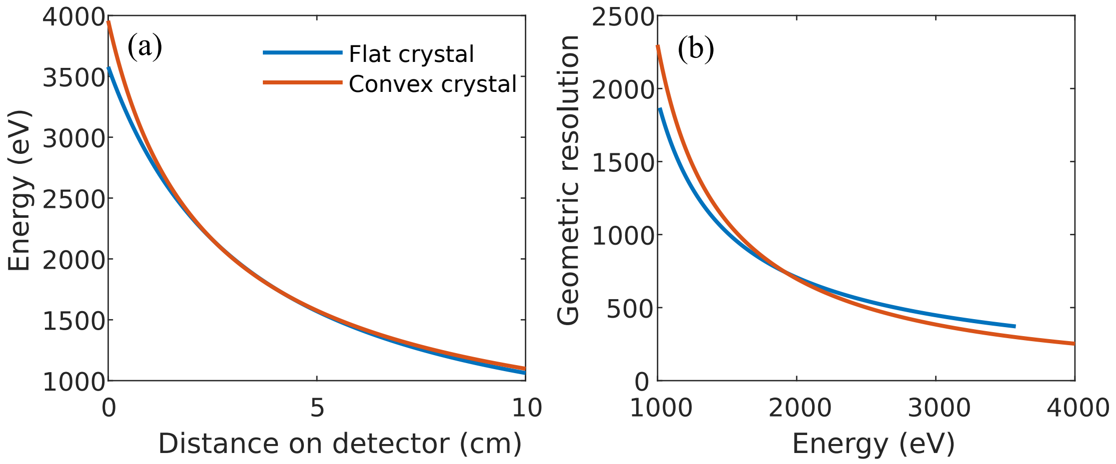

Figure 3.15: Comparison of (a) the dispersion and (b) geometric resolution (assuming 100 μm spatial resolution on detector) for flat and convex crystal spectrometers. The geometry is shown in fig. 3.14 with parameters in table 3.1.

Table 3.1: Geometric parameters for MKII convex crystal geometry

Parameter	Value (cm)
S	53.64
r	50
h	12.5
k	14.2

3.2.6 Fuji BAS-type image plate

Intense short-pulse laser-matter interactions can create harsh environments. Energetic particles and electromagnetic pulses often make the use of electronic readout devices such as CCDs impossible. Passive diagnostics like traditional film are also an option, but these have become harder to obtain, handle, and process. This has led to widespread use of Image Plate (IP) diagnostics—a set of detectors produced by Fuji Films. They contain a phosphor layer composed of BaF(Br,I):Eu^{2+}. The Eu^{2+} ions are photoionized, and the resulting electrons are trapped in lattice defects caused by the FBr^{-} and FI^{-} anions, called F-centers, where they sit in a metastable state until scanned or thermally deexcited (faded). The scanner uses a focused 632.8 nm laser to release the metastable electron from the F-center which recombines with the Eu^{3+} ions and releases a 400 nm photon. A photomultiplier tube reads this at each pixel as the plate is raster scanned to form an image.

The calibrated intensity unit is known as photostimulated luminsecense (PSL). The plates may be erased and reused by exposure to a white light source.

IPs have excellent sensitivity, good dynamic range, and acceptable spatial resolution. Image plates come in three varieties—MS, TS, and TR. Each differ in their sensitivities to x-rays, electrons, and protons and are designed for slightly different applications, based on mylar overcoat thickness and the density/thickness of their sensitive layer. The properties, as given by Meadowcroft *et al.*[206], are listed in table 3.2.

Table 3.2: Fuji BAS image plate layer composition information

Type	Mylar layer (μm)	Phosphor layer thickness (μm)	Phosphor layer density g/cm^3	Phosphor
MS	9	112	3.18	$BaFBr_{0.85}I_{0.15}$
TR	-	60	2.61	$BaFBr_{0.85}I_{0.15}$
SR	8	112	3.07	BaFBr

Image plates were designed for medical and biological industries where sources are typically brighter than necessary, and feature sizes are larger. Adoption by the laser-plasma community has led to numerous calibration papers to characterize spatial resolutions, dynamic range, fade rates, and the absolute responses to photons, electrons, protons, and alpha particles. Generally, the calibrations must be performed for the specific scanner unit as well as the plates, so a host of calibrations exist, with most larger facilities performing their own[206, 207, 208, 209]. Generally, measurements agree in functional form but experience systematic offsets of $\approx$20%. The sensitivity used to correct IP data for spectroscopic data in later chapters of this work is shown in figure 3.16 and stems from a model described by Boutoux *et al.*[209]. For all of the spectral measurements between 1–10 keV, TR image plates are used due to enhanced sensitivity of soft x-rays and the lowest sensitivity to high-energy x-rays resulting from the intense laser-plasma interaction.

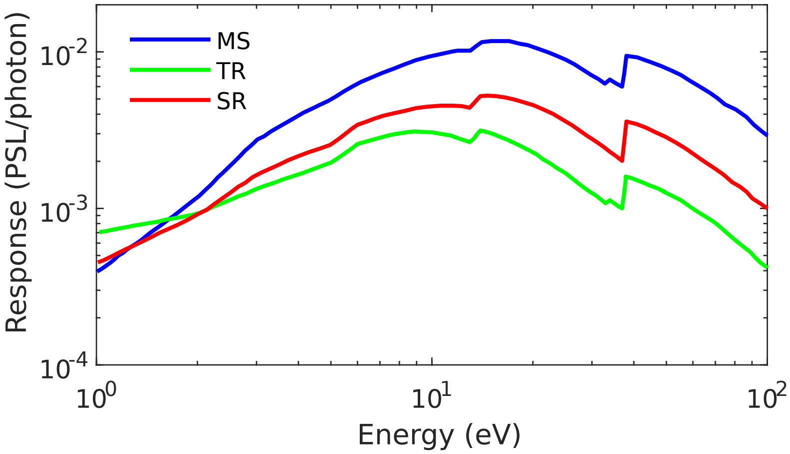

Figure 3.16: Image plate response functions calculated by Boutoux *et al.*[209].

CHAPTER 4

Thermal conductivity measurement of proton heated warm dense aluminum

4.1 Introduction

Thermal conductivity is an important component in the energy balance and thermodynamic evolution of high energy density (HED) systems. As such, electron thermal conductivity study intertwines with that of planetary cores[3, 4, 210, 1], white dwarf cores[88, 89], and in many aspects of the hohlraum and fuel capsule in current inertial confinement fusion (ICF) designs[12, 14, 15].

HED systems pose a challenge as the classical Spitzer model[63]—derived for a fully-ionized low-density plasma—breaks down. Many researchers have developed models covering parts of the HED phase space under various assumptions[71, 73, 93, 76, 13, 82]. However, development of these transport models is hampered by a scarcity of experimental data. Most models remain largely unvalidated. This vacancy is commonly filled with *ab initio* models using Kohn-Sham density functional theory (DFT) paired with molecular dynamics (MD) simulations[211, 212, 213]. These models are generally believed to provide the most accurate calculations and are used to validate or tune simpler models. However, they are computationally expensive and only exist for specific materials of interest at temperatures below 20 eV and densities above 1 g/cc. Average atom (AA) calculations, such as Purgatorio[52, 56, 55], try to maintain the best features of the electronic DFT calculation and implement them into the Ziman framework, preserving the ability to make predictions over the many decades of phase space required to model an ICF experiment.

Previous experiments have focused on the measurement of electrical conductivity (or resistivity) in strongly-coupled and degenerate systems using pulsed-power-driven capillary discharge or exploding wires[214, 83, 215]. Alternatively, the reflectivity of optical light in short-pulse laser experiments has also been used to measure AC electrical conductivities[216, 217]. Experiments such as these provided the majority of data used to benchmark current electrical transport models.

Measuring the thermal conductivity poses a greater challenge due to the additional requirement of simultaneous spatial and temporal temperature determination. Virtually no thermal conductivity measurements exist. Konopkova *et al.*[4] measured the thermal conductivity of high-pressure iron in a laser-heated diamond anvil cell. However, higher temperatures ($T_e \gtrsim$0.75 eV) can not be accessed by such an experiment in a static geometry. Dynamic measurements are extraordinarily difficult to accurately characterize due to the extremely small temporal and spatial scales and resolution limitations of modern diagnostics. However, they are likely required to reach the higher temperature regions of the warm dense matter (WDM) phase space.

In this chapter, I present the first experimental data of aluminum at 2–10 eV and 0.5–2.7 g/cc with high sensitivity to the thermal conductivity. These data stem from an experiment performed at the Titan laser at LLNL's Jupiter Laser Facility (JLF). We use a short-pulse laser to generate an intense proton beam and induce a temperature gradient in a multi-layered gold/aluminum target. Optical diagnostics measure properties at the target's rear surface as thermal energy conducts from the hot layer to the rear surface of the cold layer. Data are compared against exhaustive hydrodynamics calculations paired with a Helmholtz wave solver to accurately calculate the optical experimental observables in a self-consistent manner between tabulated electrical and thermal conductivity models. I draw conclusions about the experimental technique as well as the conductivity models available at LLNL. The experimental setup and design is laid out in Section 4.2; the analyzed data from the diagnostics are presented in Section 4.3; the hydrodynamics simulations are described and compared with data in Section 4.4; and finally, a discussion of the simulation results and interpretations is presented in Section 4.5.

4.2 Experimental setup at Titan

4.2.1 Differential heating of Au/Al targets using protons

The experimental design for this study is founded on the differential heating of a multilayer target, as described by Ping *et al.*[60]. In the case of heating with charged particles, the stopping power is determined by the Bethe formula[169], eq. (2.103). This illustrates that the energy deposited by ions increases with increasing electron density and decreasing ionization potential. It stands to reason that a bi-layer target of very different atomic numbers would experience a temperature gradient at the interface when exposed to the same proton beam, assuming the beam heats more rapidly than the heat conduction can equilibrate the layers. Figure 4.1(a) shows the difference in stopping power for cold aluminum and gold from NIST's PSTAR database[144]. The greatest heating efficiency will result from protons in the 0.1–0.2 MeV range, but the ratio of the gold stopping power to the aluminum stopping power continues to increase with energy. At 0.5 MeV, gold receives 2.4 times more energy per distance than aluminum. Thus, if we use a short-pulse laser to generate a proton beam via the TNSA effect, a sharp temperature gradient can be established. Figure 4.1(b) shows the projected range in gold and aluminum. For targets $<<1\mu$m, all but the lowest energies pass through the target, minimizing longitudinal gradients.

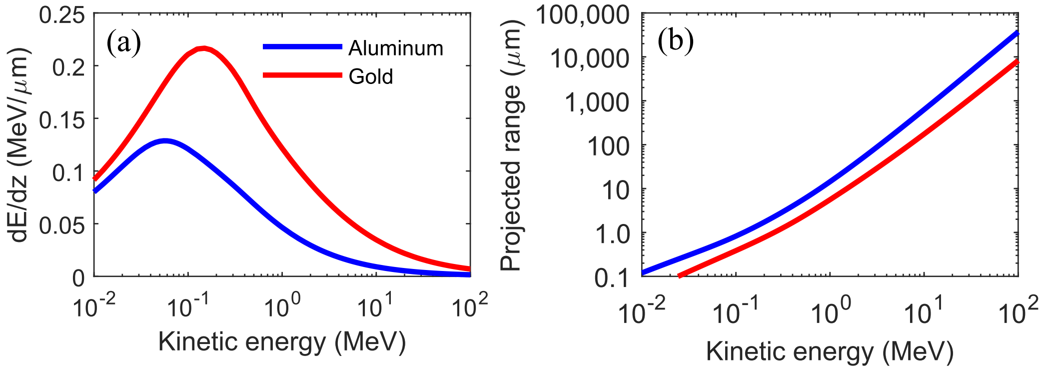

Figure 4.1: Figure (a) shows the stopping power for protons in aluminum and gold at each material's solid density and ambient temperature; (b) shows the projected range as a function of energy.

4.2.2 Target design

A schematic drawing of the target geometry used for this experiment is shown in figure 4.2. A 50-μm thick silicon wafer was coated with 100 nm of silicon nitride (Si_3N_4), then the wafer etched away. The Si_3N_4 side was then vapor-coated with gold and aluminum using electron-beam physical vapor deposition (EB-PVD). A 20-μm thick copper foil was glued to the opposite side to serve as the TNSA proton source. The open aperture was 1 mm^2 with several mm of silicon wafer frame around it for support. The assembly was glued to a glass stalk for individual shots on Titan. This design provided a consistent 50-μm gap for all targets, and the EB-PVD layers had excellent optical flatness—a constraint necessary for the use of face-on imaging optical diagnostics. The gap spacing was chosen to allow sufficient distance for the divergent proton beam to create a large heated region, but kept short to minimize the time-of-flight spread in the heating pulse due to the polychromatic proton beam.

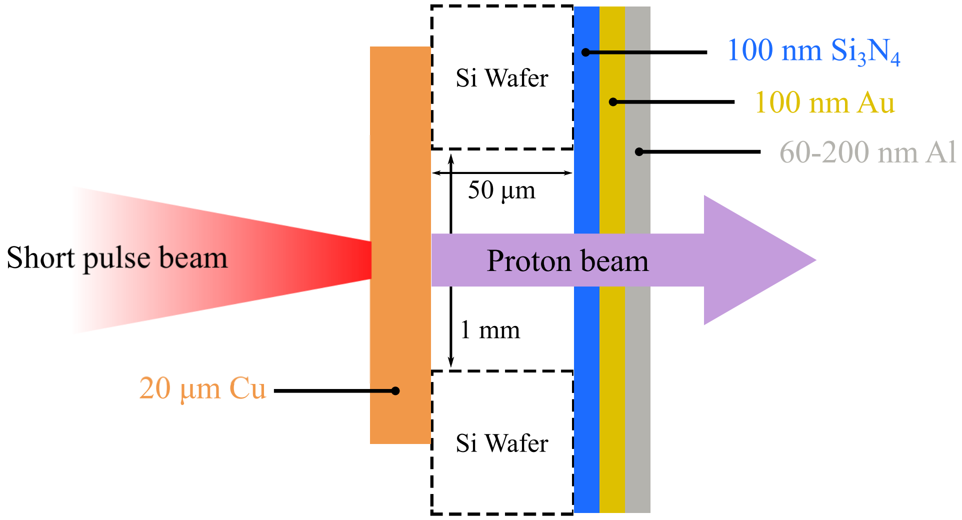

Figure 4.2: Target geometry for differential heating using proton heating.

Target thicknesses were determined according to several constraints. The large aperture silicon nitride window could support 200–400 nm of metal before strain from the EB-PVD layers caused significant warping. This set the upper limit on total thicknesses without increasing the silicon nitride layer thickness. The total thickness must also remain low enough to minimize longitudinal gradients in the proton energy deposition. Alternatively, the layers must be thick enough to remain optically thick to the optical diagnostics and contain a sufficient number of mean free paths for the diffusion-based description of thermal conductivity to be valid. Finally, a balance must be struck between cooling due to expansion and heat arriving at the back surface due to conduction. An increased aluminum thickness requires more time for the thermal energy to reach the back. This results in additional sensitivity to the conductivity model, but also increases the effect of hydrodynamic cooling, which is undesirable. These two aspects must be balanced to achieve a temperature that is both measurable and in the targeted phase space.

Full interpretation of the experiment requires a set of targets. Ideally, a set of single-layer gold and aluminum targets would be fabricated and measured to rule out uncertainties in the EOS and heat-deposition model for each material separately. This would be followed by a set of double-layer targets which would—in theory—only be sensitive to heat conduction effects. The diagnostics measure a free surface, so including aluminum layers of varied thicknesses is approximately equivalent (in the absence of expansion) to probing the heat flux at different spatial positions.

4.2.3 Laser parameters

The Titan short-pulse beam was capable of delivering up to 150 joules of 1053 nm light in approximately 1 ps. Full-energy shots were attempted but resulted in too much heat, possibly due to electrons and x-rays, and the proton spectrum was too energetic. It was observed that the entire 1 mm^2 of the target became heated, inconsistent with the angular divergence expected of a proton beam. These other heating mechanisms, while less efficient, are deleterious to the differential heating concept, so the laser energy was reduced. The data presented within this chapter were taken using 15 J focused into a 10 μm spot for approximate intensities of 10^{18}–10^{19} W/cm^2. The probe beam was frequency-doubled to 527 nm, chirped to a 50 ps pulse duration, and used at S-polarization with approximately 10 mJ defocused onto the target.

4.2.4 Diagnostic layout

The experiment utilized three main diagnostics. A schematic layout of the target chamber can be seen in figure 4.3. The Thomson parabola (TP) ion spectrometer was placed at target normal behind the target to measure the transmitted proton spectrum on each shot. Data were recorded on Fuji BAS-TR image plate films.

The S-polarized chirped probe beam was transported to the target and defocused onto the rear surface at 16 degrees from target normal for the FDI. The surface was imaged with a spherical lens to the entrance plane of the Mach-Zehnder interferometer in the FDI located outside of the chamber. A detailed layout of the LLNL FDI can be seen in fig. 3.11. Data was read out on an Apogee U9 CCD, which had a 9 μm pixel size and 27.6 by 18.4 mm active area.

The SOP was set up in the vertical plane, also at 16 degrees from target normal, with the collection lens being a 25-mm- diameter, f/4-spherical lens. The pyrometer frequency was fixed using a bandpass filter centered at 406 nm with a 60 nm FWHM width. A Hamamatsu C7700 high dynamic range optical streak camera was used to time resolve the optical emission from the target. The photocathode material was S20 ($Na_2SbK:Cs$), which provided the greatest sensitivity at these wavelengths. The absolute response was calibrated for 405 nm light on the 500 ps sweep window using the Europa laser at JLF (see Section 3.2.2.2 for details). This setup was also utilized to calibrate all of the optics within the SOP optics chain to $<1\%$ error. The optical system response was measured using CW diode lasers in-situ during the experiment. Laser parameters—such as the far- and near-field beam profiles, pulse energy, and pre-pulse level—were measured on each shot with JLF-provided instrumentation.

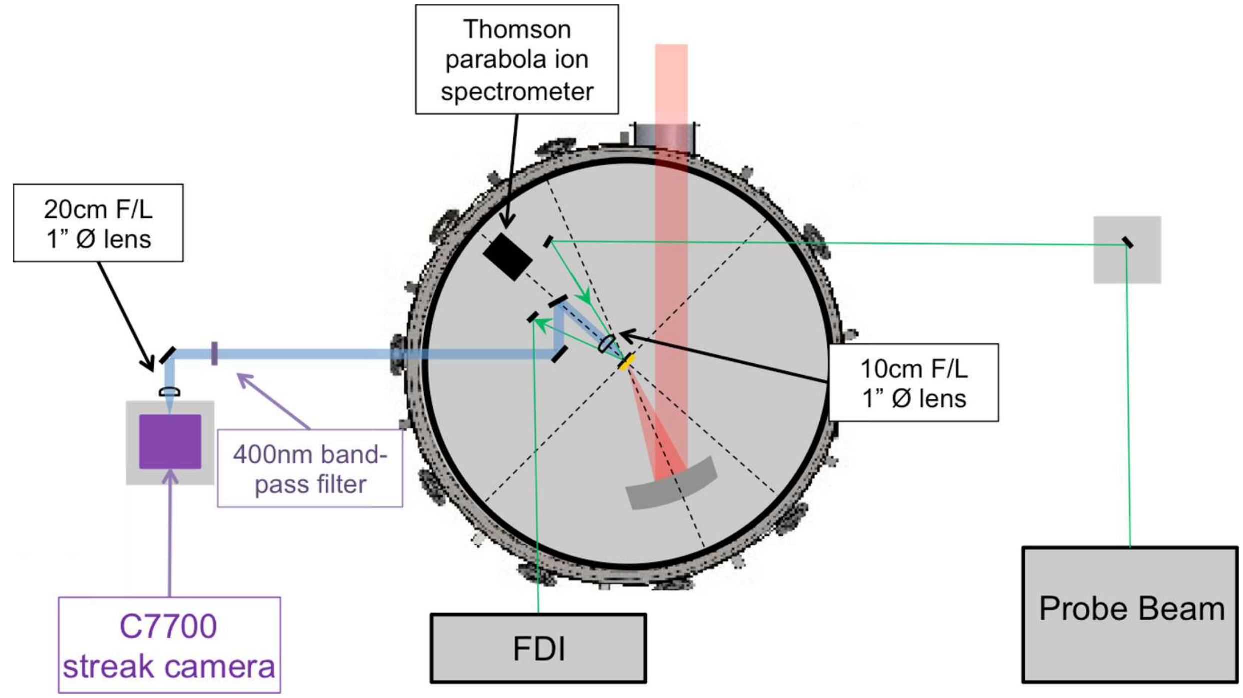

Figure 4.3: Experimental layout for thermal-conductivity measurements on the Titan laser facility.

4.3 Results

This section presents experimental data taken from a series of low-energy shots on gold and aluminum targets. A gold-only shot (100 nm Si_3N_4 + 106 nm Au) was taken with 29.3 joules to characterize the heater layer that would be otherwise be unobservable in the double layer targets. Single-layer aluminum targets were not available due to fabrication issues prior to the experiment. Three shots were taken with double-layer targets. Each had the same 100 nm Si_3N_4 + 100 nm Au layer, but the final aluminum layers were 59 nm, 105 nm, and 211 nm thick. The laser energies for these three shots were 15.7, 12.0, and 13.4 joules, respectively. All were taken on the same day with similar pre-pulse and focal spot characteristics. For simplicity, the aluminum shots are referred to as 60, 100, and 200 nm thick in the rest of this chapter. The correct thicknesses—as determined by high-accuracy profilometry measurements at JLF's target fabrication facility—was used in all modeling.

4.3.1 Thomson parabola results

The Thomson parabola was fielded and analyzed by Dr. Joohwan Kim from The University of California, San Diego. Figure 4.4 shows the analyzed proton spectra. The low-energy cutoff of the TP was 240 keV. The inset shows the peak of the spectrum on a linear scale. The peak occurs between 0.5 and 1 MeV, which is near the maximum in the stopping power curve (fig. 4.1), indicating the experimental spectra are ideal for efficient heating. At this energy, the projected range in cold material is nearly 30 times greater than the target thicknesses. For this reason, these spectra—measured in transmission—are taken to be the same as the heating source and used in the hydrodynamic modeling in Section 4.4. The laser parameters varied on a shot-to-shot basis which was emphasized in the generation of a secondary proton beam. We found that measurement of each shot's heating spectrum is essential to obtain reasonable agreement with models.

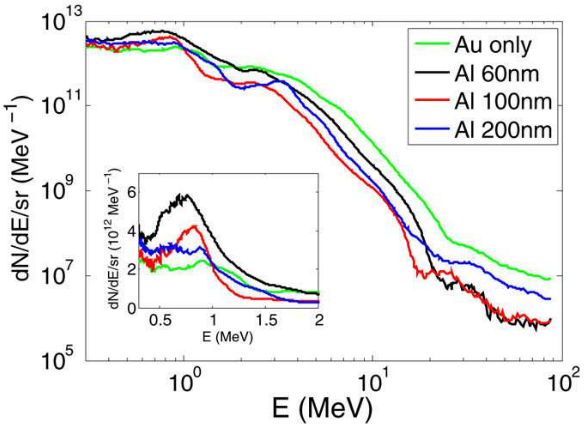

Figure 4.4: Proton spectra measured with the Thomson parabola for gold and gold/aluminum multilayer targets.

4.3.2 Fourier domain interferometry results

The FDI data presented here were analyzed by Dr. Yuan Ping from LLNL and included here for completeness. For each data shot, the target was aligned and a reference image taken. This provided the fringe locations and reflected intensity of the unheated target, crucial in accounting for spectral modulations in the probe beam. Figure 4.5 shows a sample interferrogram of the heated region.

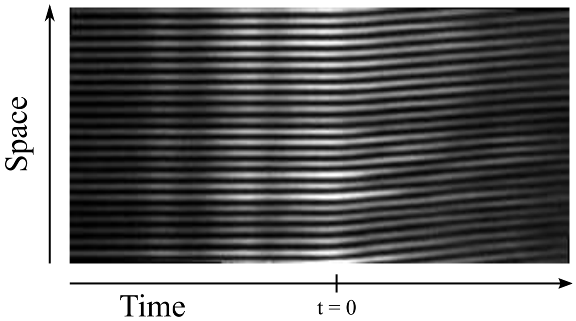

Figure 4.5: Sample FDI image of the heated region from a 15 J shot on a gold + 60 nm aluminum target.

The system magnification and image quality are measured using a known resolution target with one arm of the interferometer blocked. The temporal axis is calibrated using a variable delay line to shift the probe-beam delay relative to the short-pulse laser. A series of shots are recorded to establish a fit between wavelength and time.

A spatial lineout (vertical in fig. 4.5) will contain unshifted fringes and shifted fringes within the heated region. The detailed reconstruction procedure is described by Rebibo *et al.*[200], but the intensity of such a lineout is described by

$$I(x) = |f(\omega)|^2 \left[1 + R(x)^2 + 2R(x)cos\left[\frac{2\pi x}{d} + \Phi(x)\right]\right] \tag{4.1}$$

where $R(x)$ and $\Phi(x)$ are the reflection coefficient and phase difference we seek; $f(\omega)$ is the spectral envelope; and d, the spacing between unshifted fringes. An inverse-Fourier transform of this intensity yields three peaks in frequency space: the carrier frequency (located at $\pm k_0 = 2\pi/d$) of the unshifted fringes will be modified in the heated regions. This peak should be isolated and Fourier transformed back into the spatial domain to yield the desired information.

The reflectivity is given as a ratio relative to the unheated portion of the image. The ratio is then multiplied by the room temperature (cold) reflectivity of the target to achieve real values. Cold reflectivities for each target type were obtained at the experimental angle of incidence and polarization using constant wave (CW) diode lasers at 400 and 527 nm prior to the experiment.

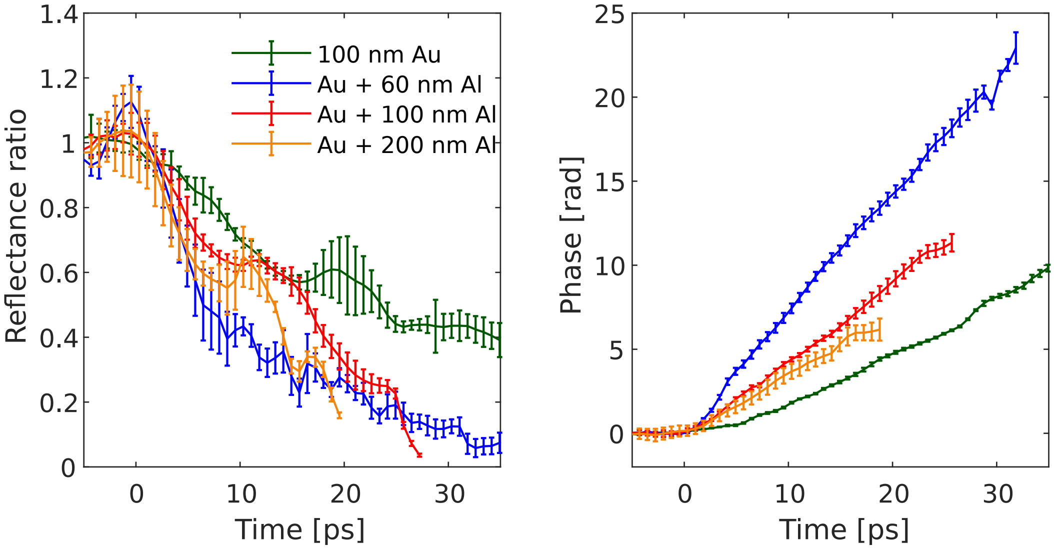

Figure 4.6: Analyzed (a) reflectivity ratio and (b) phase shift from FDI measurements.

.

Figure 4.6 shows the analyzed reflectivity and phase data from the experiment. The expansion velocity proportional to the derivative of the phase shift. As this is more prone to numeric noise, only the phase shift data are presented. The gold-only target had the slowest reflectivity decay, which is consistent with it also having the slowest expansion velocity. Thinner aluminum layers were also observed to expand more rapidly than thicker layers. The error bars were determined by the statistical variation of phase and reflectivity values within the 70 μm heated area being averaged.

4.3.3 Pyrometry results

The temperature of the rear surface was measured using streaked optical pyrometry. A schematic of the diagnostic can be seen in figure 3.6. This diagnostic measures the absolute thermal self-emission from the heated spot and infers a temperature by equating that emission to the theoretical emission from a black body at a single temperature. This is known as the brightness temperature. A correction to this temperature is made—realizing that real surfaces are not perfectly black if they are reflecting—using the emissivity to obtain an electron temperature. See Section 3.2.2 for details on the SOP theory and assumptions.

Making the temperature measurement for this experiment required tremendous care be taken to properly account for all loses of signal and correctly calibrate the imaging system. The system magnification and field of view of the SOP were measured by placing a mesh target with 10 μm bars and 250 μm period at the laser focus and illuminating it with a 405 nm CW diode laser. The scattered light was imaged onto the optical streak camera in focus mode with the adjustable slit fully open. From this, the total magnification was found to be 0.83 ± 0.025, and the field of view was greater than 500 μm on target.

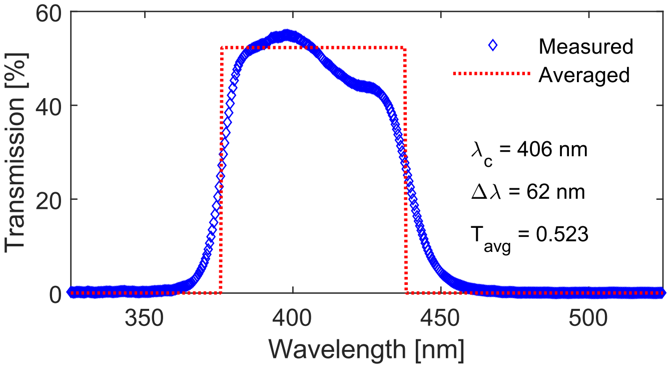

Figure 4.7: Measured response of bandpass filter used to isolate the chosen 405 nm SOP emission.

The system transmission, neglecting the bandpass filter, was measured to be 0.663 ± 0.05 at 405 nm (the central wavelength of the bandpass filter). This was measured using a CW laser aligned through an aperture at target chamber center (TCC) and another at the streak camera face. The power was measured with a Thorlabs S120C photodiode power sensor. The bandpass filter had an average transmission of 0.523, and a frequency response shown in figure 4.7. The manufacturer-stated extinction ratio was 10^{-4} outside of the transmitted band. The transport optics used Thorlabs ultraviolet (UV)-enhanced aluminum mirrors, a fused silica chamber window, and a quartz microscope slide to protect the front collection lens from debris and metal vapor accumulation. The slide was changed on each shot. The response of the mirrors and transmissive optics varied by less than 2% over the frequency band, and so their frequency response is neglected in temperature calculations, using simply the mean value.

Figure 4.8 shows raw SOP images from two data shots. The measured spot size has a 300 μm FWHM. Data was taken from the central 70 μm to match the same region averaged in the FDI and minimize any radial gradients in the data. Signal was abundant, and care was taken to minimize blooming within the streak camera and preserve the measured spatial and temporal resolutions. This was achieved by keeping the entrance slit at 15 μm and using calibrated neutral-density (ND) filters. The time resolution was measured to be approximately 6 ps near the center of the screen. The entire sweep window was 446 ps over 1024 pixels according to the calibration provided by the manufacturer. The data was oversampled by a factor of 14, which allowed some averaging to be performed to reduce signal to noise.

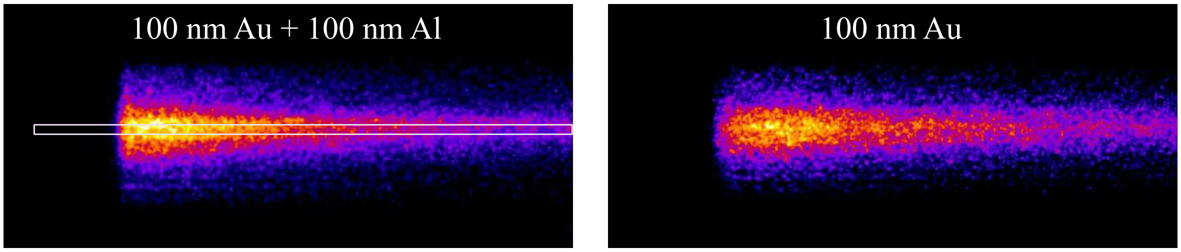

Figure 4.8: Raw SOP images for a 100 nm Au shot (right) and a 100 nm Au + 100 nm Al shot (left). The intensities of each image have been scaled separately. Temperatures presented below are taken as the average of the central 70 μm of the heated region, indicated by the white box.

Optical Transition Radiation (OTR) is generated by the relativistic electrons crossing the metal-vacuum interface[218]. This would, in principle, give an absolute measure of the time the source turned on. The signal would begin 0.2 ps after the laser-solid interaction. Two MeV protons cross the 50 μm gap in 2.6 ps, and 0.2 MeV protons cross in 8 ps. The heating due to the protons begins within one time-resolution element, and the OTR pulse is masked due to the instrumental response. However, the OTR signal was observed in several gold/carbon shots with less self-emission than OTR signal. This was due to lower temperatures in those shots. The position was correlated with an inflection in the rising edge of the signal, and a 6 ps FWHM Gaussian was subtracted to approximately account for this extra signal.

In order to infer temperature, the total counts within the heated region were summed and the temperature calculated iteratively using eq. (3.9). Figure 4.9 shows both the brightness temperature

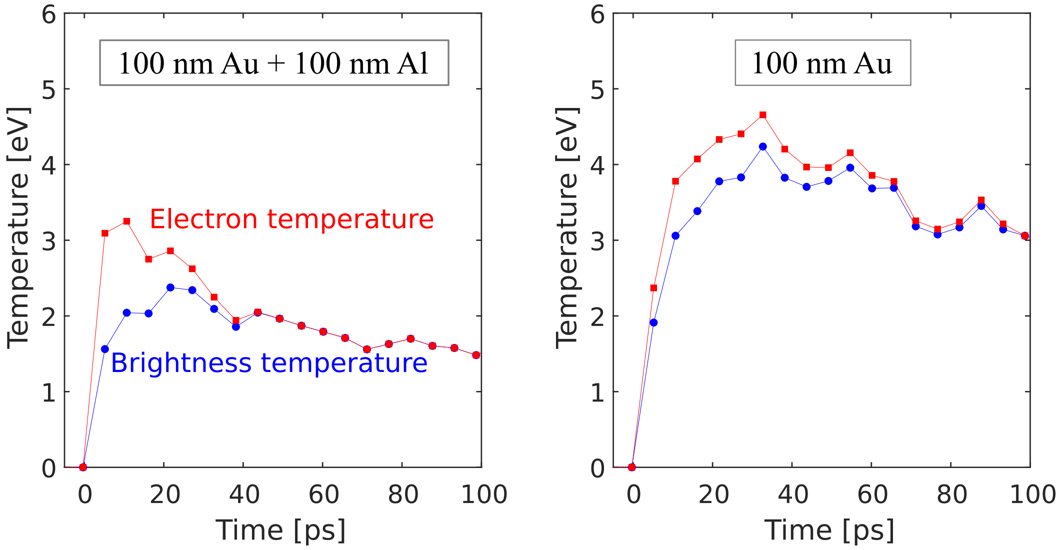

Figure 4.9: Calculated temperatures for the 100 nm Au shot (right) and 100 nm Au + 100 nm Al shot (left). Brightness temperature (blue) and electron temperature (red) calculated using the time-resolved reflectance data.

and corrected electron temperature calculated for the 100 nm gold and 100 nm gold + 100 nm aluminum shots in order to illustrate the relative importance of the emissivity correction. For these data, the FDI reflectances (shown in fig. 4.6) are scaled to the cold material values measured at 405 nm. The FDI traces were extrapolated to zero reflectance to maintain continuity in the SOP data beyond the FDI record.

Theoretical reflectances, calculated using Fresnel equations and complex dielectric function data from ref. [219], are shown in fig. 4.10. Aluminum has no significant change in reflectivity between 405 nm and the 527 nm. As such, the FDI will sample a slightly-lower critical-density surface, but the temporal evolution is expected to be very similar between the 405 and 527 nm critical surface in Al. However, gold has interband transitions that preferentially absorb blue and green light. The behavior of the band structure persists even into warm dense matter conditions[220], and the onset is near 530 nm (2.35 eV). This could result in differences in the optical properties of the 527 and 405 nm surface for gold, but it will still have a small impact on the correction of the brightness temperature, as seen in fig. 4.9. This is because of the relatively low reflectivity. Additionally, the correction becomes insignificant entirely after $\approx$ 30 ps.

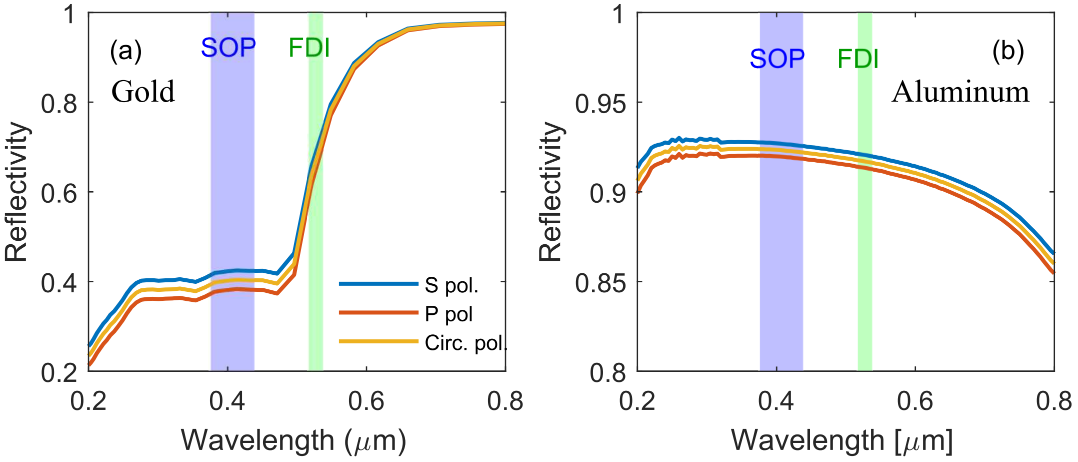

Figure 4.10: Theoretical reflectivities from the Fresnel equations for (a) gold and (b) aluminum. The bands covered by the SOP bandpass filter and FDI probe beam are indicated with shaded areas.

The final temperature profiles are shown in fig. 4.11. As shown, the gold-only shot obtains the highest temperature with a peak value of 6.7 eV. The hottest double-layer target is the 60 nm thickness with a peak temperature of 3.3 eV. It is generally expected that the thinner double-layer targets achieve higher temperatures. This occurs simply because energy from the hot gold layer arrives at a time when less energy has been lost due to expansion. Thicker targets increase the distance over which a thermal wave must propagate and the amount of material to be heated, resulting in lower temperatures. However, shot-to-shot fluctuations of the laser parameters, and consequently the generated proton spectrum, resulted in similar temperatures for the 100 and 200 nm Al layers.

Rigorous error analysis considered uncertainties due to the magnification measurement, collection aperture size, lens position, system transmission, and other optical properties. Dominant sources of systematic error included the inferred area of the emitting source, the streak camera calibration, and the early-time reflectance correction. At times where the emissivity was not 1, the temperature was assumed to be known to ±15%, and at later times, to ±10%. The statistical error—determined by the signal-to-noise level—was slightly lower at 5–10%.

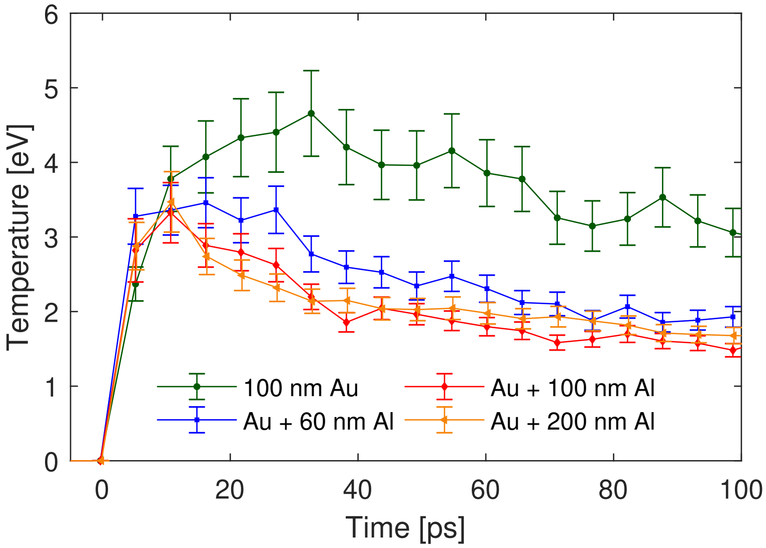

Figure 4.11: Electron temperatures, corrected for emissivity, of the gold-only and three gold/aluminum target thicknesses.

4.4 Hydrodynamic modeling

The evolution of the aluminum layer is determined by the balance between cooling mechanisms (PdV and radiative) and heat conducting into the layer. To analyze an integrated experiment such as this, we turn to 1-D, Cartesian-geometry, Lagrangian hydrodynamic simulations using the LLNL-developed code, HYDRA[221]. HYDRA is a multi-dimensional, multi-physics, arbitrary Lagrangian-Eulerian (ALE) radiation hydrodynamics code. It takes input tables for the EOS, opacity, and thermal conductivity and uses simplified, in-line models for electron-ion equilibration and ionization to solve Euler's fluid equations on a mesh.

We employ two temperature simulations which track electron and ion temperatures independently. Electron-ion energy equilibration is calculated using a collision rate determined by the Lee & More model[13]. The proton-heating source is implemented using HYDRA's heavy ion beam deposition model, which calculates the slowing down and energy deposition of protons based on the data of Betz[222] and a model developed by Tech-X Corporation based on Peter and Meyer-ter-Vehn's work[223]. The on-shot proton spectrum measured with the TP (figure 4.4) is initialized at $t = 0$, 50 μm from the target. The heating source lasts approximately 7 ps, based on the time-of-flight spread of protons traversing the gap. This is shown for the three aluminum shots in fig. 4.12. Using the transmitted proton spectrum as the source is expected to be acceptable due to the negligible slowing down of MeV protons in these ultra-thin targets. The only fitting parameter used is a

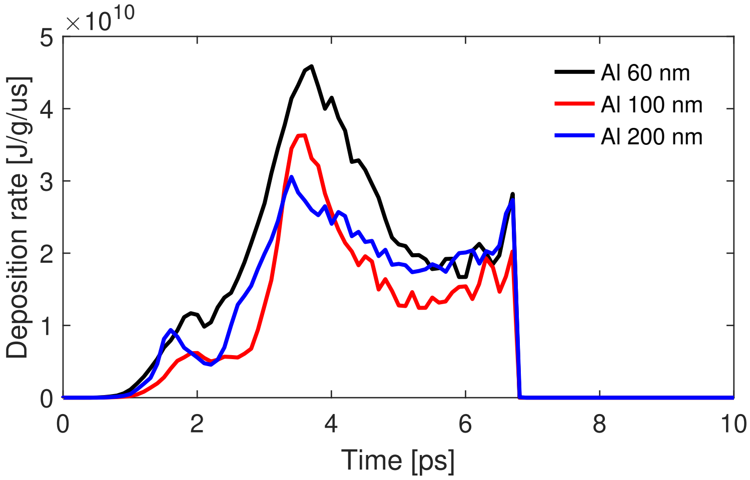

Figure 4.12: Energy-deposition rates used in HYDRA simulations for each target thickness.

source multiplier to scale the divergence angle of the proton beam. The final value, approximately 14°, is reasonable considering that the central 70 μm corresponds to a 10–15° divergence angle of the 300 μm spot. The total spot size corresponds to the expected divergence angle of TNSA protons (≈40–60°). The value of this fitting parameter is determined from the gold-only shot and left fixed for all remaining shots. Radiation transport is included using multi-group implicit Monte Carlo[224] with frequency-dependent opacity values generated by the LLNL opacity server. Optical wavelengths were resolved, though it was found through numerical testing that the radiation transport resulted in negligible energy transfer when compared with electron-thermal collisions.

4.4.1 Tabular EOS models

The EOS model used affects the calculated expansion velocity and rear surface temperature. At the time of this work, two EOS models were available to test for gold—Sesame 2700[101] and LEOS 790[96, 98]. Aluminum is a common prototype material, and more robust models exist. Three aluminum EOS models were compared—Sesame 3720[225], LEOS 130, and Lynx 130.

The Lynx tables utilize the same methodology as the LEOS tables, but use the AA code Purgatorio to calculate the electron-thermal contribution to the EOS. This approach includes effects from electron orbitals that the other Thomas-Fermi approaches average out.

This experiment relies primarily on the behavior of the EOS in material that is unloading, or releasing, into vacuum. Figure 4.13(a) shows the temperature of an isentropic release from a Hugoniot calculated from 2.7 g/cc and 5 eV for the three aluminum EOS options tested. As shown, Sesame 3720 and LEOS 130 predict similar temperatures as the profile expands, but Lynx 130 cools significantly faster. It is visible in (c) and (d) that the pressures and sound speeds are similar for all three models. The largest variance in EOS temperatures arise due to calculation differences of the specific heat (b). The structure in the specific heat at $T_e = 3.5$ eV may not be physical and could be the cause of the rapid temperature drop in the isentropic release shown in (a). From these plots, we can expect similar physical characteristics but potentially different temperature predictions.

4.4.2 Tabular electrical & thermal conductivity models

Four conductivity models were available to test: Lee & More[13], Purgatorio[52, 55], Sesame 23714[79], and Sesame 29373[82]. Sesame 23714 is based off of Rinker's AA calculations, outlined in Chapter 2. Sesame 29373 was generated by M. Desjarlais following the methodology laid out in ref. [82] and tuned to match QMD simulations. These models are referred to as LM, PG, SS (or Rinker), and LMD respectively. Figure 4.14 shows the values thermal and electrical conductivities at 2.7 and 0.5 g/cc versus temperature. At 10 eV and solid density, all models agree to within a factor 2.5. This grows to a factor of 10 at 2 eV. As the density decreases, the number of conduction electrons created through pressure ionization decreases and the thermal conductivity drops rapidly below 5 eV.

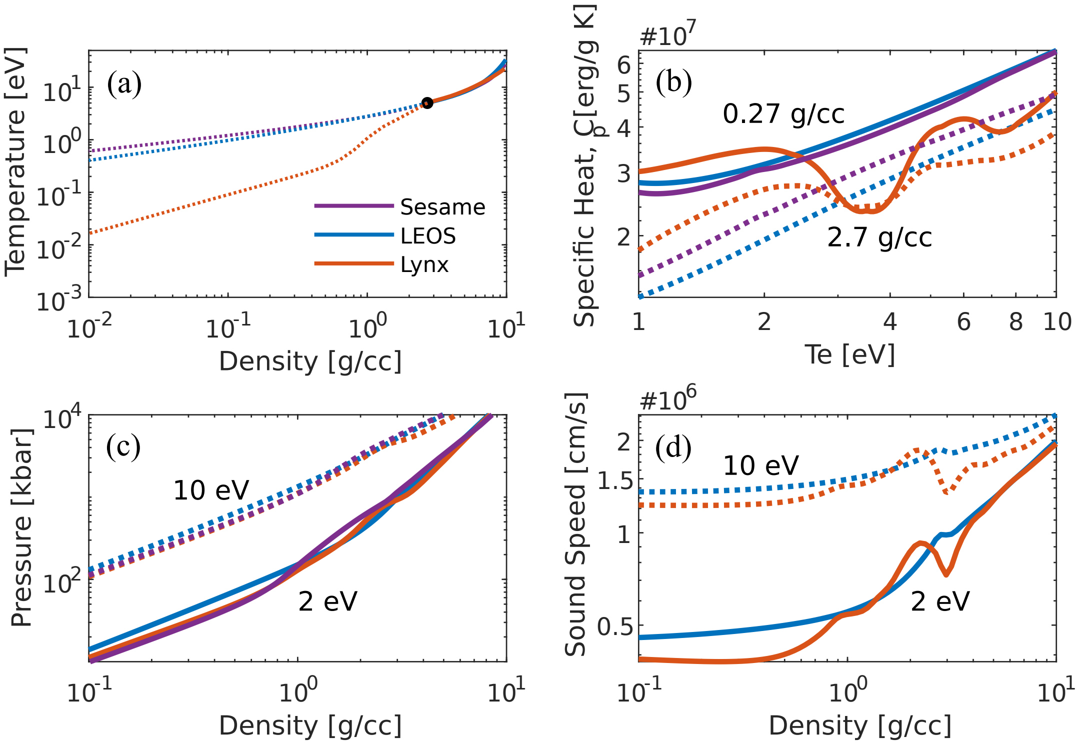

Figure 4.13: Comparison of aluminum EOS quantities for Sesame 3720, LEOS 130, and Lynx 130: (a) shows an isentropic expansion from a Hugoniot starting at 5 eV and 2.7 g/cc, (b) shows the specific heat C$_p$, (c) the pressure, and (d) the sound speed.

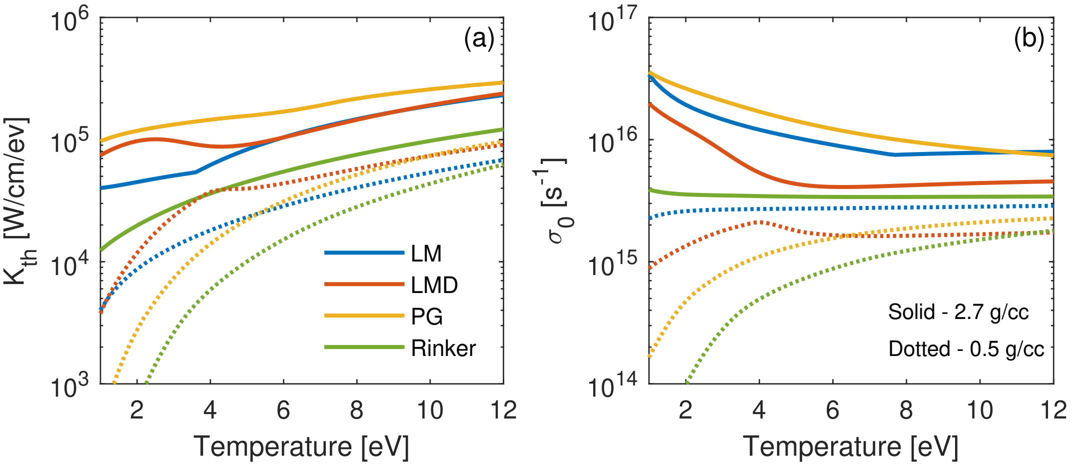

Figure 4.14: Thermal conductivity (a) and electrical conductivity (b) values for the four conductivity models compared in this work. Soid lines are at 2.7 g/cc, and dotted lines are at 0.5 g/cc.

4.4.3 Helmholtz wave solver

Hydrodynamics calculations provide temperature and density on a spatial grid. Comparison of such a simulation with measurement requires determining exactly which surface the diagnostics see and what its optical properties are. The simplest estimate of this surface is the electron critical surface at the probe wavelength. However, as the plasma expands and the scale length increases, there will be significant underdense plasma in front of the critical surface. The reflected wave energy, in the WKB (Wentzel-Kramers-Brillouin) approximation, decays as exp(-$8\nu_{ei}^{*}L/3c$) for a linear scale length where L is the scale length and ν_{ei}^{*} is the electron-ion collision frequency at the critical surface[135]. Thus, the optical behavior will depend equally on the collisionality of the plasma and the density gradient. Real systems will not have linear scale lengths, and the optical signatures will stem from a range of conditions with varied collision frequency. The most consistent way to model optical diagnostics is achieved by solving the Helmholtz wave equation for each time step of the hydrodynamics calculations.

The method has been used by Milchberg and Freeman to study short-pulse laser absorption in short scale lengths[226] and employed in the context of optical measurements of shock breakouts for EOS measurements[227]. In this work, I follow the computational study by Celliers and Ng[228], to construct a complex dielectric function and model the optical response of the expanding layer. The Helmholtz solver used was described by Gibbon[134]. Gibbon's solver was adapted from Fortran to Matlab and expanded to include the Lee & More conductivity model by Dr. Elijah Kemp of LLNL. It was further modified by the author to include P polarization, and accept tabulated electrical-conductivity input and include the spatial-absorption profile calculations necessary for modeling the SOP.

The Helmholtz equation describes the propagation of electromagnetic waves through inhomogeneous plasma. It is solved independently for S and P polarizations. The problem geometry assumes an electron-density gradient oriented along the x-axis. For S polarization, determining the z-component of the electric field (E_z) entirely determines the problem. The Helmholtz equation is given by

$$\frac{\partial^2 E_z}{\partial x^2} + k_0^2(\varepsilon - \sin^2\theta)E_z = 0 \tag{4.2}$$

where $k_0 = \omega/c$ is the vacuum wave number, θ is the angle of the Poynting vector relative to the x-axis, and ε is the dielectric function. For the case of P polarization, the problem is entirely determined by the z-component of the magnetic field, and the Helmholtz equation is

$$\frac{\partial^2 B_z}{\partial x^2} - \frac{1}{\varepsilon}\frac{\partial \varepsilon}{\partial x}\frac{\partial B_z}{\partial x} + k_0^2(\varepsilon - \sin^2\theta)B_z = 0 \tag{4.3}$$

The other components of the fields can be retrieved using Maxwell's equations[134]. These equations are numerically solved using finite-differencing and appropriate assumptions about the transmitted wave and vacuum boundary conditions.

The dielectric function is given by

$$\varepsilon(z) = 1 + i\frac{4\pi\sigma(\omega, z)}{\omega} \tag{4.4}$$

where $\sigma(\omega, z)$ is the frequency- and space-dependent electrical conductivity. We have chosen the Drude model for this function, so $\sigma(\omega, z)$ is defined as

$$\sigma(\omega, z) = \frac{\sigma_0}{1 - i\omega\tau_{ei}} \tag{4.5}$$

where σ_0 is the DC electrical conductivity, and τ_{ei} is the electron-ion collision frequency. For all models compared within this work, σ_0 and Z are tabulated or calculated with simple formulas. As such, the collision time is obtained using

$$\frac{1}{\tau_{ei}} = \frac{Zn_i e^2}{m\sigma_0} \tag{4.6}$$

where Z is the average ionization; n_i, the ion density; m, the electron mass; and e, the electron charge. It is important to note that some degree inconsistency may enter at this point. Some physical pictures—such as the average atom (AA) model in Purgatorio—calculate τ_{ei} and σ_0 self-consistently. Equation (4.6) may not exactly match the self-consistent calculation. The average ionization is vaguely defined in such a model[55], and flexibility exists. Here, we choose eq. (4.6) to more readily compare DC electrical conductivity models using the same ionization model across the comparison. When Purgatorio is tested without using the TF ionization, I use the definition $Z_{free} = \int_0^\infty f(\varepsilon, \mu) X^{ideal}(\varepsilon d\varepsilon)$, which counts the free electrons in the ideal density of states for an electron gas using the self-consistent chemical potential but ignores quasi-bound resonance features due to loosely-bound shells.

To summarize, we take model input for the DC electrical conductivity and average ionization. We further assume the Drude model is appropriate, allowing for the construction of a complex dielectric function dependent spatially on temperature and density. This is then used in the Helmholtz equation to solve for the electric and magnetic field components in space. The total reflectivity may be calculated from the incident and reflected wave amplitudes as $R_{s\lambda(\theta)} = |E_r|^2/|E_i|^2$ and $R_{p\lambda}(\theta) = |H_r|^2/|H_i|^2$ for each polarization. This allows direct comparison of different electrical conductivity models with the time-resolved FDI data.

Calculating the temperature the SOP sees requires a spatially-dependent absorption profile. This is calculated for each zone along the spatial mesh as $\frac{1}{2}\text{Re}(\sigma)|E|^2$, which yields an absorption coefficient with units of cm^{-1}. This is integrated along the mesh, yielding a total absorption fraction. This value should obey the relation $A = 1 - R$, where R is the total reflectivity—useful as a consistency check. We assume that light emitted within the target will have the same reflective/refractive behavior as if it had been incident on the target. The target has a temperature gradient, so the total emissivity is calculated using Kirchoff's law as

$$S(\theta) = \int_{-\infty}^{z} \alpha(z') I_\lambda(T(z')) \text{cos}\theta dz' \tag{4.7}$$

where $\alpha(z')$ is the local absorption coefficient, and $I_\lambda(T(z'))$ is the black-body intensity at the local electron temperature. This is performed for all visible frequencies, and the intensity weighted by the bandpass filter response and summed. This total emissivity may then be compared with the emissivity from a single black body temperature to get a brightness temperature, or paired with the calculated reflectivity to get a 'corrected' temperature as was done with the SOP data (fig. 4.9).

4.4.4 Gold simulations

Figure 4.15 shows the simulation results for the 100 nm gold target. The left column contains simulations using LEOS 790, and the right column, simulations using Sesame 2700. The in-line Lee & More (LM) model was used for all thermal conductivities, but the observed temperature and reflectivity were calculated using electrical conductivities from Purgatorio (PG) as well as with Purgatorio using the TF ionization calculated by HYDRA (PGTF). Single-layer targets are not sensitive to the value of thermal conductivity because of the volumetric heating source. This was confirmed with numeric simulations that arbitrarily scaled the thermal conductivity up and down by factors of 10. Thus, the electrical conductivity model will demonstrate the uncertainty in which surface within the gold is viewed by the SOP.

The temperature matches between 30–100 ps for LEOS. Sesame falls within the error bars, but the temporal slope is quite different. Remembering that the primary source of error is systematic in nature, the cooling rate in the data should be accurate. Scaling the amplitude of the heating source within error bars simply shifts the temperature curve up and down, leaving the temporal evolution trace unchanged. No value of the multiplier leads to a temperature match with s2700. The phase shift of the critical surface using L790 also provides an excellent match to the data while the s2700 simulation predicts a slower expansion of the critical surface. This is consistent with the rapid cooling seen in the s2700 temperature curve. Lower temperature leads to a drop in the ionization, and the critical surface moves deeper into the target where the expansion is slower. Finally, looking at the temporal reflectivity traces, both simulations do an adequate job with neither matching the entire time history but both having the correct general trend.

The early-time temperature in both calculations does not match the data. The cause of this is an open question. During the heating phase, the electron subsystem will be driven from equilibrium

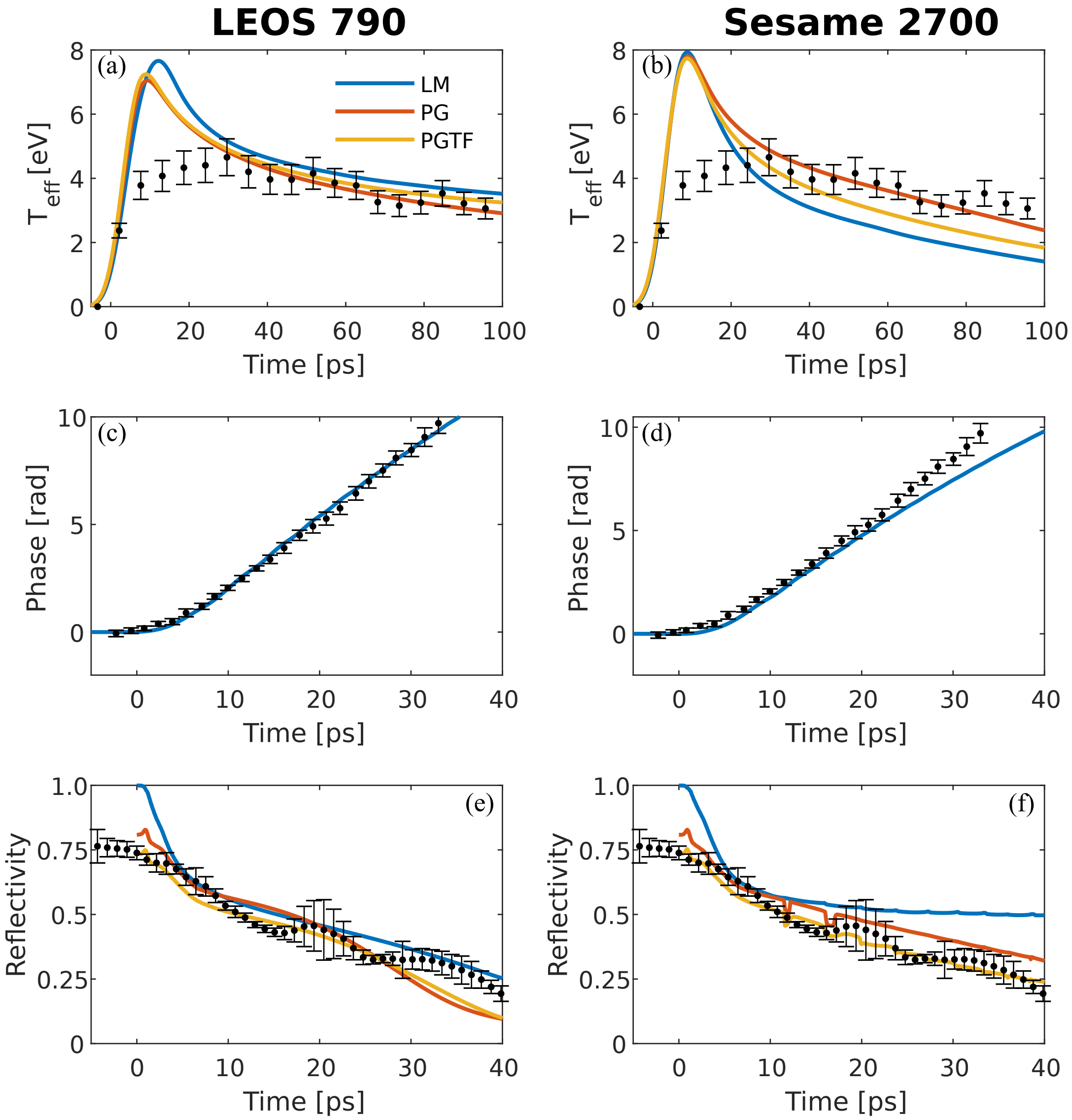

Figure 4.15: Modeling results for 100 nm Au data. The left column shows results using LEOS 790, and the right column shows Sesame 2700. All calculations use Lee & More thermal conductivity (LM), but the density profiles were also processed with Purgatorio (PG) electrical conductivities using the Purgatorio ionization and the Thomas-Fermi ionization (PGTF). At the top, (a)–(b) show the effective temperatures calculated from the Helmholtz absorption profiles. The phase of the expanding 527 nm critical surface is shown for both cases in (c)–(d). Finally the reflectivity calculated using the Helmholtz solutions at 527 nm is shown in (e)–(f).

for an unknown amount of time. The present models (EOS and electrical conductivity) are poorly defined for non-equilibrium systems and unpredictable results may occur. However, measurements in proton-heated tantalum indicate an electron-ion equilibration time of 0.5 ps[229]. This would suggest that non-equilibrium conditions should not persist for longer than 10 ps—several picoseconds past the end of the heating pulse. Another possibility is the early-time band structure of gold. The green probe will exhibit a distinct, non-Drude behavior due to the onset of conduction band transitions. Though not expected, it is possible that band-structure effects last beyond the first several picoseconds. Regardless, our aim with the gold data is to fix the heating source and gold EOS. The late-time behavior is sufficient to accomplish this.

The above comparisons make LEOS 790 the preferred gold EOS for these simulations. It is important to be clear at this point: the proton-source multiplier determined with the single-layer data impacts the final conclusions. However, the single-layer data remains the best choice to fix this free parameter. It is not sensitive to the choice of thermal conductivity model, and it does not have interface effects. Fortunately, the electrical conductivity model does not play a large role in temperature amplitude. In anchoring the divergence of the proton source using gold, we rely on the proton stopping-power calculation being as correct for gold as it is for aluminum.

4.4.5 Aluminum simulations

With the proton heating source fixed, we now consider how the data can constrain the aluminum EOS and conductivity models. There are three available EOS models—LEOS 130, Lynx 130, and Sesame 3720—and four thermal conductivity models—Lee & More[13], Purgatorio[52, 55], a Sesame table based on Rinker's calculations[79] (s23714), and a Sesame table based on the Desjarlais improvements to the Lee & More model[82] (s29373). Each of these thermal conductivity models is accompanied by a DC electrical conductivity and average ionization table. In the following simulations, electrical and thermal conductivities are always paired to keep the collision physics consistent. The temperature and reflectivity calculations are presented using the model's native ionization table as well as with the in-line TF ionization in the calculation of collision time,

τ_{ei}. These are denoted in plots, for example, as PG for Purgatorio with its native ionization, or PG-TF for Purgatorio with a Thomas-Fermi ionization model. All permutations of these models are considered. The combination of phase, reflectivity, and temperature data provide a strong constraint on all modeling parameters.

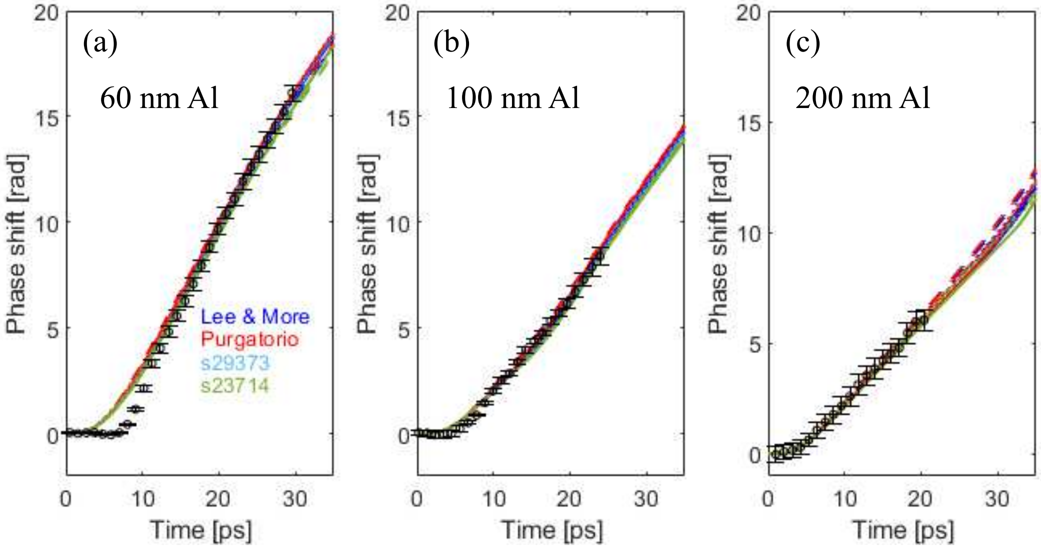

Figure 4.16: Comparison of the simulated 527 nm critical surface phase shift with FDI data. Color depicts the thermal conductivity model used and is shown in the legend.

First, we consider the phase-shift measurement. The phase shifts for all cases and target thicknesses are shown in fig. 4.16. As shown, phase shift is only weakly dependent on EOS and thermal conductivity model, with all models agreeing to better than 5%. Purgatorio is the highest-valued thermal conductivity model and has the highest phase shift, and s23714 has the lowest-valued thermal conductivity and phase shifts, but all are within the error bars. Nonetheless, it boosts confidence that the pressure and expansion predicted by the EOS options remain close enough that the phase shift differences are indistinguishable.

Figure 4.17 shows the reflectivity calculations for S polarization at 527 nm for all simulation cases. Each column represents simulations from an EOS and each row from a target thickness, as indicated by headers. For the 60 nm Al target, the LM, LMD, PG, and PG-TF models all match for the first 5 ps before deviating. No model matches for the entire time history of the measurement

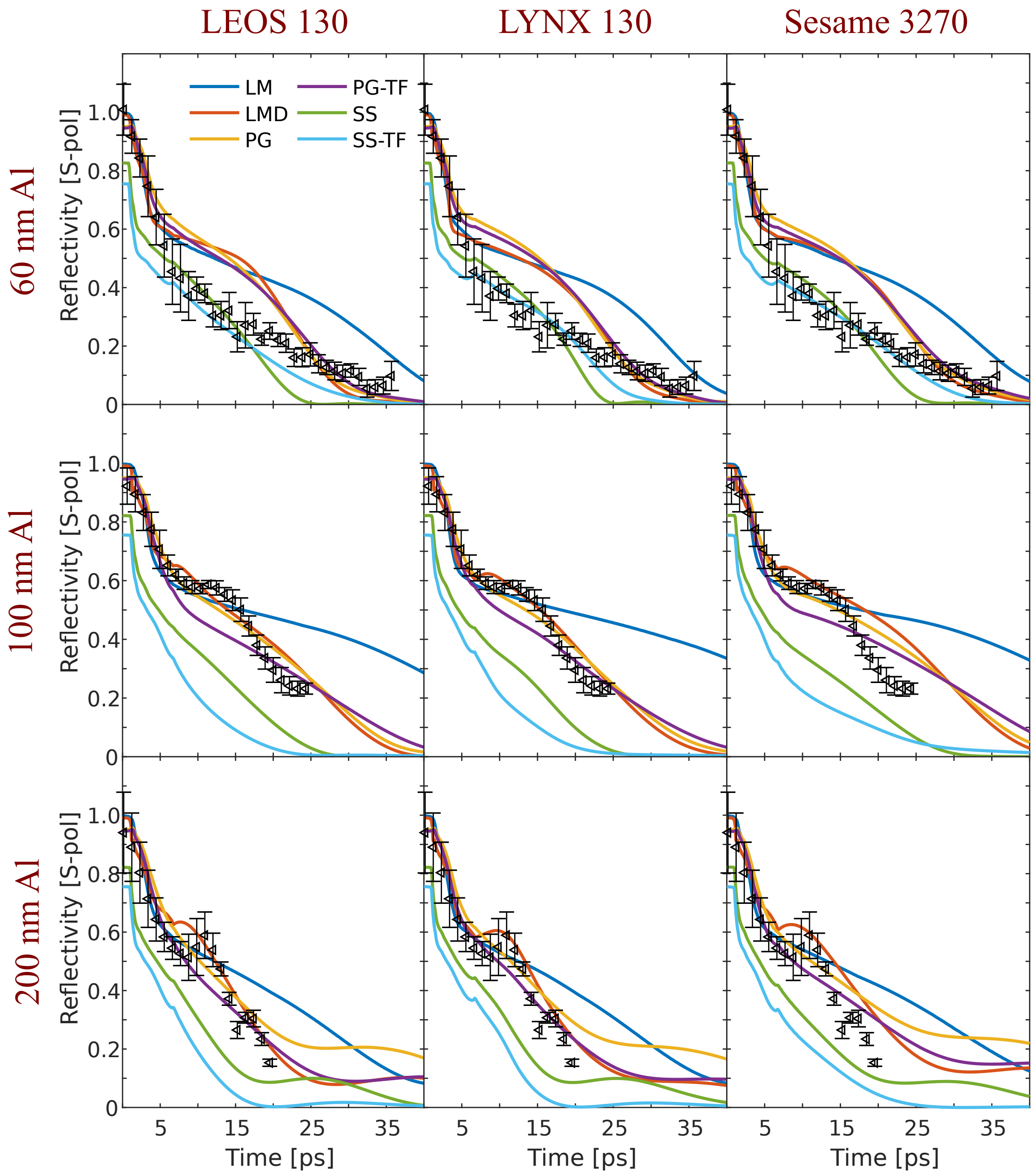

Figure 4.17: Reflectivity comparison for 100 nm Au and 60, 100, and 200 nm aluminum targets at 16 degrees from target normal for S polarization. Target thicknesses are the same across rows, and EOS model is the same down columns, as indicated by row/column headers. Different conductivity (thermal and electrical) models are indicated in the legend.

for any of the three EOS options. However, looking at both the 100 nm and 200 nm data, there is much better agreement. The reflectivity data exhibits an inflection starting at $t = 6$ ps, and a local maximum at $t \approx 12$ ps for both targets, with trends for the 200 nm data being more distinct. The only conductivity model that can replicate this feature is the Lee-More-Desjarlais (LMD) table, s29373. The Purgatorio table also closely matches the time history, though without the distinct reflectivity feature.

This feature is caused by the dynamics of the multi-layer target and corresponds to a minimum in the electron-ion collision frequency at the reflecting surface. Recalling that the reflectivity from the expanding profile approximately scales as exp(-$8\nu_{ei}^{*}L/3c$)[139], it follows that a smaller collision frequency leads to a higher reflectivity. The electron collision frequency in WDM, when $T < T_f$, is proportional to $\nu_e \propto \frac{e^2}{\hbar v_F}\frac{k_B T_i}{\hbar} \propto T_i/n^{1/3}$ due to electron-phonon scattering[7]. As the material heats, the ion temperature increases, causing the rapid rise in the collision frequency and the corresponding reflectivity drop seen at t = 0–5 ps. At $t \approx 5$ ps, the pressure and temperature reach their maxima, and the target begins to cool and decompress. The rarefaction wave passes the reflecting surface by t = 10 ps, leaving the density nearly constant for later times. Simultaneously, the temperature reaches a local minimum due to expansion cooling before thermal energy from the hot gold layer causes it to increase again. At this point, the material near the reflecting surface (1–2.5 eV and 0.2–0.7 g/cc) has been transitioning from a metal to an insulater as both thermal and pressure ionization decreases. It is precisely this regime that the LMD table was designed to improve accuracy in, so its greater agreement is unsurprising. The reflectivity then decays primarily based on the increasing plasma scale length. The collision frequency changes gradually, but hydrodynamic variables change much more slowly after the passage of the rarefaction wave.

Thus, the time-resolved reflectivity trace for double-layer targets is sensitive to the thermal conductivity, electrical conductivity, and the equation of state. Looking again at fig. 4.17, it can be seen that the Sesame 3720 EOS does not match the 100 or 200 nm reflectivities for any model between 10 and 25 ps, instead predicting a slower decay. LEOS 130 and Lynx 130 are very similar, though Lynx 130 with LMD conductivity matches the time history best near the reflectivity feature just discussed.

Finally, we look at the predicted temperature traces in fig. 4.18. In double-layer targets, we hope to see the thermal energy from the hot layer arriving at the rear surface. This energy will traverse the target at approximately the sound speed. The sound speed at solid density and 2–10 eV is 10–20 nm/ps (see fig. 4.13(d)). Thus, we would expect thermal energy from the hot layer to arrive as soon as 3/5/10 ps for 60/100/200 nm targets, respectively. Unfortunately, the time resolution of the optical streak camera—6 ps—precludes observation of a clear rise in the temperature. This is also complicated by the depth over which the SOP integrates signal around the critical surface and the extended duration of the proton beam. Nonetheless, a general trend is that the thicker targets require more time for the thermal energy to show up, and the width of the temperature peak between t = 5–40 ps increases with target thickness. A higher thermal conductivity transports energy more rapidly, reaching a higher temperature before the target expands. The ionization model complicates the observation. A lower degree of ionization will have a critical surface deeper within the target, which sees thermal energy earlier in time and also appears to our diagnostic as a higher temperature. This is seen in the 60 and 100 nm Al curves for the s23714 (SS) model, which has such a low ionization that the critical surface is actually within the gold layer for $t > 25$ ps. Purgatorio, also an AA calculation, exhibits a similar effect but to a lesser degree. These models are a poor match to the cooling history of the 60 and 100 nm data, and these ionization models are likely an underestimate.

All EOS models predict qualitatively-similar temperature evolutions for the same target thicknesses but with different temperature magnitudes. This is consistent with the phase measurement in fig. 4.16, and also with the general knowledge that the most uncertain EOS quantity is the temperature[228]. Sesame 3270 predicts temperatures above the maximum error bars in data for all target thicknesses. Considering this, along with the poor match to the reflectivity data, rules out Sesame 3270 as the best Al release EOS for conditions within these data. LEOS and Lynx are very similar, with the exception of Lynx predicting a higher peak temperature, and can not be distinguished by these data. However, the reflectivity data for Lynx matched marginally better, so

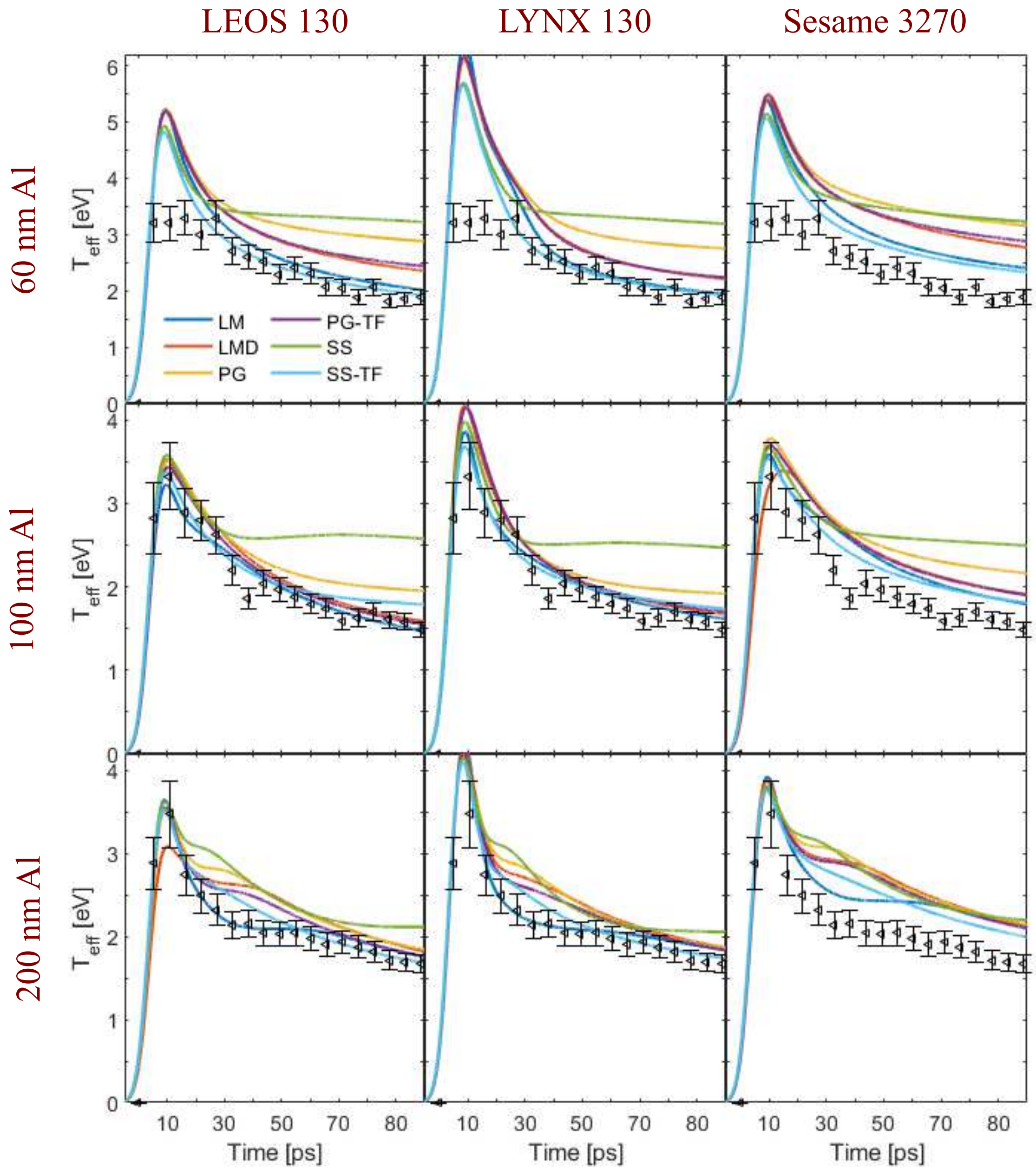

Figure 4.18: Observed SOP temperature comparison for 100 nm Au and 60, 100, and 200 nm aluminum targets. Target thicknesses are the same across rows, and EOS model is the same down columns, as indicated by row/column headers. Different conductivity (thermal and electrical) models are indicated in the legend.

it was chosen as the best EOS option.

Considering the conductivity models, only Sesame 23714 (Rinker's model) with TF ionization (SS-TF) and the Lee & More (LM) model are within error bars for all target thicknesses. Neither of these models match the reflectivity history, and thus no model matches all of the data as-is. The electrical conductivity and thermal conductivity generally rely on the same collision physics, and a correct model should match both. In this experiment, the electrical conductivity is crucial in interpretation of the optical diagnostics, while the thermal conductivity determines the evolution of the target itself. The reflectivity data is able to differentiate EOS and electrical conductivity models based on amplitude and time history. The SOP data is most sensitive to the thermal conductivity, but the 6 ps time resolution limits observation of the dynamical behavior of the thermal wave appearing. The amplitude of the rear surface temperature is still a measure of the thermal conductivity due to balance between conduction heating and expansion cooling. The LMD model (s29373) provides the best fit to all pieces of data, but the temperatures are too high, suggesting the thermal conductivity should decrease. I discuss this in the next section.

4.5 Discussion

The measurements presented in this chapter do not provide a single-state thermal conductivty measurement. By necessity, the design requires a thermal gradient, and the conductivity cannot be considered constant across the aluminum layer. The spatial profile of the electron temperature and mass density are shown at various times, starting right after peak temperature, in figure 4.19. To asses the plasma conditions in which the experiment takes place, we look at the density-temperature phase space of the simulations that match best—Lynx 130 for the EOS, and Sesame 29373 for the thermal/electrical conductivity. This is shown in fig. 4.20 for each target thickness. Conditions that exist during specific time slices are illustrated with different colors.

After heating, the targets reach 10–12 eV, with conditions being more dependent on the specific shot's proton spectrum than target thickness. Table 4.1 shows the aluminum layer mass-averaged

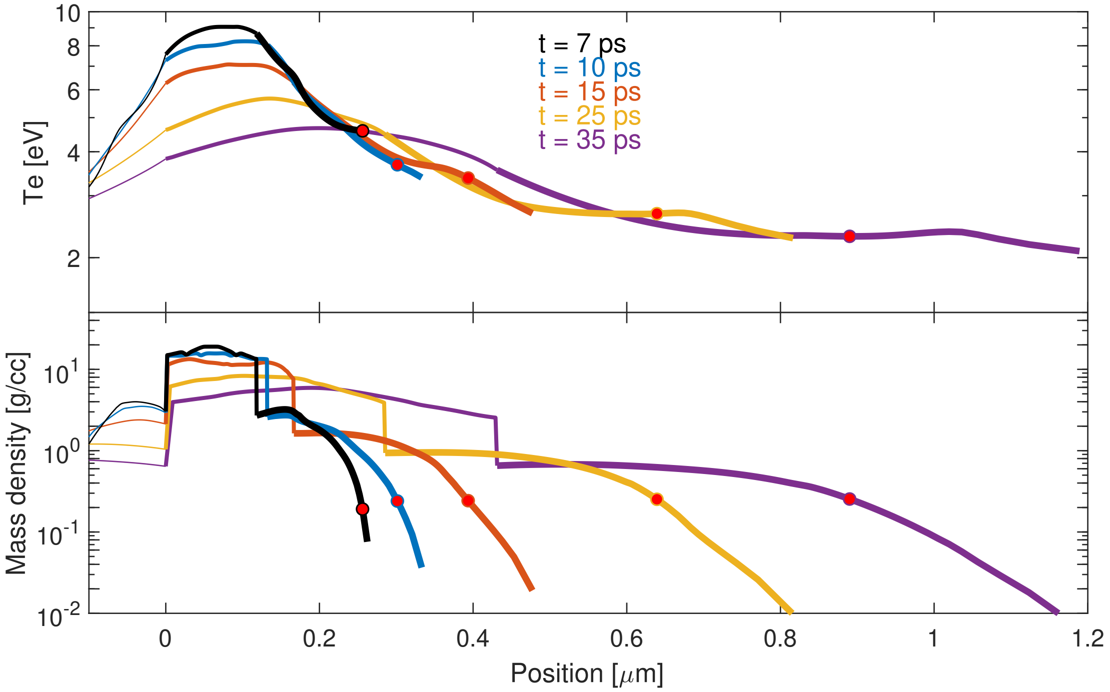

Figure 4.19: Spatial temperature (top) and density (bottom) profiles from a 100 nm Au + 100 nm Al simulation using Lynx 130 for the EOS and sesame 29373 for the thermal conductivity. The red dot indicates the position of the critical density surface for 400 nm light. The thickest portion of each line contains the aluminum zones, the intermediate thickness the gold, and the thinnest contains the Si_3N_4 zones. The profiles have been aligned to the Si_3N_4/Au interface for clarity.

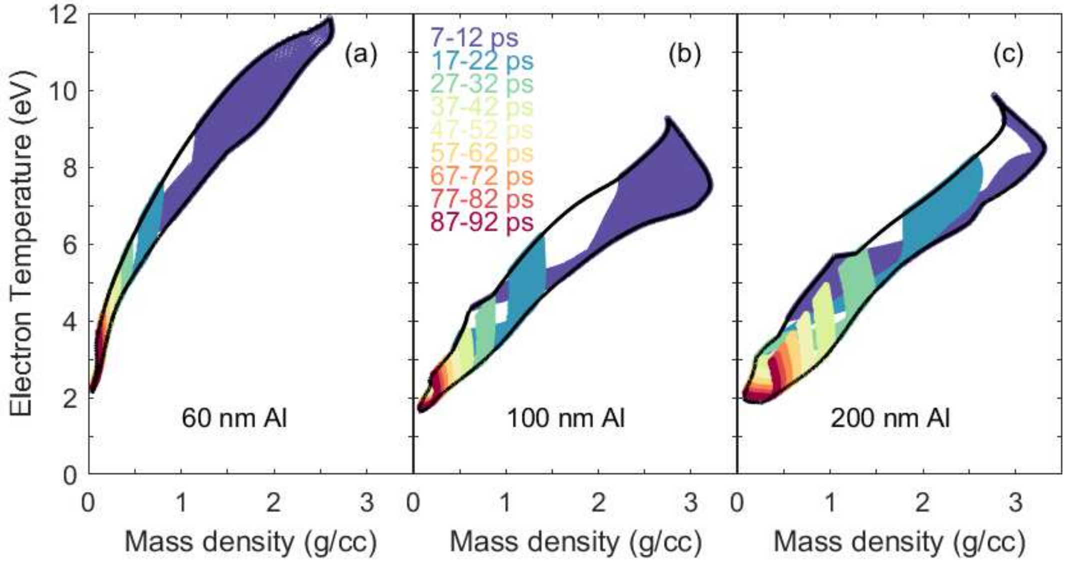

Figure 4.20: Density-temperature phase space occupied by the aluminum layer in the best-fit (Lynx 130/Sesame 29373) simulation. Colors represent the conditions occupied by the aluminum layer during the denoted time slice.

coupling parameters, Γ_{ii} & Γ_{ei}, and the electron-degeneracy parameter, Θ. The maximum value of the coupling parameter at the gold-aluminum interface is 20% higher than the listed values, while the degeneracy parameter, 35% lower. Thus, the experiment takes place in material that is moderately coupled and partially degenerate.

Table 4.1: Plasma-coupling and electron-degeneracy parameters for Al target layers

	60 nm Al			**100 nm Al**			**200 nm Al**		
Time [ps]	10	30	60	10	30	60	10	30	60
$\Gamma_{ii,avg}$	4.6	2.4	1.7	8.1	4.4	3.3	9.0	6.1	4.2
$\Gamma_{ie,avg}$	2.6	1.7	1.5	4.4	3.3	2.4	4.6	3.9	3.3
Θ_{avg}	1.7	3.3	4.4	0.9	1.4	1.9	0.8	1.1	1.4

Concerning potential causes of disagreement between the SOP data and simulations in fig. 4.18, as seen in fig. 4.21, I apply arbitrary multipliers of 4x and 0.25x to the Sesame 29373 thermal conductivity table—leaving the electrical conductivity unchanged—and plot the effective temperature and reflectivity. For the 100 nm aluminum target, this reduction in thermal conductivity bounds the error bars in the data, indicating a value between 0.25–1x of the tabulated model would fit the data. For the 200 nm data, the temporal shape of the simulation becomes a better fit at lower conductivity, but the data suggests an even lower value of the thermal conductivity. As the conductivity is decreased, sensitivity is lost due to the increasing relative contribution of hydrodynamic cooling. Nonetheless, the modeling and data clearly indicate a better fit with a lower conductivity value. The reflectivity calculation is insensitive to changes in the temperature of this scale.

The thermal conductivity could be lower than expected for several reasons. The inhibition of heat flow has been observed for cases with sharp temperature gradients[230, 231]. This occurs when the electron population responsible for carrying the bulk of the heat ($\approx 3.7 v_{th}$ for a Maxwellian[7]) has mean free paths, $\lambda_e = (\lambda_{ee}\lambda_{ei})^{1/2}$, larger than the temperature gradient scale length, $L_{th} = T_e/\nabla T_e$. In this situation, electrons deposit heat non-locally (i.e., not according to a random-walk diffusive pattern), and the depletion of electrons near the temperature gradient leads to dramatically-lower forward heat transport near the gradient itself. The ratio for the onset

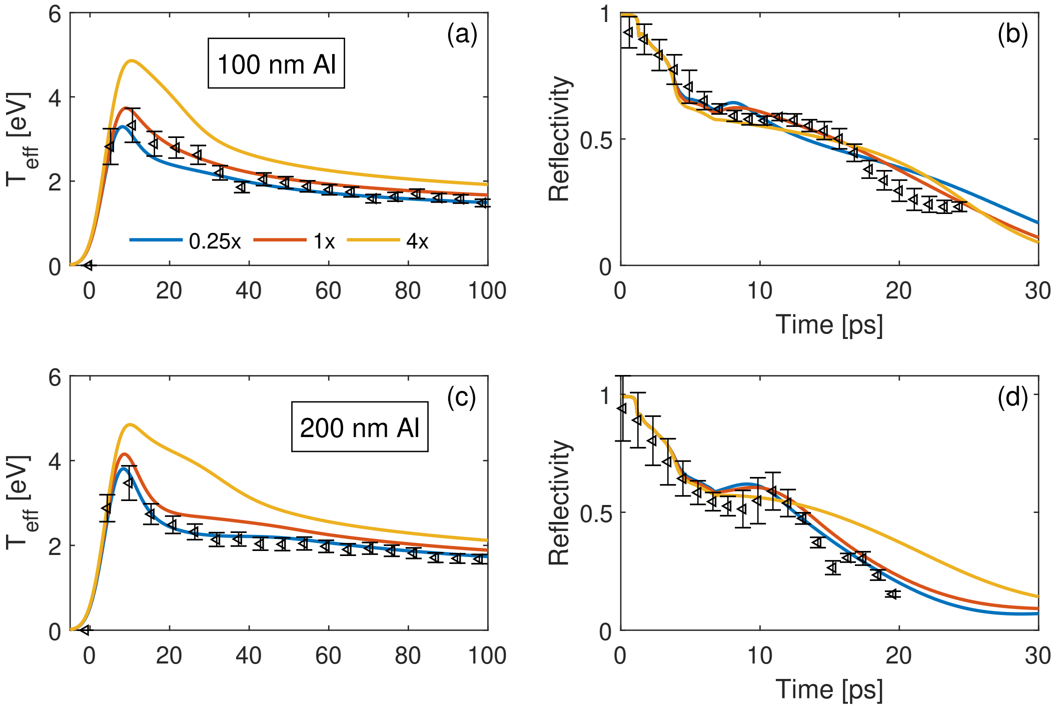

Figure 4.21: Simulation results showing the effect on T_{eff} (a)&(c) and reflectivity (b)&(d) when the LMD table (s29373) is used with fixed electrical conductivity and arbitrarily-scaled thermal conductivity.

of non-local transport has been reported for $L_{th}/\lambda_e > 50$[232]–500[233] with more recent works quoting 140[231].

According to the HYDRA simulations presented here, at $t = 7$ ps—right after the proton heating source turns off—$L_{th} = 180$ nm at the conduction interface, and $\lambda_e = 2.8$ nm. Here, the thermal velocity results from the maximum of the Fermi or thermal temperature, and the electron-collision time is taken from the predictions of Purgatorio. At this point, $L_{th}/\lambda_e = 64$, and if kinetic effects are present, they should be small. The situation may also be more favorable in degenerate matter where only electrons near the Fermi energy (chemical potential at finite T) may participate in conduction[67]. As the target decompresses, λ_e increases, but the fast time scale of conduction causes L_{th} to increase more rapidly. By $t = 20$ ps, $L_{th}/\lambda_e = 160$, and by $t = 50$ ps, $L_{th}/\lambda_e = 325$. Thus, I expect the experiment to be adequately described by diffusion-based heat transport, and heat transport could only account for thermal-conductivity reductions by several percent or less, and only at early times.

Another explanation could reside in consideration of electron-electron or electron-neutral collisions within the models. The LM model assumes a Lorentz plasma, which is increasingly inaccurate with decreasing atomic number due to the neglect of e-e collisions. The LMD and Purgatorio models attempt to include the effects of these collisions in somewhat ad hoc manners of unknown accuracy. For a fully-ionized aluminum plasma, the Spitzer result would indicate an electron-thermal conductivity that is only 79% of the Lorentz value[63] where the electical resistivity would only be reduced to 92%. Electron-electron collisions are not explicitly treated in relaxation-time approaches (such as in LM) or in Ziman theory, originally developed for strongly-degenerate liquid metals where degeneracy effects, such as Pauli blocking, limit changes to the electron distribution function due to collisions. Recent work by Reinholz *et al.*[234] and Desjarlais *et al.*[235] point out the importance of including electron-electron collisions even in so-called *ab initio* models such as DFT. Desjarlais posits that the exchange-correlation potential impacts both K_{th} and σ, reshaping the electron distribution in a mean sense, but that binary e-e scattering will only reduce K_{th} due to the inability of e-e scattering to change the charge current. The results of ref. [235] demonstrate that binary e-e scattering is not treated correctly in their QMD simulations, necessitating correction factors to match more-trusted kinetic QLB calculations. Effects like this may explain the data within this chapter, which appears to have the correct electrical conductivity but an incorrect thermal conductivity. The calculations in ref. [235] were done for hydrogen at 40 g/cc and 500–900 eV where the plasma is weakly coupled and partially degenerate (Γ_{ii} = 0.13–0.07, Θ = 1.65–2.97) because the QLB solution is trusted as a benchmark in the moderate-coupling regime. The authors reiterate that the magnitude of this effect in higher Z and more strongly-coupled plasmas is unknown and requires further investigation.

The data presented within this chapter are the first of their kind and provide a good first step toward the design of experimental measurements capable of benchmarking modern models. The experimental conditions created sit in a parameter space where the kinetic energy, Coulombic potential energy, and Fermi energy are all roughly equal with dimensionless parameters of approximately 1 (see Table 4.1), and no single theory dominates the dynamics of the system. The choice of aluminum is also sufficiently low-Z so that standard Lorentz models may not be applied without incurring error.

4.6 Conclusions

This chapter describes an experiment that uses a high-intensity short-pulse laser to generate a short-duration proton beam through the TNSA mechanism. The protons differentially heat multi-layer targets on an ultrafast time scale, inducing a thermal gradient at the interface. The rear surface of the target was observed with optical diagnostics to measure the time resolved temperature, phase shift, and reflectivity as the targets evolved over 100 ps. These data are compared against hydrodynamics modeling using the LLNL code HYDRA and a Helmholtz wave solver that self-consistently tests each conductivity model.

The best gold release EOS tested was found to be LEOS 790 based on the match to all available data. Simulations of the aluminum layers found that the release EOS could fit with both LEOS 130 and Lynx 130. The reflectivity measurements were able to constrain the best electrical conductivity model to be Sesame 29373, with Purgatorio's prediction also matching well. However, no thermal and electrical conductivity model was able to match both the rear surface temperature and the reflectivity, most likely indicating that the value of the thermal conductivities in the model is too high. This could possibly be explained through an incorrect treatment of electron-electron or electron-neutral collisions in the modeling. The data presented in this chapter are the first reported data with high sensitivity to both electrical and thermal conductivities and contribute toward the validation of transport models within the field of warm dense matter.

CHAPTER 5

Thermal conductivity studies of XFEL heated Iron

5.1 Introduction

In an effort to improve upon the experimental measurements in Chapter 4, we proposed a follow-up experiment using the XFEL at LCLS. The concept of differential heating remains the core operating principle. However, the XFEL provides an ultra-fast heating source that can be tailored to the material under consideration. This experiment provides the opportunity to better isolate the thermal wave driven between the hot and cold targets without involving the issues of an extended heating source dispersed in both time and energy, such as the protons.

Following the successful aluminum measurements, a more complex metal was chosen—iron. Iron is a suitable choice for study due to its relative importance in stellar opacities as well as geophysical applications like thermal transport within planets. Complexities arise in the theoretical description of iron because it is a transition metal with a partially filled d-shell. At solid density, these electrons are pressure-ionized and form a resonance in the density of states which can strongly impact the electron scattering cross-section.

In this chapter, I will discuss the experimental setup, analysis, and simulation of XFEL-heated iron foils as they pertain to EOS, electrical, and thermal conductivity models. Data will be compared with hydrodynamics simulations following the same procedure described in the previous chapter.

5.2 Experimental setup at LCLS

The experiment was performed at LCLS as part of beam time LJ91 at the Matter in Extreme Conditions (MEC) end station. This facility provided the ideal place to perform these differential heating transport studies due to the availability of both short-pulse optical lasers and the XFEL beam.

5.2.1 Differential heating of Au/Fe targets using x-rays

The differential heating concept applied in this experiment, as proposed by Ping *et al.*[60], uses the tunable nature of the XFEL and K-shell structure in the target to maximize the temperature gradient between the heater layer and the cold layer being studied. Figure 5.1 shows a plot of the attenuation lengths for gold and iron. This is the distance that it takes for the intensity of a beam of photons to be reduced to $1/e$ of its initial value, according to the Beer-Lambert Law. We see that if we choose a wavelength below the K-absorption edge, the difference in attenuation lengths is maximized, and we achieve the greatest difference in absorbed energy. For the gold/iron pair, 6.8 keV is an ideal XFEL pump energy.

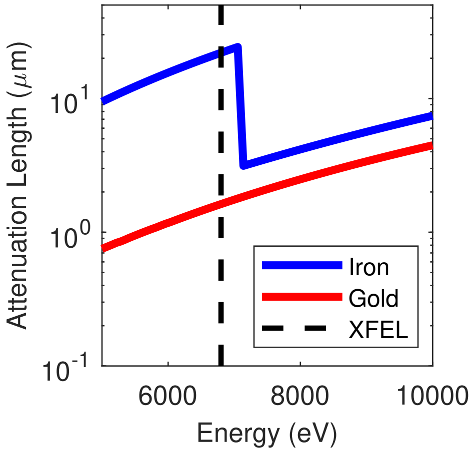

Figure 5.1: Attenuation lengths for iron and gold and the selected XFEL wavelength to maximize the absorbed energy difference. Values from the Center for X-Ray Optics (CXRO) (http://www.cxro.lbl.gov/).

A secondary benefit stems from the ultra-short pulse duration, 40 fs, of the XFEL. This enables heating on a time scale much shorter than the evolution of physical processes such as the thermal-wave propagation, hydrodynamic motion, or the measurement resolution of the streak cameras. This allows the experiment to come as close to an initial-value problem as possible; a temperature gradient is created, and then the system is observed as it evolves in LTE.

The creation of non-thermal electron populations from the recombining photoionized atoms poses the primary complication of this heating mechanism. These take the form of photoionized and auger electrons, discussed in Section 2.6.3, which have energies of several keV and will have mean free paths much longer than the characteristic thermal mean free path. The effect of these electrons on the spatial deposition of energy was investigated using Monte Carlo calculations performed by Stephen Hau-Riege at LLNL and is discussed in Section 5.5.3.

5.2.2 Diagnostic layout

This experiment utilized a diagnostic suite similar to the previous thermal conductivity experiment at Titan. Two SOPs were fielded—one using a Hamamatsu C7700 optical streak camera, and one Axis Photonique (Axis-PV) optical streak camera—along with the Livermore FDI and x-ray diodes provided by the MEC staff. Our original goal was to perform pyrometry measurements at both 450 and 800 nm, which would provide time-resolved temperatures at different physical surfaces within the target—corresponding approximately to the critical surface of each wavelength—as an additional constraint on the hydrodynamic modeling. The probe beam for the FDI could be delivered to the chamber either at its fundamental wavelength, 800 nm, or frequency-doubled to 400 nm so that reflectivity corrections would be available for both SOP wavelengths.

The experimental layout is shown in fig. 5.2. Each SOP was set at 27 degrees from target normal in the horizontal plane, and the FDI was set at 27 degrees from target normal in the vertical plane. Matching the angle of the FDI to the SOP ensures that the reflectivity, and inferred emissivity, can be applied without modification or calculation to the SOP directly.

The SOP bands were determined using band pass filters (BPF) from Edmunds Optics with

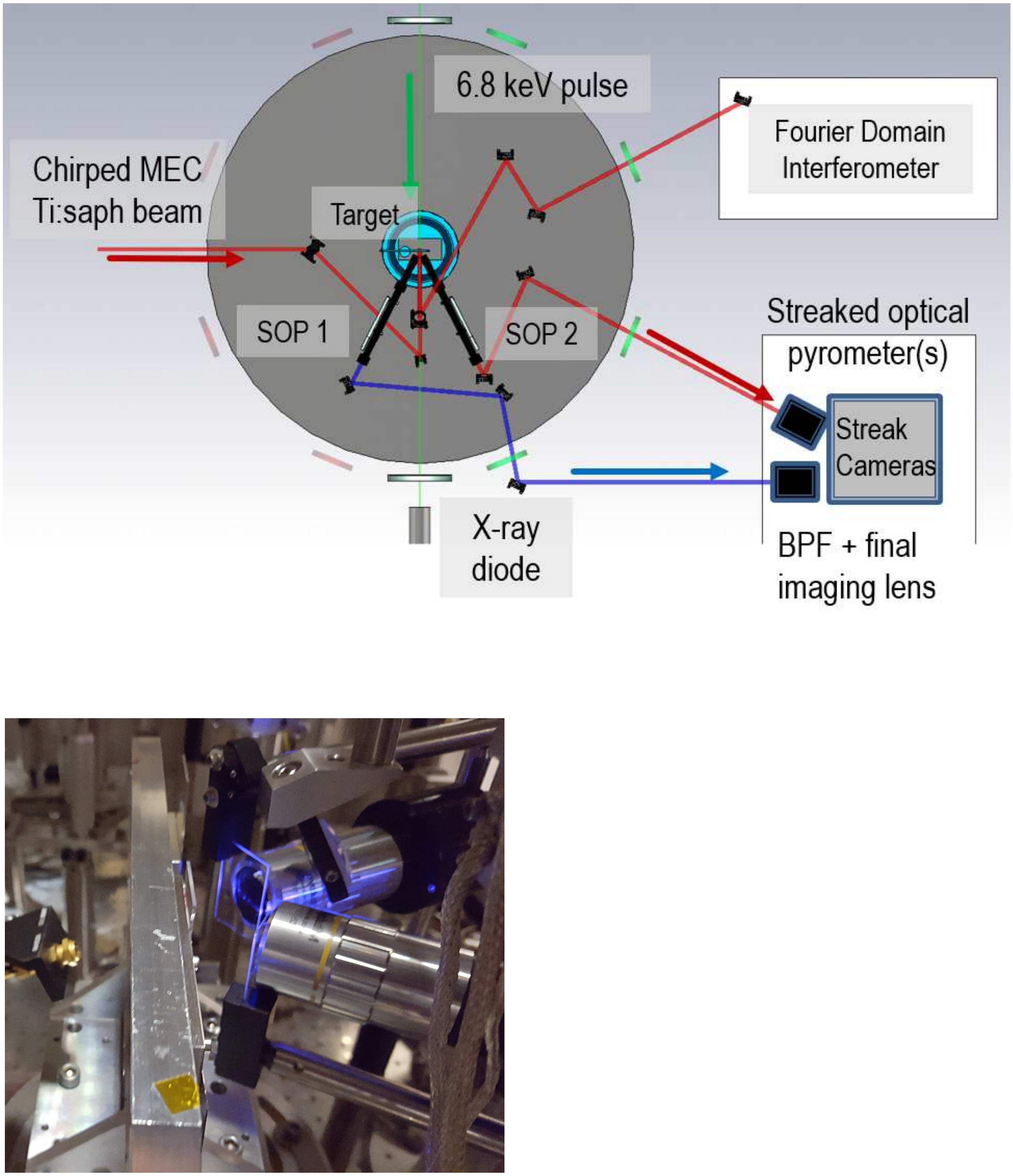

Figure 5.2: Experimental layout for thermal-conductivity measurements at LCLS MEC. Primary diagnostics include two streaked optical pyrometers and a Fourier domain interferometer.

50 nm bandwidth centered at 450 nm (P/N #84-782) and 800 nm (P/N #84-789). These filters have greater than 90% transmission within the bands and greater than four orders of magnitude of attenuation outside of them.

Our central concern when designing this experiment was the signal level. At MEC, the XFEL pulse in SASE mode arrives at the hutch with approximately 3 mJ of 6.8 keV energy. Roughly 20–50% of the energy is lost in the beryllium lens, resulting in 1.5–2.4 mJ of energy on target. According to CXRO, the attenuation length of these x-rays in gold is 1.62 μm, 16 times greater than our standard 100 nm thick Au heater layer, and $< 5\%$ of the pulse is absorbed. This creates an ideal situation with a very low longitudinal temperature gradient, but contributes to the lack of signal. Finally, the choice of focal spot size impacts the total signal. A small spot will reach a higher, more easily observed, temperature but emit from less area and suffer from large radial gradients. A large spot alleviates the gradient issue but may not reach a high enough temperature to be observed. We decided on a 10 μm spot, primarily because it was the largest defocused spot achievable with the available lenses before losing radial symmetry.

Thus, we emphasized high collection efficiency with the additional requirement of sub-10 μm spatial resolution. Fortunately, our collaborators from AWE provided the optical design of the Orion facility pyrometer[236], which was designed to satisfy these requirements. Both pyrometers used an f/1.4 Mitutoyo M Plan APO 10x objective as the collection optic with several trailing lenses—as outlined in ref. [236]—to correct collimation, and broadband dielectric mirrors (Thorlabs E02 coating) to transport the beam to the streak cameras. Figure 5.2 shows a photograph of the target frame with two SOP f/1.4 objectives and a f/2 lens for the FDI. Maintaining the simultaneous focus and pointing of three highly-sensitive optics throughout the course of the experiment proved to be a significant challenge.

5.3 Target design

The targets for this experiment had firm requirements for optical flatness, just like those fabricated for Titan. From a diagnostic standpoint, the FDI requires optical-quality surfaces in order to image the target surface in the probe beam. Additionally, interpretation of results is simplified by having very smooth interfaces which alleviate concerns such as spurious interface resistance due to surface roughness or seeding instabilities that could cause layer mixing once heated.

The high repetition rate of LCLS imposes the additional requirement of needing a large number of targets. We met this requirement by designing an array of 30 x 30 silicon nitride windows arranged within a 1.25 inch silicon wafer frame. Figure 5.3 shows a photograph of one of these frames. The Si_3N_4 layer was chosen to be as thin as possible while maintaining sufficient strength

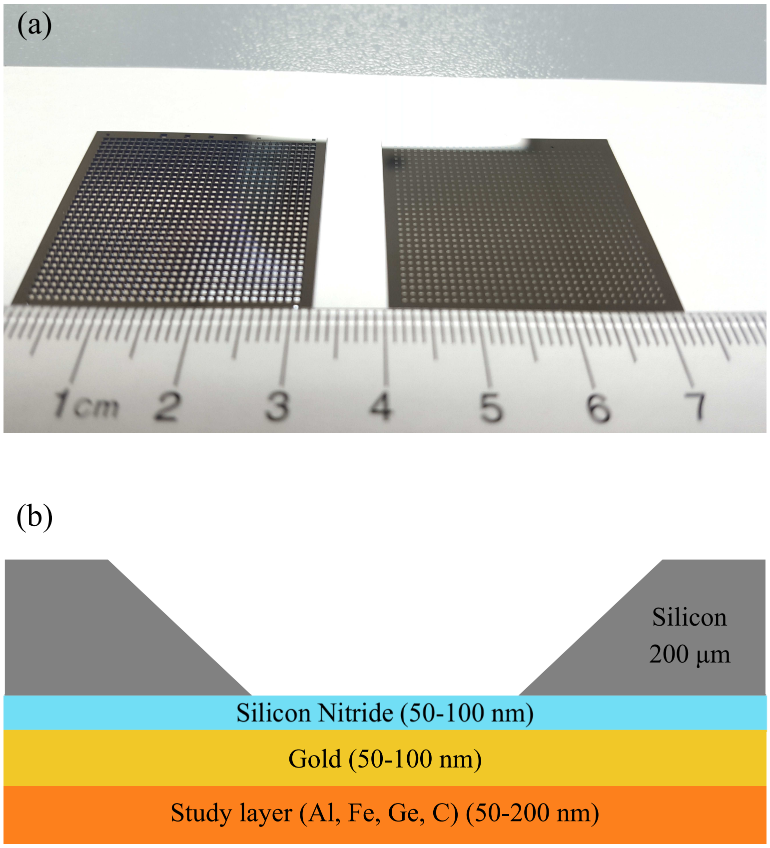

Figure 5.3: Target design for LCLS thermal conductivity experiments. The etched silicon wafers and silicon nitride membranes are visible in (a). Each array has 30 x 30, 400 nm square windows with a 40 nm thick membrane. A schematic of the metal layers that are EB-PVD coated onto the membrane is shown in (b).

to support metal coatings of several-hundred nanometers. Through trial and error, we found that 40 nm was sufficient. Materials of interest were coated using electron-beam physical vapor deposition (EB-PVD) at JLF's target fabrication facility. Layer thicknesses were measured with a calibrated profilometer on a witness slide and given as part of target fabrication. As a rule of thumb, our uncertainty in the resulting target thickness was less than 10%.

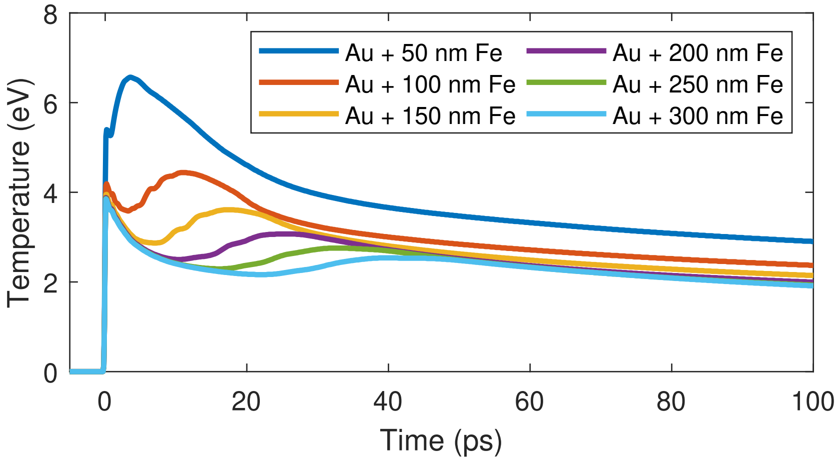

Figure 5.4: Simulations of the observed rear-surface temperature of multi-layer gold and iron targets with a 100 nm gold layer followed by increasing thicknesses of the iron layer.

The constraints placed on the targets from the perspective of a successful physics measurement are the same as for the Titan experiment in Chapter 4. The targets must be thick enough to slow the arrival of thermal energy so that the streak cameras may resolve it while remaining optically thick for the entire observation duration. However, targets must remain thin enough that the temperature signature created by conduction is sufficiently bright. Figure 5.4 shows HYDRA simulations that demonstrate the effect on SOP temperature as the iron layer thickness increases.

Table 5.1: List of Au/Fe targets resulting in data collection

Target	Materials	Thickness (nm)	Purpose
Single layer Au	Si_3N_4 + Au	40 + 100	Heater layer source & Au EOS
Single layer Fe	Si_3N_4 + Fe	40 + 47	Cold material T & Fe EOS
Double layer Fe	Si_3N_4 + Au + Fe	40 + 100 + 53	Thermal conductivity
Double layer Fe	Si_3N_4 + Au + Fe	40 + 100 + 108	Thermal conductivity

An integrated experiment such as this requires data to provide as many constraints as possible.

Thus, the experiment is designed around a set of targets, each with specific purposes. I list the targets for which we collected data in table 5.1 along with their intended purpose. In the rest of this chapter, targets will occasionally be referred to as single- or double-layer targets—in reality, this refers to Si_3N_4 + Au/Fe and Si_3N_4 + Au + Fe respectively, with the nitride layer often not mentioned for brevity. Single-layer targets are intended to constrain the individual material EOS and verify that the heating source accurately reproduces temperature profiles. Double-layer targets are then intended to study the heat conduction between layers.

5.4 Results

5.4.1 FDI Results

We fielded the FDI for all data shots, but upon analysis, determined that the spatial resolution of the imaging system was insufficient to resolve the 10 μm heated region. This resulted in the inability to extract a phase shift from all data. However, one shot on a 50 nm Au target had a sufficiently large heated spot to obtain a time-resolved reflectivity ratio. This shot was analyzed by Yuan Ping, and presented in figure 5.5.

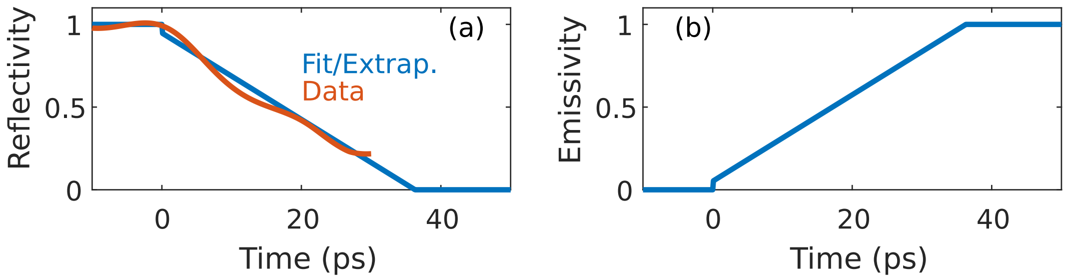

Figure 5.5: Reflectivity ratio from FDI data on a 50 nm Au target. Figure (a) shows the reflectivity ratio with a linear fit and extrapolation, and (b) the inferred emissivity using Kirchoff's Law.

This reflectivity ratio was used for the emissivity corrections for gold and for the final SOP data presented in fig. 5.9. Each material used this ratio normalized by the appropriate cold reflectivity shown below in fig. 5.6. The data is extrapolated below $R \approx 0.2$ with a linear fit to provide a continuous function for the pyrometer correction. This inherently makes the assumption that the transmission through the target remains zero, neglects scattering, and requires the absorption approaches 1.

Using the gold reflectivity for iron shots is an approximation made by necessity rather than choice. The reflectivity contains information about the electron-ion collision frequency through the complex dielectric function by way of the electrical conductivity. This is almost certainly different between gold and iron. However, in the absence of data, applying a general emissivity correction will result in a ‘true’ temperature closer to reality than simply a brightness correction. It is likely that this will only give approximate temperature amplitudes. The dynamics that arise in double-layer targets will be lost.

5.4.1.1 Cold reflectivity measurements

The FDI provides a time-resolved reflectivity ratio. This ratio is relative to the unheated portion of the target. In order to get the absolute reflectivity values, I performed a set of measurements for the full list of targets using 450 and 405 nm CW lasers (Thorlabs CPS405 and CPS450 laser diode modules). Figure 5.6 shows the results for the targets used in this experiment.

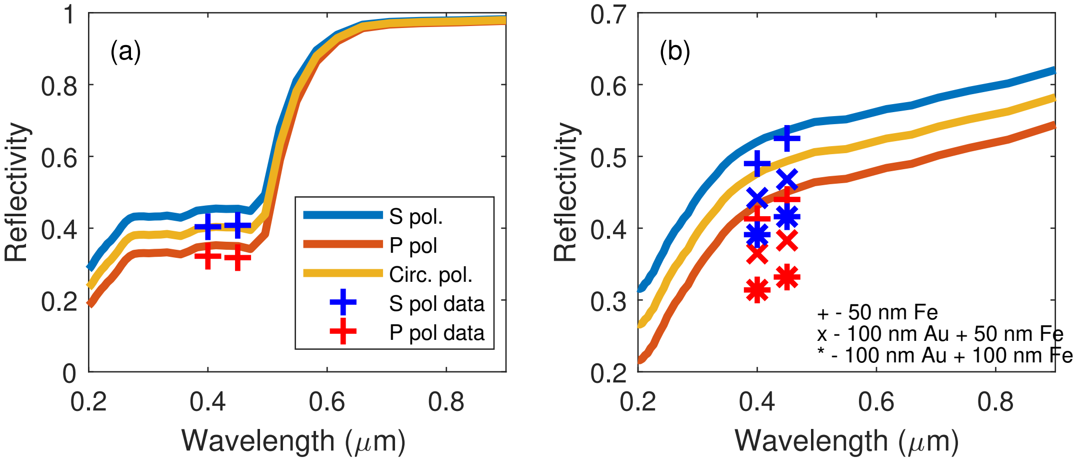

Figure 5.6: Theoretical Fresnel reflectivity for (a) bulk gold and (b) bulk iron. Reflectivity measurements of the experimental targets at 405 and 450 nm are overlaid with S polarization in blue and P in red. Indices of refraction accessed from https://refractiveindex.info[219], with gold data from [237] and iron data from [238].

5.4.2 Pyrometry results

Two streaked optical pyrometers were initially fielded. Figure 5.7 shows raw data for the brightest targets—100 nm Au—from both the AXIS and the Hamamatsu SOPs filtered to view 425–475 nm. The signal strength in the 800 nm band of emission was not large enough to observe. This was due to 7–9x weaker black-body emission at 800 nm rather than 450 nm. This was further exacerbated by the drop in the S20 photocathode response (see fig. 3.2). In figure 5.7, the AXIS (left) has better signal-to-noise than the Hamamatsu (right). This primarily resulted from less magnification in the optics (12.95 for the AXIS and 49 for the Hamamatsu), but the slit electrode in the AXIS also collects more signal than the fixed-slit design of the Hamamatsu. Time constraints during the beam time prevented modification of the optical system once data collection began, and the Hamamatsu SOP signal was not strong enough to collect a complete data set. The results in this section will focus on the data collected with the AXIS SOP at 450 nm.

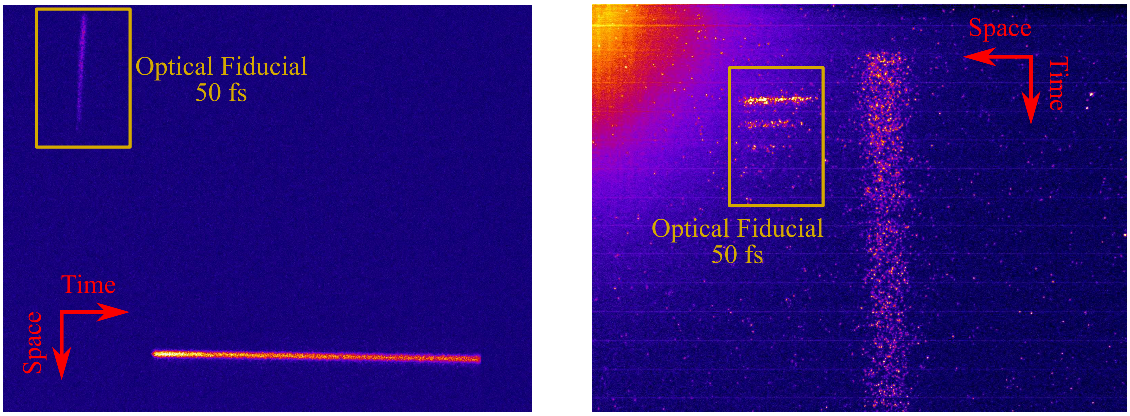

Figure 5.7: Streaked optical pyrometry raw data for 100 nm gold targets. The image on the left comes from the AXIS SOP at 450 nm with a 1 ns sweep window, while the image on the right comes from the Hamamatsu SOP also at 450 nm with a 500 ps sweep window. The gold-only target is the hottest and therefore brightest target. As such, these data represent the highest single-shot, signal-to-noise data collected.

5.4.2.1 Shot averaging

Data quality was improved by the high repetition rate available at LCLS. Pyrometer data were collected and averaged from each target type. An optical fiducial, pictured in figure 5.7, was set up to allow automated alignment of each data shot. However, jitter between the optical fiducial and XFEL arrival led to approximately 5 ps of scatter in the rising edges of individual shots. Simultaneously, the f/1.4 collection objectives were extremely sensitive, and shot-to-shot alignment caused small spatial walks. To minimize spatial and temporal blurring resulting from averaging, each image was manually aligned in both dimensions. The averaged, streaked images are shown in figure 5.8 along with the total counts within the spot.

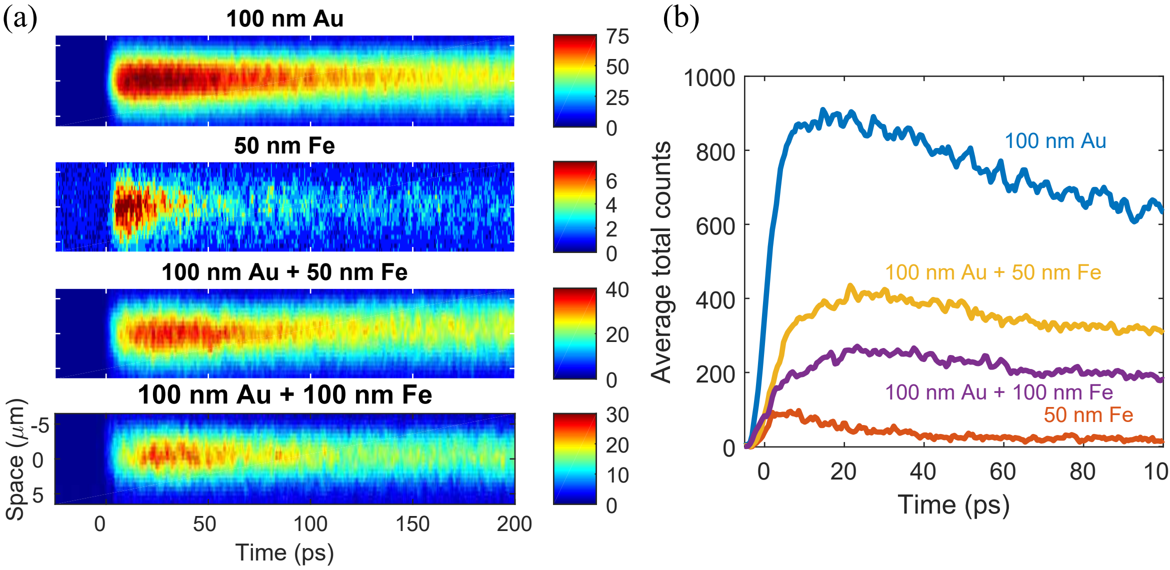

Figure 5.8: Averaged pyrometry data for the iron data set. Figure (a) shows the temporally- and spatially-aligned and averaged heated regions against time in counts above background, and (b) shows spot-summed counts.

The statistical information for each target type is listed in table 5.2. The average energy was recorded with an x-ray diode prior to entering the MEC chamber. The standard deviation in the pulse energy was $<$ 10% for each case. Approximately 20 individual shots were averaged for each data set. The total quantity of data that could be collected was limited by the time it took to align each shot individually, but this still resulted in significant improvement over single-shot data.

Table 5.2: Statistical information for each data set

-	100 nm Au	50 nm Fe	Au + 50 nm Fe	Au + 100 nm Fe
# of shots	21	13	18	19
FWHM (μm)	7.7	6.8	7.6	6.8
E$_{avg}$ (mJ)	3.117	2.878	2.977	3.009
σ_{stdev} (mJ)	0.159	0.337	0.275	0.174

5.4.2.2 Rear-surface temperatures

The rear-surface temperatures are calculated from spot-summed counts using the measured reflectivity and optical constants listed in table 5.3, according to eq. (3.9). The system transmission is assumed spectrally flat, based on the use of broadband dielectric mirrors (Thorlabs E02 coating). Only the bandpass filter and streak camera response are considered inside of the spectral integral of eq. (3.9). The frequency response of the streak camera calibration is shown in fig. A.3. The spatial, temporal, and energy calibrations necessary for calculating temperature are described in Appendix A.

Table 5.3: Experimental parameters of the AXIS SOP

Parameter	Value
Working distance	33.5 mm
Front aperture diameter	24 mm
Total magnification	21.5
Electrical magnification	1.66
Total transmission	0.35
BPF center	450 nm
BPF bandwidth	50 nm
t$_{dwell}$/pixel	0.507 ps

The emitting spot size area requires careful calculation; the optical and electrical magnification must be separated, as typically the entire heated spot will not make it past the 100 μm entrance slit of the streak camera. The emitting area assumed to bypass the entrance slit is an important lever on the temperature calculation. The SOP provides a time-resolved spot-size measurement, but it was found that this size decreased in time. This most likely occurred as the signal fell beneath the detection threshold of the streak camera rather than a true shrinking of the spot (caused by cooling). For this reason, the time-integrated spot sizes listed in table 5.2 were used to calculate the emitting area. These spots are smaller than the nominal x-ray spot of 9 μm, showcasing the general trend of enlarging for more intense emitters.

The calculated temperatures for the complete data set are shown in figure 5.9. The left pane shows the brightness temperatures while the right pane shows the emissivity-corrected temperature. The data demonstrate expected trends. The gold is the hottest, with a peak temperature of 8 eV, and iron the coldest with a peak temperature of 2 eV. For the double layers, the Au + 50 nm Fe target is hotter than the Au + 100 nm Fe target and peaks earlier in time. Both double-layer targets also exhibit a slower cooling rate due to the thermal source behind them, as designed.

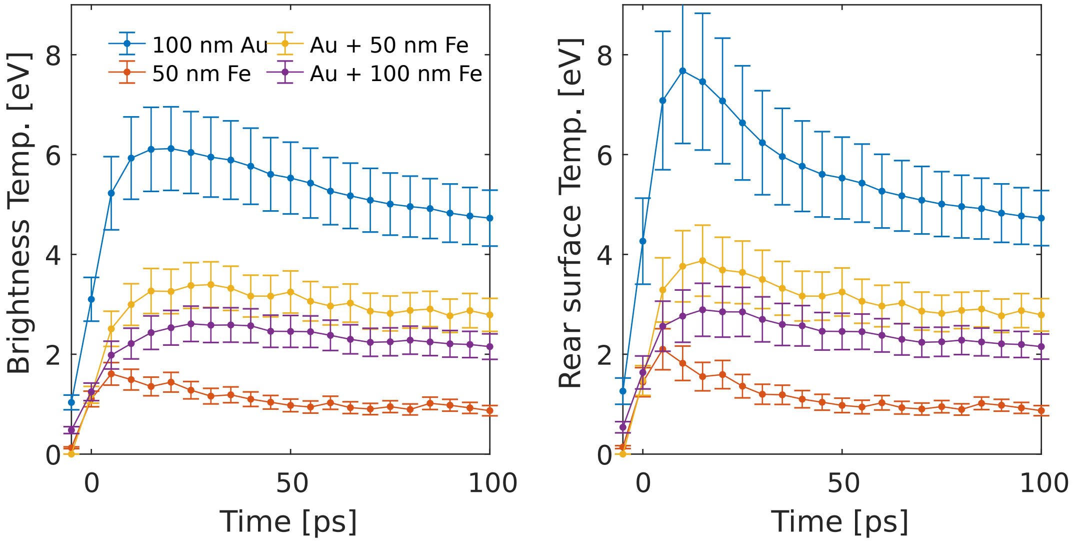

Figure 5.9: Brightness temperature (left) of the rear surface for 100 nm Au, 50 nm Fe, Au + 50 nm Fe, and Au + 100 nm Fe targets. The emissivity-corrected temperature is shown on the right using the linear fit in figure 5.5.

The data are plotted along with their systematic error bars of ±20%. The systematic error is dominated by the streak camera calibration[198] and the error in the emitting hot-spot area, both approximately 20%. Both of these errors stem from the design of the AXIS streak camera, which uses an accelerating slit extraction electrode. This style of electrode improves the spatial resolution and sensitivity, but leads to uncertainty in how much area of cathode passes the internal aperture. Error in the area and calibration will not change as a function of plasma conditions or time, and thus this stated systematic error will only shift inferred temperatures up or down within the range. The random error bars due to noise and the shot averaging are smaller at approximately $\pm 12\%$ for the dimmest 50 nm Fe targets and $\pm 8\%$ for the brightest Au targets.

5.5 Hydrodynamic modeling

Like the previous chapter, hydrodynamics simulations were used to model the target evolutions. HYDRA[221] was again used in 1-D Cartesian geometry. The heated region was 10 μm in diameter and 0.2 μm thick, justifying the use of 1-D simulations.

The 1-D model tracks separate electron and ion temperatures (1D2T) which are equilibrated according to a relaxation rate calculated with the collision frequencies from Lee & More[13]. Radiation is handled using an Implicit Monte Carlo (IMC) multi-group calculation, which uses effective photon transport cross-sections to probabilistically model radiation transport[224]. This package handles x-ray absorption but does not include the non-local electron dynamics known to occur as the photo-ionized material relaxes. Any in-line calculations requiring an average ionization (such as Lee & More thermal conductivity) use a Thomas-Fermi model.

The modeling effort is designed to match the entire data set. Single-layer targets—which are not sensitive to thermal conductivity—intend to constrain the energy deposition (the only free parameter) and EOS model. Then the double-layer targets, which *are* sensitive to thermal conductivity, provide the desired benchmark for conductivity models. Calculations are performed to test the sensitivity to other modeling variables such as gold or silicon nitride thermal conductivity values, layer thicknesses, or the electron-ion equilibration rate. I discuss these results in Appendix B. Fortunately, the experimental observables are more sensitive to models for the iron layer than to uncertainties in the gold and silicon nitride layers.

5.5.1 Tabular EOS models

Three EOS models were available to test—LEOS 260, Lynx 260, and Sesame 2140. Both LEOS and Lynx were constructed in the improved QEOS framework[98, 99] with Lynx using Purgatorio to generate the electron-thermal contribution to the internal energy and pressure. Sesame 2140 is an older iron model that uses Thomas-Fermi-Dirac theory for the electron-thermal component and the a Cowan model for the thermal-nuclear part[101]. The differences in EOS models for iron are very similar to the differences in aluminum options shown in Chapter 4. Similar expansion velocities are expected, with the greatest uncertainty expected in the specific heat and final temperatures.

5.5.2 Tabular electrical & thermal conductivity models

Four conductivity models were available to test—(1) Lee & More, (2) Purgatorio, (3) Sesame 22144 (Rinker's average atom model[79]), and (4) Sesame 29273 (Desjarlais' LMD model for stainless steel[239]). No LMD model was available for pure iron, but s2927 is 70% iron, 20% chromium, and 10% nickel. All of the metals are transition metals, and the composition leads to an effective Z of 25.8, very close to iron. This is based on the Lee-More-Desjarlais framework[82] but tuned with QMD/Kubo-Greenwood electrical-conductivity calculations. Of these models, only Lee & More does not include electron-shell effects that may be important in transition metals. However, the increased atomic number of iron may also make the application of Lee & More—which assumes a Lorentz model—more accurate.

Figure 5.10 shows the tabulated thermal and electrical conductivities for these models at T_e = 1–12 eV. The thermal conductivities are all within a factor of 2 at 10 eV and 7.87 g/cc. The differences rise to greater than a factor of 5 at 2 eV and 0.5 g/cc. The application of Lee & More predicts dramatically-higher DC electrical conductivities, which will lead to smaller collision frequencies and a higher reflectivity as the target cools. The optical diagnostics will mostly probe lower densities and temperatures. At 0.5 g/cc, the electrical conductivity models will predict very similar optical responses for the diagnostics at 5 eV, but rapidly diverge at colder temperatures.

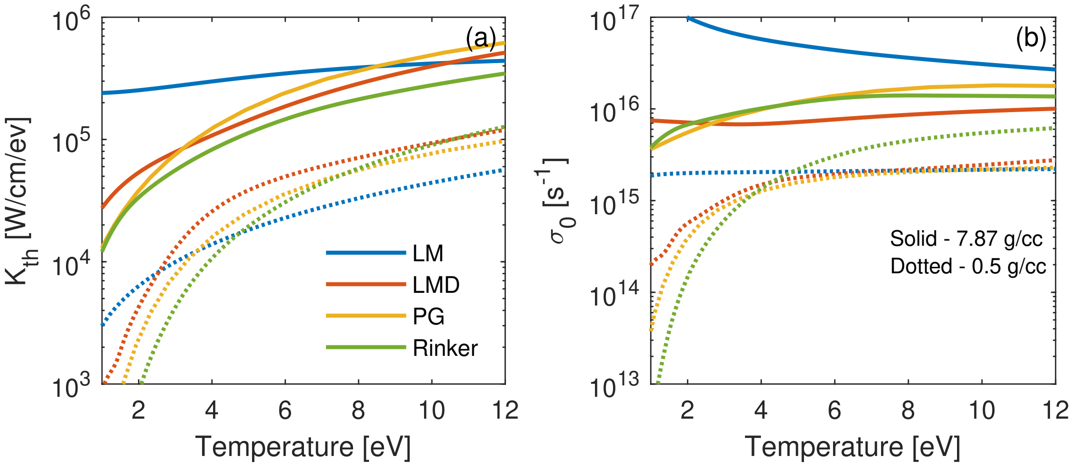

Figure 5.10: Thermal (a) and electrical (b) conductivity models for iron. LM is the widely used Lee & More model, LMD is the Sesame 29273 table for stainless steel, PG is the Purgatorio calculation, and Rinker is the Sesame 22144 table.

5.5.3 Non-local energy deposition using Monte Carlo

A question of import to the experimental design using XFELs is how well the x-ray differential heating establishes a sharp temperature gradient. How impactful are the non-local Auger and photoionized electrons? How much do they blur the gradient?

Monte Carlo (MC) calculations performed by Dr. Stefan Hau-Riege (LLNL) addressed this issue. His method is described for similar circumstances in ref. [240]. The target stack is modeled in a 2-D, radially-symmetric geometry with 2 mJ of 6.8 keV x-rays focused into a 10 μm Gaussian spot with a 40 fs pulse duration. As the pulse propagates through the material, the x-ray photoabsorption is calculated according to the shell-dependent photoionization cross-section. When photoionization occurs, a photo electron and Auger electron may be created at that spatial location. These are also propagated using a Monte Carlo algorithm, and their slowing down and energy deposition are tracked within the material. Subsequent radiation or electron production is not considered. The material is assumed to remain cold, and charging of layers due to ballistic electron transport is not considered.

Figure 5.11 shows the calculated dose for three targets—(1) 40 nm silicon nitride + 100 nm gold (2) 40 nm silicon nitride + 47 nm iron and (3) 40 nm silicon nitride + 100 nm gold/53 nm iron.

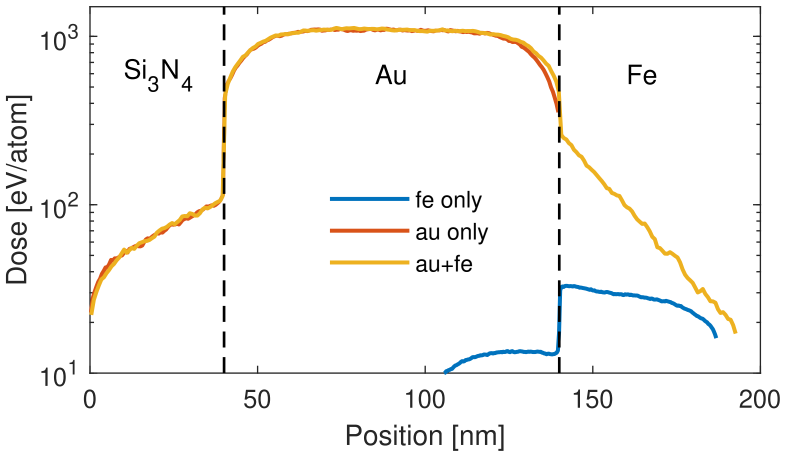

Figure 5.11: Monte Carlo simulation results of dose deposited into 40 nm Si_3N_4 + 100 nm Au, 40 nm Si_3N_4 + 53 nm Fe, and 40 nm Si_3N_4 + 47 nm Fe targets by a 6.8 keV XFEL beam. Dose is averaged over the center 1 μm of heated spot. Calculation by S. Hau-Riege (LLNL).

Case (2) represents the energy deposition by the XFEL in iron only (with only slight modification by the silicon nitride), while case (3) includes contributions from the gold layer. It is clear that the ballistic electrons from the gold layer (KE $\approx$ 2–4 keV) do smear the temperature gradient. The electrons contribute additional dose across most of the 50 nm target thickness. The total dose within the iron layer next to gold is 3.7-times higher than for the isolated iron layer. However, the total dose in the gold layer is 21-times higher than the dose in the case (3) iron layer, and 76-times higher than in the case (2) iron layer.

To assess the impact of non-local dose on the observed temperature, the MC calculations were implemented in HYDRA as a spatially-dependent electron internal energy source. This used the temperature-dependent heat capacity to convert dose to temperature. The dose was deposited over 1 ps, though the results are insensitive to the rate of energy deposition over such a short time scale. A multiplier on the entire dose was used to match the single-layer SOP data. The iron calculation matched with a multiplier of 0.92, but the gold required a multiplier of 0.28. This indicates that additional energy loss mechanisms exist in the gold, or that intensity effects of the XFEL pulse are modifying the ionization dynamics, resulting in less deposited energy.

The most important question is how these non-local electrons impact the interpretation of the thermal conduction results. As a worst-case scenario, the dose in the gold-layer was multiplied by 0.28 while the iron dose shown in case (3) in figure 5.11 was left unmodified for a set of double-layer simulations. This resulted in a 0.5 eV temperature increase, for all times, at the rear surface for the Au + 50 nm Fe case and a 0.1 eV shift in the Au + 100 nm Fe case. No modification to the temporal evolution occurred because of the rapid time scales of conduction across such thin layers and the limited 5 ps temporal resolution of the optical streak camera. The blurred thermal gradient simply manifests itself as extra energy deposited within the iron at $t = 0$.

These shifts are a worst-case scenario, and the effect is likely much smaller than these stated values. A nearly 4-fold reduction in the deposition in the gold would also significantly reduce the ballistic electron transport into the iron. The remainder of the calculations in this chapter do not use the MC source due to the discrepancy between the correct gold and iron deposition rates, but the above discussion may be informative to final conclusions.

5.5.4 Single-layer targets

The modeling begins with a simplified system—single-layer targets. The single-layer gold and iron targets were modeled to ensure that the source deposition and equation of state chosen were correct.

5.5.4.1 Single-layer gold

Figure 5.12 compares SOP data with the rear-surface temperature for the 100 nm gold target for both LEOS 790 and Sesame 2700 EOS options. The rear-surface temperatures from HYDRA were calculated using the Helmholtz solver and methodology outlined in Chapter 4. For gold, only the in-line Lee & More thermal conductivity was available. However, electrical conductivity from Purgatorio was also used to process the rear-surface temperatures. Single-layer targets are insensitive to thermal conductivity, and thus differing electrical-conductivity models simply provide an estimate on the variance of the observation.

It is clear that LEOS 790 provides much better agreement with data than Sesame 2700, reaf-

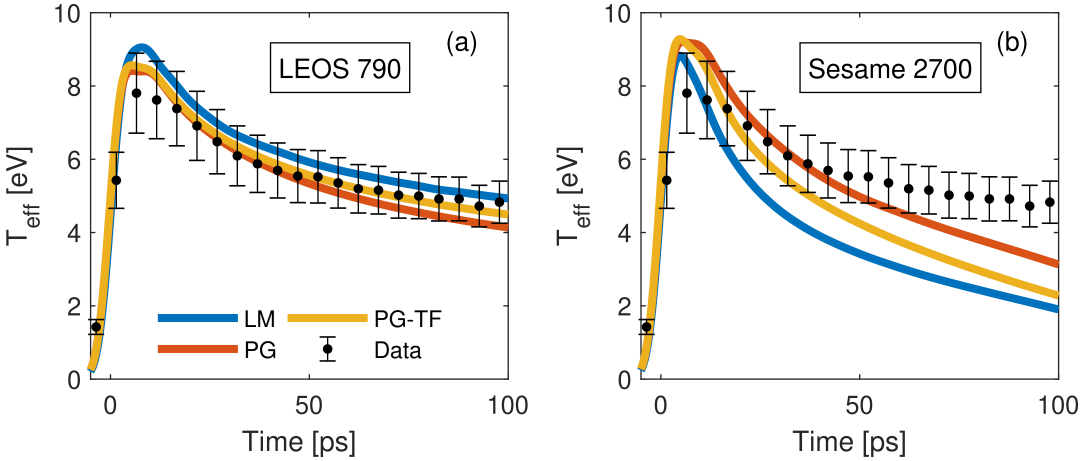

Figure 5.12: Comparison of the rear surface temperature for 100 nm Au targets with (a) LEOS 790 and (b) Sesame 2700. Lee & More, Purgatorio, and Purgatorio-TF electrical conductivities were used to calculate T_{eff}.

firming Chapter 4's conclusion that the best gold release EOS near these conditions is LEOS. Predictions from LM and PG models are similar, with PG displaying a slightly faster cooling rate. This is partially due to the ionization model and partially due to the conductivity value itself, as shown by the PG-TF prediction between LM and PG.

Here, the error bars represent the random error caused by uncertainty in the FDI emissivity correction, statistical averaging of shots, and readout noise. These are approximately 15% at peak temperature, and 5% by 100 ps. This provides a measure of the uncertainty in the shape of the temporal evolution. However, it is important to remember that the systematic error in the streak camera calibration could shift the entire temperature curve up or down by ±20%. The reflectivity and phase measurements show similar trends to the comparison shown for the proton-heated data, with LEOS predicting a larger phase shift than s2700. It is interesting to note that the early-time discrepancy shown in the proton data (fig. 4.15) is not repeated here. Perhaps this is because the probe used for the reflectivity correction is now 400 nm rather than 527 nm. It could also be attributed to different equilibration rates for protons and x-rays[229].

Unfortunately, a precise measurement of the absorbed x-ray dose was unattainable using equipment available at the time of the experiment. Even with a precise measurement, more sophisticated modeling would have been required to properly treat the dynamics of XFEL energy deposition. Instead, the choice was made to scale the energy in the gold simulations until data reached agreement, fixing the source at that value for all subsequent calculations. There was $< 10\%$ difference in the mean pulse energy for each data set (see table 5.2). To keep the source consistent across data sets, it was multiplied by the ratio of the measured average pulse energy to the average pulse energy of gold—i.e., $S_{fixed} * (E_{avg,Fe}/E_{avg,Au})$.

5.5.4.2 Single-layer iron

The 50 nm iron temperature data is compared with models in figure 5.13. Lynx 260 and the LM electrical conductivity provide the best match, closely followed by Purgatorio with a TF ionization. These models work best because they predict the highest collisionality for the plasma.

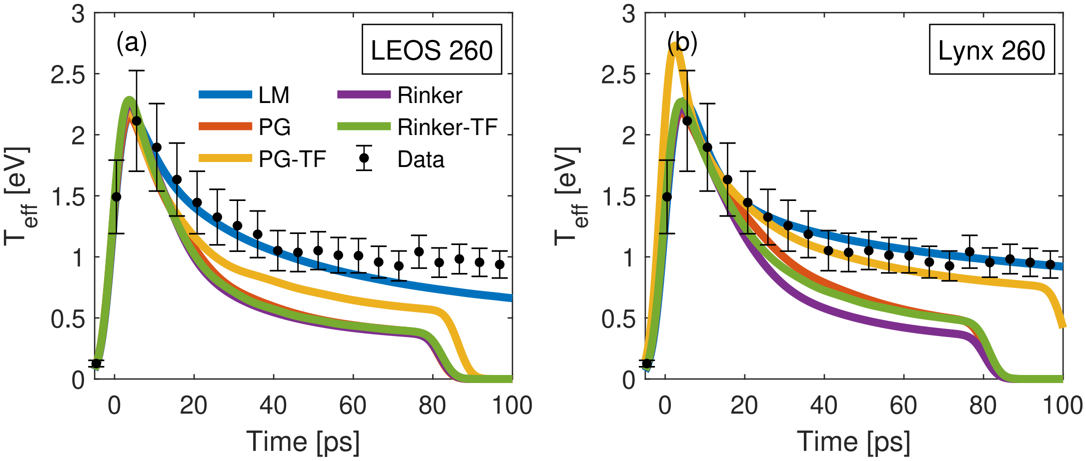

Figure 5.13: Rear-surface temperature for 50 nm Fe targets with (a) LEOS 260 and (b) Lynx 260.

These results should be regarded with caution as the target fails to remain opaque out to 100 ps. This invalidates both the Helmholtz solution for light reflecting from an overdense electron density gradient as well as the opaque black-body assumptions the SOP relies on. Transmitted energy will not be accounted for properly. This is seen in figure 5.13 beyond 80 ps when the entire target is below the critical electron density for 450 nm photons, though the effect begins at much earlier times.

However, results still bear presenting as they indicate that the iron EOS options and the source multiplier achieve the correct temperature for iron, as well. This is confirmed by the early-time behavior. Sesame 2140 is not compared because it has a liquid-vapor critical point at 0.75 eV, and multiple phases may exist. The current simulations handle phase changes incorrectly or unreliably, and exhibit clustering of matter. For this reason, s2140 is excluded from these low-temperature comparisons, with the focus shifted to LEOS 260 and Lynx 260 which are smoother and show no signs of a phase change.

5.5.5 Double-layer targets

With the heating source and, tentatively, the equation of state model shown to agree with single-layer data, we shift attention to the more complicated double-layer gold/iron system. We collected data from two thicknesses of iron to provide a stronger constraint on the models.

Figure 5.14 shows the measured brightness temperatures for all EOS and conductivity model combinations. Here, brightness temperature is compared rather than the emissivity-corrected effective temperature because the available experimental emissivity correction (from a gold target) would not provide an accurate temporal evolution.

Looking at the figure, it is seen that general agreement with all three EOS models is reasonable. LEOS 260 seems to predict lower temperatures, as was seen in the single-layer iron data (fig. 5.13), while Sesame 2140 predicts the highest temperatures. All are within the $\pm 10\%$ random error bars, and no strong distinction can be made between EOS models. However, Lynx 260 seems to provide slower cooling rates for all three iron target types. These match the temporal shape of the data better, and Lynx is likely—narrowly—outperforming the others.

Temperatures predicted by the different conductivity models are within 25% of one another during $t = 5$–30 ps, and within 10–15% from t = 30–100 ps. Differentiating models within such a small scatter would have required smaller error bars on the data. While no model may be clearly distinguished, these data do provide confidence that the models sufficiently reproduce the experimental conditions.

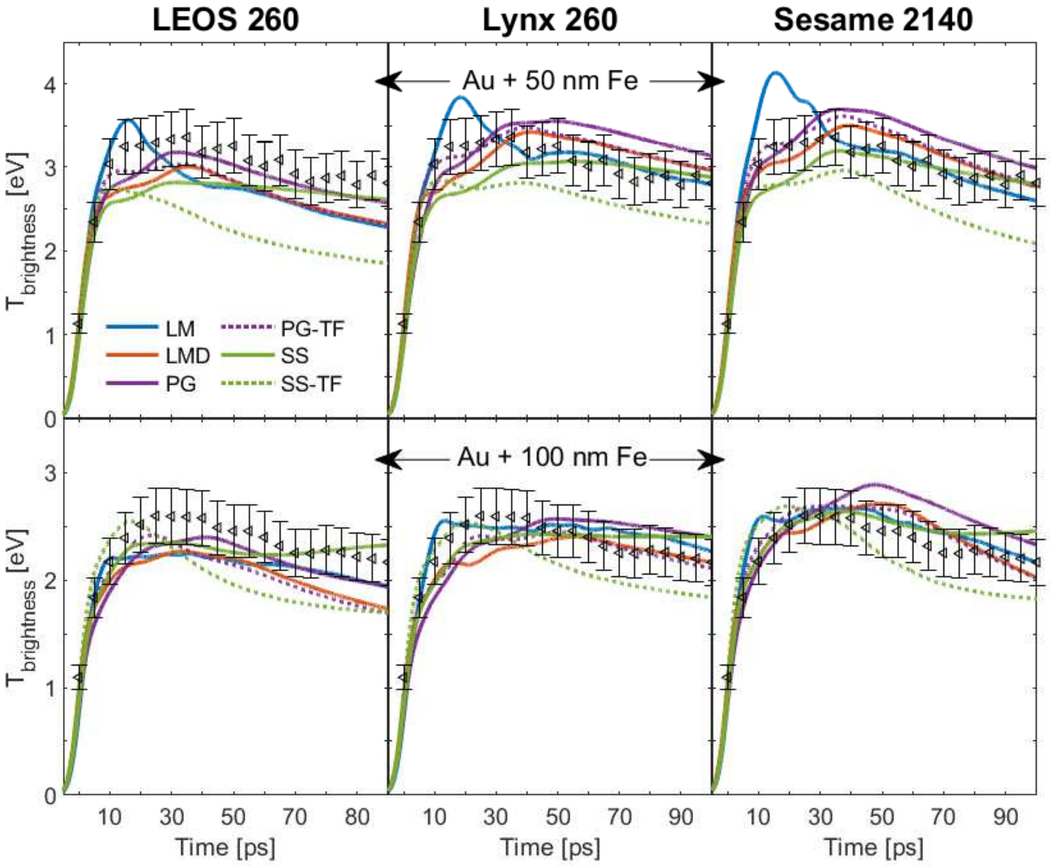

Figure 5.14: Comparison of the brightness temperature for 100 nm Au + 50 nm Fe (row 1) and 100 nm Au + 100 nm Fe (row 2) targets for LEOS 260, Lynx 260, and Sesame 2140. Thermal and electrical conductivity models are designated with color, and the dotted lines are models using TF ionization rather than their self-consistent model.

No data were obtained for the time-resolved reflectivity, but the calculations show that reflectivity may have been able to constrain the electrical conductivity model and, to a lesser extent, the EOS model.

Figure 5.15 shows the calculated S polarized time-resolved reflectivities at the SOP angle (27°). The thermal wave crosses the 50 nm target rapidly (< 5 ps), and the thermal dynamics cannot be resolved in time. The observation is still dependent on the thermal conductivity, but rather than viewing the thermal wave itself, we see the unloading derived from the system heated by the thermal wave. The reflectivity predictions only vary by 5–15% at any given time.

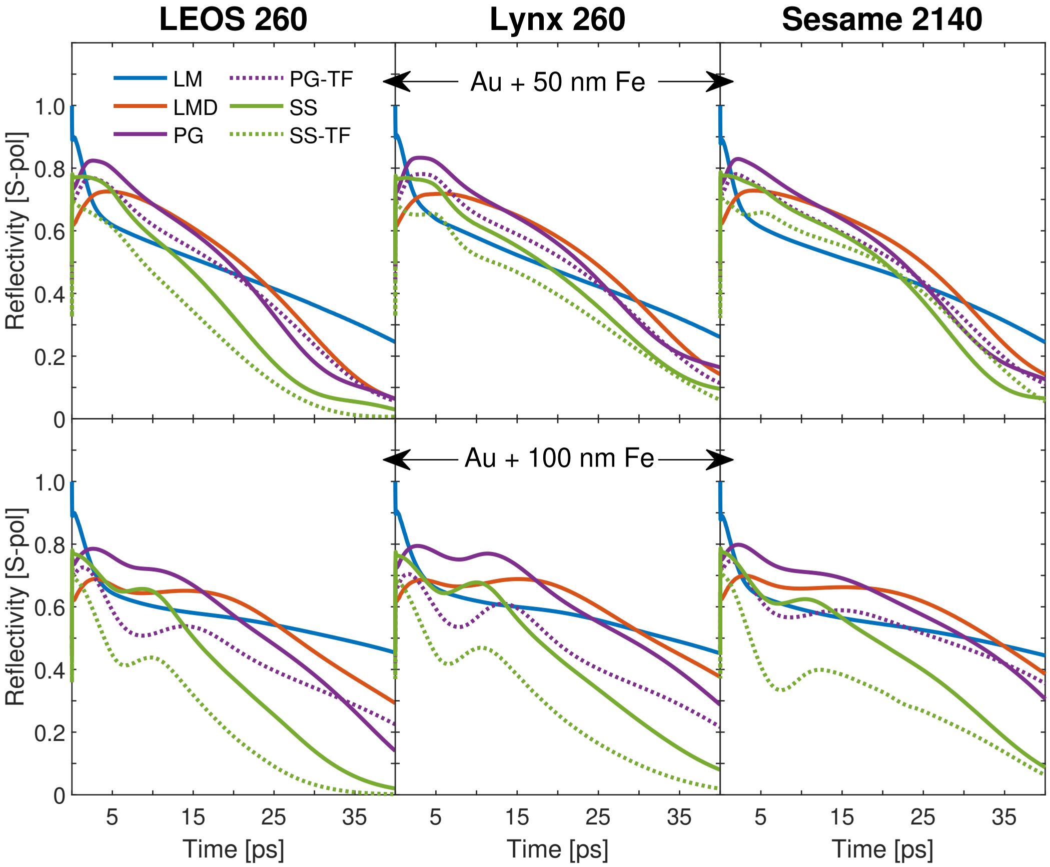

Figure 5.15: Comparison of the reflectivity for 100 nm Au + 50 nm Fe (row 1) and 100 nm Au + 100 nm Fe (row 2) targets for LEOS 260, Lynx 260, and Sesame 2140. Thermal and electrical conductivity models are designated with color, and the dotted lines are models using TF ionization rather than their self-consistent model.

However, for the gold + 100 nm Fe target, the heat conduction and resolution time scales are more compatible. We recall the simple expression given by Kruer[135] for reflection from an electron-density gradient scales as exp(-$\nu_{ei}L$). The scale length will expand rapidly during the rarefaction wave ($t \approx$ 0–7 ps) and then continue to increase at a slower rate. The thermal energy from the hot gold layer provides a dynamic change to ν_{ei}, which manifests itself in the reflectivity data. This effect was observed in the proton-heated aluminum data shown in Section 4.4.5 but was washed out by the duration of the proton-heating pulse. In fig. 5.15, this effect is present for three of the four conductivity models, demonstrating improvement of the experimental design using the XFEL. The minimum in the reflectivity—corresponding to the maximum in ν_{ei}—occurs at different times for each model. The timing of this feature, along with the amplitude of the reflectivity, would likely provide a strong constraint on the electrical conductivity model.

The lack of data for the present experiment precludes our ability to reach definitive conclusions about the conductivity of iron. In spite of this, these calculations show promise, indicating that sufficient difference exists between conductivity models, and that a reflectivity measurement with a time history of $\sim$30 ps and $< 10\%$ random error bars could constrain the EOS and electrical conductivity. This would be easily achievable at a high-repetition rate facility such as LCLS. With the uncertainty in modeled SOP temperatures due to the EOS resolved, the amplitude of that data would indicate if the thermal conductivity should increase or decrease. Assuming Lynx 260 remained the best EOS in a comparison of reflectivity data with the model—as it did for aluminum—the SOP temperatures indicate that the thermal conductivity for the current iron models is accurate within the error bars of this measurement.

5.6 Discussion

Analysis of the simulations allows for characterization of the phase space this reached in this experiment. Figure 5.16 shows the electron temperature and mass density of the 100 nm Au + 100 nm Fe target at times ranging from the end of the heating pulse to 35 ps. The profiles have been aligned to the left edge of the gold for clarity. Comparing these profiles with the ones from Titan in fig. 4.19, the XFEL's greater efficiency at creating differentially-heated target stacks is immediately clear. The gold is heated to a peak temperature of 15 eV while the iron starts at 4.5 eV. The temperature and densities occupied by just the iron layer are shown in fig. 5.17. The resulting conditions are comparable to the aluminum experiment with peak temperatures of approximately 10 eV in the multi-layer targets, and the average density remains above 0.7 g/cc for the entire 100 ps.

The coupling and degeneracy parameters are shown in table 5.4. Due to the prompt heating

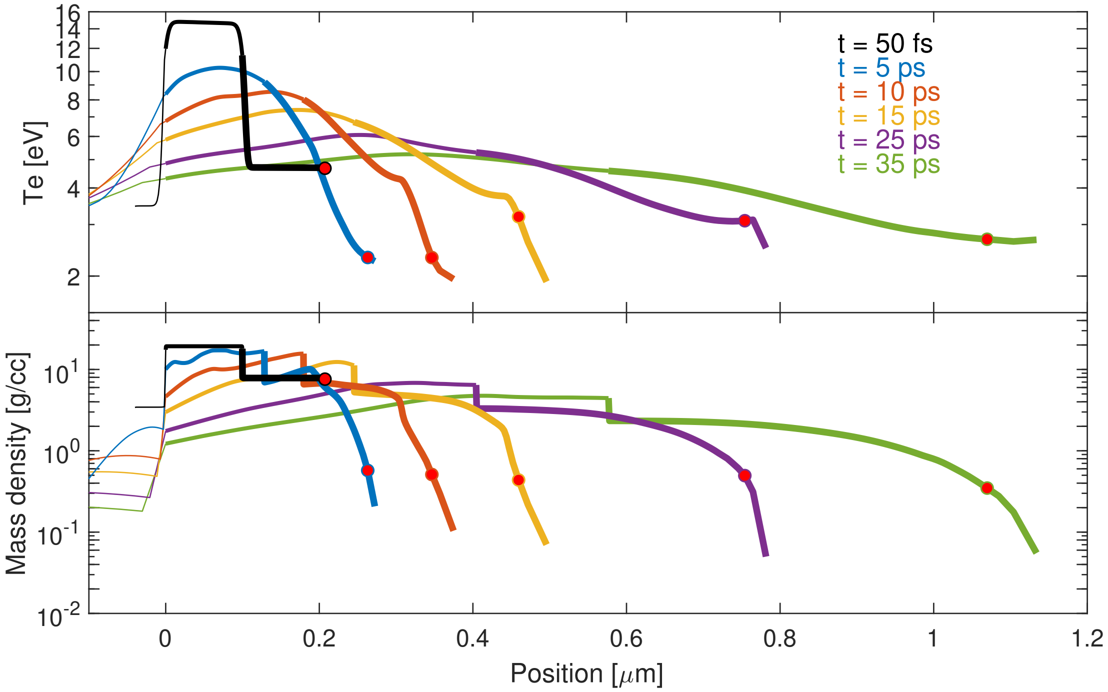

Figure 5.16: Spatial temperature (top) and density (bottom) profiles from a 100 nm Au + 100 nm Fe simulation using Lynx 260 for the EOS and Purgatorio for the thermal conductivity. The red dot indicates the position of the critical density surface for 450 nm light. The thickest portion of each line contains the iron zones; the intermediate thickness, the gold; and the thinnest contains the Si_3N_4 zones. The profiles have been aligned to the Si_3N_4/Au interface for clarity.

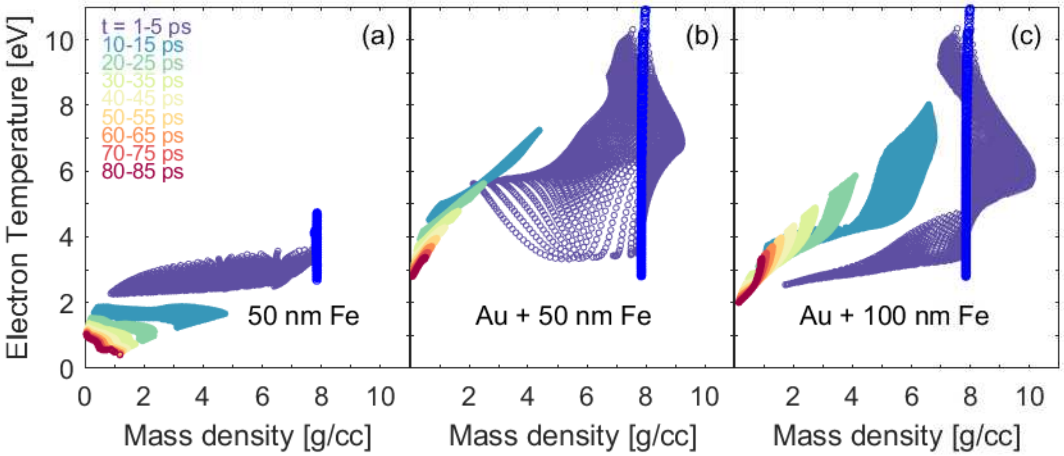

Figure 5.17: Electron temperature vs. mass density phase space from best matched targets: (a) 50 nm Fe, (b) 100 nm Au + 50 nm Fe, and (c) 100 nm Au + 100 nm Fe. The phase space is shown in 5-ps sections, represented with color.

source and higher density of iron, the coupling parameters are 2–3x higher than they were for the aluminum, with an average Γ_{ii} value of 25 at t = 10 ps for the 100 nm Fe target. The degeneracy parameters are also a factor of 2 smaller. However, the general conditions are still moderately coupled and partially degenerate—similar to the aluminum experiment in Chapter 4—and provide an excellent test for theories in WDM.

Table 5.4: Plasma-coupling and electron-degeneracy parameters for Fe target layers

	50 nm Fe				**100 nm Fe**			
Time [ps]	5	10	30	60	5	10	30	60
$\Gamma_{ii,avg}$	19	12	5.5	3.5	32	25	11	6.2
$\Gamma_{ie,avg}$	7.6	5.5	3.3	2.4	12	9.8	5.8	4.0
Θ_{avg}	0.6	0.9	1.8	2.8	0.4	0.5	0.8	1.3

The validity of the local-heat transport assumption was checked under these conditions. The electron mean free path was calculated using electron-electron and electron-ion collision times from Purgatorio and an average velocity that was either the maximum of the Fermi velocity or the thermal velocity. The electron mean free path was defined as $\lambda_e = (\lambda_{ee}\lambda_{ei})^{1/2}$, and the thermal scale length, $L = T/\nabla T$, was determined from the spatial profiles in the hydrodynamics calculation. I found that the ratio L/λ_e dipped as low as 25 at t = 5 ps, rose to 50 by t = 7.5 ps, and exceeded greater than 225 beyond 15 ps. Early times may experience slight kinetic effects due to non-local heat transport, but the target should rapidly approach diffusion conditions. For very thin targets, the time scales for diffusive transport across the target may coincide with the time it takes for non-local effects to dissipate, and future experiments should aim for targets greater than 100 nm with these conditions. Problems may also arise if a material with significantly lower density than iron is chosen. To mitigate these problems, consider tuning the XFEL to a higher energy (which is absorbed less efficiently), using a different element for the heater layer (which absorbs less strongly), or using a larger x-ray focal spot.

Successful fabrication of thicker targets allowing us to obtain the reflectivity measurement from the FDI would have significantly improved the present experiment. Figure 5.19 shows the S-polarized reflectivity and the rear-surface temperature for 100 nm Au + 100–300 nm Fe targets.

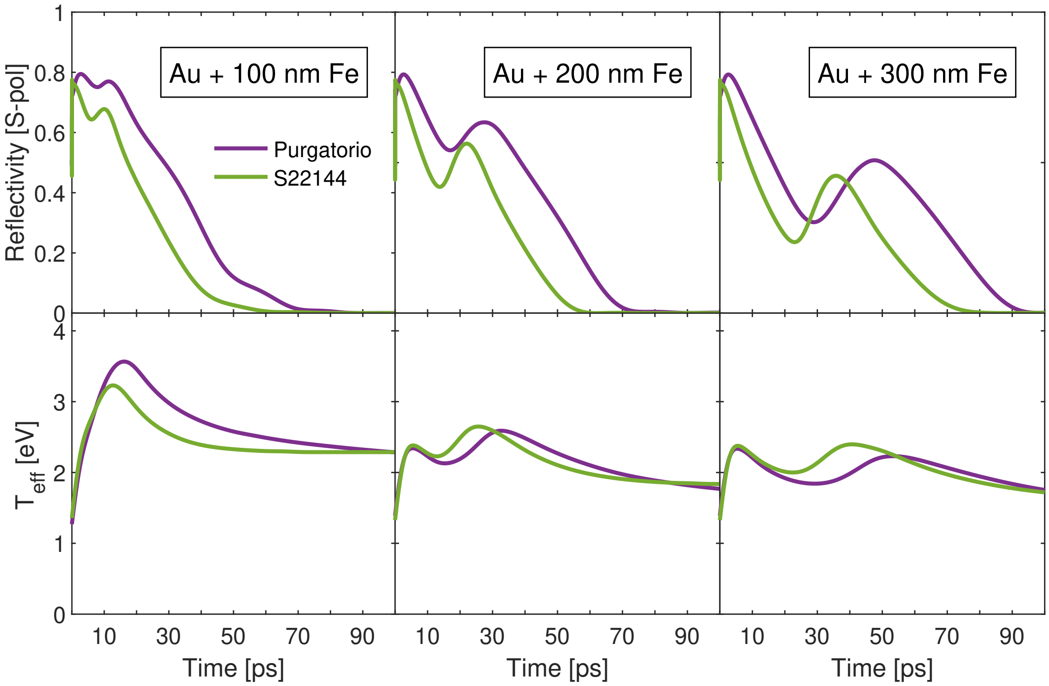

Figure 5.18: Calculated reflectivity (top) and rear-surface temperature (bottom) of Au/Fe targets of increasing iron thickness. Purgatorio and Sesame 22144 are compared .

The conduction dynamics are greatly emphasized in the 200 and 300 nm iron layers. The calculation for s22144 shows $> 20\%$ difference from the minimum at $t = 23$ ps to the maximum at $t = 36$ ps. This difference would be well within typical measurement uncertainties. The temporal evolution is even slow enough that currently-available equipment with a 5 ps time resolution could resolve the feature. During the design process of the experiment, the rear-surface temperature was assumed to be the most distinguishable observable. However, for the successfully measured target thicknesses, the target's rarefaction and the propagation of the thermal wave are on nearly-identical time scales. This led to suppression of features in the brightness temperature alone, making the obtainment of a quality, time-resolved reflectivity measurement *imperative*.

Figure 5.19 shows the effect on calculated observables if the entire thermal conductivity table is scaled up or down by a factor of 4. The temperature data is sensitive to higher thermal conductivity values, showing a $\sim$40% increase but losing all features as the thermal energy arrives much sooner.

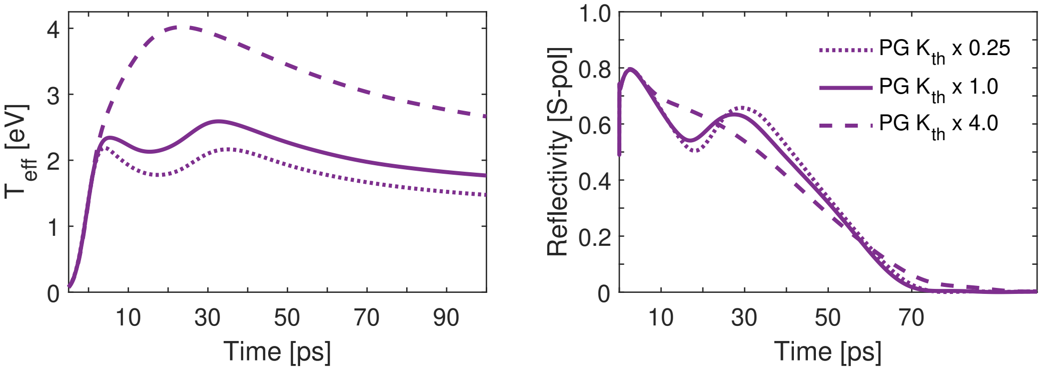

Figure 5.19: Rear-surface temperature (left) and S-polarized reflectivity for 100 nm Au + 200 nm Fe target calculated with the Purgatorio model. Arbitrary multipliers of 0.25x and 4.0x are shown in dotted and dashed lines, respectively.

This increase also serves to blur the feature visible in the reflectivity, resulting in a nearly 20% change near the reflectivity features. Conversely, the reduction in thermal conductivity serves to sharpen them. This effect is certainly smaller, but within resolvable limits. These types of measurements are particularly well-suited to a high repetition-rate facility where quality statistics can reduce errors caused by digital readout and low signal to very small levels. This reflectivity shows great promise, likely distinguishing at least factors of 4—though possibly smaller changes—to the conductivity.

5.7 Conclusions

This chapter described an experimental campaign performed at the LCLS using the XFEL as a pump and the short-pulse Ti:Sapphire laser as a probe to diagnose differentially-heated high-Z/low-Z target stacks. We measured the brightness temperature of the rear-target surface for a set of single- and double-layer gold and iron targets designed to constrain hydrodynamics models. The modeling—performed using HYDRA—tested three EOS models and four thermal/electrical conductivity models against the data. The electrical and thermal conductivity models were used self-consistently with a Helmholtz wave solver to calculate the observed optical behavior assuming a Drude model. Reasonable agreement between temperature data and models was found for all

EOS and conductivity models. Calculations were presented that indicate the strongest evidence of thermal conduction would have been present in the reflectivity data. The ultrashort heating duration of the XFEL emphasizes a minimum in the reflectivity that is highly sensitive to the EOS and conductivity models. The platform exhibited the ability to create moderately-coupled, partially-degenerate warm dense matter in a temperature range of 2–10 eV and 0.5–10 g/cc.

The demonstration of measurable signal levels establishes the possibility for future, improved experiments. This future work should focus on enhanced target fabrication techniques capable of creating targets of 200–400 nm thickness. These target improvements would significantly heighten sensitivity to the thermal evolution, keep the experiment at higher densities, and mitigate the impact of ballistic and other non-local electron heat transport.

CHAPTER 6

Radiation transfer in dense short-pulse laser-heated targets

6.1 Introduction

In high-temperature matter, radiation plays a crucial role in the energy balance and system evolution as well as the experimental diagnosis of the thermodynamic state of the system. Plasma spectroscopy is a staple in the diagnosis of the temperature, density, and ionization balance of astrophysical and laboratory plasmas[241, 242]. By blending a target of interest with low- to mid-Z elements and observing the K-shell emission, one may infer the plasma conditions. If the dopant is kept to a sufficiently low concentration, the impact of an impurity usually remains small. This technique is commonly used at facilities such as the National Ignition Facility to diagnose imploding capsules. It has also been demonstrated as an effective temperature and density diagnostic for the opacity experiments related to the work presented within this chapter[243, 244].

The most accurate determination of temperature and density requires fitting as many spectral features as possible to a self-consistent synthetic spectrum. These calculated spectra are most commonly generated using Collisional Radiative (CR) models such as FLYCHK[105], Cretin[106], or SCRAM[107]. CR models must solve a coupled local and non-local problem that treats large numbers of individual atomic transitions (see Section 2.5.1) in addition to satisfactorily accounting for dense-plasma effects not present in isolated atoms. These include ionization potential depression, line shifts, and line shape calculations. Ongoing NLTE workshops focus on benchmarking codes against one another, and recent workshops have begun extensive comparison with experimental data[116, 117, 118]. The scarcity of well-characterized and benchmarked experimental data relevant to NLTE conditions is highlighted among the conclusions of these workshops. This has sparked experimental efforts to create platforms that determine temperature and density independently of spectroscopic measurements[245], but data remains scarce.

The brightest spectral lines often result from optically-thick transitions. Photons within such spectral lines experience many absorptions and re-emissions before exiting a plasma, leading to a trapped radiation field within the volume. In practice, the effects of this trapped radiation are often neglected entirely using optically-thin models or are incorporated probabilistically through the escape factor approximation (see Section 2.5.2 for a description) in lieu of a full radiation transfer solution. This approximation—viewed as a correction to an optically-thin model—provides more accurate results while minimizing the tremendous computational burden of solving the full radiation transfer equation. However, the use of these escape factors has not been well benchmarked with experimental data, and their impact on inferred temperatures from optically-thick lines is nebulous.

Previous work by Kerr *et al.*[246] used Cretin to compare a radiation-transfer calculation with an escape-factor calculation and found modest disagreement for Fe XV ions with column densities between 10^{17}–10^{19} cm^{-2}, with the escape-factor method over-predicting the escape of radiation. Dumont *et al.*[247] performed a comparison between escape factors and full radiation transfer in simulations of active galactic nuclei using the photoionization code, Titan. They modeled a hydrogen slab of particle density n = 10^{12} cm^{-3} and a total column density of 5x10^{24} cm^{-2} that was irradiated by a constant external continuum source. They concluded that the escape factor calculation significantly over-estimated the line emission (by $\approx$30%), with the best agreement found for transitions without significant overlap with the continuum. Minguez *et al.* presented a comparison of calculations done with 1-D radiation transfer and escape factors for a laser-produced plasma[248]—100 μm thick Al, 300 eV, 10^{23} cm^{-3}—representing the closest comparison between existing literature and this current work. They found excellent agreement for the population fraction and specific intensity in the case of a uniform plasma, but began to see significant deviation for non-uniform density and temperature profiles.

In this chapter, I will present angularly- and temporally-resolved K-shell spectra from silicon plasmas at 450–650 ev and 1–2 g/cc. These data will be presented along with a computational study of escape factors in 0-D and 1-D compared with radiation transfer in 1-D and 2-D. General uncertainty in the inference of temperature from these spectroscopic models will be compared, as well as an assessment of other significant experimental uncertainties such as radial temperature gradients.

6.2 Radiation transfer and escape factor simulations

Here, we choose two codes for comparison. The first is the NIST version of FLYCHK[105]. FLYCHK is widely used in the laser-plasma community because of its accessibility, simplicity, and accuracy. All FLYCHK calculations assume a uniform 0-D slab geometry. A thickness over which to calculate opacity effects (using the escape factor formalism) may be specified, or else an optically thin model is assumed. The second code, Cretin[106], is a powerful tool with the capability to perform direct comparisons between model assumptions using the same numerics and atomic data. Cretin was developed by Howard Scott at LLNL and can perform detailed 0-D or multi-dimensional radiation-transfer calculations. These calculations either utilize escape factors or a formal transfer solution that treats small groups of interacting spectral lines independently with a complete linearization technique[103]. The continuum and spectral lines are treated separately, allowing for differentiation between cases where the continuum is important to the overall problem.

Within Cretin, individual transitions must be specifically chosen for a detailed transfer treatment. The rest are treated with the escape factor formalism. All components of the $1s^2$-1s2p (He-α), 1s-2p (Ly-α), $1s^2$-1s3p (He-β), and 1s-3p (Ly-β) transitions are transferred in detail, where the satellites are always treated with escape factors. This is considered acceptable as the satellites remain optically thin and will never contribute to an internal radiation field. Line shapes for these spectral lines are calculated using TOTAL[249].

Both models require detailed atomic data as input. FLYCHK uses detailed data from HULLAC[108] and calculations from the original FLY code[250] for the most commonly used diagnostic ions (Li, He, and H-like). Beryllium-like ions to neutral atoms are represented with only a ground state, ionization potential, and statistical weight. The current silicon FLYCHK model includes 380 levels and 3749 transitions. Cretin may use any atomic model provided, but all of the results presented here are from a detailed K-shell model provided by H. Scott (LLNL), calculated with FAC[109]. This model used full-level detail calculated with FAC for H, He, Li, and Be ions. The Be ion model is averaged based on principal quantum number, n, to match the structure of a screened-hydrogenic model. Levels within H, He, and Li ions are averaged or combined for n$\geq$4. Finally, all ions from B to neutral silicon are included from a simple screened-hydrogenic model. This results in a model with 552 levels and 19,460 photoexcitation transitions; 7,059 photoionization transitions; 13,445 collisional excitation transitions; 7,116 collisional-ionization transitions; and 7,554 Auger-ionization transitions.

The model parameters in this section are chosen for their similarity to the data presented in later sections. The targets are 1500 Å thick, 300–900 eV, and 1–2 g/cc. All models are run in steady-state conditions with constant mass density and varied temperature profiles. The electron and ion temperatures are held equal to one another. A characteristic simulation result from Cretin is shown in figure 6.1. The energy range of interest is 1800–2500 eV for the silicon K-shell. The primary features are the He-α, Ly-α, He-β, and Ly-β resonance lines, along with dielectronic satellites from Be, Li, and He-like ions. Finally, the He-like free-bound continuum is seen between the Helium and Hydrogen beta lines. The intensity of all continua are low through the entire energy range.

At first glance, these conditions might be expected to be sufficiently collisional to be in LTE. In this case, escape factors—which enter only in calculating radiative rates—would be insignificant. However, the elevated temperatures mean that trapped radiation from spectral lines might play a role in the kinetics, particularly for the n = 2 $\rightarrow$ 1 alpha lines which are moderately trapped. It is

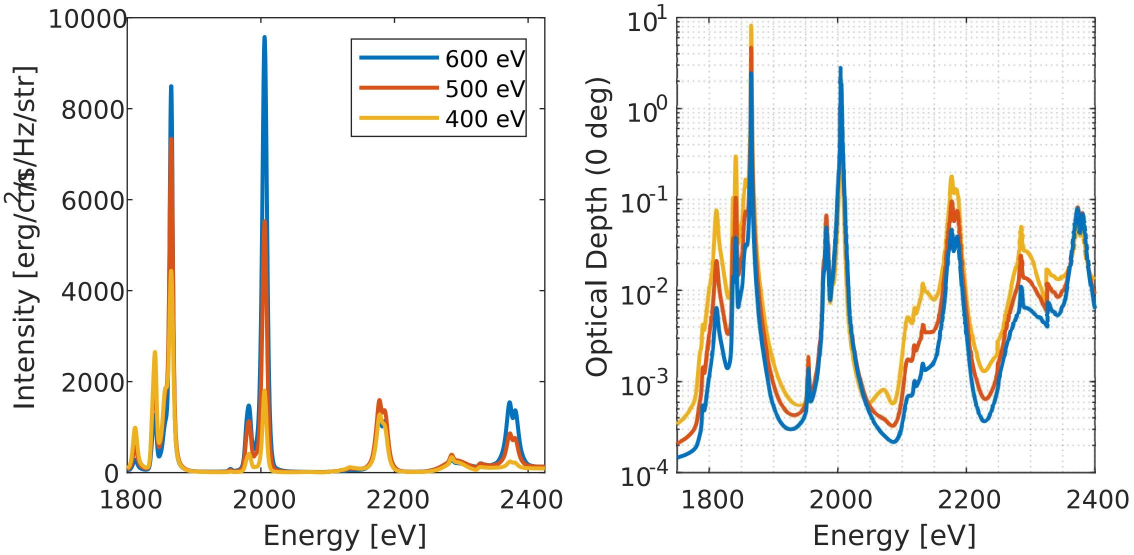

Figure 6.1: Characteristic silicon K-shell spectrum at 1 g/cc and 400–600 eV for a 1500 Å thick target. At the thinnest dimension, the alpha lines have optical depth of 2–10, and the beta lines and dielectronic satellites are optically thin.

precisely in this region of moderate optical depth that the approximation may fail. The aim is then to determine how far from LTE the samples are, how the escape factor formalism compares with a full transfer calculation, and assess how different the model-inferred temperatures are.

6.2.1 Kinetics comparison

First, we look at the population balance determined from the FLYCHK and Cretin kinetics calculations. Figure 6.2 shows a comparison of the average ionization and ionization distribution calculated by both codes for 0-D geometry using Apruzese-style planar escape factors[251] for the line radiation only. The plasma was assumed to be 1500 Å thick Si at 1 g/cc mass density. This corresponds to a 3000 Å thickness in FLYCHK. This is the 60° chord length corresponding to the planar volume-averaged path length which should be used for the volume-averaged escape factor[129]).

Below 300 eV, we observe all models for the average ionization converging to LTE—as expected. As the temperature increases and the role of radiation becomes more important, the models diverge. Above 900 eV, the silicon becomes fully stripped, and line radiation again becomes less

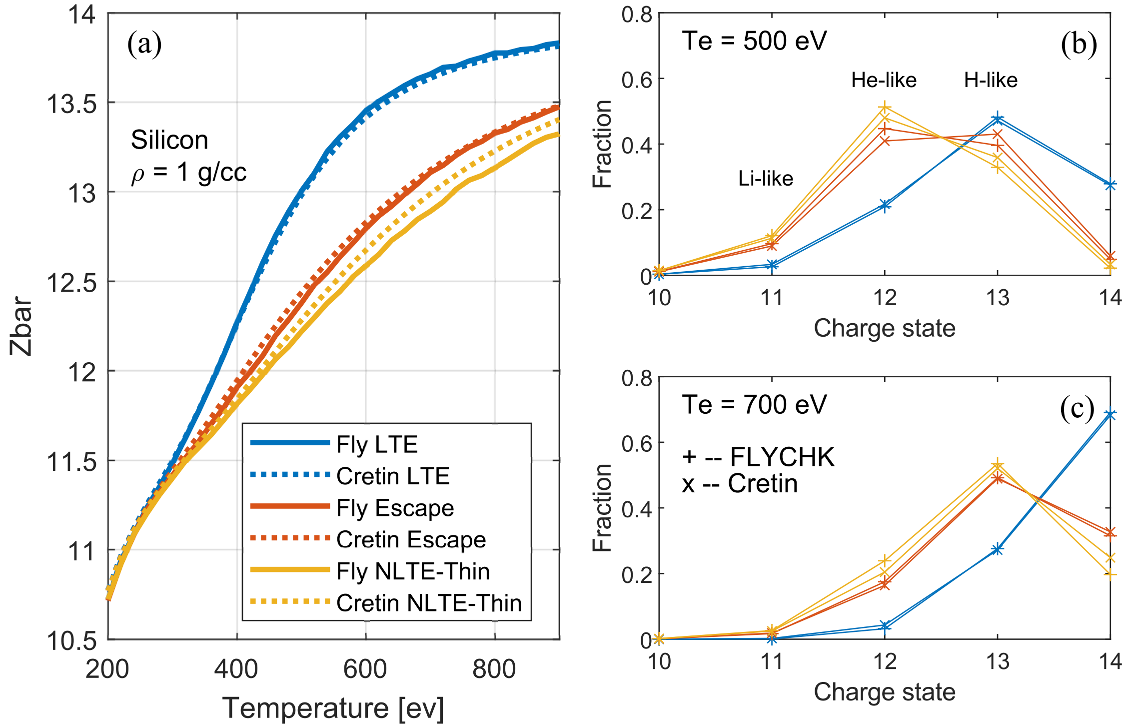

Figure 6.2: Comparison of 0-D kinetics models calculated by FLYCHK and Cretin for the LTE case (blue), optically-thin NLTE case (yellow), and the NLTE case with opacity included in the escape factor formalism (red).

important. The region between these two limits sees the maximum difference in the models. For these conditions, both Cretin (dotted line) and FLYCHK (solid line) predict very similar average ionizations. Small differences are attributable to the specific level structure in the atomic data.

Under these conditions, the inclusion of the trapped radiation leads to only a 1.5% increase in average ionization, relative to the optically-thin case. However, the ratio of helium to hydrogen-like ions at 500 eV is 0.95 using escape factors and 1.34 in the optically-thin case, a 40% change. Remembering that the temperature inference is sensitive to the ratio of these ions, radiation trapping is an important effect to include. FLYCHK consistently predicts more He-like ions than Cretin does.

A key difference between an escape-factor calculation and a spatially-dependent transfer solution is the inclusion of a boundary layer. All plasmas have a skin depth over which populations vary due to escaping radiation. Thus, even with a uniform temperature, the population balance will have a spatial dependence that is a function of the optical depth of each transition. This is illustrated in figures 6.3 and 6.4 for the ground states of hydrogen- and helium-like ions as well as the upper level of the Ly-α ($2p^1$) transition and a Li-like dielectronic satellite ($1s^1 2s^2$). Escape factors rely on a volume-averaged probability of a photon escaping which, by definition, remains constant throughout the volume. Thus, all escape factor calculations will have a constant value in space.

The H-like ground state is elevated relative to the optically-thin limit, decreasing close to the edge, while the He-like ground state is suppressed but increases close to the edge. This has been discussed previously by Apruzese *et al.*[252] and results from a process called ladder ionization. The trapped radiation pumps the upper level of He-like ions, moving them closer to the continuum. This reduces the energy required for collisional ionization, causing the observed decrease in the He-like ground state and corresponding increase in the H-like ground. The radiation field decreases toward the edges and populations tend toward the optically-thin limit. The upper levels of H-α and He-α are both pumped by trapped radiation and decrease toward the edges, though only H-α is shown in fig. 6.4. The population fractions from Cretin 0-D and 1-D escape factor calculations are all reasonably close to the mass-average of the transfer calculation, but do vary some. This is likely due to numerical and atomic model differences.

Figure 6.5 shows a comparison between ionization balances calculated with a 0-D FLYCHK escape factor model, 0-D & 1-D Cretin escape factor models, and a 1-D Cretin transfer model. The populations for the 1-D transfer model are the mass-averaged value. At 700 eV, the models all agree very closely, predicting less He- and H-like ions but more fully stripped than the optically-thin model. However, at 500 eV the optically-thin model predicts helium as the dominant charge state while the 1-D transfer predicts hydrogen. This is due to the ladder ionization previously discussed. The trapped He-α photons increase the number of ions excited to the upper level, which is 1865 eV. The ionization potential of the helium atom is 2436 eV, so the thermal temperature of 500 eV approximately provides the difference required to ionize the closed helium shell and increase the degree of ionization.

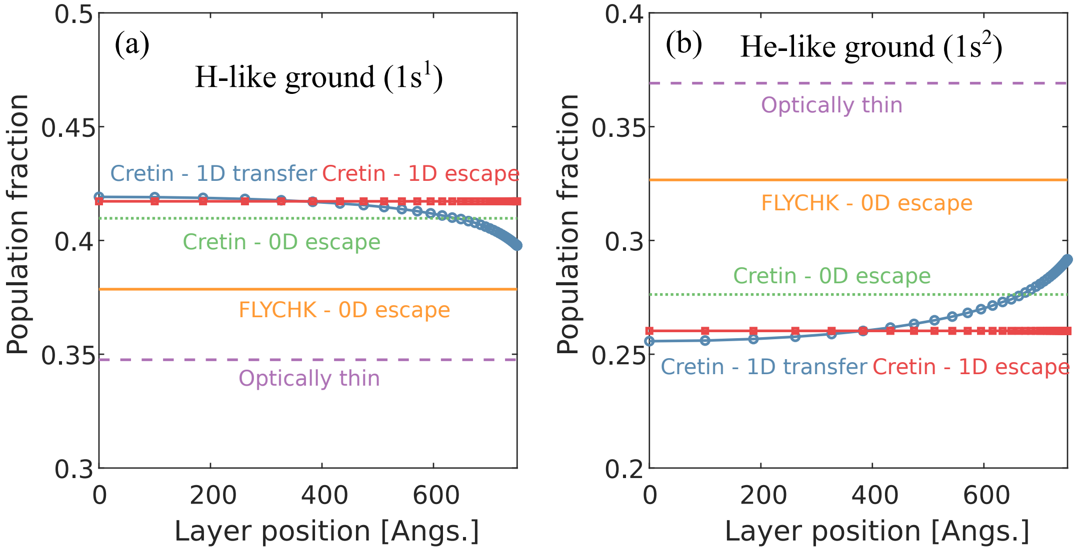

Figure 6.3: Spatially-dependent ground state population fractions for H- and He-like ions in half of the target. The H-like is elevated relative to the optically-thin limit, but the He-like is suppressed. This effect is known as ladder ionization—where the trapped radiation excites He-like ions, moving them closer to the continuum where they are easier to collisionally ionize. The Li-like ground state (not shown) demonstrates the same trend. The transfer solution confirms this effect, showing an increase near the plasma edges where the radiation field is lower.

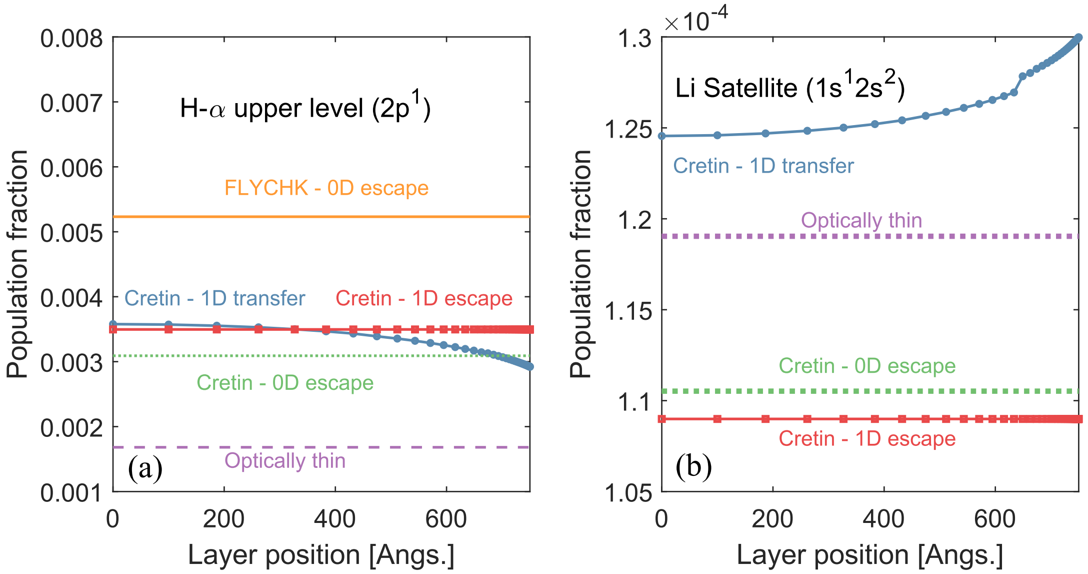

Figure 6.4: Population fractions for selected upper levels of ground states shown in fig. 6.3. On the left is the upper level of the H-α transition which shows enhancement relative to the optically-thin model. The upper level of the He-α is not shown, but demonstrates the same trends. On the right is the upper level of the Lithium-like satellites to the He-α transition.

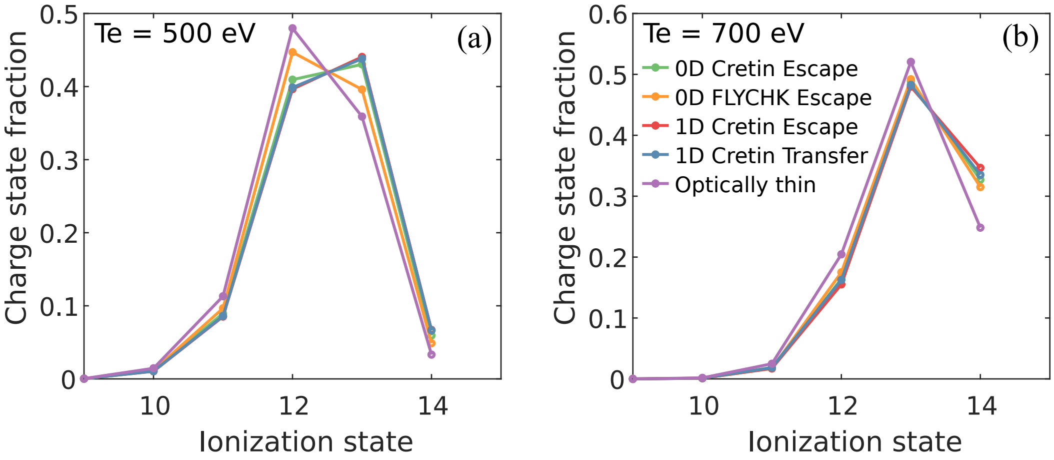

Figure 6.5: Ionization balance calculated by several models. At T_e = 500 eV, the optically-thin model predicts a He-to-H population ratio greater than one, as does FLYCHK. The 0-D and 1-D escape factor models from Cretin predict a ratio less than 1 with the 1-D transfer and escape models agreeing closely. The difference is less significant at 700 eV as the He-like population is ionized away.

6.2.2 Spectral intensity comparison

The experimental plasma conditions are determined using the specific intensity predicted by the CR model. The escape-factor and radiation-transfer calculations predict varying ionization balances, and thus are expected to predict different specific intensities.

The current NIST FLYCHK implementation is limited by the inability to specify separate volume-averaged and viewing chord lengths. Previous work by Kerr *et al.*[253] demonstrated the necessity of using the volume-averaged line of sight for the escape-factor calculation, but calculating the spectrum along the observed line of sight. For any convex geometry, the volume-averaged line of sight is $\bar{l} = 4V/S$, where V is the volume and S is the surface area. For planar geometry, this is 60 degrees. In FLYCHK, the ‘size’ field refers to this quantity. When analyzing data, one is left with the choice of potentially misusing this field. It can be set to match the diagnostic chord length at the risk of inaccurate kinetics, or set to the mean chord—causing incorrect intensities at any angle other than 60. These fields can be correctly set in the input-file-initialized versions of FLYCHK (available at some institutions).

Figure 6.6 shows a comparison between the spectral output for FLYCHK and Cretin models at

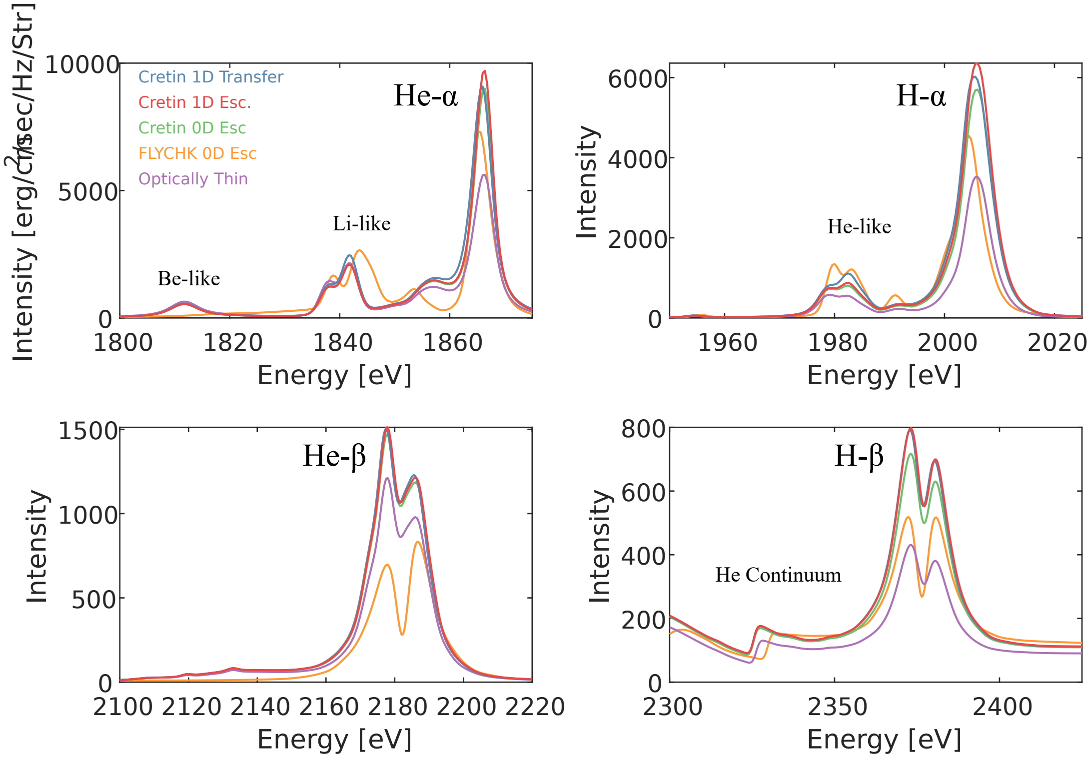

Figure 6.6: Calculated specific intensity for a 500 eV, 1 g/cc, and 1500 Å thick Si target. Models include 1-D Cretin transfer and escape factor, along with 0-D Cretin and FLYCHK escape-factor calculations. The optically-thin case, generated from Cretin, is included to show the effect of neglecting opacity entirely.

500 eV, 1 g/cc, and 1500 Å thickness. All spectra are shown for a 60° line of sight in order to get both correct kinetics and intensity out of FLYCHK. The primary differences in models occur for the optically-thin case, which would predict a temperature $\sim$40 eV lower ($<$ 10%) than the 1-D Cretin transfer solution. Additional differences arise in the line shapes of Stark-broadened beta lines due to the averaging of spectral line components and the line-shape calculations.

6.2.3 Angular dependence

The experimental data presented below were collected at several angles for the same spectral region. This is an uncommon measurement and provides an opportunity to benchmark the angularly-resolved spectra that Cretin produces. Figure 6.7 shows the emitted spectrum at several angles for the silicon targets considered. The optically-thin beta lines and dielectronic satellites gain intensity relative to the optically-thick alpha lines with increasing angle of incidence. This follows from the standard solution to the transfer equation for an optically-thin transition[253]

$$I_{ul,thin} = \frac{1}{4\pi}\int n_u A_{ul} h\nu_{ul} ds \tag{6.1}$$

where $I_{ul,thin}$ is the specific intensity for an optically-thin line; n_u, the population density of the upper state; A_{ul}, the Einstein coefficient for spontaneous emission; ν_{ul}, the frequency of the transition; and s, the path length along the ray. There is no difference between escape-factor and transfer calculations for the optically-thin beta lines, but some discrepancy can be seen for the optically-thick alpha lines at large angles. The transfer calculation predicts a self-reversal of both alpha lines, while the escape factor does not. Self-reversal occurs when the opacity in the line core is sufficiently large that all photons of that frequency are reabsorbed within the plasma and distributed into the wings.

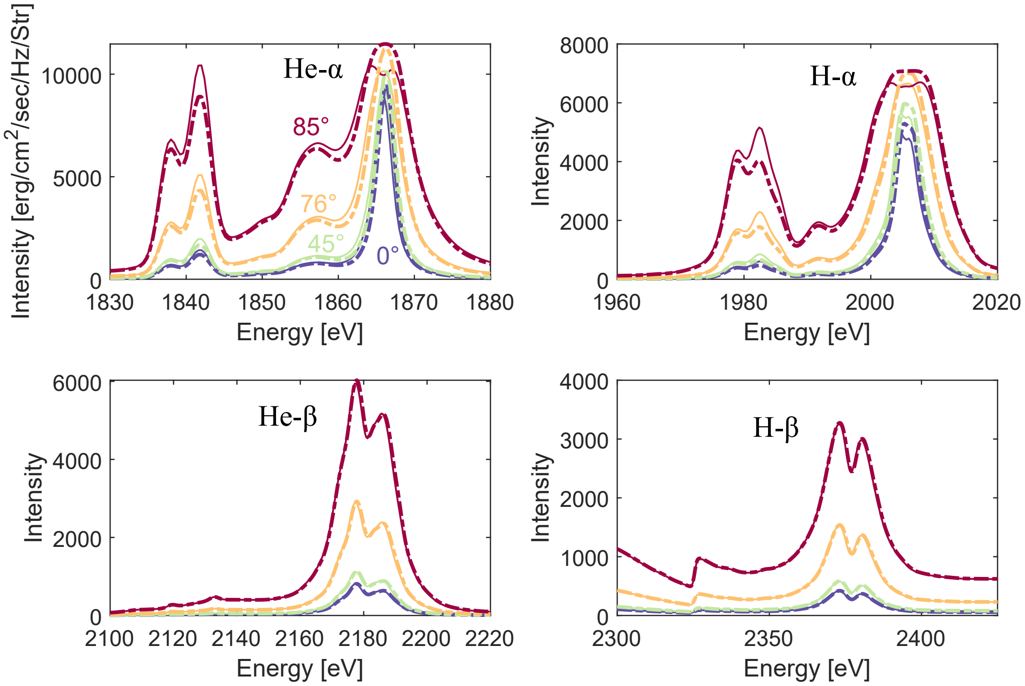

Figure 6.7: Specific intensity for increasing angles from target normal for the four observable Si lines. Conditions are T_e = 500 eV, ρ = 1 g/cc, and ΔZ = 1500 Å. **Solid lines** are from a 1-D Cretin full-transfer simulation, and the **dashed** show the same 1-D model using planar escape factors.

6.2.4 Radial temperature gradients

Gradients are always present in experimental plasma measurements despite often heroic efforts to mitigate them. The buried-layer platform at Orion[243] has demonstrated the ability to create nearly-uniform plasmas in space—both in temperature and density—through the use of thin microdot targets. These are tamped to constrain the density longitudinally and heated with a laser spot that over-fills the dot to control radial gradients. Nonetheless, radial gradients have been measured in Orion experiments[244] and invoked as a possible cause of disagreement in the time history of spectral measurements[254, 255].

Existing models that consider radial gradients in spectroscopic measurements are incorporated in large-scale integrated simulation efforts[254, 256] that combine particle-in-cell (PIC), hydrodynamics, and atomic-physics calculations. Here, I want to explore the *possible* impact of radial gradients on the presently-discussed experiments arising solely from radiation transfer. I present 2-D (RZ) transfer and escape-factor simulations with fixed mass density and radially-symmetric electron and ion ($T_e = T_i$) temperature profiles. These are all performed in the steady-state approximation.

Figure 6.8 shows the population distributions vs. the radial dimension of the target. The temperature profile is shown in black. The temperatures peaked at 500 eV with super-Gaussian temperature profiles (eq. (6.2)) with exponents n = 2, 4, and 10 and a FWHM of 60 μm. Shallower temperature gradients contain large regions of material in which helium and lithium are the dominant ions.

When CR models are used to match temperatures, single-temperature calculations are commonly used. If a radial gradient is present, contributions from colder regions of the target make the spectrum appear to have come from a colder ionization balance. The inferred temperature will come from an emission-, rather than mass-, averaged spectrum. Figure 6.9 shows the error that arises from fitting the spatially-integrated emission from the 2-D radial-gradient simulations—described by their peak temperatures—to a single-temperature model. The best fit between the calculations is determined by minimizing Chi^2 of the helium- and Lyman-beta lines. Below 300

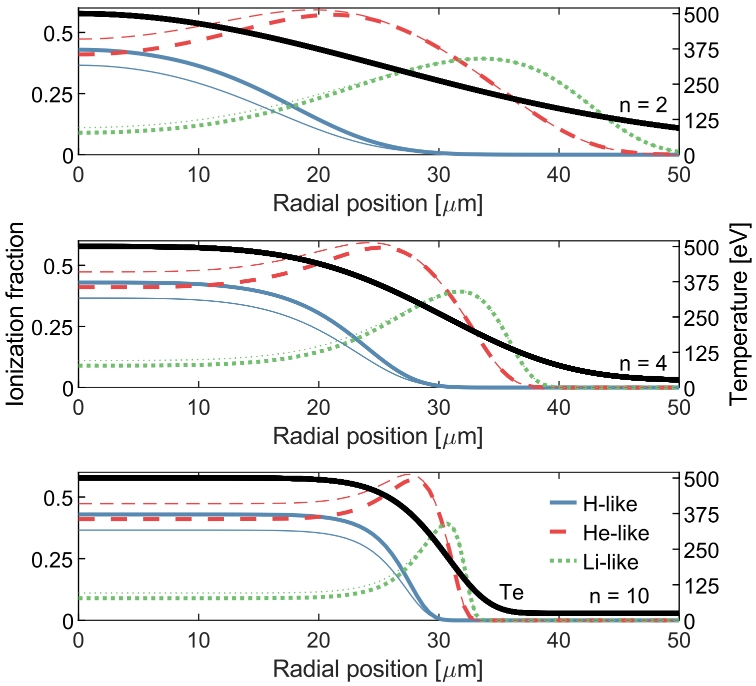

Figure 6.8: Spatially-dependent ion fractions for hydrogen, helium, and lithium from a Cretin 2-D radial gradient transfer simulation with detailed transfer. Thin lines are from a 2-D escape-factor calculation, and thick from the transfer calculation. Plotted in heavy black are the super-Gaussian temperature profiles, all peaked at 500 eV, with exponents n = 2, 4, & 10. All distributions have a 60 μm FWHM.

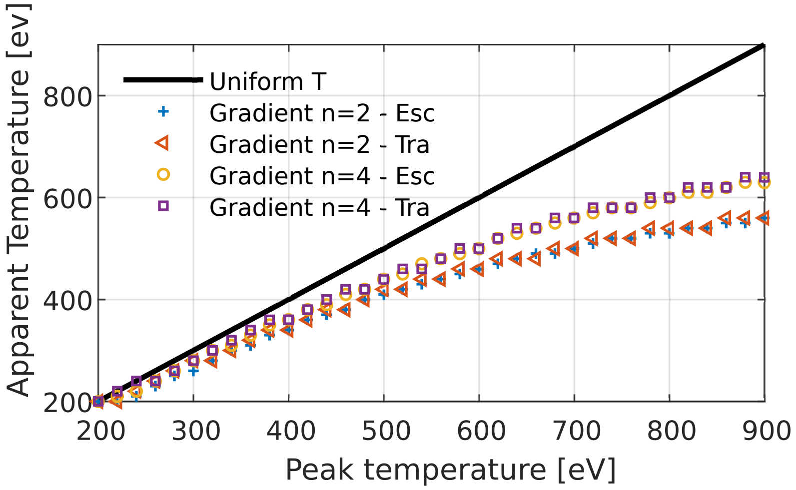

Figure 6.9: The apparent temperature inferred by matching a 1-D single-temperature synthetic spectrum to the spatially-integrated emission from a 2-D radial-temperature-gradient simulation characterized by its peak temperature.

eV, the error is small. As temperature increases, the error approaches 50 percent. This can lead to significant underestimation of the peak temperatures that exist within the plasma.

Figure 6.10 shows the observed spectrum for a uniform 500 eV target and a Gaussian (n = 2, FWHM = 60μm)) radial-gradient simulation with peak temperature of 680 eV. The optically-thin beta lines are indistinguishable, even in the absence of noise that typically accompanies a measurement. The only diagnostic signature that exists to differentiate the models would be total emitted flux or the ratios of the satellites. The gradient simulation predicts lower intensity for the helium dielectronic satellites to Ly-α and higher lithium dielectronic satellites to He-α.

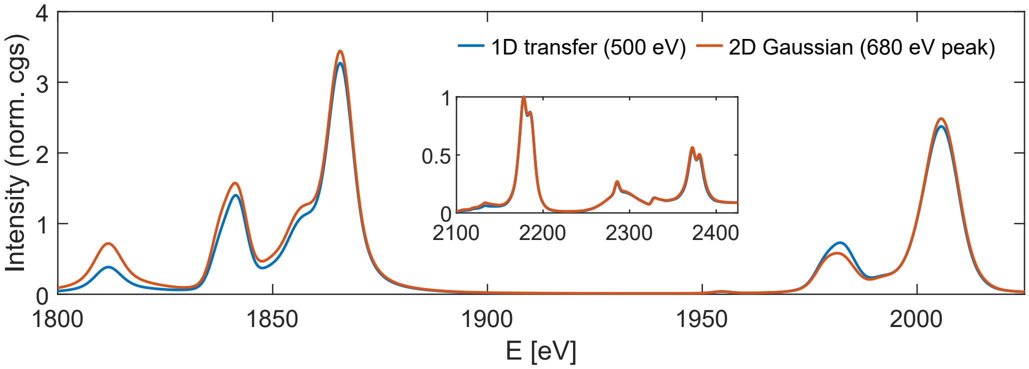

Figure 6.10: Comparison of the emitted spectrum at 76° from a uniform 500 eV Si target, and one with a 60 μm FWHM Gaussian temperature profile with peak temperature 680 eV.

6.2.5 Longitudinal temperature gradients

Heating a target with a laser on only one side invariably leads to a degree of longitudinal gradient. The dominant heating mechanism for these targets is believed to result from a return current that counters the fast electron flux generated at the laser interaction point[156]. However, the complicated field geometry and charged particle interactions that exist at the laser-interaction point may cause the front surface to become hotter than the rear.

To determine if a longitudinal gradient would be spectroscopically observable for these conditions, a 1-D simulation was run which assumed a linear temperature gradient throughout the target. The results are shown in figure 6.11. The front surface was held at 625 eV, and the rear at 375 eV.

This corresponds to a ±25% variation from the mean of 500 eV. The spectra observed from each surface, at 76 degrees from target normal, are plotted for escape-factor and transfer calculations. The large angle was chosen to match angles for which data exists. The difference between escape-factor and transfer treatments is minimal and could likely not be experimentally determined. The optically-thin n = 3→1 lines are identical from both views and are not shown. The primary difference resides in the alpha lines, which exhibit reduced intensity when viewed through less-ionized material on the cold side. The optically-thin satellites have the same intensity when viewed from either side. Thus, the satellite-to-resonance line ratios should detect a longitudinal gradient if a measurement is produced from both sides.

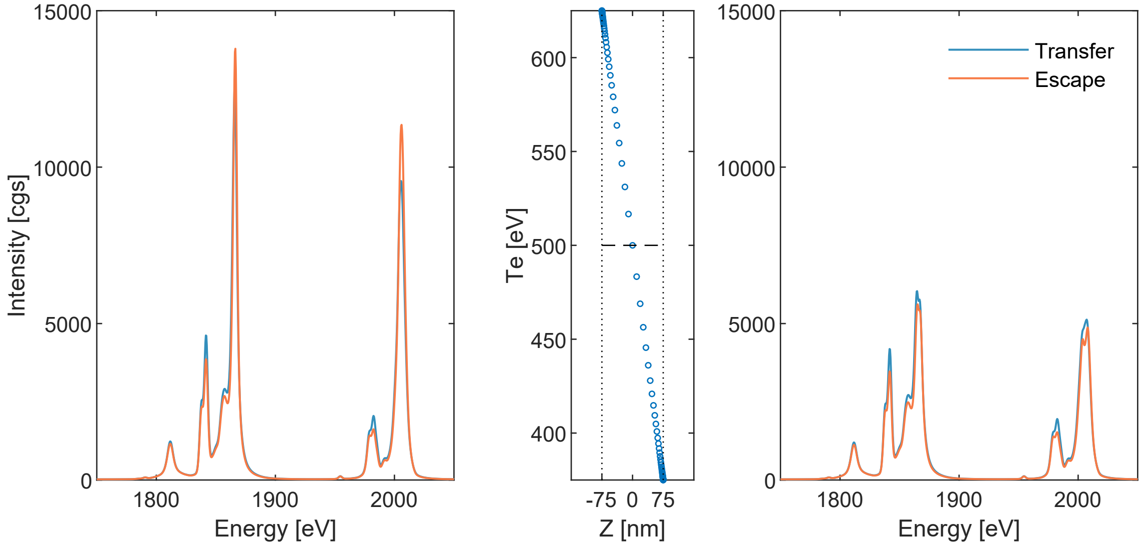

Figure 6.11: 1-D Cretin simulations for a 1500 Åthick Si target assuming a ±25% linear longitudinal gradient with an average temperature of 500 eV. The spectrum on the left is observed from the high-temperature side at 76° from normal, and the right spectrum viewed from the same angle on the low-temperature side.

6.3 Experimental setup at Orion

The data presented within this chapter were collected during a series of ongoing experimental campaigns using the Orion laser located at the Atomic Weapons Establishment (AWE) in the United

Kingdom as part of a collaboration between AWE and LLNL. These measurements served to characterize the experimental platform to better facilitate high-accuracy LTE opacity measurements. Details of the facility itself are outlined in Chapter 3. This section will focus on the specific setup for the campaign in which these data were collected.

6.3.1 Buried-layer platform

The current buried-layer platform at Orion[243] continues the similar short-pulse work performed in the late 1990's at Rutherford Appleton Laboratory[257], LLNL[258, 259], and Orion's predecessor, Helen[260, 261]. The concept is to inertially tamp the material of interest between layers that do not interfere with the method of temperature and density measurement. The tamp limits the expansion of the material, minimizing longitudinal spatial gradients, and thereby improving measurement accuracy. These high-accuracy methods generate opacity measurements with sufficiently small uncertainties as to instruct theoretical improvements to existing opacity models.

The favored approach uses K-shell spectroscopy to diagnose plasma conditions. Targets contain an active layer of low- to mid-Z elements—either in pure or co-mixed form—that are chosen based on the expected peak temperature. The material is isochorically heated, causing the high-density buried layer to expand into the lower-density tamp until it reaches pressure equilibrium. The targets are left highly ionized and at a constant density until the rarefaction wave propagates through the tamp material. The temperature and density may be inferred from comparison of the helium- and hydrogen-like ion emission with detailed atomic physics models.

To achieve high-fidelity measurements from a plasma in a single-state, the targets must be carefully chosen. Figure 6.12 shows a schematic of the targets presented in this work. The tamp layers are made of low-Z plastics such as polypropylene (C_3H_6) or parylene-N (C_8H_8). The choice of a low-Z tamp layer ensures that the tamp material will remain optically thin to the multi-keV transition radiation from the targets and free of significant spectral contamination. It also sets the effective mass density at which the spectral measurement will be made due to the pressure balance between the tamp layers at 1.1 g/cc and the active layer at 2.33 g/cc, in the case of silicon.

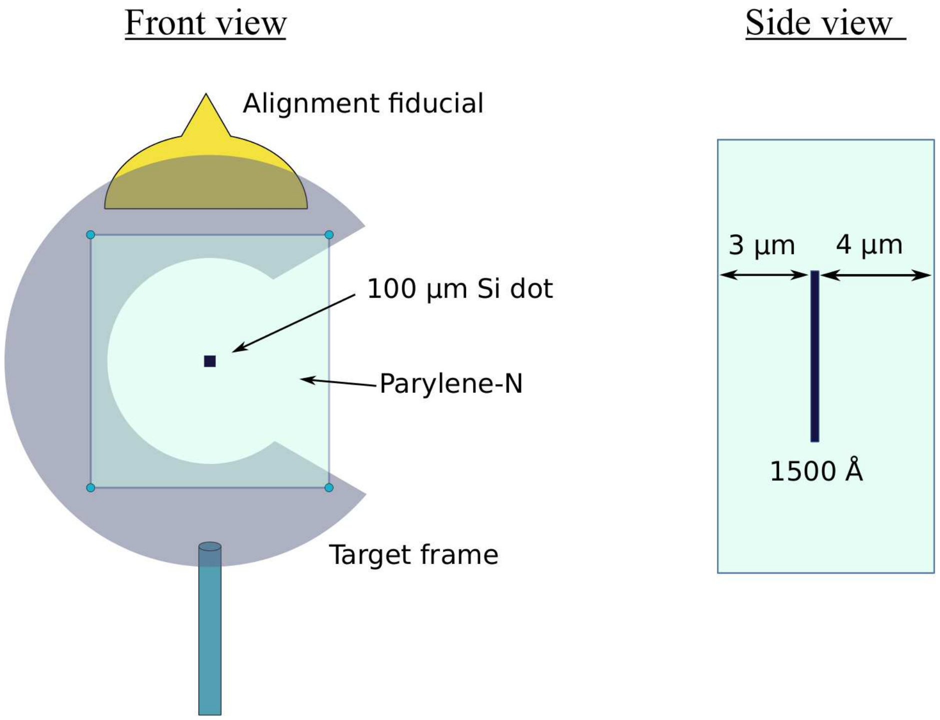

Figure 6.12: Schematic drawing of Si buried-layer targets shot at the Orion Laser Facility. Square, silicon microdots with a 100 μm side are tamped within parylene-N plastic and mounted on a washer and stalk for shots. The thickness of front and back tamps may be varied based on the specific shot requirements, but generally are 2–10 μm. The microdots were fabricated at LLNL and target assemblies, constructed by target fabrication at AWE.

The active layer is most commonly a square microdot of 50–100 μm length that is EB-PVD coated onto a 1 μm layer of polypropylene. The assembly is then submerged into a parylene-N vapor coater which adds a typical 3 μm of tamp on either side. This results in an asymmetric tamp with 3 μm on the front and 4 μm on the back. In some instances, greater asymmetry is desired. This is achieved by varying the thickness of the initial polypropylene layer. The thickness of the active layer is chosen so that the hydrogen- and helium-like beta lines (n = 3→1) remain optically thin. A balance must be struck between having enough material to ensure sufficient signal while minimizing possible optical depth effects and spatial gradients that can complicate the interpretation of temperature and density. This thickness is in the range of 1000–2000 Å.

Finally, the target Z should be chosen carefully based on the expected temperature range of the experiment. The temperatures are inferred by fitting an entire spectrum to the data, but in principle, two resonance lines from different ions—typically helium and hydrogen—are sufficient.

The sensitivity of this temperature measurement relies on the relative populations between the two ions; sensitivity is lost if the temperature is so low there are no hydrogen ions or so high that there are no helium ions.

6.3.2 Diagnostic layout

Orion is uniquely suited to spectroscopic studies of hot dense matter. A wealth of spectroscopic instruments have been developed by the Orion facility staff and physicists[181] and through collaboration with LLNL[196, 262]. The combination of TIM-based diagnostics with those mounted on the chamber walls enables a large number of instruments to be fielded simultaneously. For the experiment presented here, the angular distribution of fielded diagnostics is shown in figure 6.13. There were five time-integrated spectrometers, two time-resolved spectrometers, and three hot-spot imaging diagnostics. The spectrometers all utilized curved crystals. The spectral ranges, angle of incidence, filtering, and crystal information may be found in table 6.1.

Table 6.1: Orion diagnostic list with accompanying instrument information.

Diagnostic	Range (eV)	Θ_{norm} (°)	Filter	Crystal	RoC (mm)	2d (Å)
MKII	1800-2500	76.0	16 μm Be	CsAP	+500	25.65
Titan	1800-2500	76.0	16 μm Be	CsAP	+500	25.65
OHREX 1	2300-2450	46.2	50 μm Be	Quartz $10\bar{1}1$	-672	6.687
OHREX 2	1800-1900	58.3	50 μm Be	Quartz $10\bar{1}0$	-672	8.512
Axis 608	1800-2250	65.0	16 μm Be	CsAP	+500	25.65
Axis 609	1800-2275	25.0	16 μm Be	CsAP	+500	25.65
PHC	Hot-spot	20.0	8 μm Be	-	-	-
KB91	Hot-spot	11.9	8 μm Be	-	-	-
KB21	Hot-spot	27.3	8μm Be	-	-	-

Both of the time-resolved spectrometers were used with Axis-PX ultrafast x-ray streak cameras[193], which are operated with approximately 1–2 ps temporal resolution. Both used CsI photocathodes on Be substrates, were fitted with image intensifiers, and read out to SI1000 CCDs. All of the other instruments utilized Fuji BAS-TR image plate detectors that were scanned 15–30 minutes after each shot with 25 μm pixel size on a Fuji FLA7000 IP scanner.

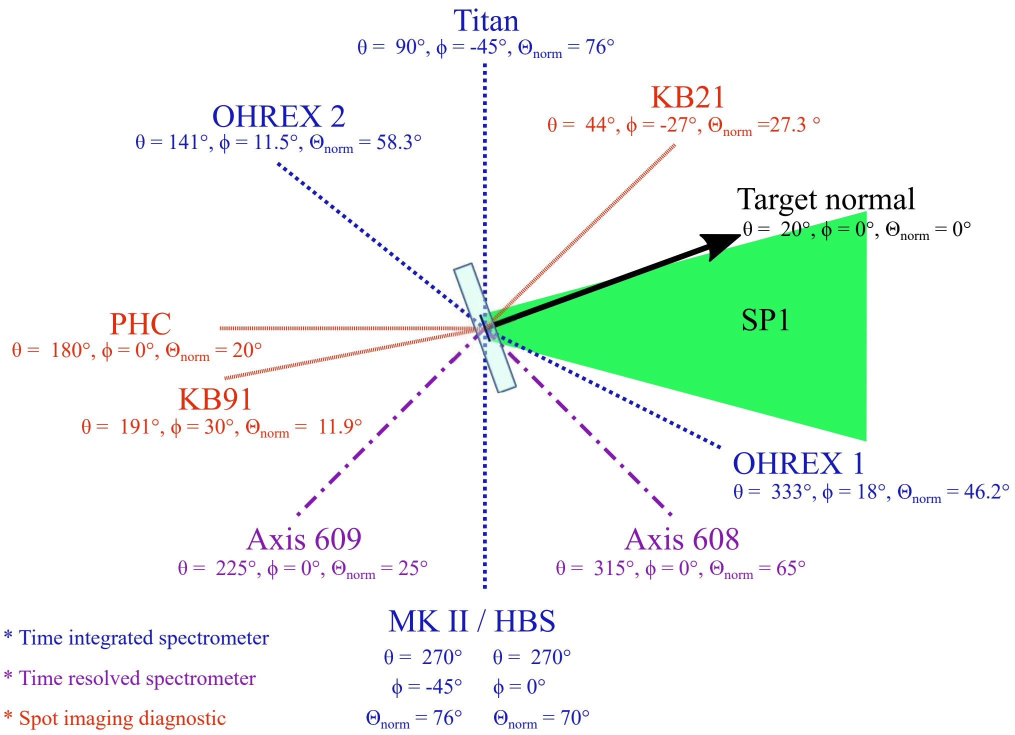

Figure 6.13: Diagnostic arrangement for angularly-resolved spectroscopic measurements at Orion. Names written in blue are time-integrated spectrometers, those in purple are time-resolved spectrometers, and those in red are spatial-imaging diagnostics. The azimuthal angle, θ, is measured counter-clockwise from the short-pulse laser, and the polar angle, ϕ, is given as the angle above or below the equatorial plane shown. Finally, the angle from the target normal surface, Θ_{norm}, is listed for each instrument.

6.3.3 Laser parameters

All of the shots described here used the short-pulse beam line, SP1, frequency-doubled from 1054 nm to 527 nm using a KDP crystal to improve the nanosecond Amplified Spontaneous Emission (ASE) contrast ratio (to $\approx 10^{-18}$ [181]) as well as heating efficiency[156].

Prior to the time of this experiment, the maximum pulse energy was limited to 100 J in a 700 fs pulse by the doubling crystal; however, improvements prior to this experiment allowed for delivery of 200 J to the target. This was achieved by passing the beam through two sub-aperture doubling crystals before refocusing using the same final f/3 parabolic mirror[182]. The temporal offset of the pulses was determined to be better than the pulse duration by the presence of interference fringes. The effects of the interference fringes on the laser-plasma interaction are not known, but the fringes do not show up in imaging of the x-ray spot. For high-energy shots, both beams were spatially defocused to create a 75 μm spot, overfilling the standard 50 μm microdots to decrease radial gradients. Both configurations delivered approximate intensities of 5x10^{18} W/cm^2.

6.4 Experimental Results

In this section, I present analyses of data collected from 100 μm, square, microdot targets. The pure Si layer is 1500 Å thick and asymmetrically tamped with 3, 7, or 10 μm front tamps and varied rear tamps. Table 6.2 summarizes the target and laser specifications for each shot.

Table 6.2: Shot list for analyzed silicon data

Shot number	Materials	Thickness (μm)	Focal spot size (μm)	Laser Energy (J)	Pulse width (ps)
6583	PyN / Si / PyN	3 / 0.15 / 20	50	182	0.62
6597	PyN / Si / PyN	7 / 0.15 / 3	75	162	1.5
6598	PyN / Si / PyN	10 / 0.15 / 3	75	184	1.49

6.4.1 Spot size measurements

The spot sizes of each target were measured with a pinhole camera (PHC) and two Kirkpatrick and Baez (KB) microscopes[263]. The pinhole camera provided the best images due to its 20° viewing angle. The PHC magnification was set to 10, and data were recorded on TR IP for an on-target resolution of 10 μm. Stray light and soft x-rays were rejected with an 8 μm-thick beryllium front filter. After correcting for the viewing angle, the resulting x-ray spot sizes were by 69x66 μm, 63x60 μm, and 66x55 μm, respectively, for the three shots shown in fig. 6.14. These values are close to the expected spot size and indicate that the laser was not grossly misaligned with the microdot. Furthermore, the spot is fairly uniform without any clear evidence of the two separate focal spots or interference fringes.

The heated regions are smaller than the 100 μm microdot size, so a radial gradient is expected. The plots in fig. 6.14 show the radially-averaged hot-spot profiles. These are the average of 12 profiles taken 15 degrees apart to span the full rotational symmetry of the images. They were fitted

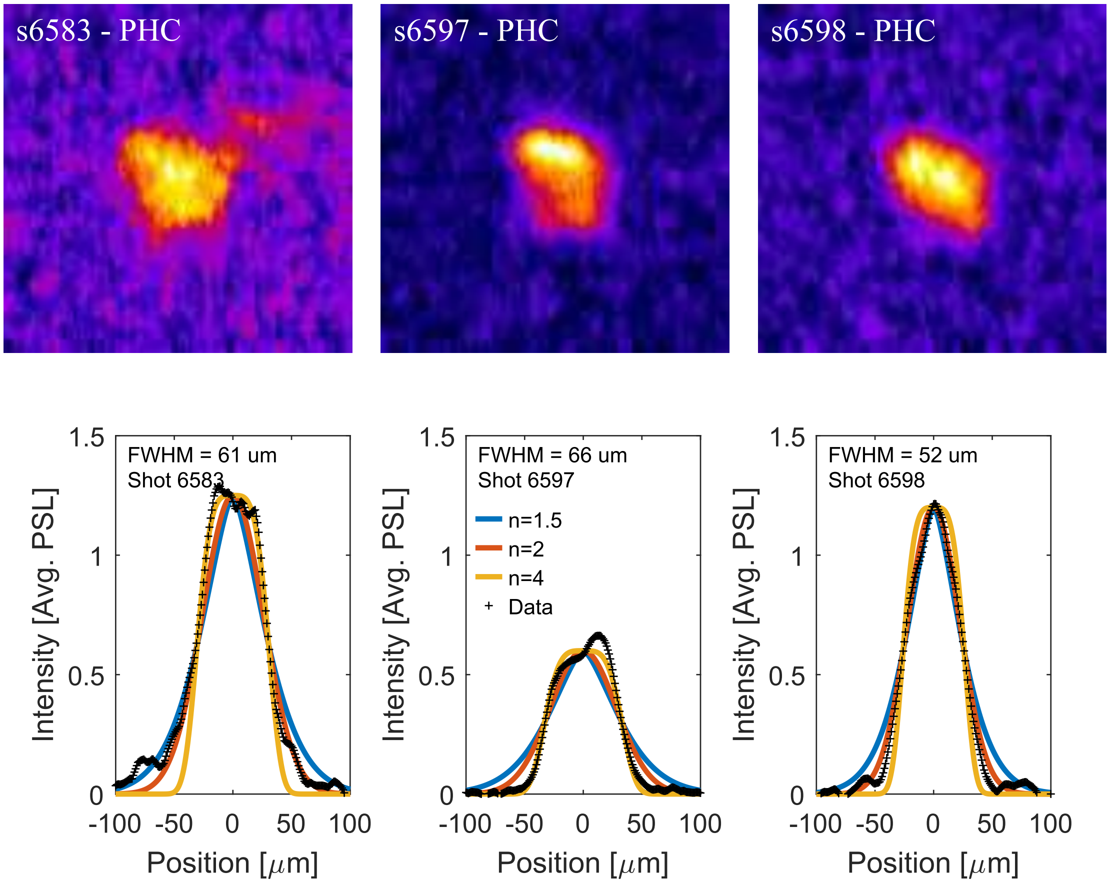

Figure 6.14: Heated region images from the pinhole camera (PHC) for Orion facility shots 6583, 6597, and 6598. The images are oriented so that vertical is vertical in the experimental configuration. The spot sizes, after correcting for the viewing angle, are (width x height) 69x66 μm, 63x60 μm, and 66x55 μm, respectively. The bottom row show the radially-averaged images (over 12 lineouts, 15-degree separation) along with super-Gaussian fits with exponents n = 1.5, 2, and 4.

with a super-Gaussian of the form

$$I(r) = I_0 e^{-0.5\left(\frac{r-r_0}{w_0}\right)^n} \tag{6.2}$$

where $w_0 = \frac{FWHM}{2\,(2\,ln2)^{1/n}}$. In general, the heated region is well-fit by an exponent n = 3–4. Some signal persists beyond the 100 μm of the target; this is likely caused by the plastic and could be eliminated with thicker filters or a Ross filter pair.

6.4.2 Time-integrated spectra

Time-integrated spectra provide the average temperature and density while the target emits at its brightest. If the temperature or density change significantly while signal from the target is measurable, the time-integrated spectrum will contain emission from charge state distributions that existed at different phases of the target's evolution. The benefit of spectra created by a short-pulse laser is that material does not emit for extended times relative to hydrodynamic time scales, and only spectra from a narrow range of conditions are recorded. This is further improved by the buried-layer experimental platform which limits expansion of the active layer to the time it takes a rarefaction wave to travel through the tamp layer. Thus, the time-integrated spectra presented here are averages but only include emission from a narrow temperature and density phase space.

Three spectrometers—the MKII, the Titan, and the HBS—measured most of the K-shell. They captured the He-α (1s^2-1s2p), Ly-α (1s-2p), He-β (1s^2-1s3p), Ly-β (1s-3p), and associated satellites. It is possible the He-γ (1s^2-1s4p) also exists during some late times, but the transition is broad and signal sufficiently low that it merges with the continuum and is poorly resolved. All transitions from higher principal quantum number states are pressure ionized into the continuum and do not exist[243].

Figure 6.15 shows IP data for the Titan and MKII spectrometers on shot 6598. The white boxes show the area over which an average lineout was taken. The TR image plate has 100 μm spatial resolution[264], so the MKII is averaged over 680, 25 μm pixels, or 170 resolution elements. The Titan is averaged over 70 resolution elements. This averaging provides good count statistics for each energy, but the resolution of the spectrometers using CsAP will be determined by the crystal-intrinsic resolution. According to rocking curve measurements by Beck, this will be $E/\Delta E \approx$ 600–900 [205].

The OHREX 1 spectrometer measured the Si He-α complex, and the OHREX 2 measured the Si Ly-β transition. These are used as a consistency check—particularly for the density—on the plasma conditions inferred from the Titan and MKII because of the OHREX diagnostic's superior resolution ($E/\Delta E \approx$ 9000 [262]).

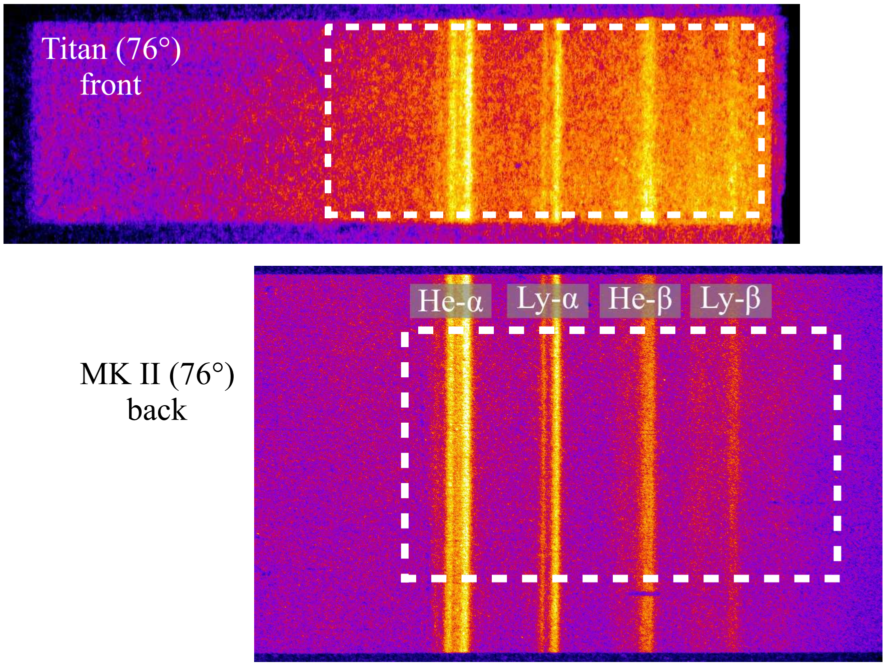

Figure 6.15: Time-integrated silicon spectra for shot 6598 for the Titan and MKII time-integrated spectrometers. The white dotted boxes represent the area over which an average lineout was taken.

The time-integrated spectrometer data shown in fig. 6.16 have been corrected for background, Be filters, CsAP-integrated reflectivity, TR image plate response, and converted to CGS-specific intensity units. The energy dependence of the solid angle is small and, therefore neglected. The background is subtracted as a low-order polynomial fit to points between spectral lines and away from satellites.

Figure 6.16 shows three shots of increasing temperature (S6598, S6597, and S6583) as measured by spectrometers at three unique angles. These data have been normalized by the amplitude of the He-β transition—the simplest, optically-thin feature present on all spectra. This normalization removes the effect of increasing path length and leaves only differences due to opacity. This is verified in the amplitude of Ly-β and in the Li- and He-like satellites to the alpha lines, which are also optically thin and share very similar amplitudes after the normalization. The intensity of the alpha lines decrease with increasing angle of observation from target normal, as expected. The MKII and Titan view the same angle on opposite sides of the target. They look through different thicknesses of CH tamp but remain very similar, supporting the choice to neglect the tamp layers in

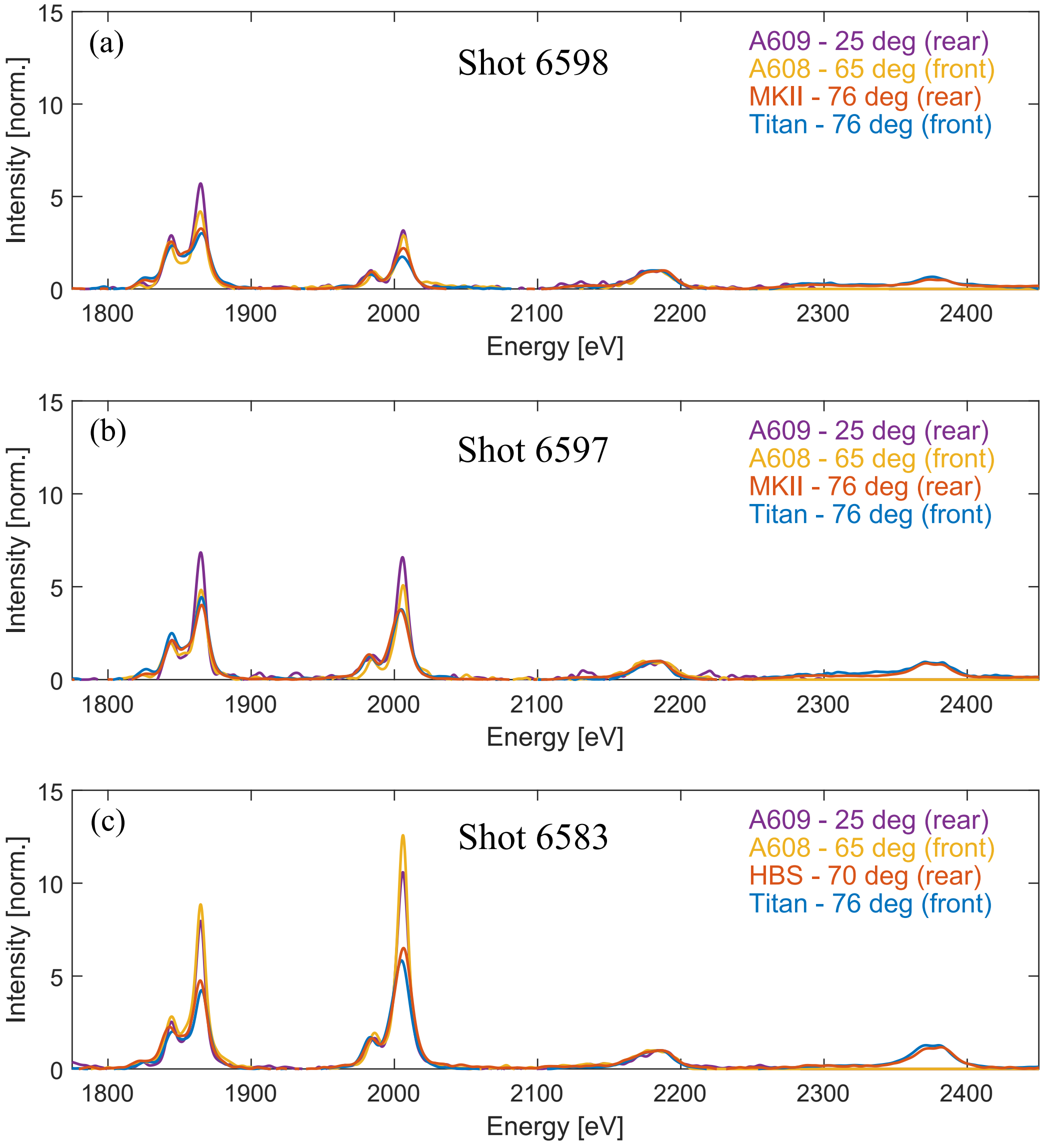

Figure 6.16: Time-integrated silicon spectra measured for shots 6598, 6597, and 6583. Each shot has four time-integrated spectra—two from the integrated signal of a streak camera, and two from image plate detectors—at three unique angles. Intensity units have been converted to be in CGS and normalized to the amplitude of the He-β transition. All spectra have been convolved with a 4 eV FWHM Gaussian ($E/\Delta E \approx 500$) for equivalent comparison across instruments. The optically-thick alpha lines follow the expected trend, decreasing relative to the He-β line, with increasing angle from target normal.

the modeling efforts. Additionally, the similarity between data measured from the front and back indicates the longitudinal gradient within the target remains small or, at the very least, is symmetric about its mid-plane (see fig. 6.11).

6.4.3 Time-resolved spectra

Two time-resolved spectra were measured for each shot using the Axis x-ray streak cameras[193]. The images required correction for temporal distortion using the onset of the continuum emission between spectral lines as $t = 0$. Figure 6.17 shows the streaked images for shot 6598 after making these corrections.

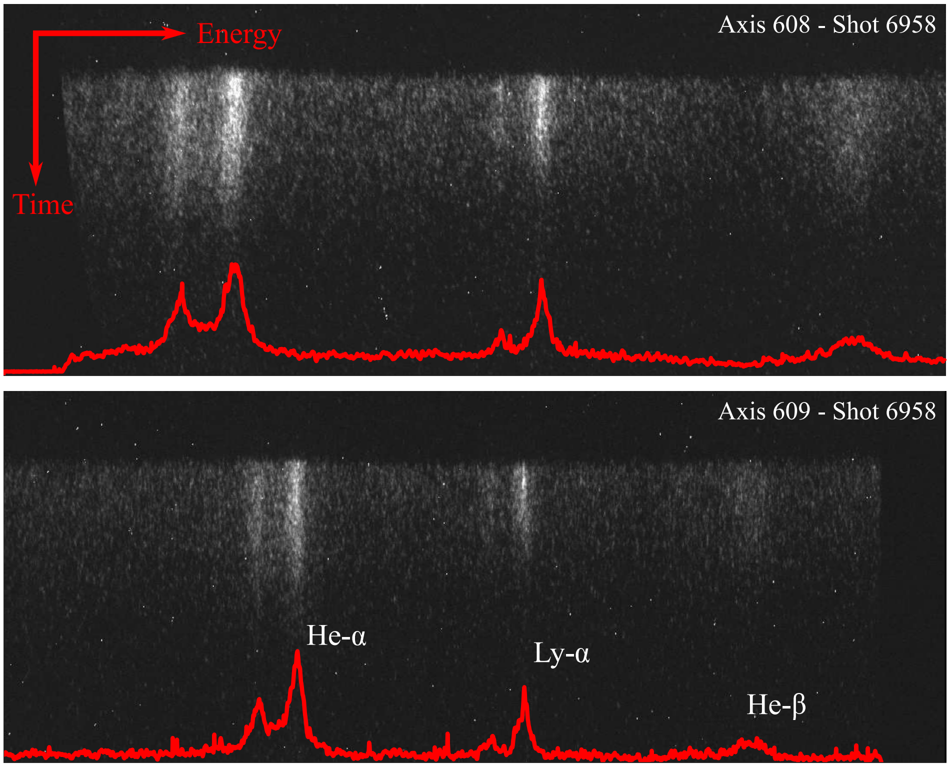

Figure 6.17: Streaked images from the Axis 608 (65° from target normal) and the Axis 609 (25°) for shot 6598. The He-α complex with lithium-like satellites, the Ly-α with helium-like satellites, and the He-β are within spectral coverage. The red overlaid line is the time-integrated spectrum of the streak.

The sweep speed is 0.25 ps/pixel based on the knowledge of the 500 ps sweep window spread over 2000 active pixels of the CCD. One way to improve this would be to perform a sweep-speed calibration with an interferometer and pulsed UV light source. Assuming a temporal resolution of 1 ps, the data is oversampled by a factor of 4. However, to improve the signal-to-noise, the data is binned in 3 ps segments. This provides 17 spectra before the signal is too weak to analyze. The previously-mentioned intensity corrections have been reapplied here (with the detector response being that of a CsI photocathode, rather than TR image plate). The background is subtracted from flat regions between spectral features for each time slice assuming insignificant underlying continuum.

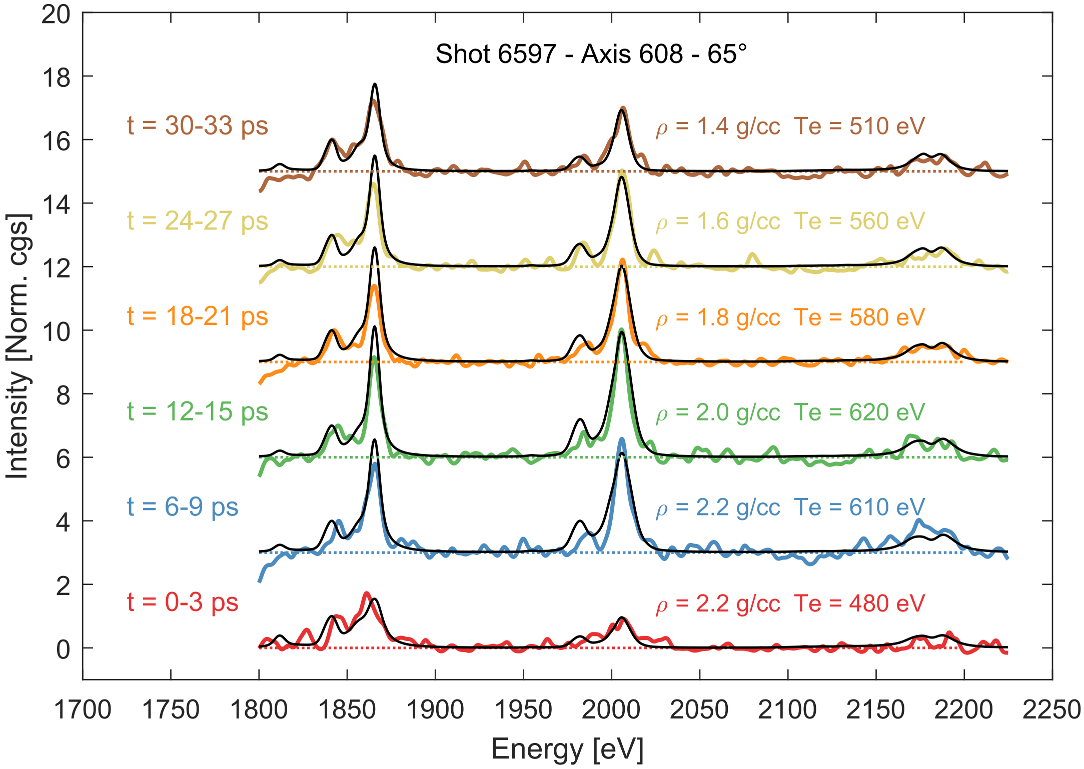

Figure 6.18: Time-resolved data from shot 6597 for the Axis 608 streak camera with a viewing angle of 65 degrees from target normal. The data have been integrated into 3 ps bins and convolved with a 4 eV Gaussian ($E/\Delta E \approx 500$) to improve the signal-to-noise and reduce the electronic noise introduced by the streak camera intensifier and CCD.

Figure 6.18 shows spectra from the Axis608 instrument for shot 6597 at six times. At the earliest times, there are no significant emissions from hydrogen-like ions in addition to large beryllium- and lithium-like satellites. By the 6–9 ps time slice, the Ly-α is nearly maximized. Beyond this point, the Ly-α begins decreasing again as the plasma cools. Temperatures can be inferred for approximately 45 ps before the signal is too dim. The density starts at roughly 2.2 g/cc and decreases to 1.4 by t = 30 ps. However, the signal in the beta line is quite faint, and the uncertainty in the inferred density is as large as $\pm 50\%$ when below solid density.

The opacity of the alpha lines makes them challenging to fit satisfactorily, as shown in figure 6.18. Matching the temperatures for the time-resolved data was done by fitting voigt and Lorentzian curves to the models and data, then comparing the integrated signal of the Ly-α to the He-α lines. This captures kinetic effects on the ionization balance due to radiation trapping but to some extent bypasses uncertainties in line-broadening calculations. This ratio is shown in fig. 6.19(b) for the 1-D transfer, optically-thin, and radial-gradient case. Figure 6.19(a) shows an example of how the curves were fit to the He-α line complex. The PeakFit tool for Matlab, written and maintained by Professor Tom O'Haver, was used to fit these curves[265]. Curves 1 and 2 are due to lithium-like dielectronic satellites. Obtaining a unique fit to curves 2 and 3 proved challenging, so all of the presented ratios are the integral of curves 2 and 3 combined. The satellite contributions are optically thin and the resonance line optically thick, so this contamination introduces some angular dependence on the ratio. The ratios for 65° are shown, though each diagnostic is matched to a curve calculated at its angle in the analysis. The time-resolved temperature profiles are shown in the following section.

6.5 Discussion

The principle aim of this work is to compare the escape-factor approximation with a more complete radiation-transfer calculation. This comparison is shown for shot 6597 in figure 6.20. The agreement between a Cretin 0-D escape factor calculation—using the Apruzese escape factors for voigt line shapes[251]—with the 2-D transfer calculation is excellent. The agreement with a 1-D transfer calculation, which removes skin-depth effects in one dimension, is even better. The beta lines are identical between both models, resulting in the same inferred temperatures to within a few

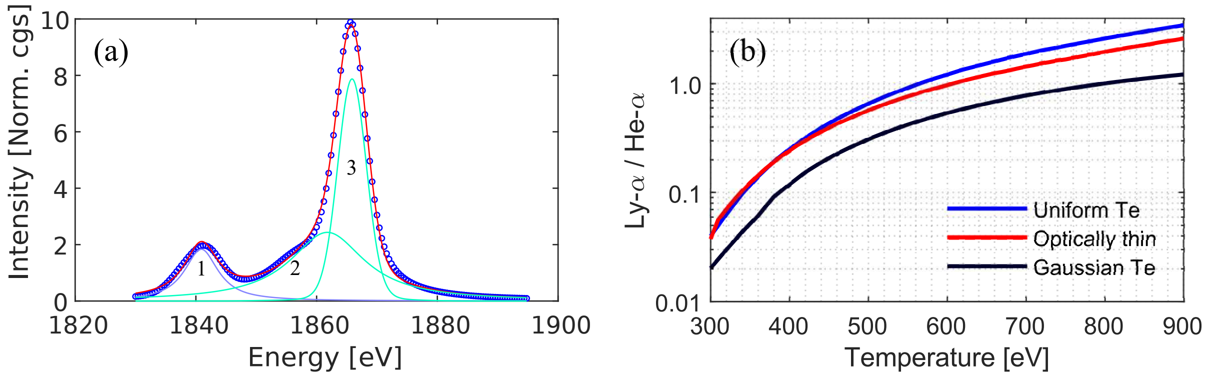

Figure 6.19: The He-α complex has been fit to three curves for integration. Curves 1 and 2 arise due to Li-like satellites and curve 3 from the resonance line. Curves 2 and 3 are included in the ratios shown in (b). The ratios used to fit temperatures to the alpha lines are shown in (b) for a single-temperature, optically-thin, and a Gaussian temperature profile case.

percent. The escape-factor calculation predicts slightly higher intensities in the optically-thick alpha lines, and lower intensities in the Li- and He-like satellites to the alpha lines. This is consistent with the findings of Kerr *et al.*[246] and Dumont *et al.*[247].

This excellent agreement is not unexpected. The material is relatively low-Z, the plasma sufficiently collisional, and the average ionization is close to the closed helium shell. These conditions all minimize the effect of radiative transitions or the uncertainty in calculating them. Additionally, high material density reduces the number of bound states through pressure ionization, and the lines are well separated in frequency. This limits radiative pumping of one transition by another. Finally, the targets are thin enough that the underlying continuum radiation is quite low, and the tamp prevents density gradients. Nonetheless, validating this approximation here is a valuable first step before moving on to systems where agreement is less likely.

The model agrees quite well with the data, but several differences do exist. The positions of the dielectronic satellites to He-α are calculated by FAC[109] and are 3 eV too low in energy. The beryllium satellites are 15 eV too low in energy. This will change the shape of the calculated He-α complex slightly, but play no significant role in the kinetics.

The most notable difference is the intensity of the alpha lines. He-α and Ly-α are both over-predicted at 25 degrees and under-predicted at 76 degrees. Figure 6.21 shows the ratio of the

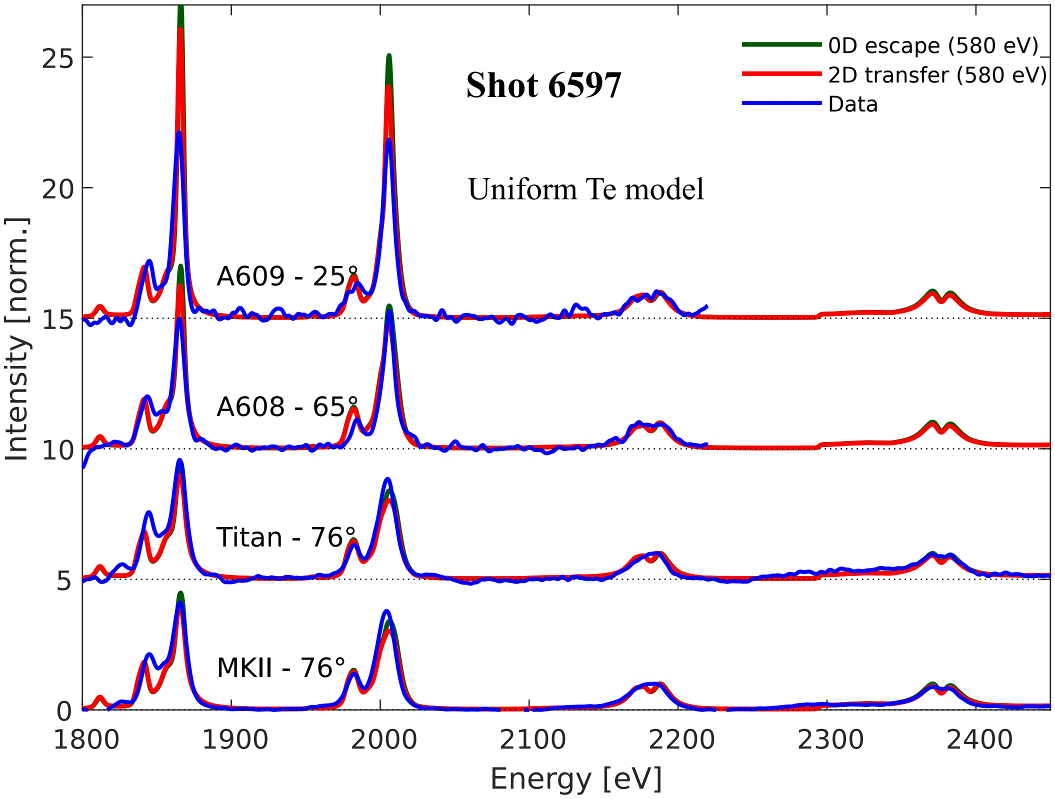

Figure 6.20: Comparison of time-integrated spectra at 25°, 65°, and 76° from shot 6597 with 0-D escape factor and 2-D transfer calculations from Cretin.

simulated line-integrated intensity to the data. The error bars on the plot are based on the uncertainty added to the integration due to satellite contamination (see fig. 6.19). This trend with increasing angle persists for shot 6598. The causes for this discrepancy remain an open question. The most likely suspects are the line shapes. At small angles, the intensity of the optically-thick alpha lines will be determined by the plasma conditions—though n = 2 lines are insensitive to Stark broadening. As the angle increases, opacity broadening dominates, and this could mask errors in the line intensity. More work is required to explain the nature of this observation.

The secondary aim of this work is to quantify the effect of radial gradients on spectroscopically-inferred temperatures. The 2-D simulations described in Section 6.2.4 are compared against the data from shot 6597 for the n = 2 (Gaussian) case in figure 6.22. The disagreement in the amplitudes of the alpha lines persists in the radial-gradient calculations, ruling this out as a cause for the

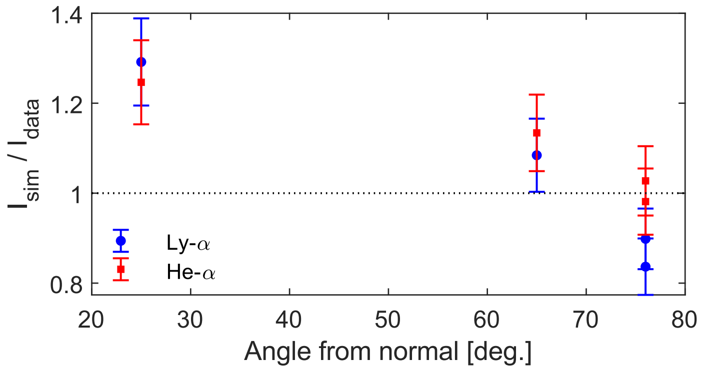

Figure 6.21: Comparison of predicted, integrated, alpha line intensity at each angle to the measured. Small angles are over-predicted by current simulations, and large angles are correct or slightly under-predicted.

discrepancy shown in figure 6.21. The most striking difference appears in the inferred peak temperatures. The Gaussian case fits—based on the ratio of beta lines, which are not shown—with a peak temperature of 840 eV, compared with the single-temperature fit of 580 eV. This corresponds to a mass-averaged value of 526 eV over the 100 μm target. Spectrally, the only thing that sets the radial gradient case apart is the increased Be- and Li-like satellite emission in the He-α complex. In fact, it appears that the Li-like satellites are overestimated in the $n = 2$ case, but underestimated in the uniform case when compared with data. This would be consistent with the radially-averaged spot size measurement presented in fig. 6.14, which shows that the heated region in shot 6597 is best fit by a super-Gaussian with $n = 4$. For the $n = 4$ case, the best-fit peak temperature is 680 eV with a 500 eV mass average (taken over the 1/e^2 spot $\approx$ 78 μm). For this case, the satellites most closely fit the data.

Radial gradients can play a significant role in the interpretation of a time-resolved temperature. Figure 6.23 shows time-resolved temperatures inferred from streak camera data for shot 6597. The temperatures were determined by comparing the integrated alpha-line ratios for each 3 ps time slice to theory. The left pane is the time history inferred by fitting the data to a uniform temperature model, the middle to a 2-D radial gradient model with a super-Gaussian temperature distribution with $n = 4$, and the right a 2-D radial gradient model with a Gaussian temperature distribution. The y-axis displays the peak temperature of each model. The red data points come from

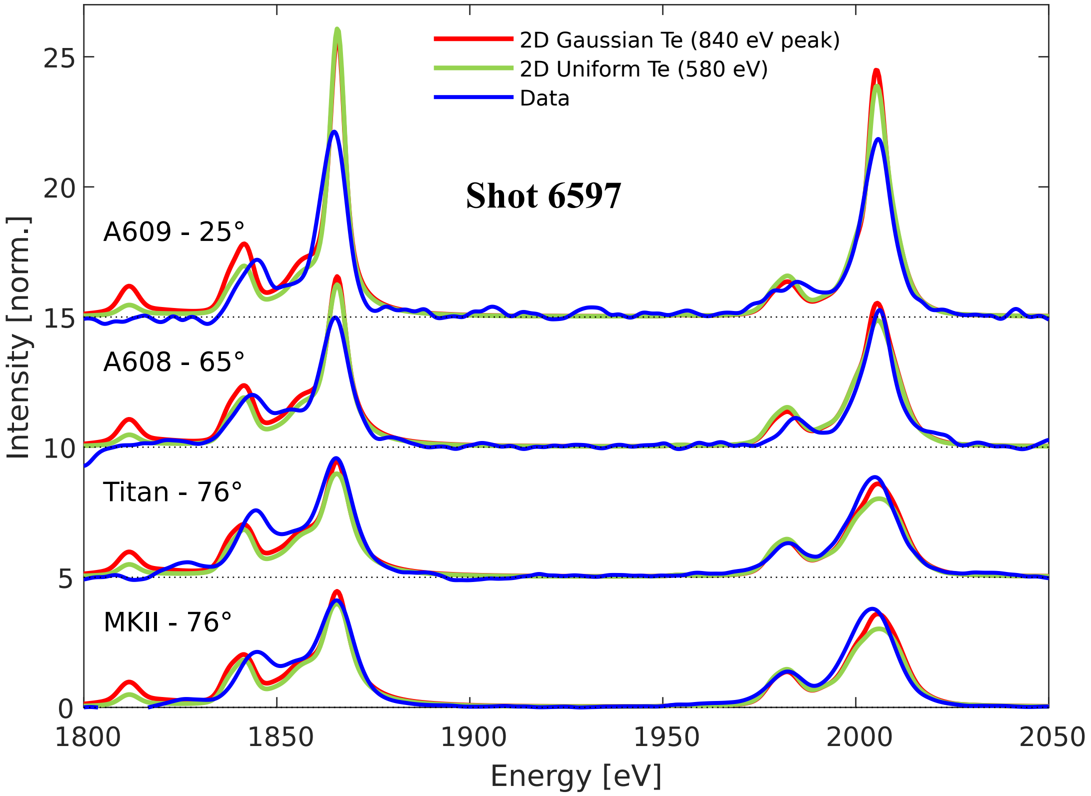

Figure 6.22: Comparison of a uniform Te calculation at 580 eV with a Gaussian temperature simulation with a FWHM of 60 um and peak Te of 840 eV.

the streak camera measuring at 25°, and the blue from the camera at 65°. The profiles are similar, indicating opacity effects do not significantly alter the use of integrated alpha lines as a temperature diagnostic. However, A609—which looks through a smaller optical depth—does exhibit a more sharply-peaked temperature profile. This trend is observed in the other two analyzed data shots. Though this could be an opacity effect, the larger-angle streak camera also has more signal, indicating that it could be suffering degraded resolution due to space charge. More investigation would be required to resolve this.

The light blue line corresponds to the value determined from the time-integrated spectral data (the MKII, Titan, or HBS). The time-integrated temperature inferred from the beta-line ratios matches the one from alpha ratios to within a few percent, establishing confidence in the method. Summing a synthetic spectrum for each point in the streaked time history yields time-integrated

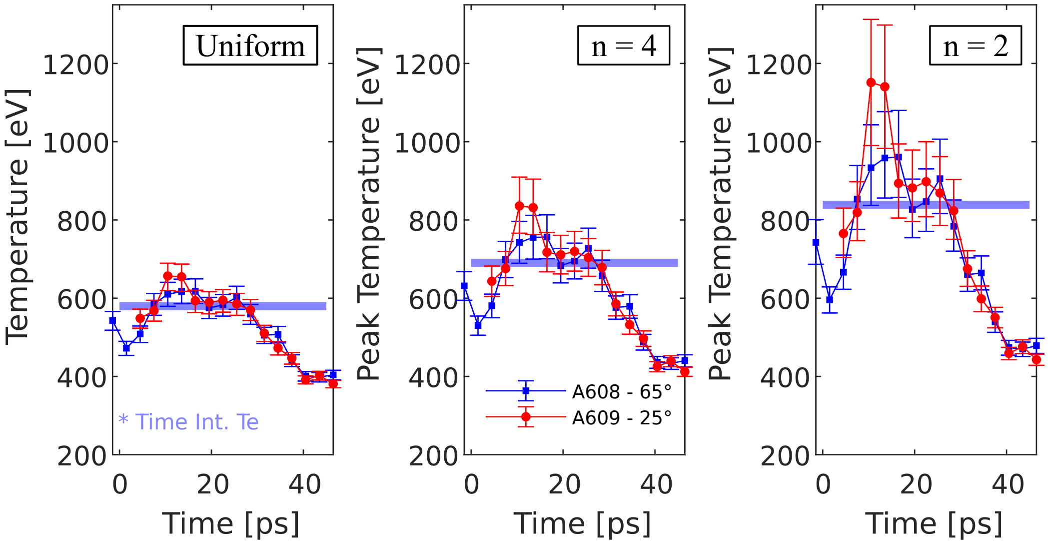

Figure 6.23: Time-resolved temperatures for shot 6597 for Axis 609 at 25° and Axis 608 at 65°. Each pane represents the inferred peak temperature at each time assuming a uniform temperature target, a super-Gaussian Te target with $n = 4$, and a Gaussian target with $n = 2$. Error bars are determined assuming a $\pm 10\%$ uncertainty in the integrated line ratio, leading to larger fractional error bars toward higher temperatures.

temperatures within several percent of the one inferred from the time-integrated spectrometers. This is true for each of the three hypothetical time histories in fig. 6.23, indicating the temporal gradient places no constraint on the radial gradient assumed to analyze the data. This is quite troublesome. The assumption of a radial gradient leads to nearly a factor of 2 difference in the peak temperature inferred.

The temporal evolution measured from similar aluminum buried-layer targets has been shown to disagree with hydrodynamics simulations by Marley *et al.*[255, 266]. The measured cooling rate of these targets is too slow relative to hydrodynamics predictions. Marley demonstrated agreement with 1-D hydrodynamics simulations using a temporally-extended heat source. This was physically motivated by a description of lingering hot electrons due to electron refluxing. This idea was experimentally supported by prior measurements done by Chen *et al.*[267]. These measurements show that the time history of titanium K-α emission from a tamped target, irradiated with 1x10^{18} W/cm^2 of 1054 nm laser light, was greater than 13 ps—very similar to the length of the heating source used Marley used to match the data. Marley achieved the best agreement with data using a 2-

D particle-in-cell (PIC) simulation. The calculation incorporated a radial-intensity profile derived from the measured focal-spot profile, using the energy content of the hot electron population as a fitting parameter. The excellent fit was attributed to the inclusion of a more accurate treatment of electron refluxing in the PIC simulation, but radial temperature variations were also included in this modeling.

The data presented in figure 6.23 indicate that the derived cooling rate can be strongly influenced simply by the presence of a radial gradient. In particular, when temperatures are high enough to fully ionize the hottest region in the target, as is the case for aluminum and silicon, a radial gradient will act to flatten the cooling curve by significantly underestimating the peak temperature. This situation corresponds to the 50 percent error shown in the inferred temperature at 900 eV in figure 6.9.

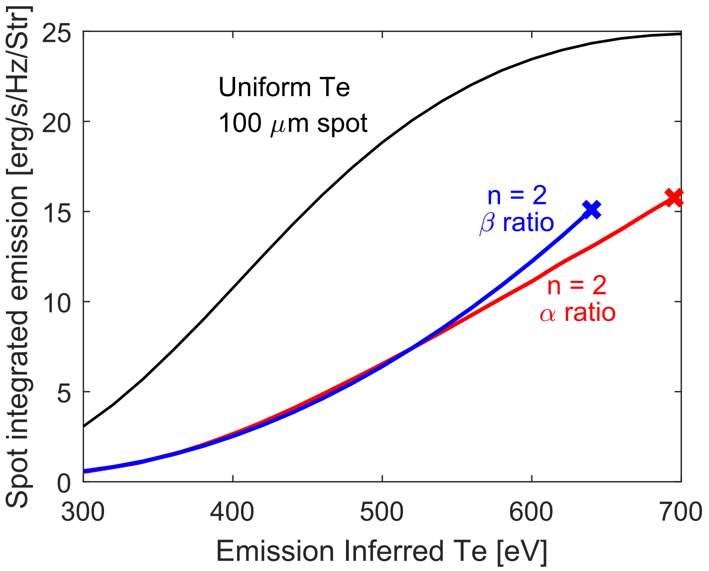

Figure 6.24: Spatially- and spectrally-integrated intensity as a function of the spectroscopically-inferred temperature for a single Te target and a 60 μm FWHM Gaussian temperature distribution target. Both targets are 100 μm in size.

It appears that spectral measurements alone struggle to determine the presence of a radial gradient. The ratio of the satellites changes, but one would have to use a well-benchmarked model with particular care taken in the calculation of these transitions. Experimentally, these lines are often very weak and have poor signal-to-noise—especially in time-resolved diagnostics. The total emitted signal may be used as an additional constraint. Figure 6.24 shows the spatially- and spectrally-integrated emission (from 1700–2500 eV) calculated by Cretin for a 100 μm-diameter target. At 300 eV, the uniform-temperature spot has 4-times more signal than a Gaussian-distributed spot with the same spectrally-inferred temperature. At 650 eV, the uniform spot still emits nearly twice the signal. According to the calculation, a Gaussian spot on a target this size cannot appear to be hotter than 700 eV. This occurs as a result of the over-ionization of the target center, which will not contribute to the measured emission when it becomes fully stripped. Nonetheless, the difference between a Gaussian temperature distribution and uniform temperature distribution should still be experimentally observable. The total emission from the uniform temperature evolution shown in fig. 6.23 is 1.52-times higher than the total emission from the $n = 2$ Gaussian temperature distribution. This indicates that an absolutely-calibrated crystal spectrometer, or even an appropriately-filtered x-ray diode, is essential in distinguishing the presence of a radial gradient.

6.6 Conclusions

In this chapter, I have presented a study of the effects of trapped radiation on ionization balance and inferred temperature for conditions relevant to the buried-layer opacity experiments underway at the Orion Laser Facility. These targets are 1–2 g/cc, 1500 Å thick, and have temperatures ranging from 500–1000 eV. For these conditions, the helium- and Lyman-alpha lines have maximum optical depths of 5–10 at normal incidence, and up to 40 for the larger measurement angles of 76°. It was shown that the radiation field resulted in increased ionization due to the ladder-ionization mechanism. This results in a lower temperature required to achieve the same ionization balance. However, for silicon, neglecting radiation trapping entirely only results in an approximate 10% temperature error.

The use of escape factors to calculate the synthetic spectrum was compared with a full linearized solution of the radiation transfer equation with Cretin. Using Apruzese's planar escape factor for voigt line shapes, agreement with inferred temperatures and ionization balance was found to be better than 5% for all conditions tested. This is largely attributed to the simplicity of the system studied. It is low-Z, without underlying continuum, has reasonably small gradients, has largely non-overlapping lines, and is strongly collisional. For these conditions, the escape-factor approximation is excellent and limits the computational demand without loss of accuracy. The 0-D model runs in seconds compared to approximately 10 minutes for the 1-D radiation-transfer model and 2 hours for the 2-D radiation-transfer model. Future work should verify this agreement for targets of increasing atomic number, higher temperatures, and for the case when spectral lines from mixed targets overlap in some portion of the spectrum.

A study of radial gradients was also presented. It demonstrated that for plausible radially-symmetric temperature profiles, a spectral measurement alone can result in inferred peak temperature errors of up to 50 percent. This occurs when the central peak temperature is high enough to fully strip all bound electrons, and the sensitivity of inferred temperatures due to the hydrogen-helium ion ratio is lost. This effect also exhibited strong flattening of the cooling rate in the time-resolved data. Errors of this kind may be alleviated by using a sufficiently high-Z material to keep the ionization peaked near the helium shell for the measured temperatures. However, the maximum temperature is not always known a priori to aid in material selection. In that case, the presence of a radial gradient may be inferred from absolute measurements of the emitted K-shell intensity and an accurate heated region profile measurement in the K-shell wavelengths.

CHAPTER 7

Summary

The aim of this thesis was to generate experimental data capable of benchmarking the commonly-used physics models within simulation codes utilized by the HED community. All experiments demonstrate the use of short-pulse drivers (laser or XFEL) to produce plasmas at high density resulting from short time scales. These materials quickly evolve to LTE conditions due to their high collisionality, allowing for comparison with developed LTE theories. Short-pulse plasma physics experiments pose challenges as many exhibit characteristically small spatial scales and rapid temporal evolutions. Those presented here utilize facilities with sufficient energy to generate large spots ($\sim$10–100 μm) and diagnostics with picosecond-scale temporal resolutions. In the following sections, experiments on thermal conductivity and radiation transport are discussed separately, with a summary of lessons learned and an outlook given for each method.

7.1 Thermal conductivity experiments

7.1.1 Titan experiment

Chapter 4 presented an experiment performed on the Titan laser system at LLNL's Jupiter Laser Facility. A sub-picosecond-duration optical laser was focused onto a solid target, generating an intense proton beam via the TNSA mechanism. Multilayer gold/aluminum targets utilized the Z-dependent difference in the proton stopping power to induce a temperature gradient between the two materials. The rear, and coldest, surface of the target was observed with a streaked optical pyrometer (SOP) and a chirped-pulse Fourier Domain Interferometer (FDI). These provided complimentary time-resolved temperature, reflectivity, and phase shift data as the thermal energy from the hot gold conducted through the aluminum layer. 1D2T hydrodynamics calculations were paired with a Helmholtz wave solver to calculate the optical spatial absorption profiles and reflectivity for each time. The assumption of a Drude model allowed the self-consistent use of tabulated DC electrical conductivities with their thermal conductivities for comparison with temperature and reflectivity data.

The temperature and phase-shift data illuminated the most appropriate gold release EOS, allowing the only free parameter in the simulations (the proton-divergence angle) to be fixed. For the double-layer targets, the reflectivity data proved essential. It showcased a subtle feature—a local minimum followed by an increase in the reflectivity before decaying again. This feature resulted from a maximum in the collision frequency due to the thermal energy arriving at the surface probed by the FDI, a feature sensitive to the EOS, electrical, and thermal conductivity models. Only Sesame 29373—a conductivity model based on the Lee-More-Desjarlais (LMD) framework and tuned with QMD simulations—successfully replicated the feature shown in the data. However, the predicted temperatures were still higher than data for all target thicknesses.

Multiple explanations may account for this. Fixing the free parameter of the heating source based on the single-layer gold data assumes conclusions dependent on the energy-deposition model in gold relative to aluminum. If that model is correct (or equally wrong) for both gold and aluminum, the next most likely conclusion is that the thermal conductivity values are too high. It was shown that reducing the thermal conductivities by as much as a factor of four provided a better fit—both in amplitude and temporal shape—for the two thicker targets. Experimental error bars prevented a finer determination of how much the conductivity model should be reduced.

Lower thermal conductivity values could be explained by the exclusion of e-e collisions in the tested models. For a fully-ionized aluminum plasma in which the Spitzer model is valid, we would predict a 21% reduction in thermal conductivity. This value for material in the WDM regime remains unclear. However, these are the first experimental results for warm dense aluminum that demonstrate large sensitivity to the thermal conductivity, and provide a valuable benchmark in a regime where models are largely untested.

7.1.2 LCLS experiment

Building on the lessons learned from the experiment performed at Titan, Chapter 5 presents a follow-on experiment designed to measure gold/iron at the Linac Coherent Light Source (LCLS). The XFEL differential-heating concept exploits K-shell structure—tuning the pump energy just below the iron edge—to maximize the difference in absorption between gold and iron. The x-ray-heated design provides a prompt, monochromatic heating source without the presence of secondary radiation or particles typically generated by a laser-created proton beam.

I presented an experimental design including two pyrometers at 450 and 800 nm with provisions for the FDI at two wavelengths (400 nm and 800 nm). The finite energy available in the XFEL pulse, low absorption fraction of our targets, and focal characteristics of the beryllium lens meant that the largest radially-symmetric spot size that could be created and measured was approximately 9 μm. This placed the experiment in a signal-starved state requiring collection/imaging optics with very short focal lengths. Keeping three f/1–f/2 optics precisely imaging a 9 μm spot and aligned through many-component, $\sim$5 meter optics chains crossing a vacuum-chamber boundary proved to be extraordinarily difficult. As such, only a partial data set containing brightness temperatures for all target types could be obtained within the allotted beam time.

These brightness temperatures were enough to fix the x-ray heating source and provide a good match to the single-layer gold and iron data. When reapplied here, application of the simulation methodology outlined in Chapter 4 yielded reasonable agreement between the brightness temperature and all combinations of EOS and conductivity models. This instills confidence in the overall simulation technique, lending credence to the accompanying reflectivity calculations—the most promising aspect of the work. The ultrashort heating source generated distinct features in the reflectivity history which—if successfully measured—would clearly differentiate thermal and electrical conductivity models. In particular, targets greater than 100 nm thick demonstrated this feature's ability to constrain the thermal conductivity to better than factors of 4, and possibly 2.

7.1.3 Outlook on thermal conductivity measurements

The method of differential heating provides valuable experimental data sensitive to the electron-thermal and AC electrical conductivities. This builds on previous experimental results which use optical probing of material releasing into vacuum to determine the EOS[228, 227, 165, 268] by introducing the dynamics of a multilayer target with a sharp temperature gradient. The combination of time-resolved temperature and reflectivity data—used in conjunction—provide a powerful tool capable of constraining the detailed evolution of thin targets and can produce high-quality data capable of educating integrated hydrodynamics simulations. The experiments within this dissertation have demonstrated the viability of creating moderately-coupled and partially-degenerate WDM in multiple metals at 2–10 eV and 0.5–10 g/cc.

That said, some limitations exist. Differential heating is not a single-state measurement. While it is most sensitive to thermal conductivities at peak temperature and density conditions, all conditions between the conduction interface and optically-probed surface must be considered. Optical diagnostics initially probe high-density material, but the expanding material rapidly shifts through the complicated metal-insulator transition as the density and temperature drop and the valence electrons become localized. This provides a rich topic of study, but may convolute interpretation of the diagnostics. The accessible physical conditions are currently limited by the ambient density of cold material and the peak temperature reached in the heater layer. Temperature is more-readily varied, but reliable control would require significant effort to achieve.

Target materials must be carefully chosen. Aside from the obvious material requirements necessary to induce a temperature gradient, the experiment should be run in a regime where observables are only sensitive to the thermal conductivity of the rear layer. This is attained when the thermal conductivity of the heater layer is large enough to make it isothermal. In this situation, thermal transport is dominated by the rear layer's ability to receive heat and not the transport of heat within the heater layer. On the other hand, if the rear layer's conductivity is too low, expansion dynamics will dominate thermal signatures in the data.

Future work may enhance experimental results and reach more concrete conclusions, with suggested areas for improvement enumerated as follows:

1. **Reduction of systematic error bars**—Systematic error bars ranged from 10–20%. These result from uncertainty in diagnostic calibrations. They add uncertainty in the absolute temperature, but do not change temporal evolutions. With precise calibrations, it should be possible to achieve $<$ 5–10% at select wavelengths. Harmonics of short-pulse lasers provide ideal candidates for bright-pulsed sources that can calibrate the shortest sweep speeds of the optical streak cameras used here.

2. **Reduction of stochastic error bars**—The stochastic error bars—those arising from random statistical processes in the electronics of diagnostics—ranged from 5–15% throughout these experiments. These result in uncertainty in the temporal traces measured and play a larger role in obscuring comparison with models. High-repetition rate facilities with energetically-stable drivers are highly desirable and capable of providing the shot statistics necessary to generate precise temporal traces for both reflectivity and temperature. Random error bars below 5% should be achievable with modest statistics.

3. **Reduction of electrical-conductivity uncertainty**—The AC electrical conductivity is necessary for interpretation of optical diagnostics. An expanded set of single-layer data or QMD/Kubo-Greenwood calculations at experimental conditions would increase the precision of thermal-conductivity determination. Improving this data set could relax the current reliance on the Drude model which grows increasingly questionable with decreasing density.

4. **Fabrication of thicker targets**—Targets greater than 200 nm would improve the clarity of thermal traces in the reflectivity, particularly for XFEL-heated targets. A complete set of data for an expanded range of target thicknesses would provide a very tight constraint on thermal-conductivity models. Thicker targets also test conduction at densities closer to solid and increase certainty that electron and ion temperatures are equilibrated.

5. **Detailed energy-deposition modeling**—Currently, the energy deposition is treated as a free parameter in the modeling. Detailed energy-deposition modeling would remove the relative nature of fixing the heating source for all materials based on the heater layer. This could be done using the same data set as the electrical-conductivity measurements.

6. **Reflectivity measurements with P polarization**—Including P-polarization reflectivity measurements in addition to S would provide greater constraint. P-polarized light can drive electron-plasma resonances at the critical surface and is thus more sensitive to both the density scale length (EOS) and the collision frequency.

7. **Varied atomic number targets**—Discrepancies in the thermal conductivity most often arise from a theoretical model's treatment of e-e collisions. This platform is capable of testing most elements that form a homogeneous solid. After reducing the above uncertainties, future experiments could systematically vary Z to test the effect of e-e collisions in WDM.

In summary, the measurement of thermal conductivity of dense plasmas proves extremely difficult yet feasible. Before this work, no measurements in this regime existed. Using the method of differential heating—as presented in this thesis—in lock-step with theoretical modeling heightens our understanding of the complex and intriguing warm dense matter phase space.

7.2 Radiation transfer experiments

Chapter 6 presents data collected during an ongoing collaboration between LLNL and AWE in the United Kingdom to measure the opacity of short-pulse-heated buried layer targets. A fundamental requirement to improving opacity models is benchmarking them at well-known temperatures and densities. For these experiments, temperatures are inferred by matching synthetic spectra generated by a CR model to K-shell spectra from low-Z tracer elements. Therefore, success in benchmarking the opacity is linked to the degree of uncertainty in the modeling technique used to infer experimental temperatures. At high densities, alpha or beta lines often remain the only ones available to infer temperatures. When the lines become optically thick, they form an internal radiation field that impacts the ionization balance and emergent spectrum. Calculation of this radiation field is often neglected or greatly simplified out of necessity.

In this chapter, I present angularly- and temporally-resolved silicon K-shell data and test several assumptions commonly made in CR modeling. First, I test linearized radiation-transfer and simplified escape-factor calculations from Cretin against the angularly-resolved data to quantify how different treatments of the trapped radiation field impact the ionization balance and inferred temperature. The results show that the ratio of helium- to hydrogen-like ions may increase significantly—particularly for temperatures just below the thermal ionization threshold of the closed helium shell—by including treatments of the trapped radiation. However, calculated spectra from both full-transfer solutions and escape-factor methods matched the data closely and inferred the same temperature to within 5 percent for all conditions tested.

The impact of a radial temperature gradient in tamped targets was explored and the inclusion of one led to errors between 20–50% in the peak temperature if the spatially-integrated data were fit using a single-temperature spectrum. Spectra from spatially-integrated targets with super-Gaussian-distributed temperature profiles were compared against uniform temperatures, and virtually no experimentally-resolvable diagnostic evidence of the gradient was present. This error in the peak temperature was shown to change the inferred cooling rate of the time-resolved data. It was shown that an absolutely-calibrated spectral-intensity measurement can provide sensitivity to the presence of a gradient.

Future work should check the escape-factor approximation in situations where spectral lines overlap. For instance, this could occur when multiple K-shell tracers are used in conjunction to maintain sensitivity of the He:H ion ratios across a broad temperature range, or in mixes with higher-Z materials where higher shells may overlap the K-shell diagnostic wavelength. Testing the approximation should also be considered in standard cases where radiation plays a larger role relative to collisions—increasing atomic number, decreasing density, or increasing temperature.

APPENDIX A

LCLS Pyrometer Calibrations

The SOP is relatively simple in concept but quite challenging to implement accurately. Determining a temperature from the target's self-emission requires detailed knowledge of the streak camera and optical system. To get the most accurate measurement, it is best to measure as much as possible in-situ at the experiment. The spatial and temporal calibrations used in the data analysis are presented below.

A.1 Spatial calibration

The first step in characterizing the imaging system was collecting the calibration images. For this purpose, a quad-mesh—purchased from SPI, Inc.—makes an ideal resolution target. The variety used in this work has 10 μm bars throughout, but has four meshes of different periods (125–62–165–83 μm) joined by a vertex at the center. Illuminating the mesh with a sufficiently-bright CW light source and imaging the scattered light provides a minimum resolution, magnification, and field of view in a single image at the correct imaging wavelength. The calibration images from the Axis and Hamamatsu SOPs are shown in figure A.1 along with the mesh geometry. From these images, the total magnifications are determined as 21.5 $\pm$0.5 for the 450 nm SOP and 24.5 $\pm$0.6 for the 800 nm SOP. Using the magnification for the 450 nm SOP along with the diameter of the measured wires gives a 11.3 μm measurement of the 10 μm (nominal) wires. This demonstrates that the imaging system is at least resolving the XFEL spot, enabling the use of the streaked spot size for the SOP calculation of emitting area.

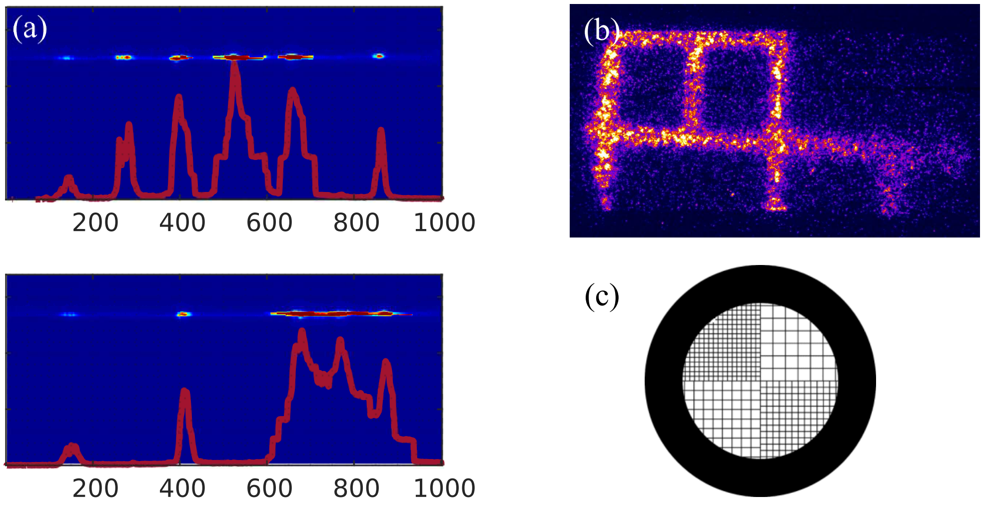

Figure A.1: Spatial calibration images for the (a) 450 nm Axis SOP and the (b) 800 nm Hamamatsu SOP. Both image the SPI quad-mesh (c) illuminated with 405 nm light and imaged in their static imaging modes. Mesh image courtesy of SPI Supplies (www.2spi.com).

A.2 Temporal resolution

The time resolution of the data can be inferred from the data itself in two ways. The first is using the optical fiducial. The fiducial beam originated as a leakage through one of the FDI probe mirrors and was re-compressed to a pulse width of less than one picosecond in a dedicated compressor. The FWHM of the probe on the streaked image is a measure of the temporal response. Figure A.2 shows lineouts of the fiducial on the 450 nm SOP, giving an average FWHM of 5.3 picoseconds. The 800 nm SOP was calibrated at Europa prior to the experiment (fig. 3.9), but fiducial measurements gave a comparable 5 ps at the time of the experiment.

Alternatively, the time resolution can be inferred from the rising edge of the emission in the single-layer data. The time required to heat with an XFEL is expected to be less than a picosecond for solid density material. As such, the rising edge of the emissivity (counts) measured will also be limited by the instrumental response. Assuming instrumental response acts to broaden a Delta function input into a Gaussian distribution, the time from 10% to 90% intensity closely matches the FWHM of the Gaussian response. Taking the time from 10- to 90-percent intensity of the fast rising edge of the LCLS data provides a measure of the time resolution. This comparison was

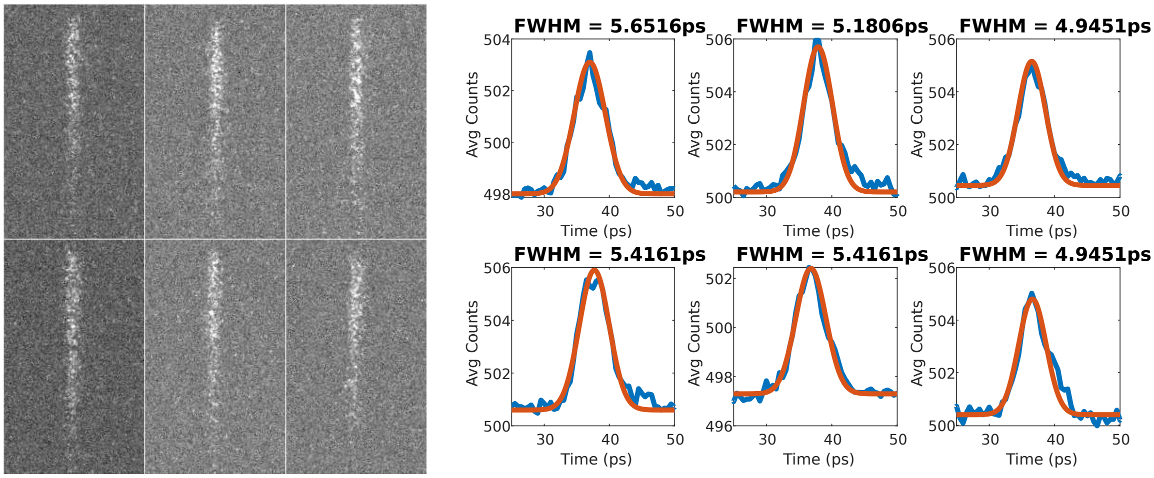

Figure A.2: Shown above are six measurements of the compressed temporal fiducial for the Axis SOP. On the left are the data, and on the right, the corresponding Gaussian fits to the averaged fiducial profile. The average time resolution inferred from this method was 5.3 ps.

completed (not shown) and agreed closely with the prior method of taking the fiducial widths.

A.3 Energy calibration

Finally, the energy calibration of the collection optics, transport optics, and streak camera must be absolutely calibrated. The streak camera response was calibrated on the experimental sweep speed between 425 and 650 nm using a supercontinuum white light source generated by focusing a 2 mJ, 500 fs, Ti:sapphire pulse into a liquid cell containing K_2ZnCl_4[198, 236]. Figure A.3 shows the frequency response in the calibration for the unit used for this experiment in addition to the band in which our BPF allowed signal. The transmission of the optics in the experimental geometry was measured to be 0.35 ±0.02 using a 450 nm CW laser and calorimeter, ensuring that all of the angle-dependent transmission and reflectivity values were as true to reality as achievable.

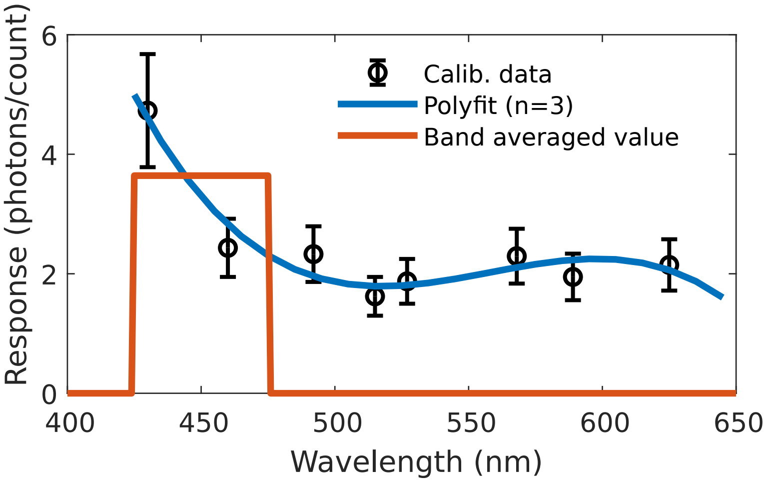

Figure A.3: Axis optical streak camera response used in calculation of temperatures. Shown with the band pass filter used to limit spectrum to 425–475 nm.

APPENDIX B

Thermal-conductivity simulation sensitivity scans

When modeling an integrated experiment, one important aspect is understanding the impact of the uncontrollable and/or immeasurable experimental variables. In this section, I outline some of the experimental uncertainties and present modeling results to state the quantitative impact of these on the primary experimental observable—the rear surface temperature.

- **Impact of Si_3N_4 thickness**

  The silicon-nitride membrane is grown onto a silicon wafer by low-pressure chemical vapor deposition (LPCVD), and the silicon is etched away to create the free-standing membrane. Uncertainty in layer thickness enters through the growth rate and how much is etched away while etching the Si wafer, but is estimated to be 10 percent for layers of this thickness. Figure B.1 shows simulations where the layer thickness is increased to 100 nm, 2.5-times larger than the nominal case, as a worst-case scenario. It can be seen that for the 100 nm Au and 100 nm Au + 100 nm Fe cases, the increased layer thickness causes no noticeable change in the observed temperature. For the 50 nm Fe case, the significantly-increased mass results in the iron layer staying at higher density and temperature longer, and therefore in a slightly-increased temperature from t = 10–40 ps. This difference, considering the extreme upper bound, would not impact results.

- **Impact of Si_3N_4 thermal conductivity**

  The Si_3N_4 thermal conductivity was not the focus of study for this work and so remains

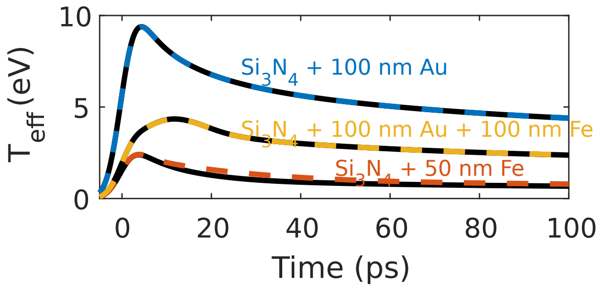

Figure B.1: Effect of changing Si_3N_4 layer thickness from nominal 40 nm layer (black on plot) to 100 nm for three calculation types.

an uncertainty. To quantify the impact of the unknown amplitude of this thermal conductivity, simulations were run with this varied, as shown in figure B.2. Increased K_{th} in the silicon-nitride layer reduces available energy in the iron layer, which is observed as a lower temperature. A two-order of-magnitude change results in a peak difference in the 50 nm Fe of 15%, in the 100 nm Au simulation by 4%, and in the Au + 100 nm Fe simulation by less than 3%. A change to the thermal conductivity this substantial is again physically unlikely, and therefore this is expected to play a minimal impact in data interpretation.

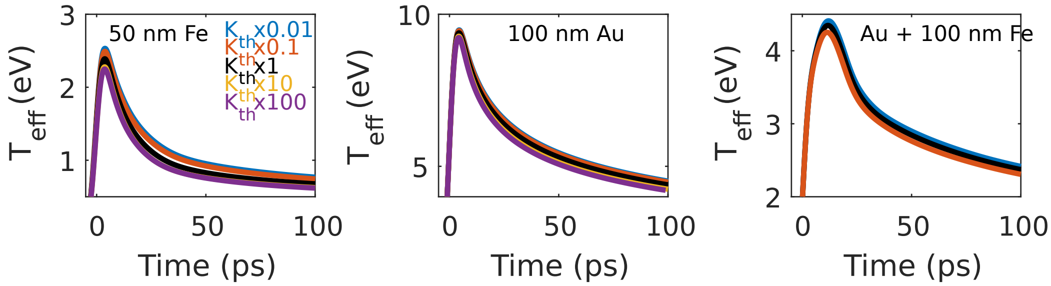

Figure B.2: Effect of changing Si_3N_4 thermal conductivity, using the Lee & More model[13] in HYDRA, by ±2 orders of magnitude.

- **Impact of gold thickness**

  The single-layer gold data is used as the anchor to determining the x-ray source amplitude to use in the simulations. As such, uncertainties in the thickness could potentially be important. The uncertainty in the coating process and measurement of layer thickness on a witness-slide is ±10%. Figure B.3 shows the impact of changing the gold thickness by ±25%, two-and-a-half-times the expected uncertainty, with the impact in the temperature being less than 9%

for thinner targets and less than 6% for thicker targets. Thinner targets demonstrate a larger temperature drop on the 100 ps time scale due to the rarefaction wave propagating through the target sooner.

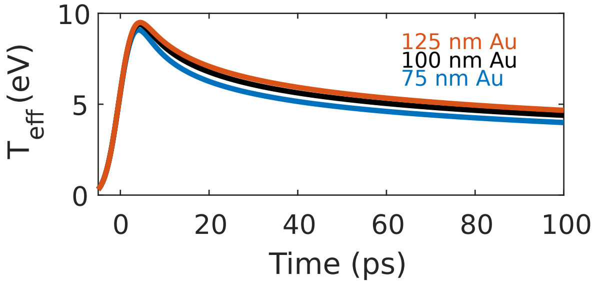

Figure B.3: Effect of changing the thickness of the gold layer in single-layer simulations.

- **Impact of gold thermal conductivity**

  Similarly to the uncertainty in the silico- nitride thermal conductivity is the gold thermal conductivity. In the experimental design, the heater layer's conductivity is much higher than the layer under study, so the thermal transfer is dominated by the conductivity of the study layer. Figure B.4 shows the impact of varying the gold thermal conductivity on single- and double-layer targets.

  In the 100 nm Au target, the nominal case is on a local maximum. If the thermal conductivity is higher than expected, the layer can redistribute heat within itself faster than expansion can introduce a temperature gradient; this is observed as a higher peak temperature but a faster cooling rate at the observed surface. Alternatively, if the thermal conductivity is significantly lower than expected, heat from the densest regions in the target cannot reach the rear surface being observed, and again, the temperature remains low.

  In the double-layer case, the expected saturation for high thermal conductivity values is seen. The 1x, 10x, and 100x cases all have near-identical temperature profiles. However, if the conductivity is much lower than expected, the balance between the gold and iron thermal conductivities become important.

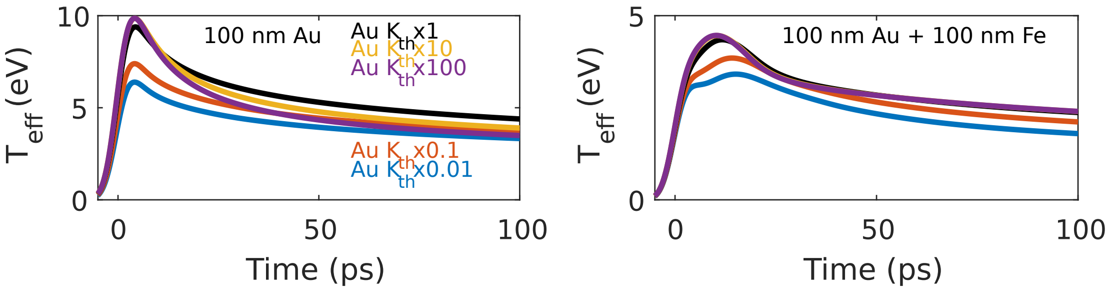

Figure B.4: Effect of changing the thermal conductivity, using the model of Lee & More[13] in HYDRA, in the gold layer for (a) 100 nm Au and (b) 100 nm Au + 100 nm Fe.

While there is a demonstrated sensitivity to the gold's thermal conductivity value, it remains unlikely that the true values will be wrong by multiple orders of magnitude. We expect greater accuracy from the Lee & More model for high-Z metals as the material is more representative of a Lorentz plasma. Furthermore, the physical quantities impacting the conductivity—the density of charge carriers and scattering cross-sections—are unlikely to vary from model to model by enough to result in such large factors. This is, however, the most impactful of the tested uncertainties and a potentially non-negligible uncertainty.

- **Impact of electron-ion equilibration rate**

  The electron-ion equilibration rate is itself an active area of experimental[229, 269] and theoretical[81, 270, 42, 271] study in HED physics. It enters into these simulations through the energy balance within the expanding plasma. The ions carry the majority of the energy and lose it as the plasma expands into the vacuum. The electron temperature is dragged down by the equilibration rate with the cooling ions. In the un-rarefied layer, the density remains high, and there is little deviation between ion and electron temperatures. In the outer regions, there can be deviation.

  These models in HYDRA use an equilibration rate determined by the collision frequencies within the Lee & More model. Figure B.5 shows the impact on the observed temperature of varying the equilibration rate in single- and double-layer iron targets. In both cases, there is not much sensitivity to the equilibration rate. Increasing the equilibration rate by a factor of 10 results in less than a 2% change, while increasing it results in the electrons retaining a larger proportion of the heat, and the observed temperature would increase by 8% for the single-layer iron and 4% for the double-layer case.

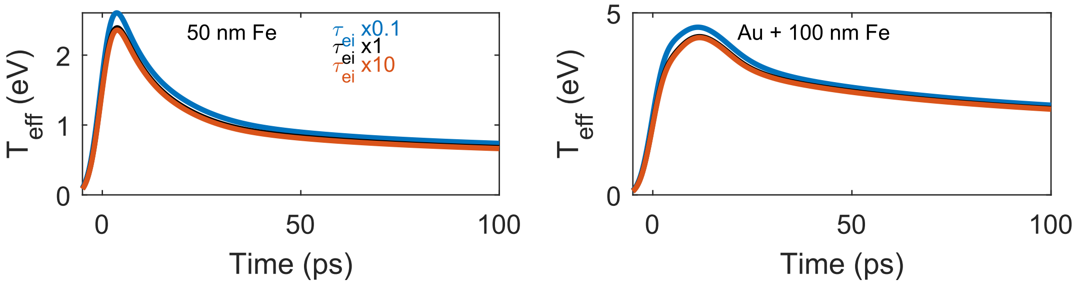

Figure B.5: Simulated temperatures for cases where the electron-ion equilibration rate has been multiplied by 0.1 and 10.0.

- **Meshing convergence study**

  To ensure the final results were fully converged, I performed a convergence study in the spatial meshing of the simulation. The mass-per-cell was matched across material interfaces to prevent numerical artifacts, and the mesh density was increased until the difference in observed temperature was less than 0.1%. The problem is well-converged using at least 1.5 cells per nm thickness of solid density material.

BIBLIOGRAPHY

[1] Q. Williams. The thermal conductivity of earth's core: A key geophysical parameter's constraints and uncertainties. *Annual Review of Earth and Planetary Sciences*, 46:47–66, 2018.

[2] A. J. Biggin, E. J. Piispa, L. J. Pesonen, R. Holme, G. A. Paterson, T. Veikkolainen, and L. Tauxe. Palaeomagnetic field intensity variations suggest Mesoproterozoic inner-core nucleation. *Nature*, 526:245–248, 2015.

[3] K. Ohta, Y. Kuwayama, K. Hirose, K. Shimizu, and Y. Ohishi. Experimental determination of the electrical resistivity of iron at Earth's core conditions. *Nature*, 534:95098, 2016.

[4] Z. Konôpková, R. S. McWilliams, N. Gómez-Pérez, and A. F. Goncharov. Direct measurement of thermal conductivity in solid iron at planetary core conditions. *Nature*, 534:99–101, 2016.

[5] P. Olson. The new core paradox. *Science*, 342:431–432, 2013.

[6] A. S. Bishop and U.S. Atomic Energy Commission. *Project Sherwood: The U. S. Program in Controlled Fusion*, pages v–vi. Addison-Wesley Publishing Company, Reading, 1958.

[7] S. Atzeni and J. Meyer-ter Vehn. *The Physics of Inertial Fusion: Beam Plasma Interaction, Hydrodynamics, Hot Dense Matter*, pages 198–201. International series of monographs on physics. Oxford University Press, Oxford, 2004.

[8] J. M. Di Nicola, T. Bond, M. Bowers, L. Chang, M. Hermann, R. House, T. Lewis, K. Manes, G. Mennerat, B. MacGowan, R. Negres, B. Olejniczak, C. Orth, T. Parham, S. Rana, B. Raymond, M. Rever, S. Schrauth, M. Shaw, M. Spaeth, B. Van Wonterghem, W. Williams, C. Widmayer, S. Yang, P. Whitman, and P. Wegner. The national ignition facility: laser performance status and performance quad results at elevated energy. *Nuclear Fusion*, 59:032004, 2018.

[9] J. Lindl, O. Landen, J. Edwards, and E. Moses. Review of the National Ignition Campaign 2009-2012. *Physics of Plasmas*, 21:020501, 2014.

[10] LLNL. How icf works. `https://lasers.llnl.gov/science/icf/how-icf-works`. Accessed 2019-08-1.

[11] R. Betti and O. A. Hurricane. Inertial-Confinement fusion with lasers. *Nature Physics*, 12:435, 2016.

[12] B. A. Hammel, S. W. Haan, D. S. Clark, M. J. Edwards, S. H. Langer, M. M. Marinak, M. V. Patel, J. D. Salmonson, and H. A. Scott. High-mode rayleigh-taylor growth in nif ignition capsules. *High Energy Density Physics*, 6:171–178, 2010.

[13] Y. T. Lee and R. M. More. An electron conductivity model for dense plasmas. *The Physics of Fluids*, 27:1273–1286, 1984.

[14] V. Recoules, F. Lambert, A. Decoster, B. Canaud, and J. Clérouin. Ab initio determination of thermal conductivity of dense hydrogen plasmas. *Phys. Rev. Lett.*, 102:075002, 2009.

[15] F. Lambert, V. Recoules, A. Decoster, J. Clrouin, and M. Desjarlais. On the transport coefficients of hydrogen in the inertial confinement fusion regime. *Physics of Plasmas*, 18:056306, 2011.

[16] T. C. Killian. Ultracold neutral plasmas. *Science*, 316:705–708, 2007.

[17] R. Rosner, D. Hammer, and T. Rothman. Basic research needs for high energy density laboratory physics. In *Office of Science of Department of Energy (DOE), and National Nuclear Security Administration, Report of the Workshop on High Energy Density Laboratory Research Needs*, page 92, 2009.

[18] F. F. Chen. *Introduction to Plasma Physics and Controlled Fusion: Volume 1: Plasma Physics*, pages 225–285. Springer US, New York, 1983.

[19] S. I. Braginskii. Transport processes in a plasma. *Reviews of Plasma Physics*, 1:205, 1965.

[20] A. R. Hochstim. *Kinetic processes in gases and plasmas*. Reentry physics series. Academic Press, New York, 1969.

[21] P. L. Bhatnagar, E. P. Gross, and M. Krook. A model for collision processes in gases. I. Small amplitude processes in charged and neutral one-component systems. *Phys. Rev.*, 94:511–525, 1954.

[22] J. R. Haack, C. D. Hauck, and M. S. Murillo. A conservative, entropic multispecies BGK model. *Journal of Statistical Physics*, 168:826–856, 2017.

[23] S. Livi and E. Marsch. Comparison of the Bhatnagar-Gross-Krook approximation with the exact coulomb collision operator. *Phys. Rev. A*, 34:533–540, 1986.

[24] E. M. Lifshitz and L. P. Pitaevski. Chapter IV - collisions in plasmas. In *Physical Kinetics*, volume 10 of *Course of Theoretical Physics*, pages 168–216. Pergamon Press Inc, New York, 1981.

[25] M. N. Rosenbluth, W. M. MacDonald, and D. L. Judd. Fokker-Planck equation for an inverse-square force. *Phys. Rev.*, 107:1–6, 1957.

[26] A. Lenard. On Bogoliubov's kinetic equation for a spatially homogeneous plasma. *Annals of Physics*, 10:390–400, 1960.

[27] R. Balescu. Irreversible processes in ionized gases. *The Physics of Fluids*, 3:52–63, 1960.

[28] A. G. R. Thomas, M. Tzoufras, A. P. L. Robinson, R. J. Kingham, C. P. Ridgers, M. Sherlock, and A. R. Bell. A review of Vlasov-Fokker-Planck numerical modeling of inertial confinement fusion plasma. *Journal of Computational Physics*, 231:1051–1079, 2012.

[29] N. A. Krall and A. W. Trivelpiece. *Principles of plasma physics*, pages 78–129. International series in pure and applied physics. McGraw-Hill, New York, 1973.

[30] P. M. Bellan. *Fundamentals of Plasma Physics*, pages 35–46. Cambridge University Press, New York, 2006.

[31] R. P. Drake. *High-Energy-Density Physics: Fundamentals, Inertial Fusion, and Experimental Astrophysics*, pages 26–33. Shock Wave and High Pressure Phenomena. Springer, Berlin, 2006.

[32] S. Chapman and T. G. Cowling. *The Mathematical Theory of Non-uniform Gases*. Cambridge University Press, Cambridge, 1960.

[33] E. M. Epperlein and M. G. Haines. Plasma transport coefficients in a magnetic field by direct numerical solution of the Fokker-Planck equation. *The Physics of Fluids*, 29:1029–1041, 1986.

[34] D. Kang and J. Dai. Dynamic electron-ion collisions and nuclear quantum effects in quantum simulation of warm dense matter. *Journal of Physics: Condensed Matter*, 30:073002, 2018.

[35] P. Hohenberg and W. Kohn. Inhomogeneous electron gas. *Phys. Rev.*, 136:B864–B871, 1964.

[36] W. Kohn and L. J. Sham. Self-consistent equations including exchange and correlation effects. *Phys. Rev,*, 140:A1133–A1138, 1965.

[37] N. D. Mermin. Thermal properties of the inhomogeneous electron gas. *Phys. Rev.*, 137:A1441–A1443, 1965.

[38] V. V. Karasiev, L. Calderín, and S. B. Trickey. Importance of finite-temperature exchange correlation for warm dense matter calculations. *Physical Review. E*, 93:063207, 2016.

[39] M. W. C. Dharma-wardana. Current issues in finite-T density-functional theory and warm-correlated matter. *Computation*, 4:16, 2016.

[40] V. V. Karasiev, T. Sjostrom, D. Chakraborty, J. W. Dufty, K. Runge, F. E. Harris, and S. B. Trickey. Innovations in finite-temperature density functionals. In F. Graziani, M. P. Desjarlais, R. Redmer, and S. B. Trickey, editors, *Frontiers and Challenges in Warm Dense Matter*, pages 61–85. Springer International Publishing, Cham, 2014.

[41] F. R. Graziani, J. D. Bauer, and M. S. Murillo. Kinetic theory molecular dynamics and hot dense matter: Theoretical foundations. *Phys. Rev. E*, 90:033104, 2014.

[42] L. X. Benedict, M. P. Surh, J. I. Castor, S. A. Khairallah, H. D. Whitley, D. F. Richards, J. N. Glosli, M. S. Murillo, C. R. Scullard, P. E. Grabowski, D. Michta, and F. R. Graziani. Molecular dynamics simulations and generalized Lenard-Balescu calculations of electron-ion temperature equilibration in plasmas. *Phys. Rev. E*, 86:046406, 2012.

[43] H. D. Whitley, C. R. Scullard, L. X. Benedict, J. I. Castor, A. Randles, J. N. Glosli, D. F. Richards, M. P. Desjarlais, and F. R. Graziani. Lenard-Balescu calculations and classical molecular dynamics simulations of electrical and thermal conductivities of hydrogen plasmas. *Contributions to Plasma Physics*, 55:192–202, 2015.

[44] R. Car and M. Parrinello. Unified approach for molecular dynamics and density-functional theory. *Phys. Rev. Lett.*, 55:2471–2474, 1985.

[45] W. Lorenzen, A. Becker, and R. Redmer. Progress in warm dense matter and planetary physics. In F. Graziani, M. P. Desjarlais, R. Redmer, and S. B. Trickey, editors, *Frontiers and Challenges in Warm Dense Matter*, pages 203–234. Springer International Publishing, Cham, 2014.

[46] P. A. Sterne. Private Communication, August 2018.

[47] F. Perrot. Ion-ion interaction and equation of state of a dense plasma: Application to beryllium. *Phys. Rev. E*, 47:570–582, 1993.

[48] F. Perrot and M. W. C. Dharma-wardana. Equation of state and transport properties of an interacting multispecies plasma: Application to a multiply ionized al plasma. *Phys. Rev. E*, 52:5352–5367, 1995.

[49] C. Blancard and G. Faussurier. Equation of state and transport coefficients for dense plasmas. *Phys. Rev. E*, 69:016409, 2004.

[50] D. A. Liberman. Self-consistent field model for condensed matter. *Phys. Rev. B*, 20:4981–4989, 1979.

[51] D. A. Liberman. Inferno: A better model of atoms in dense plasmas. *Journal of Quantitative Spectroscopy and Radiative Transfer*, 27:335–339, 1982.

[52] B. Wilson, V. Sonnad, P. Sterne, and W. Isaacs. Purgatorio—a new implementation of the Inferno algorithm. *Journal of Quantitative Spectroscopy and Radiative Transfer*, 99:658–679, 2006.

[53] L. Hedin and B. I. Lundqvist. Explicit local exchange-correlation potentials. *Journal of Physics C: Solid State Physics*, 4:2064, 1971.

[54] J. K. Yuan, Y. S. Sun, and S. T. Zheng. Calculation of the electrical conductivity of strongly coupled plasmas. *Phys. Rev. E*, 53:1059–1067, 1996.

[55] S. B. Hansen, W. A. Isaacs, P. A. Sterne, B. G. Wilson, V. Sonnad, and D. A. Young. Electrical conductivity calculations from the purgatorio code. In *Proc. of the NEDPC*, 2006.

[56] P. A. Sterne, S. B. Hansen, B. G. Wilson, and W. A. Isaacs. Equation of state, occupation probabilities and conductivities in the average atom purgatorio code. *High Energy Density Physics*, 3:278–282, 2007.

[57] B. G. Wilson, D. D. Johnson, and A. Alam. Multi-center electronic structure calculations for plasma equation of state. *High Energy Density Physics*, 7:61–70, 2011.

[58] M. W. C. Dharma-wardana, D. D. Klug, L. Harbour, and L. J. Lewis. Isochoric, isobaric, and ultrafast conductivities of aluminum, lithium, and carbon in the warm dense matter regime. *Phys. Rev. E*, 96:053206, 2017.

[59] D.W. Hahn and M.N. Ozisik. *Heat Conduction*, pages 236–273. Wiley & Sons, Hoboken, 2012.

[60] Y. Ping, A. Fernandez-Panella, H. Sio, A. Correa, R. Shepherd, O. Landen, R. A. London, P. A. Sterne, H. D. Whitley, D. Fratanduono, T. R. Boehly, and G. W. Collins. Differential heating: A versatile method for thermal conductivity measurements in high-energy-density matter. *Physics of Plasmas*, 22:092701, 2015.

[61] A. I. Chugunov and P. Haensel. Thermal conductivity of ions in a neutron star envelope. *Monthly Notices of the Royal Astronomical Society*, 381:1143–1153, 2007.

[62] I. P. Shkarofsky, M. P. Bachynski, and T. W. Johnston. *The Particle Kinetics of Plasmas*. Addison-Wesley Publishing Co., Reading, 1966.

[63] L. Spitzer and R. Harm. Transport phenomena in a completely ionized gas. *Phys. Rev.*, 89:977–981, 1952.

[64] L. Onsager. Reciprocal relations in irreversible processes. I. *Phys. Rev.*, 37:405–426, 1931.

[65] L. Onsager. Reciprocal relations in irreversible processes. II. *Phys. Rev.*, 38:2265–2279, 1931.

[66] J. M. Ziman. *Principles of the Theory of Solids*. Cambridge University Press, Cambridge, 2 edition, 1972.

[67] N. W. Ashcroft and N. D. Mermin. *Solid State Physics*, pages 314–328. Holt, Rinehart and Winston, New York, 1976.

[68] M. Lampe. Transport coefficients of degenerate plasma. *Phys. Rev.*, 170:306–319, 1968.

[69] M. Lampe. Transport theory of a partially degenerate plasma. *Phys. Rev.*, 174:276–280, 1968.

[70] B. Holst, M. French, and R. Redmer. Electronic transport coefficients from ab initio simulations and application to dense liquid hydrogen. *Phys. Rev. B*, 83:235120, 2011.

[71] W. B. Hubbard. Studies in stellar evolution. V. Transport coefficients of degenerate stellar matter. *Astrophysical Journal*, 146:858, 1966.

[72] G. V. Chester and A. Thellung. The Law of Wiedemann and Franz. *Proceedings of the Physical Society*, 77:1005–1013, 1961.

[73] W. B. Hubbard and M. Lampe. Thermal Conduction by Electrons in Stellar Matter. *Astrophysical Journal*, 18:297, 1969.

[74] G. A. Rinker. The electrical conductivity of an arbitrarily dense plasma. Technical Report LA-9872-MS, Los Alamos, 1984.

[75] G. A. Rinker. Electrical conductivity of a strongly coupled plasma. *Phys. Rev. B*, 31:4207–4219, 1985.

[76] R. Evans, B. L. Gyorffy, N. Szabo, and J. M. Ziman. The properties of liquid metals. Wiley, New York, 1973.

[77] D. A. Liberman, D. T. Cromer, and J. T. Waber. Relativistic self-consistent field program for atoms and ions. *Computer Physics Communications*, 2:107–113, 1971.

[78] G. A. Rinker. Thermal conductivity of a strongly coupled plasma. *Phys. Rev. B*, 31:4220–4229, 1985.

[79] G. A. Rinker. Systematic calculations of plasma transport coefficients for the periodic table. *Phys. Rev. A*, 37:1284–1297, 1988.

[80] R. J. Rogers, D. A. Young, H. E. DeWitt, and M. Ross. One-component plasma structure factor in tabular form. *Phys. Rev. A*, 28:2990–2992, 1983.

[81] D. O. Gericke, M. Murillo, and M. Schlanges. Dense plasma temperature equilibration in the binary collision approximation. *Phys. Rev. E*, 65:036418, 2002.

[82] M. P. Desjarlais. Practical improvements to the Lee-More conductivity near the metal-insulator transition. *Contributions to Plasma Physics*, 41:267–270, 2001.

[83] A. W. DeSilva and J. D. Katsouros. Electrical conductivity of dense copper and aluminum plasmas. *Phys. Rev. E*, 57:5945–5951, 1998.

[84] R. M. More. Pressure ionization, resonances, and the continuity of bound and free states. In D. R. Bates and B. Bederson, editors, *Advances in Atomic and Molecular Physics Volume 21*, Advances in Atomic and Molecular Physics, pages 305–356. Academic Press, Orlando, 1985.

[85] J. C. Pain, G. Dejonghe, and T. Blenski. Quantum mechanical model for the study of pressure ionization in the superconfiguration approach. *Journal of Physics A: Mathematical and General*, 39:4659–4666, 2006.

[86] D. A. Baiko, A. D. Kaminker, A. Y. Potekhin, and D. G. Yakovlev. Ion structure factors and electron transport in dense coulomb plasmas. *Phys. Rev. Lett.*, 81:5556–5559, 1998.

[87] S. B. Hansen. Private Communication, August 2018.

[88] A. Y. Potekhin, D. A. Baiko, P. Haensel, and D. G. Yakovlev. Transport properties of degenerate electrons in neutron star envelopes and white dwarf cores. *Astron. Astrophys.*, 346:345, 1999.

[89] S. Cassisi, A. Y. Potekhin, A. Pietrinferni, M. Catelan, and M. Salaris. Updated electron-conduction opacities: The impact on low-mass stellar models. *The Astrophysical Journal*, 661:1094, 2007.

[90] R. Franz and G. Wiedemann. Ueber die wärme-leitungsfähigkeit der metalle. *Annalen der Physik*, 165:497–531, 1853.

[91] R. Kubo. Statistical-mechanical theory of irreversible processes. I. general theory and simple applications to magnetic and conduction problems. *Journal of the Physical Society of Japan*, 12:570–586, 1957.

[92] R. Redmer. Physical properties of dense, low-temperature plasmas. *Physics Reports*, 282:35–157, 1997.

[93] J. M. Ziman. A theory of the electrical properties of liquid metals. I: The monovalent metals. *The Philosophical Magazine: A Journal of Theoretical Experimental and Applied Physics*, 6:1013–1034, 1961.

[94] C. E. Starrett, J. Clerouin, V. Recoules, J. D. Kress, L. A. Collins, and D. E. Hanson. Average atom transport properties for pure and mixed species in the hot and warm dense matter regimes. *Physics of Plasmas*, 19:102709, 2012.

[95] B. B. L. Witte, P. Sperling, M. French, V. Recoules, S. H. Glenzer, and R. Redmer. Observations of non-linear plasmon damping in dense plasmas. *Physics of Plasmas*, 25:56901, 2018.

[96] R. M. More, K. H. Warren, D. A. Young, and G. B. Zimmerman. A new quotidian equation of state (qeos) for hot dense matter. *The Physics of Fluids*, 31:3059–3078, 1988.

[97] S. C. Burnett, D. G. Sheppard, K. G. Honnell, and T. Sjostrom. Sesame-style decomposition of KS-DFT molecular dynamics for direct interrogation of nuclear models. *AIP Conference Proceedings*, 1979:030001, 2018.

[98] D. A. Young and E. M. Corey. A new global equation of state model for hot, dense matter. *Journal of Applied Physics*, 78:3748–3755, 1995.

[99] E. M. Corey and D. A. Young. A new prototype equation of state data library. *AIP Conference Proceedings*, 429:43–46, 1998.

[100] S. P. Lyon and J. D. Johnson. Sesame: the Los Alamos National Laboratory equation of state database. Technical Report LA-UR-92-3407, Los Alamos, 1992.

[101] V. Montoya. T-4 handbook of material properties data bases vol Ic: Equations of state. Technical Report LA-10160-MS, Los Alamos, 1984.

[102] J. I. Castor. *Radiation Hydrodynamics*, pages 179–211. Cambridge University Press, New York, 2004.

[103] I. Hubeny and D. Mihalas. *Theory of stellar atmospheres: an introduction to astrophysical non-equilibrium quantitative spectroscopic analysis*. Princeton series in astrophysics. Princeton University Press, Princeton, 2015.

[104] H. K. Chung, R. W. Lee, M. H. Chen, and Y. Ralchenko. *The How To For FLYCHK @ NIST*. NIST, 2008. `https://nlte.nist.gov/FLY/Doc/Manual_FLYCHK_Nov08.pdf`.

[105] H. K. Chung, M. H. Chen, W. L. Morgan, Y. Ralchenko, and R. W. Lee. FLYCHK: Generalized population kinetics and spectral model for rapid spectroscopic analysis for all elements. *High Energy Density Physics*, 1:3–12, 2005.

[106] H. A. Scott. Cretin–a radiative transfer capability for laboratory plasmas. *Journal of Quantitative Spectroscopy and Radiative Transfer*, 71:689–701, 2001.

[107] S. B. Hansen, J. Bauche, C. Bauche-Arnoult, and M. F. Gu. Hybrid atomic models for spectroscopic plasma diagnostics. *High Energy Density Physics*, 3:109–114, 2007.

[108] A. Bar-Shalom, M. Klapisch, and J. Oreg. HULLAC, an integrated computer package for atomic processes in plasmas. *Journal of Quantitative Spectroscopy and Radiative Transfer*, 71:169–188, 2001.

[109] M. F. Gu. The flexible atomic code. *Canadian Journal of Physics*, 86:675–689, 2008.

[110] S. B. Hansen. Balancing detail and completeness in collisional-radiative models. In Y. Ralchenko, editor, *Modern Methods in Collisional-Radiative Modeling of Plasmas. Springer Series on Atomic, Optical, and Plasma Physics, vol 90.*, pages 1–15. Springer, Cham, 2016.

[111] R. W. Lee, J. K. Nash, and Y. Ralchenko. Review of the NLTE kinetics code workshop. *Journal of Quantitative Spectroscopy and Radiative Transfer*, 58:737–742, 1997.

[112] C. Bowen, A. Decoster, C. J. Fontes, K. B. Fournier, O. Peyrusse, and Y. Ralchenko. Review of the NLTE emissivities code comparison virtual workshop. *Journal of Quantitative Spectroscopy and Radiative Transfer*, 81:71–84, 2003.

[113] C. Bowen, R. W. Lee, and Y. Ralchenko. Comparing plasma population kinetics codes: Review of the NLTE-3 Kinetics workshop. *Journal of Quantitative Spectroscopy and Radiative Transfer*, 99:102–119, 2006.

[114] J. G. Rubiano, R. Florido, C. Bowen, R. W. Lee, and Y. Ralchenko. Review of the 4th NLTE code comparison workshop. *High Energy Density Physics*, 3:225–232, 2007.

[115] C. J. Fontes, J. Abdallah, C. Bowen, R. W. Lee, and Y. Ralchenko. Review of the NLTE-5 kinetics workshop. *High Energy Density Physics*, 5:15–22, 2009.

[116] H. K. Chung, C. Bowen, C. J. Fontes, S. B. Hansen, and Y. Ralchenko. Comparison and analysis of collisional-radiative models at the NLTE-7 workshop. *High Energy Density Physics*, 9:645–652, 2013.

[117] R. Piron, F. Gilleron, Y. Aglitskiy, H. K. Chung, C. J. Fontes, S. B. Hansen, O. Marchuk, H. A. Scott, E. Stambulchik, and Y. Ralchenko. Review of the 9th NLTE code comparison workshop. *High Energy Density Physics*, 23:38–47, 2017.

[118] S. B. Hansen, H. K. Chung, C. J. Fontes, Yu. Ralchenko, H. A. Scott, and E. Stambulchik. Review of the 10th Non-LTE Code Comparison Workshop. *arXiv e-prints*, page 1903.09605, 2019.

[119] G. Ecker and W. Kröll. Lowering of the ionization energy for a plasma in thermodynamic equilibrium. *The Physics of Fluids*, 6:62–69, 1963.

[120] J. C. Stewart and K. D. Pyatt. Lowering of ionization potentials in plasmas. *Astrophysical Journal*, 144:1203, 1966.

[121] F. E. Irons. On the equality of the mean escape probability and mean net radiative bracket for line photons. *Monthly Notices of the Royal Astronomical Society*, 182:705–709, 1978.

[122] F. E. Irons. The escape factor in plasma spectroscopy–I. the escape factor defined and evaluated. *Journal of Quantitative Spectroscopy and Radiative Transfer*, 22:1–20, 1979.

[123] F. E. Irons. The escape factor in plasma spectroscopy–II. The case of radiative decay. *Journal of Quantitative Spectroscopy and Radiative Transfer*, 22:21–36, 1979.

[124] F. E. Irons. The escape factor in plasma spectroscopy–III. Two case studies. *Journal of Quantitative Spectroscopy and Radiative Transfer*, 22:37–44, 1979.

[125] F. E. Irons. The escape factor in plasma spectroscopy–IV. The case of an overlapping doublet. *Journal of Quantitative Spectroscopy and Radiative Transfer*, 24:119–132, 1980.

[126] R. C. Mancini, R. F. Joyce, and C. F. Hooper Jr. Escape factors for stark-broadened line profiles. *Journal of Physics B: Atomic and Molecular Physics*, 20:2975, 1987.

[127] A. K. Bhatia and S. O. Kastner. Local doppler-profile escape factors within the cylinder. *Journal of Quantitative Spectroscopy and Radiative Transfer*, 60:543–549, 1998.

[128] A. K. Bhatia and S. O. Kastner. Global and local doppler-profile escape factors for plane-parallel geometry. *Journal of Quantitative Spectroscopy and Radiative Transfer*, 67:55–63, 1999.

[129] G. J. Phillips, J. S. Wark, F. M. Kerr, S. J. Rose, and R. W. Lee. Escape factors in zero-dimensional radiation-transfer codes. *High Energy Density Physics*, 4:18–25, 2008.

[130] D. Strickland and G. Mourou. Compression of amplified chirped optical pulses. *Optics Communications*, 55:447–449, 1985.

[131] L. V. Keldysh. Ionization in the field of a strong electromagnetic wave. *Sov. Phys. JETP*, 20:1307, 1964.

[132] M. V. Fedorov. L. V. Keldysh's 'Ionization in the field of a strong electromagnetic wave' and modern physics of atomic interaction with a strong laser field. *Journal of Experimental and Theoretical Physics*, 122:449–455, 2016.

[133] S. C. Wilks and W. L. Kruer. Absorption of ultrashort, ultra-intense laser light by solids and overdense plasmas. *IEEE Journal of Quantum Electronics*, 33:1954–1968, 1997.

[134] P. Gibbon. *Short Pulse Laser Interactions with Matter*. Imperial College Press, London, 2005.

[135] W. L. Kruer. *The Physics of Laser Plasma Interactions*. Frontiers in physics. Westview Press, Boulder, 2003.

[136] S. Pfalzner and P. Gibbon. Direct calculation of inverse-bremsstrahlung absorption in strongly coupled, nonlinearly driven laser plasmas. *Phys. Rev. E*, 57:4698–4705, 1998.

[137] T. Y. B. Yang, W. L. Kruer, A. B. Langdon, and T. W. Johnston. Mechanisms for collisionless absorption of light waves obliquely incident on overdense plasmas with steep density gradients. *Physics of Plasmas*, 3:2702–2709, 1996.

[138] F. Brunel. Not-so-resonant, resonant absorption. *Phys. Rev. Lett.*, 59:52–55, 1987.

[139] W. L. Kruer and K. Estabrook. JxB heating by very intense laser light. *The Physics of Fluids*, 28:430–432, 1985.

[140] S. C. Wilks, W. L. Kruer, M. Tabak, and A. B. Langdon. Absorption of ultra-intense laser pulses. *Phys. Rev. Lett.*, 69:1383–1386, 1992.

[141] F. N. Beg, A. R. Bell, A. E. Dangor, C. N. Danson, A. P. Fews, M. E. Glinsky, B. A. Hammel, P. Lee, P. A. Norreys, and M. Tatarakis. A study of picosecond laser-solid interactions up to 10^{19} w cm^{-2}. *Physics of Plasmas*, 4:447–457, 1997.

[142] H. Chen, S. C. Wilks, W. L. Kruer, P. K. Patel, and R. Shepherd. Hot electron energy distributions from ultraintense laser solid interactions. *Physics of Plasmas*, 16:020705, 2009.

[143] M. G. Haines, M. S. Wei, F. N. Beg, and R. B. Stephens. Hot-electron temperature and laser-light absorption in fast ignition. *Phys. Rev. Lett.*, 102:045008, 2009.

[144] M. J. Berger, J. S. Coursey, and M. A. Zucker. ESTAR, PSTAR, and ASTAR: Computer programs for calculating stopping-power and range tables for electrons, protons, and helium ions. `http://physics.nist.gov/Star`, 1999. Accessed 2019-01-28.

[145] A. J. Mackinnon, Y. Sentoku, P. K. Patel, D. W. Price, S. Hatchett, M. H. Key, C. Andersen, R. Snavely, and R. R. Freeman. Enhancement of proton acceleration by hot-electron recirculation in thin foils irradiated by ultraintense laser pulses. *Phys. Rev. Lett.*, 88:215006, 2002.

[146] R. A. Snavely, M. H. Key, S. P. Hatchett, T. E. Cowan, M. Roth, T. W. Phillips, M. A. Stoyer, E. A. Henry, T. C. Sangster, M. S. Singh, S. C. Wilks, A. MacKinnon, A. Offenberger, D. M. Pennington, K. Yasuike, A. B. Langdon, B. F. Lasinski, J. Johnson, M. D. Perry, and E. M. Campbell. Intense high-energy proton beams from petawatt-laser irradiation of solids. *Phys. Rev. Lett.*, 85:2945–2948, 2000.

[147] M. Nakatsutsumi, R. Kodama, Y. Aglitskiy, K. U. Akli, D. Batani, S. D. Baton, F. N. Beg, A. Benuzzi-Mounaix, S. N. Chen, D. Clark, J. R. Davies, R. R. Freeman, J. Fuchs, J. S. Green, C. D. Gregory, P. Guillou, H. Habara, R. Heathcote, D. S. Hey, K. Highbarger, P. Jaanimagi, M. H. Key, M. Koenig, K. Krushelnick, K. L. Lancaster, B. Loupias, T. Ma, A. Macphee, A. J. Mackinonn, K. Mima, A. Morace, H. Nakamura, P. A. Norryes, D. Piazza, C. Rousseaux, R. B. Stephans, M. Storm, M. Tampo, W. Theobald, L. V. Woerkom, R. L. Weber, M. S. Wei, and N. C. Woolsey. Heating of solid target in electron refluxing dominated regime with ultra-intense laser. *Journal of Physics: Conference Series*, 112:022063, 2008.

[148] P. M. Nilson, W. Theobald, J. Myatt, C. Stoeckl, M. Storm, O. V. Gotchev, J. D. Zuegel, R. Betti, D. D. Meyerhofer, and T. C. Sangster. High-intensity laser-plasma interactions in the refluxing limit. *Physics of Plasmas*, 15:056308, 2008.

[149] J. Myatt, W. Theobald, J. A. Delettrez, C. Stoeckl, M. Storm, T. C. Sangster, A. V. Maximov, and R. W. Short. High-intensity laser interactions with mass-limited solid targets and implications for fast-ignition experiments on OMEGA EP. *Physics of Plasmas*, 14:056301, 2007.

[150] W. Theobald, K. Akli, R. Clarke, J. A. Delettrez, R. R. Freeman, S. Glenzer, J. Green, G. Gregori, R. Heathcote, N. Izumi, J. A. King, J. A. Koch, J. Kuba, K. Lancaster, A. J. MacKinnon, M. Key, C. Mileham, J. Myatt, D. Neely, P. A. Norreys, H.-S. Park, J. Pasley, P. Patel, S. P. Regan, H. Sawada, R. Shepherd, R. Snavely, R. B. Stephens, C. Stoeckl, M. Storm, B. Zhang, and T. C. Sangster. Hot surface ionic line emission and cold k-inner shell emission from petawatt-laser-irradiated cu foil targets. *Physics of Plasmas*, 13:043102, 2006.

[151] P. Neumayer, B. Aurand, M. Basko, B. Ecker, P. Gibbon, D. C. Hochhaus, A. Karmakar, E. Kazakov, T. Kühl, C. Labaune, O. Rosmej, An. Tauschwitz, B. Zielbauer, and D. Zimmer. The role of hot electron refluxing in laser-generated K-alpha sources. *Physics of Plasmas*, 17:103103, 2010.

[152] P. M. Nilson, W. Theobald, J. F. Myatt, C. Stoeckl, M. Storm, J. D. Zuegel, R. Betti, D. D. Meyerhofer, and T. C. Sangster. Bulk heating of solid-density plasmas during high-intensity-laser plasma interactions. *Phys. Rev. E*, 79:016406, 2009.

[153] Michael E. Glinsky. Regimes of suprathermal electron transport. *Physics of Plasmas*, 2:2796–2806, 1995.

[154] A. R. Bell, J. R. Davies, S. Guerin, and H. Ruhl. Fast-electron transport in high-intensity short-pulse laser - solid experiments. *Plasma Physics and Controlled Fusion*, 39:653, 1997.

[155] A. J. Kemp, Y. Sentoku, V. Sotnikov, and S. C. Wilks. Collisional relaxation of superthermal electrons generated by relativistic laser pulses in dense plasma. *Phys. Rev. Lett.*, 97:235001, 2006.

[156] C. R. D. Brown, D. J. Hoarty, S. F. James, D. Swatton, S. J. Hughes, J. W. Morton, T. M. Guymer, M. P. Hill, D. A. Chapman, J. E. Andrew, A. J. Comley, R. Shepherd, J. Dunn, H. Chen, M. Schneider, G. Brown, P. Beiersdorfer, and J. Emig. Measurements of electron transport in foils irradiated with a picosecond time scale laser pulse. *Phys. Rev. Lett.*, 106:185003, 2011.

[157] A. Compant La Fontaine. X-ray emission reduction and photon dose lowering by energy loss of fast electrons induced by return current during the interaction of a short-pulse high-intensity laser on a metal solid target. *Physics of Plasmas*, 25:043301, 2018.

[158] S. C. Wilks, A. B. Langdon, T. E. Cowan, M. Roth, M. Singh, S. Hatchett, M. H. Key, D. Pennington, A. MacKinnon, and R. A. Snavely. Energetic proton generation in ultra-intense laser-solid interactions. *Physics of Plasmas*, 8:542–549, 2001.

[159] M. Hegelich, S. Karsch, G. Pretzler, D. Habs, K. Witte, W. Guenther, M. Allen, A. Blazevic, J. Fuchs, J. C. Gauthier, M. Geissel, P. Audebert, T. Cowan, and M. Roth. Mev ion jets from short-pulse-laser interaction with thin foils. *Phys. Rev. Lett.*, 89:085002, 2002.

[160] E. L. Clark, K. Krushelnick, J. R. Davies, M. Zepf, M. Tatarakis, F. N. Beg, A. Machacek, P. A. Norreys, M. I. K. Santala, I. Watts, and A. E. Dangor. Measurements of energetic proton transport through magnetized plasma from intense laser interactions with solids. *Phys. Rev. Lett.*, 84:670–673, 2000.

[161] S. P. Hatchett, C. G. Brown, T. E. Cowan, E. A. Henry, J. S. Johnson, M. H. Key, J. A. Koch, A. B. Langdon, B. F. Lasinski, R. W. Lee, A. J. Mackinnon, D. M. Pennington, M. D. Perry, T. W. Phillips, M. Roth, T. C. Sangster, M. S. Singh, R. A. Snavely, M. A. Stoyer, S. C. Wilks, and K. Yasuike. Electron, photon, and ion beams from the relativistic interaction of petawatt laser pulses with solid targets. *Physics of Plasmas*, 7:2076–2082, 2000.

[162] A. Maksimchuk, S. Gu, K. Flippo, D. Umstadter, and V. Yu. Bychenkov. Forward ion acceleration in thin films driven by a high-intensity laser. *Phys. Rev. Lett.*, 84:4108–4111, 2000.

[163] K. Krushelnick, E. L. Clark, M. Zepf, J. R. Davies, F. N. Beg, A. Machacek, M. I. K. Santala, M. Tatarakis, I. Watts, P. A. Norreys, and A. E. Dangor. Energetic proton production from relativistic laser interaction with high density plasmas. *Physics of Plasmas*, 7:2055–2061, 2000.

[164] P. K. Patel, A. J. Mackinnon, M. H. Key, T. E. Cowan, M. E. Foord, M. Allen, D. F. Price, H. Ruhl, P. T. Springer, and R. Stephens. Isochoric heating of solid-density matter with an ultrafast proton beam. *Phys. Rev. Lett.*, 91:125004, 2003.

[165] G. M. Dyer, A. C. Bernstein, B. I. Cho, J. Osterholz, W. Grigsby, A. Dalton, R. Shepherd, Y. Ping, H. Chen, K. Widmann, and T. Ditmire. Equation-of-state measurement of dense plasmas heated with fast protons. *Phys. Rev. Lett.*, 101:015002, 2008.

[166] W. Bang, B. J. Albright, P. A. Bradley, E. L. Vold, J. C. Boettger, and J. C. Fernández. Uniform heating of materials into the warm dense matter regime with laser-driven quasimonoenergetic ion beams. *Phys. Rev. E*, 92:063101, 2015.

[167] J. Kim, C. McGuffey, B. Qiao, M. S. Wei, P. E. Grabowski, and F. N. Beg. Varying stopping and self-focusing of intense proton beams as they heat solid density matter. *Physics of Plasmas*, 23:043104, 2016.

[168] S. N. Chen, S. Atzeni, T. Gangolf, M. Gauthier, D. P. Higginson, R. Hua, J. Kim, F. Mangia, C. McGuffey, J. R. Marquès, R. Riquier, H. Pépin, R. Shepherd, O. Willi, F. N. Beg, C. Deutsch, and J. Fuchs. Experimental evidence for the enhanced and reduced stopping regimes for protons propagating through hot plasmas. *Scientific Reports*, 8:14586, 2018.

[169] S. P. Ahlen. Theoretical and experimental aspects of the energy loss of relativistic heavily ionizing particles. *Rev. Mod. Phys.*, 52:121–173, 1980.

[170] L. B. Fletcher, H. J. Lee, T. Döppner, E. Galtier, B. Nagler, P. Heimann, C. Fortmann, S. LePape, T. Ma, M. Millot, A. Pak, D. Turnbull, D. A. Chapman, D. O. Gericke, J. Vorberger, T. White, G. Gregori, M. Wei, B. Barbrel, R. W. Falcone, C. C. Kao, H. Nuhn, J. Welch, U. Zastrau, P. Neumayer, J. B. Hastings, and S. H. Glenzer. Ultrabright X-ray laser scattering for dynamic warm dense matter physics. *Nature Photonics*, 9:274–279, 2015.

[171] H. A. Kramers. XCIII. On the theory of X-ray absorption and of the continuous X-ray spectrum. *The London, Edinburgh, and Dublin Philosophical Magazine and Journal of Science*, 46:836–871, 1923.

[172] Y. Sentoku, I. Paraschiv, R. Royle, R. C. Mancini, and T. Johzaki. Kinetic effects and nonlinear heating in intense x-ray-laser-produced carbon plasmas. *Phys. Rev. E*, 90:051102, 2014.

[173] M. O. Krause. Atomic radiative and radiationless yields for K and L shells. *Journal of Physical and Chemical Reference Data*, 8:307–327, 1979.

[174] F. P. Larkins. Semiempirical Auger-electron energies for elements $10 \leq Z \leq 100$. *Atomic Data and Nuclear Data Tables*, 20:311–387, 1977.

[175] J. Park, H. A. Baldis, and H. Chen. The implementation and data analysis of an interferometer for intense short pulse laser experiments. *High Power Laser Science and Engineering*, 4:e26, 2016.

[176] J. Feldhaus, J. Arthur, and J. B. Hastings. X-ray free-electron lasers. *Journal of Physics B: Atomic, Molecular and Optical Physics*, 38:S799, 2005.

[177] W. Amann, J.and Berg, V. Blank, F.-J. Decker, Y. Ding, P. Emma, Y. Feng, J. Frisch, D. Fritz, J. Hastings, Z. Huang, J. Krzywinski, R. Lindberg, H. Loos, A. Lutman, H. D. Nuhn, D. Ratner, J. Rzepiela, D. Shu, Yu Shvyd'ko, S. Spampinati, S. Stoupin, S. Terentyev, E. Trakhtenberg, D. Walz, J. Welch, J. Wu, A. Zholents, and D. Zhu. Demonstration of self-seeding in a hard-x-ray free-electron laser. *Nature Photonics*, 6:693, 2012.

[178] C. Bostedt, S. Boutet, D. M. Fritz, Z. Huang, H. J. Lee, H. T. Lemke, A. Robert, W. F. Schlotter, J. J. Turner, and G. J. Williams. Linac coherent light source: The first five years. *Rev. Mod. Phys.*, 88:015007, 2016.

[179] B. Nagler, B. Arnold, G. Bouchard, R. F. Boyce, R. M. Boyce, A. Callen, M. Campell, R. Curiel, E. Galtier, J. Garofoli, E. Granados, J. Hastings, G. Hays, P. Heimann, R. W. Lee, D. Milathianaki, L. Plummer, A. Schropp, A. Wallace, M. Welch, W. White, Z. Xing, J. Yin, J. Young, U. Zastrau, and H. J. Lee. The Matter in Extreme Conditions instrument at the Linac Coherent Light Source. *Journal of Synchrotron Radiation*, 22:520–525, 2015.

[180] N. Hopps, C. Danson, S. Duffield, D. Egan, S. Elsmere, M. Girling, E. Harvey, D. Hillier, M. Norman, S. Parker, P. Treadwell, D. Winter, and T. Bett. Overview of laser systems for the Orion facility at the AWE. *Appl. Opt.*, 52:3597–3607, 2013.

[181] N. Hopps, K. Oades, J. Andrew, C. Brown, G. Cooper, C. Danson, S. Daykin, S. Duffield, R. Edwards, D. Egan, S. Elsmere, S. Gales, M. Girling, E. Gumbrell, E. Harvey, D. Hillier, D. Hoarty, C. Horsfield, S. James, A. Leatherland, S. Masoero, A. Meadowcroft, M. Norman, S. Parker, S. Rothman, M. Rubery, P. Treadwell, D. Winter, and T. Bett. Comprehensive description of the Orion Laser Facility. *Plasma Physics and Controlled Fusion*, 57:064002, 2015.

[182] S. Parker, C. Danson, D. Egan, S. Elsmere, M. Girling, E. Harvey, D. Hillier, D. Hussey, S. Masoero, and J. McLoughlin. 400 TW operation of Orion at ultra-high contrast. *High Power Laser Science and Engineering*, 6:e47, 2018.

[183] D. I. Hillier, S. Elsmere, M. Girling, N. Hopps, D. Hussey, S. Parker, P. Treadwell, D. Winter, and T. Bett. Contrast enhancements to petawatt lasers using short pulse optical parametric amplifiers and frequency doubling. *Appl. Opt.*, 53:6938–6943, 2014.

[184] M. M. Murnane, H. C. Kapteyn, and R. W. Falcone. Xray streak camera with 2 ps response. *Applied Physics Letters*, 56:1948–1950, 1990.

[185] D. J. Bradley, A. G. Roddie, W. Sibbett, M. H. Key, M. J. Lamb, C. L. S. Lewis, and P. Sachsenmaier. Picosecond x-ray chronoscopy. *Optics Communications*, 15:231–236, 1975.

[186] Z. Chang, A. Rundquist, H. Wang, M. Murnane, H. C. Kapteyn, X. Liu, B. Shan, J. Liu, L. Niu, M. Gong, X. Zhang, and R. W. Lee. Demonstration of a 0.54-ps x-ray streak camera. *Proc. of SPIE*, 2869:971–976, 1997.

[187] R. Kalibjian. Space-charge temporal broadening effects in streak-camera tubes. *Proc. of SPIE*, 0189:452–455, 1979.

[188] B. Qian and H. E. Elsayed-Ali. Electron pulse broadening due to space charge effects in a photoelectron gun for electron diffraction and streak camera systems. *Journal of Applied Physics*, 91:462–468, 2002.

[189] S. O. Flyckt and C. Marmonier. Photomultiplier tubes principles and applications. Technical report, Photonis, 2002.

[190] B .L. Henke, J. A. Smith, and D. T. Attwood. 0.1–10-kev x-ray-induced electron emissions from solids–Models and secondary electron measurements. *Journal of Applied Physics*, 48:1852–1866, 1977.

[191] Burton L. Henke, John Liesegang, and Steven D. Smith. Soft-x-ray-induced secondary-electron emission from semiconductors and insulators: Models and measurements. *Phys. Rev. B*, 19:3004–3021, 1979.

[192] B .L. Henke, J. P. Knauer, and K. Premaratne. The characterization of x-ray photocathodes in the 0.1–10kev photon energy region. *Journal of Applied Physics*, 52:1509–1520, 1981.

[193] Axis-px: Subpicosecond x-ray streak camera. `https://www.axis-photon.com/streak-camera/axis-px-subpicosecond-x-ray-streak-camera/`. Accessed 2018-12-16.

[194] M. H. Edwards, N. Booth, Z. Zhai, G. J. Tallents, T. Dzelzainis, C. L. S. Lewis, P. Foster, M. Streeter, and D. Neely. Space charge effects in the Axis-Photonique PX-1 x-ray streak camera. *Proc. of SPIE*, 6703:67030L–67030L–7, 2007.

[195] R. Shepherd, R. Booth, D. Price, M. Bowers, D. Swan, J. Bonlie, B. Young, J. Dunn, B. White, and R. Stewart. Ultrafast x-ray streak camera for use in ultrashort laser-produced plasma research. *Review of Scientific Instruments*, 66:719–721, 1995.

[196] E. V. Marley, R. Shepherd, S. Fulkerson, L. James, J. Emig, and D. Norman. Ultra fast x-ray streak camera for ten inch manipulator based platforms. *Review of Scientific Instruments*, 83:10E106, 2012.

[197] J. R. Mahan. *Radiation Heat Transfer A Statistical Approach*, pages 26–68. John Wiley & Sons, New York, 2002.

[198] S. Patankar, E. T. Gumbrell, T. S. Robinson, E. Floyd, N. H. Stuart, A. S. Moore, J. W. Skidmore, and R. A. Smith. Absolute calibration of optical streak cameras on picosecond time scales using supercontinuum generation. *Appl. Opt.*, 56:6982–6987, 2017.

[199] D. Mihalas. *Stellar Atmospheres*. Astronomy and Astrophysics Series. W. H. Freeman and Co., San Francisco, second edition, 1978.

[200] S. Rebibo, J. P. Geindre, P. Audebert, G. Grillon, J. P. Chambaret, and J. C. Gauthier. Single-shot spectral interferometry of femtosecond laser-produced plasmas. *Laser and Particle Beams*, 19:67–73, 2001.

[201] J. J. Thomson. Bakerian Lecture—Rays of positive electricity. *Proceedings of the Royal Society of London A: Mathematical, Physical and Engineering Sciences*, 89:1–20, 1913.

[202] C. G. Freeman, G. Fiksel, C. Stoeckl, N. Sinenian, M. J. Canfield, G. B. Graeper, A. T. Lombardo, C. R. Stillman, S. J. Padalino, C. Mileham, T. C. Sangster, and J. A. Frenje. Calibration of a Thomson parabola ion spectrometer and Fujifilm imaging plate detectors for protons, deuterons, and alpha particles. *Review of Scientific Instruments*, 82:073301, 2011.

[203] W. H. Bragg and W. L. Bragg. The reflection of x-rays by crystals. *Proceedings of the Royal Society of London A: Mathematical, Physical and Engineering Sciences*, 88:428–438, 1913.

[204] L. N. Koppel and J. D. Eckels. High resolution x-ray crystal spectrographs. Technical Report UCRL-79781, Lawrence Livermore National Laboratory, 1977.

[205] L. Beck, P. Stemmler, and F. Legrand. Measurement of the x-ray spectrometric properties of cesium hydrophthalate (CsAP) crystal with the synchrotron radiation. *Review of Scientific Instruments*, 66:1601–1603, 1995.

[206] A. L. Meadowcroft, C. D. Bentley, and E. N. Stott. Evaluation of the sensitivity and fading characteristics of an image plate system for x-ray diagnostics. *Review of Scientific Instruments*, 79:113102, 2008.

[207] B. R. Maddox, H. S. Park, B. A. Remington, N. Izumi, S. Chen, C. Chen, G. Kimminau, Z. Ali, M. J. Haugh, and Q. Ma. High-energy x-ray backlighter spectrum measurements using calibrated image plates. *Review of Scientific Instruments*, 82:023111, 2011.

[208] T. Bonnet, M. Comet, D. Denis-Petit, F. Gobet, F. Hannachi, M. Tarisien, M. Versteegen, and M. M. Alonard. Response functions of imaging plates to photons, electrons and 4He particles. *Review of Scientific Instruments*, 84:103510, 2013.

[209] G. Boutoux, D. Batani, F. Burgy, J.-E. Ducret, P. Forestier-Colleoni, S. Hulin, N. Rabhi, A. Duval, L. Lecherbourg, C. Reverdin, K. Jakubowska, C. I. Szabo, S. Bastiani-Ceccotti, F. Consoli, A. Curcio, R. De Angelis, F. Ingenito, J. Baggio, and D. Raffestin. Validation of modelled imaging plates sensitivity to 1-100 kev x-rays and spatial resolution characterisation for diagnostics for the petawatt Aquitaine Laser. *Review of Scientific Instruments*, 87:043108, 2016.

[210] D. Dobson. Earth's core problem. *Nature*, 534:45, 2016.

[211] Da.E. Hanson, L. A. Collins, J. D. Kress, and M. P. Desjarlais. Calculations of the thermal conductivity of national ignition facility target materials at temperatures near 10 ev and densities near 10 g/cc using finite-temperature quantum molecular dynamics. *Physics of Plasmas*, 18:082704, 2011.

[212] S. X. Hu, L. A. Collins, T. R. Boehly, J. D. Kress, V. N. Goncharov, and S. Skupsky. First-principles thermal conductivity of warm-dense deuterium plasmas for inertial confinement fusion applications. *Phys. Rev. E*, 89:043105, 2014.

[213] S. X. Hu, L. A. Collins, V. N. Goncharov, J. D. Kress, R. L. McCrory, and S. Skupsky. First-principles investigations on ionization and thermal conductivity of polystyrene for inertial confinement fusion applications. *Physics of Plasmas*, 23:042704, 2016.

[214] R. L. Shepherd, D. R. Kania, and L. A. Jones. Measurement of the resistivity in a partially degenerate, strongly coupled plasma. *Phys. Rev. Lett.*, 61:1278–1281, 1988.

[215] J. F. Benage, W. R. Shanahan, and M. S. Murillo. Electrical resistivity measurements of hot dense aluminum. *Phys. Rev. Lett.*, 83:2953–2956, 1999.

[216] H. M. Milchberg, R. R. Freeman, S. C. Davey, and R. M. More. Resistivity of a simple metal from room temperature to 10^6 K. *Phys. Rev. Lett.*, 61:2364–2367, 1988.

[217] K. Widmann, T. Ao, M. E. Foord, D. F. Price, A. D. Ellis, P. T. Springer, and A. Ng. Single-state measurement of electrical conductivity of warm dense gold. *Phys. Rev. Lett.*, 92:125002, 2004.

[218] J. Zheng, K. A. Tanaka, T. Miyakoshi, Y. Kitagawa, R. Kodama, T. Kurahashi, and T. Yamanaka. Spectrum of transition radiation from hot electrons generated in ultra-intense laser plasma interaction. *Physics of Plasmas*, 9:3610–3616, 2002.

[219] M. N. Polyanskiy. Refractive index database. `https://refractiveindex.info`. Date accessed: 2018-11-22.

[220] Y. Ping, D. Hanson, I. Koslow, T. Ogitsu, D. Prendergast, E. Schwegler, G. Collins, and A. Ng. Broadband dielectric function of nonequilibrium warm dense gold. *Phys. Rev. Lett.*, 96:255003, 2006.

[221] M. M. Marinak, R. E. Tipton, O. L. Landen, T. J. Murphy, P. Amendt, S. W. Haan, S. P. Hatchett, C. J. Keane, R. McEachern, and R. Wallace. Three-dimensional simulations of Nova high growth factor capsule implosion experiments. *Physics of Plasmas*, 3:2070–2076, 1996.

[222] H. Betz. Charge states and charge-changing cross sections of fast heavy ions penetrating through gaseous and solid media. *Rev. Mod. Phys.*, 44:465–539, 1972.

[223] T. Peter and J. Meyer-ter Vehn. Energy loss of heavy ions in dense plasma. I. Linear and nonlinear Vlasov theory for the stopping power. *Phys. Rev. A*, 43:1998–2014, 1991.

[224] J. A. Fleck and J. D. Cummings. An implicit Monte Carlo scheme for calculating time and frequency dependent nonlinear radiation transport. *Journal of Computational Physics*, 8:313–342, 1971.

[225] S. D. Crockett. Analysis of Sesame 3720, a new aluminum equation of state. Technical Report LA-UR-04-6442, Los Alamos, 2004.

[226] H. M. Milchberg and R. R. Freeman. Light absorption in ultrashort scale length plasmas. *J. Opt. Soc. Am. B*, 6:1351–1355, 1989.

[227] M. Basko, T. Löwer, V. N. Kondrashov, A. Kendl, R. Sigel, and J. Meyer-ter Vehn. Optical probing of laser-induced indirectly driven shock waves in aluminum. *Phys. Rev. E*, 56:1019–1031, 1997.

[228] P. Celliers and A. Ng. Optical probing of hot expanded states produced by shock release. *Phys. Rev. E*, 47:3547–3565, 1993.

[229] N. J. Hartley, P. Belancourt, D. A. Chapman, T. Döppner, R. P. Drake, D. O. Gericke, S. H. Glenzer, D. Khaghani, S. LePape, T. Ma, P. Neumayer, A. Pak, L. Peters, S. Richardson, J. Vorberger, T. G. White, and G. Gregori. Electron-ion temperature equilibration in warm dense tantalum. *High Energy Density Physics*, 14:1–5, 2015.

[230] D. R. Gray, J. D. Kilkenny, M. S. White, P. Blyth, and D. Hull. Observation of severe heat-flux limitation and ion-acoustic turbulence in a laser-heated plasma. *Phys. Rev. Lett.*, 39:1270–1273, 1977.

[231] R. J. Henchen, M. Sherlock, W. Rozmus, J. Katz, P. E. Masson-Laborde, D. Cao, J. P. Palastro, and D. H. Froula. Measuring heat flux from collective Thomson scattering with non-Maxwellian distribution functions. *Physics of Plasmas*, 26:032104, 2019.

[232] A. R. Bell. Non-Spitzer heat flow in a steadily ablating laser-produced plasma. *The Physics of Fluids*, 28:2007–2014, 1985.

[233] P. Mora and H. Yahi. Thermal heat-flux reduction in laser-produced plasmas. *Phys. Rev. A*, 26:2259–2261, 1982.

[234] H. Reinholz, G. Röpke, S. Rosmej, and R. Redmer. Conductivity of warm dense matter including electron-electron collisions. *Phys. Rev. E*, 91:043105, 2015.

[235] M. P. Desjarlais, C. R. Scullard, L. X. Benedict, H. D. Whitley, and R. Redmer. Density-functional calculations of transport properties in the nondegenerate limit and the role of electron-electron scattering. *Phys. Rev. E*, 95:033203, 2017.

[236] E. Floyd, E. T. Gumbrell, J. Fyrth, J. D. Luis, J. W. Skidmore, S. Patankar, S. Giltrap, and R. Smith. A high spatio-temporal resolution optical pyrometer at the ORION laser facility. *Review of Scientific Instruments*, 87:11E546, 2016.

[237] P. B. Johnson and R. W. Christy. Optical constants of the noble metals. *Phys. Rev. B*, 6:4370–4379, 1972.

[238] P. B. Johnson and R. W. Christy. Optical constants of transition metals: Ti, V, Cr, Mn, Fe, Co, Ni, and Pd. *Phys. Rev. B*, 9:5056–5070, 1974.

[239] T. R. Mattsson and M. P. Desjarlais. Equation of state and electrical conductivity of stainless steel. Technical Report SAND 2004-5253, Sandia National Laboratories, 2004.

[240] S. P. Hau-Riege and T. Pardini. The effect of electron transport on the characterization of x-ray free-electron laser pulses via ablation. *Applied Physics Letters*, 111:144102, 2017.

[241] H. R. Griem. *Principles of Plasma Spectroscopy*. Cambridge Monographs on Plasma Physics. Cambridge University Press, Cambridge, 1997.

[242] H. J. Kunze. *Introduction to Plasma Spectroscopy*. Springer Series on Atomic, Optical, and Plasma Physics. Springer Berlin Heidelberg, New York, 2009.

[243] D. J. Hoarty, P. Allan, S. F. James, C. R. D. Brown, L. M. R. Hobbs, M. P. Hill, J. W. O. Harris, J. Morton, M. G. Brookes, R. Shepherd, J. Dunn, H. Chen, E. Von Marley, P. Beiersdorfer, H. K. Chung, R. W. Lee, G. Brown, and J. Emig. The first data from the Orion laser; measurements of the spectrum of hot, dense aluminium. *High Energy Density Physics*, 9:661 – 671, 2013.

[244] D. J. Hoarty, E. Hill, P. Beiersdorfer, P. Allan, C. R. D. Brown, M. P. Hill, L. M. R. Hobbs, S. F. James, J. Morton, N. Sircombe, L. Upcraft, J. W. O. Harris, R. Shepherd, E. V. Marley, E. Magee, J. Emig, J. Nilsen, and S. J. Rose. Measurements of plasma spectra from hot dense elements and mixtures at conditions relevant to the solar radiative zone. *AIP Conference Proceedings*, 1811:050001, 2017.

[245] A. C. Bourgaux, S. Bastiani-Ceccotti, P. Audebert, J. R. Marquès, L. Vassura, T. Vinci, F. Dorchies, P. M. Leguay, H. K. Chung, C. Bowen, V. Dervieux, P. Renaudin, V. Silvert, and S. Jacquemot. X-ray emission spectroscopy of well-characterised non-LTE plasmas. *Journal of Physics: Conference Series*, 688:012039, 2016.

[246] F. M. Kerr, S. J. Rose, J. S. Wark, and F. P. Keenan. Enhancement of optically thick to thin line intensities in solar and stellar coronal plasmas through radiative transfer effects: An angularly resolved study. *The Astrophysical Journal Letters*, 613:L181, 2004.

[247] A. M. Dumont, S. Collin, F. Paletou, S. Coupé, O. Godet, and D. Pelat. Escape probability methods versus ”exact” transfer for modeling the X-ray spectrum of Active Galactic Nuclei and X-ray binaries. *A&A*, 407:13–30, 2003.

[248] E. Minguez, R. Rodriguez, J.M. Gil, P. Sauvan, R. Florido, J.G. Rubiano, P. Martel, and R. Mancini. Opacities and line transfer in high density plasma. *Laser and Particle Beams*, 23:199–203, 2005.

[249] L. Godbert, A. Calisti, R. Stamm, B. Talin, R. Lee, and L. Klein. Plasma diagnostics with spectral profile calculations. *Phys. Rev. E*, 49:5644–5651, 1994.

[250] R. W. Lee and J. T. Larsen. A time-dependent model for plasma spectroscopy of K-shell emitters. *Journal of Quantitative Spectroscopy and Radiative Transfer*, 56:535–556, 1996.

[251] J. P. Apruzese. An analytic Voigt profile escape probability approximation. *Journal of Quantitative Spectroscopy and Radiative Transfer*, 34:447–452, 1985.

[252] J. P. Apruzese, J. L. Giuliani, and S. B. Hansen. Benchmarking multilevel, 2-D cylindrical radiation transport in a high energy density plasma environment. *High Energy Density Physics*, 8:231–237, 2012.

[253] F. M. Kerr, S. J. Rose, J. S. Wark, and F. P. Keenan. An analytic geometry-variant approach to line ratio enhancement above the optically thin limit. *The Astrophysical Journal*, 629:1091, 2005.

[254] D. J. Hoarty, N. Sircombe, P. Beiersdorfer, C. R. D Brown, M.P. Hill, L.M R. Hobbs, S.F. James, J Morton, E. Hill, M. Jeffery, J.W.O Harris, R. Shepherd, E. V. Marley, E. Magee, J. Emig, J. Nilsen, H.K. Chung, R.W. Lee, and S.J. Rose. Modelling K-shell spectra from short pulse heated buried microdot targets. *High Energy Density Physics*, 23:178–183, 2017.

[255] E. V. Marley. *The production and spectroscopic characterization of high temperature high density pleamsas with minimal gradients*. PhD thesis, University of California Davis, 2016.

[256] V. Dervieux, B. Loupias, S. Baton, L. Lecherbourg, K. Glize, C. Rousseaux, C. Reverdin, L. Gremillet, C. Blancard, V. Silvert, J.-C. Pain, C.R.D. Brown, P. Allan, M.P. Hill, D.J. Hoarty, and P. Renaudin. Characterization of near-LTE, high-temperature and high-density aluminum plasmas produced by ultra-high intensity lasers. *High Energy Density Physics*, 16:12–17, 2015.

[257] K. Nazir, S. J. Rose, A. Djaoui, G. J. Tallents, M. G. Holden, P. A. Norreys, P. Fews, J. Zhang, and F. Failles. X-ray spectroscopic studies of hot, dense iron plasma formed by subpicosecond high intensity KrF laser irradiation. *Applied Physics Letters*, 69:3686–3688, 1996.

[258] B. K. F. Young, B. G. Wilson, D. F. Price, and R. E. Stewart. Measurement of x-ray emission and thermal transport in near-solid-density plasmas heated by 130 fs laser pulses. *Phys. Rev. E*, 58:4929–4936, 1998.

[259] K. B. Fournier, B. K. F. Young, S. J. Moon, M. E. Foord, D. F. Price, R. L. Shepherd, and P. T. Springer. Characterization of time resolved, buried layer plasmas produced by ultra-short laser pulses. *Journal of Quantitative Spectroscopy and Radiative Transfer*, 71:339–354, 2001.

[260] D. J. Hoarty, J. W. O. Harris, P. Graham, S. J. Davidson, S. F. James, B. J. B. Crowley, E. L. Clark, C. C. Smith, and L. Upcraft. Measurements of niobium absorption spectra in plasmas with nearly full M-shell configurations. *High Energy Density Physics*, 3:325 – 334, 2007.

[261] D. J. Hoarty, S. F. James, C. R. D. Brown, B. M. Williams, H. K. Chung, J. W. O. Harris, L. Upcraft, B. J. B. Crowley, C. C. Smith, and R. W. Lee. Measurements of emission spectra from hot, dense germanium plasma in short pulse laser experiments. *High Energy Density Physics*, 6:105–108, 2010.

[262] P. Beiersdorfer, E. W. Magee, G. V. Brown, H. Chen, J. Emig, N. Hell, M. Bitter, K. W. Hill, P. Allan, C. R. D. Brown, M. P. Hill, D. J. Hoarty, L. M. R. Hobbs, and S. F. James. Lineshape spectroscopy with a very high resolution, very high signal-to-noise crystal spectrometer. *Review of Scientific Instruments*, 87:063501, 2016.

[263] P. Kirkpatrick and A. V. Baez. Formation of optical images by X-rays. *J. Opt. Soc. Am.*, 38:766–774, 1948.

[264] G. Fiksel, F. J. Marshall, C. Mileham, and C. Stoeckl. Note: Spatial resolution of Fuji BAS-TR and BAS-SR imaging plates. *Review of Scientific Instruments*, 83:086103, 2012.

[265] T. O'Haver. A pragmatic introduction to signal processing. `https://terpconnect.umd.edu/%7Etoh/spectrum/`, 2019. Accessed: 2019-06-10.

[266] E. V. Marley, R. Shepherd, P. Beiersdorfer, G. Brown, H. Chen, J. Dunn, M. Foord, H. Scott, R. London, A.B. Steel, D. Hoarty, S. James, C.R.D. Brown, M. Hill, P. Allan, and L. Hobbs. Measurement and simulation of the temperature evolution of a short pulse laser heated buried layer target. *High Energy Density Physics*, 25:15–19, 2017.

[267] H. Chen, R. Shepherd, H. K. Chung, A. Kemp, S. B. Hansen, S. C. Wilks, Y. Ping, K. Widmann, K. B. Fournier, G. Dyer, A. Faenov, T. Pikuz, and P. Beiersdorfer. Fast-electron-relaxation measurement for laser-solid interaction at relativistic laser intensities. *Phys. Rev. E*, 76:056402, 2007.

[268] S. Feldman, G. Dyer, D. Kuk, and T. Ditmire. Measurement of the equation of state of solid-density copper heated with laser-accelerated protons. *Phys. Rev. E*, 95:031201, 2017.

[269] B. I. Cho, T. Ogitsu, K. Englehorn, A. A. Correa, Y. Ping, J. W. Lee, L. J. Bae, D. Prendergast, R. W. Falcone, and P. A. Heimann. Measurement of electron-ion relaxation in warm dense copper. *Scientific Reports*, 6:18843, 2016.

[270] J. N. Glosli, F. R. Graziani, R. M. More, M. S. Murillo, F. H. Streitz, M. P. Surh, L. X. Benedict, S. Hau-Riege, A. B. Langdon, and R. A. London. Molecular dynamics simulations of temperature equilibration in dense hydrogen. *Phys. Rev. E*, 78:025401, 2008.

[271] C. R. Scullard, S. Serna, L. X. Benedict, C. L. Ellison, and F. R. Graziani. Analytic expressions for electron-ion temperature equilibration rates from the Lenard-Balescu equation. *Phys. Rev. E*, 97:013205, 2018.